



Corrosion Mechanisms and Structural Performance Evolution of Alkali-Activated Fly Ash
and Slag Concretes

Feng Zhang

Department of Civil and Environmental Engineering
University of Strathclyde, Glasgow

Thesis submitted to the Department of Civil and Environmental Engineering, University of
Strathclyde, Glasgow, in fulfilment of the requirement for the degree of Doctor of Philosophy

February 2025

Declaration of authenticity and author's right

This thesis is the result of the author's original research. It has been composed by the author and has not been previously submitted for examination which has led to the award of a degree. The copyright of this thesis belongs to the author under the terms of the United Kingdom Copyright Acts as qualified by University of Strathclyde Regulation 3.50. Due acknowledgment must always be made of the use of any material contained in, or derived from, this thesis.

Signature and Date:

Feng Zhang 24/02/2025

Acknowledgements

I would like to express my deepest gratitude to my supervisor, Dr. Shangtong Yang, for his unwavering support throughout this research. I am truly thankful for his patience, understanding, and expert guidance, which have been invaluable in leading me toward the successful completion of this dissertation. His support has not only enabled me to conduct meaningful research but has also provided me with opportunities to grow both personally and professionally.

A heartfelt thanks goes to the lab technicians, James Francis, Gain Gibson, Derek McNee, Tatyana Peshkur, and our lab manager, Mara Knapp, for their diligent assistance in teaching me how to utilise the equipment and providing technical support on specialised, non-standard questions.

I would also like to extend my sincere appreciation to my colleagues, Qinxin Hu, Dr. Guijie Sang, Dr. Xun Xi, Dr. Huachuan Wang, Dr. Hamish Dow, and Dr. Qi Zhang for their valuable knowledge, help, friendship and support throughout my research. Their kindness and encouragement have made my experience abroad both manageable and memorable.

Finally, I would like to thank my family, who have been a constant source of inspiration, support, and encouragement. Without their unwavering backing, I could never have reached my goals.

Abstract

Alkali-activated materials (AAMs) have garnered significant interest as sustainable alternatives to Portland cement, playing an important role in the transition towards a low-carbon society. This research is focused on understanding the chloride-ingress-induced corrosion in reinforced alkali-activated fly ash and slag (AAFS) mortars and their structural implications.

The influence of aggregate types (gravel and limestone) and precursor composition on the mechanical and fracture properties of AAFS concrete and mortar were investigated. While concrete generally shows lower compressive strength than mortar, the 50SA-50FA gravel and 30SA-70FA limestone concretes exhibit higher strength due to improved particle distribution and precursor effects. Furthermore, limestone aggregates further enhance fracture energy and toughness compared to gravel. Additionally, increasing slag content boosts early strength and toughness but also increases brittleness of AAFS concrete.

By systematically investigating electrochemical parameters, including corrosion potential, linear polarisation resistance, and Tafel constant values under both passive and active conditions, this study provides critical insights into the corrosion behaviour of reinforced AAFS mortars. It has been found that Tafel constant values range from 20 to 22 mV for the passive condition and from 50 to 58 mV for the active condition. These values serve as key indicators for assessing the corrosion rate of embedded steel reinforcements. In addition, the chloride thresholds for reinforced AAFS mortars at the steel-mortar interface were determined upon corrosion initiation. The chloride thresholds were found to be inversely proportional to the slag content in AAFS mortars. This phenomenon was thoroughly analysed in conjunction with the morphological characteristics of the steel-mortar interface.

Both microcell and macrocell corrosion were identified at the steel-mortar interface. Microcell corrosion, characterised by localised corrosion cells, was found to dominate in regions with

thicker interfacial zones ($>10\text{ }\mu\text{m}$), while macrocell corrosion was prevalent in areas with thinner interfacial zones ($<2\text{ }\mu\text{m}$). Furthermore, the role of each corrosion cell was classified and validated through numerical simulations. Finally, a practical corrosion determination method for reinforced AAFS mortars is proposed to help engineers and asset managers make informed decisions regarding the long-term performance of AAFS structures.

Table of Contents	
Acknowledgements	II
Abstract	III
List of Figures	IX
List of Tables	XIII
List of Equations	XIV
List of Symbols and Abbreviations	XVI
1 Introduction	1
1.1 Background	1
1.2 Research Significance	3
1.3 Aim and Objectives	4
1.4 Scope of Thesis	5
2 Literature Review	8
2.1 Precursors, Activators and Microstructural Characteristics of AAMs	8
2.2 Mechanical Strength and Key Issues of AAFS	12
2.2.1 Compressive Strength	12
2.2.1.1 Effect of SA Content	12
2.2.1.2 Effect of Curing Regimes	14
2.2.1.3 Effect of alkaline activator	17
2.2.2 Fracture Properties	19
2.2.2.1 Influence of Precursors	19
2.2.2.2 Influence of Temperature	20
2.2.2.3 Influence of Specimen size	20
2.2.2.4 Fracture model	21
2.2.3 Key Issues	21
2.2.3.1 Shrinkage-Induced Cracks	22
2.2.3.2 Efflorescence	23
2.3 Corrosion of Reinforced AAFS	24
2.3.1 Microcell and Macrocell corrosion	25
2.3.2 Electrochemical (Half-Cell) Reactions	26
2.3.3 Chloride-Induced Reinforced AAFS Concrete Corrosion	27
2.3.3.1 Chloride resistance of AAFS samples	27
2.3.3.2 Chloride Binding Capacity	29

2.3.3.3	Chloride Threshold	31
2.4	Electrochemical Properties Measurement	33
2.4.1	Open Circuit Potential	33
2.4.2	Linear Polarisation Resistance and Tafel Extrapolation Method	36
2.5	Bond Properties, Morphology and Spatiotemporal Evolution of Corrosion at SMI/SCI	39
2.5.1	Bond Properties for Reinforced AAC	39
2.5.2	Morphology at the steel-mortar/concrete interface	41
2.5.3	Spatiotemporal Evolution of Corrosion at SCI and SMI	44
2.6	Numerical simulations of corrosion in reinforced concrete or mortar	47
2.7	Summary	50
3	Methodology	52
3.1	Materials, Sample and Experiment Preparation	52
3.1.1	Precursors, Alkaline Activator and Casting Procedure	52
3.1.2	Sample Preparation	56
3.1.3	Exposure Environments	60
3.2	Mechanical Test	61
3.2.1	Compressive Strength Test	61
3.2.2	Tensile Splitting Strength Test	63
3.2.3	Three-Point Bending Test for Mortar Samples	64
3.2.4	Three-Point Bending Test for Notched AAFS Concrete Beams	65
3.2.5	Pull-Out Test	67
3.3	Electrochemistry Measurements	69
3.4	Interface Characterisation at the SMI	72
3.4.1	Free and Bound Chloride Content at the SMI	72
3.4.2	SEM-EDS Sample Preparation and Analysis at SMI	75
3.4.3	X-CT analysis	78
3.4.3.1	Introduction	78
3.4.3.2	Pre-Processing	79
3.4.3.3	Material Phases Segmentation	81
3.4.3.4	Data processing	82
3.5	Numerical simulations	83
3.5.1	Geometric Configuration	83

3.5.2	Chloride Diffusion and Oxygen Transport in Mortar	84
3.5.3	Potential Distribution in Mortar	86
3.5.4	Microcell and Macrocell electric current densities	88
3.5.5	Corrosion of Steel Bar and Rust Expansion	91
4	Mechanical Properties of AAFS Concretes	93
4.1	Introduction	93
4.2	Flexural Strength and Compressive Strength of Mortar Samples	93
4.3	Mechanical Strength Properties for AAFS Concretes	95
4.3.1	AAFS Gravel Concretes	95
4.3.2	AAFS Limestone Concretes	96
4.4	Fracture Properties of AAFS Concrete	102
4.4.1	AAFS Gravel Concrete beams	103
4.4.2	AAFS Limestone Concrete beams	104
4.5	Discussion	107
4.6	Summary	109
5	Electrochemical Properties of AAFS	111
5.1	Introduction	111
5.2	Corrosion Potential (E_{corr}) and Polarisation Resistance (R_p)	111
5.3	Corrosion Initiation and Chloride Threshold (C_{crit})	118
5.3.1	Corrosion Initiation Determination	118
5.3.2	Chloride Threshold	119
5.4	Tafel Constant B Values	121
5.5	Discussion	124
5.6	Summary	127
6	Interfacial Behaviour Between Steel and AAFS	129
6.1	Introduction	129
6.2	SEM-EDS Analysis	129
6.2.1	Morphology and topographic analysis at the SMI	129
6.2.2	Corrosion Mechanisms at SMI	140
6.3	X-CT Analysis	145
6.3.1	X-CT Image Processing and Spatiotemporal Evolution of Corrosion	145
6.3.2	Spatiotemporal Evolution of Corrosion of Reinforced AAFS Mortar	151
6.3.2.1	Corrosion degree	151

6.3.2.2	Radial loss of steel bar	154
6.3.2.3	Corrosion rust distribution	156
6.4	Bond Strength.....	162
6.5	Discussion.....	168
6.6	Summary.....	170
7	Numerical Modelling Simulations	173
7.1	Introduction.....	173
7.2	Chloride Diffusion and Oxygen Transportation	174
7.3	Corrosion Initiation and Propagation.....	177
7.4	Corrosion Rust Distribution	181
7.5	Discussion.....	185
7.6	Summary.....	188
8	Conclusions and Future Work	190
8.1	Conclusions.....	190
8.2	Future work.....	192
	References.....	193

List of Figures

Figure 1. The correlation between world cement production consumed (left) and world population (right), adapted from Scrivener et al. [1]	2
Figure 2. 2D schematic of C-A-S-H gel and N-A-S-H gel, adapted from Zhang et al. [43]	9
Figure 3. Ternary diagram of gel phases evolution trends, derived from various studies [46,50-54].....	11
Figure 4. The effect of alkali concentration, curing temperature and SA content on 28-day compressive strength of AAFS mortar, adapt from Mallikarjuna Rao and Gunneswara Rao [63].....	14
Figure 5. Relationship between carbonate ions and bicarbonate ions in pore solution under different CO ₂ concentration, adapted from Bernal et al. [97].....	17
Figure 6. Efflorescence in AAFS mortar	23
Figure 7. Sketch of microcell and macrocell corrosion in reinforced concrete	26
Figure 8. Setting up the OCP measurement of embedded reinforcement.....	34
Figure 9. Example of the Tafel plot	38
Figure 10. Sketch of wall effect	42
Figure 11. BSE image for porous structure around the steel	43
Figure 12. Examples of SEM images in BSE mode (left) and SE mode (right).....	43
Figure 13. Two different types of Hobart mixers: a) mortar mixer; b) concrete mixer	55
Figure 14. The alkaline solution mixed using a magnetic stirrer.....	55
Figure 15. a) Corrosion environment chamber; b) the placement of electrochemical and X-CT samples in the corrosion environment chamber.....	60
Figure 16. Setup for the impressed current method for pull-out test samples: (a) a 30 V power supply; (b) a joint electric circuit to ensure that the corrosion current density remains consistent for a group of three samples.....	61
Figure 17. Setup for compressive strength test of AAFS concrete cube	63
Figure 18. Setup for tensile splitting strength test of AAFS concrete cylinder	64
Figure 19. Setup for three-point bending test for AAFS mortar: a) The flexural strength test; b) The compressive strength test for the halves of the mortar prism.....	65
Figure 20. The experimental setup for the three-point bending test of notched beam: (a) the installation of knife edge (b) Setup of clip gauge (c) Setup of LVDTs.....	66
Figure 21. Setup for the reinforced AAC pull-out test: (a) Load control method; (b) Displacement control method	69
Figure 22. Setup for the three-electrode system	71
Figure 23. Ion Chromatography Professional (ICP) 850	73
Figure 24. Experimental setup for chloride content analysis (a) shaking process (b) centrifuge (c) separation of liquid and solid phases after centrifugation	75
Figure 25. (a) The ATM Brilliant 220 precision cutter; (b) using vacuum chamber to eliminate the air bubbles from samples pore structure	77
Figure 26. Sample setup in the Axia ChemiSEM for SEM-EDS measurement (the bottom left and right); with synchronized graphical view for SE mode (top-left) and BSE mode (top-right).....	78
Figure 27. a) NiKon XT H 320 for X-ray and CT inspection; b) test sample setup.....	79

Figure 28. Reconstructed 3D structure from the initial scanning at x-z axis view, (a) non geometrically processed image, (b) image after correction	80
Figure 29. Volume edit treatment on images (a) before treatment (b) after treatment	81
Figure 30. Phase identification in X-CT image through using grey values	82
Figure 31. Processing on (a) corrosion rusts and (b) corroded steel.....	83
Figure 32. Geometric configuration for middle positioned steel bar and side positioned bar.	84
Figure 33. The sketch of microcell and macrocell electric current density	91
Figure 34. Histogram of the three-point bending test and compression test: (a) Flexural strength and (b) compressive strength for AAFS mortars and OPC reference mortar	93
Figure 35. The 28-day strength results for three types of AAFS concretes and OPC reference concrete with gravel aggregate: (a) average compressive strength and (b) average splitting tensile strength	96
Figure 36. The average compressive strength of AAFS and OPC concretes at 14 days and 28 days	97
Figure 37. Ternary diagram illustrating the composition distribution of Groups 1-7.....	99
Figure 38. Representative Load-CMOD curve (a) and Load-Deflection curve (b) for AAFS concrete beams (100 mm x 100 mm x 500 mm)	104
Figure 39. Representative Load-CMOD curve (a) and Load-Deflection curve (b) for AAFS concrete beams (150 mm x 150 mm x 600 mm)	105
Figure 40. Failure of the AAFS limestone concrete beam.....	105
Figure 41. Comparison of compressive strength among mortar and concretes.....	108
Figure 42. The condition of the gravel and limestone after tests were finished, (a) and (b) the compression test, (c) and (d) the three-point bending test	109
Figure 43. Increasing trend in E_{corr} from high-calcium to low-calcium samples	113
Figure 44. Evolution of E_{corr} and R_p values over time for 100SA samples.....	114
Figure 45. Evolution of E_{corr} and R_p values over time for 70SA-30FA samples	114
Figure 46. Evolution of E_{corr} and R_p values over time for 50SA-50FA samples	115
Figure 47. Evolution of E_{corr} and R_p values over time for 30SA-70FA samples	115
Figure 48. Evolution of E_{corr} and R_p values over time for 100FA samples.....	115
Figure 49. Evolution of E_{corr} and R_p values over time for OPC samples.....	116
Figure 50. Effect of efflorescence for electrochemical sample before (left) and after (right) w/d cyclic accelerated corrosion under the same time: a) 100SA sample; b) 70SA-30FA sample; c) 50SA-50FA sample; d) 30SA-70FA sample; e) 100FA sample.....	118
Figure 51. Difference in the Tafel plot for steel-reinforced AAFS mortar under passive and active conditions	124
Figure 52. Distribution of Tafel constant B values for steel-reinforced AAFS mortars at (a) passive condition; (b) active condition	124
Figure 53. Comparison of the E_{corr} values for samples under different exposure conditions	126
Figure 54. Morphology at the SMI for 100SA sample	131
Figure 55. BSE images of porous band and micro-gap for 100SA sample after ImageJ processed.....	132
Figure 56. Morphology at the SMI for 70SA-30FA sample	133

Figure 57. BSE images of porous band and micro-gap for 70SA-30FA sample after ImageJ processed.....	134
Figure 58. Morphology at the SMI for 50SA-50FA sample	135
Figure 59. BSE images of porous band and micro-cracks for 50SA-50FA sample after ImageJ processed.....	135
Figure 60. Morphology at the SMI for 30SA-70FA sample	137
Figure 61. BSE images of porous band and micro-cracks for 30SA-70FA sample after ImageJ processed.....	137
Figure 62. Morphology at the SMI for 100FA sample.....	138
Figure 63. BSE images of porous band and micro-cracks for 100FA sample after ImageJ processed.....	139
Figure 64. Thickness range of porous band and micro-gap for each sample.....	140
Figure 65. BSE-SE-EDS images for corrosion in 100SA sample	141
Figure 66. BSE-SE-EDS images for corrosion in 70SA-30FA sample	142
Figure 67. BSE-SE-EDS images for corrosion in 50SA-50FA sample	143
Figure 68. BSE-SE-EDS images for corrosion in 30SA-70FA sample	144
Figure 69. BSE-SE-EDS images for corrosion in 100FA sample.....	144
Figure 70. Three-dimensional views of (a) mortar, (b) steel bar, (c) pores and (d) cracks and voids.....	147
Figure 71. Change of outer surface for specimen during the accelerated corrosion period ..	147
Figure 72. Surface change of sample at (a) 97 cycles and (b) 186 cycles	148
Figure 73. Evolution of corrosion of on the steel surface for M1 (left) and S2 (right)	148
Figure 74. Evolution of steel corrosion rust for M1 (left) and S2 (right)	149
Figure 75. Reconstructed X-CT data for corrosion evolution on the steel surface.....	149
Figure 76. Evolution of cracks in mortar along with the accelerated corrosion progression	151
Figure 77. Corrosion degree of the steel bar along the longitudinal direction.	153
Figure 78. Maximum radial loss of steel bar in sample M1 and S2 along the longitude direction	155
Figure 79. Average radial loss of steel bar in sample M1 and S2 along the longitude direction	155
Figure 80. Ratios of maximum radial loss to average radial loss of the steel bar along the longitude direction	156
Figure 81. Corrosion rust thickness along the circumference of the steel bar	156
Figure 82. Coefficient of determination R^2 of fitting results for M1 and S2	158
Figure 83. The comparison between slice 851 for S2 at 137 and 186 cycles	158
Figure 84. Regression analysis of von Mises model with X-CT data	159
Figure 85. Comparison between the fitting of von Mises model and AGvM model.....	161
Figure 86. Comparison of R^2 for M1 (a), after 137 cycles (b) after 186 cycles, S2, (c) after 137 cycles and (d) after 186 cycles.....	161
Figure 87. The comparison between the bond stress-slip curve for Load-control and Displacement-control methods	162
Figure 88. (a) The representative bond stress-slip curve for the AAFS-G samples, (b) the fracture surface of sample after split failure	163

Figure 89. Pull-out test results for 50SA-50FA AAFS group and control OPC group	165
Figure 90. Plastic deformation of the steel bar	165
Figure 91. Bond stress-slip curve for AAFS sample under displacement control.	166
Figure 92. Surface after corrosion was split.	167
Figure 93. Bond strength relates to the corrosion degree	168
Figure 94. COMSOL operation interface	173
Figure 95. Concentration of chloride ions in mortars at different days of diffusion	176
Figure 96. The diffusion pattern of chloride ions across the steel bar	177
Figure 97. Oxygen concentration in the mortar for two models after 1-day	177
Figure 98. The evolution of the electrolyte potential (left) and electrode potential (right) for M1-S after corrosion initiation.....	179
Figure 99. The evolution of the electrolyte potential (left) and electrode potential (right) for S2-S after corrosion initiation.....	180
Figure 100. Electric current densities at electrode after corrosion initiation at 4 hours, (a) the active region and (b) the corresponding of anodic, cathodic and total electric current densities, (c) the passive region of the electrode and (d) the corresponding cathodic electric current densities at this region	181
Figure 101. Radial loss of steel bar at different simulation hours after corrosion initiation .	183
Figure 102. Corrosion condition for side-positioned steel bar at the 240 h after corrosion initiation	183
Figure 103. Ratios of maximum radial loss to average radial loss of the steel bar along the longitude direction	183
Figure 104. The corrosion distribution around the steel circumference at the 240 hours of accelerated corrosion	184
Figure 105. Corrosion rust thickness with von Mises model fitting of simulation results	185
Figure 106. Comparison of von Mises model in real X-CT measurement and simulated results	187

List of Tables

Table 1. Different expression for the chloride thresholds	31
Table 2. C_{crit} values obtained from the published literature	32
Table 3. The E_{corr} values and related corrosion probability of reinforcement embedded in concrete [195]	34
Table 4. E_{corr} values for reinforcement embedded in concrete with different moisture content, data adapt from Elsener et al. [28]	35
Table 5. Ranges of i_{corr} values related to corrosion probability of the reinforcement, adapted from [27].	37
Table 6. Chemical composition of precursors determined by X-Ray fluorescence analysis [wt.%].....	52
Table 7. Mix proportions for AAFS samples (Unit: kg/m^3).....	54
Table 8. Samples information including oven curing time, sketches, and selected mix proportions (as per Table 7)	59
Table 9. Geometric and materials parameters	86
Table 10. Electrochemical parameter used in numerical modelling simulations.....	91
Table 11. Average flexural strength (MPa) and compressive strength (MPa) of AAFS mortars at 14 days and 28 days	94
Table 12. Average compressive strength for concrete samples at 14 days and 28 days	98
Table 13. The ratios of main elements for AAFS concrete groups	99
Table 14. Mean fracture energy and fracture toughness of gravel type AAFS concrete beams	104
Table 15. Mean fracture energy and fracture toughness of AAFS concrete beams	107
Table 3. Re-label of samples for each mix group	112
Table 16. Free and Bound Chloride for five kinds of AAFS mortars	120
Table 17. Tafel constant B values for five kinds of steel-reinforced AAFS groups.....	123
Table 18. An adaption from ASTM C876 for corrosion determination to suit for steel-reinforced AAFS mortars measured under non-saturated condition.....	125
Table 19. Thickness range of porous band and micro-gap for each sample	140

List of Equations

Eq. 1 Steel passive film disruption	26
Eq. 2 Andoic reaction of corrosion	26
Eq. 3 Cathodic reaction of corrosion	26
Eq. 4 Formation of ferric hydroxide	27
Eq. 5 Formation of hydrated ferric oxide.....	27
Eq. 6 Linear polarisation resistance	36
Eq. 7 Corrosion current density	36
Eq. 8 Tafel constant B	37
Eq. 9 Compressive strength for concrete	62
Eq. 10 Tensile splitting strength.....	63
Eq. 11 Flexural strength for mortar.....	64
Eq. 12 Compressive strength for mortar	64
Eq. 13 Fracture energy	66
Eq. 14 Fracture toughness.....	67
Eq. 15 Bond strength.....	68
Eq. 16 Chemical reaction of titration method	73
Eq. 17 Influence of sulphide in titration method	73
Eq. 18 Chloride diffusion.....	84
Eq. 19 Oxygen diffusion	85
Eq. 20 Nernst-Planck equation	87
Eq. 21 Simplified Nernst-Planck equation.....	87
Eq. 22 Electric current density based on Faraday's law	87
Eq. 23 Boundary condition of electric current density in mortar	87
Eq. 24 Ohm's law.....	88
Eq. 25 Spatial distribution of potential	88
Eq. 26 Macrocell current density	88
Eq. 27 Boundary condition on the mortar surface	88
Eq. 28 Anodic polarisation equation.....	89
Eq. 29 Cathodic polarisation equation	89
Eq. 30 Limiting current density	89
Eq. 31 Diffusion distance of oxygen.....	90
Eq. 32 Final cathodic polarisation equation.....	90
Eq. 33 Microcell current density.....	90
Eq. 34 Macrocell current density	90
Eq. 35 Total current density	91
Eq. 36 Radial loss of steel bar	91
Eq. 37 Corrosion rust evolution around the steel bar	92
Eq. 38 Student t-distribution	139
Eq. 39 Corrosion degree of the steel	152
Eq. 40 Average radial loss of steel bar	154
Eq. 41 Maximum radial loss of steel bar	154
Eq. 42 Ratio between the maximum and average radial losses	154

Eq. 43 Corrosion rust thickness	157
Eq. 44 Modified Beseel function	157

List of Symbols and Abbreviations

Abbreviations

AAMs	Alkali-activated materials
AAFS	Alkali-activated fly ash and slag
AAFA	Alkali-activated fly ash
AASA	Alkali-activated slag
C-A-S-H	Calcium aluminium silicate hydrate
C-S-H	Calcium silicate hydrate
CSE	Copper/copper sulphate electrode
CO ₂	Carbon dioxide
Ca(OH) ₂	Calcium hydroxide
FA	Fly ash
FEM	Finite element method
GGBS	Ground granulated blast slag
ITZ	Interfacial transition zone
MK	Metakaolin
LPR	Linear polarisation resistance
LSP	Limestone powder
LVDTs	Linear variable differential transducers
N-A-S-H	Sodium aluminosilicate hydrate
NaOH	Sodium hydroxide
NaCl	Sodium chloride
Na ₂ O	Sodium oxide
OPC	Ordinary Portland cement
RE	Reference electrode
SA	Slag
SCI	Steel-concrete interface
SCE	saturated calomel electrode
SMI	Steel-mortar interface
SiO ₂	Silicon dioxide
SEM-EDS	Scanning Electron Microscopy-Energy Dispersive Spectroscopy
WE	Working electrode
X-CT	X-ray computed tomography

Symbols

R _p	polarisation resistance
E _{corr}	Corrosion potential
E	Potential
mV _{SCE}	mV versus saturated calomel electrode
i _{corr}	Corrosion current density
i	Current density

B	Tafel constant
β_a	Anodic Tafel slope
β_c	Cathodic Tafel slope
Cl^-	Chloride ions
ϕ	Diameter of steel bar
w/d	Wetting/drying
f_c	Compressive strength of concrete
F	Maximum load at failure
A_C	Cross-section area of the specimen
f_{ct}	Tensile splitting strength
L	Length of the specimen
d	Diameter of the cylinder specimen
R_f	Flexural strength
F_f	Load applied to the middle of the prism at failure
b	Width of square section of the prism
l	Distance between the support
R_c	Compressive strength of mortar
F_c	Maximum load at of mortar
G_F	Fracture energy
W_0	Area under the Load-Deflection curve
m	Mass of the beam between two supports
g	Gravity acceleration
δ_0	Deflection at the final failure position of the beam
A_{lig}	Area of the ligament
K_{IC}	Fracture toughness
P_{max}	Maximum load for beam test
l_b	Span of beam
d	Depth of beam
a_0	Notched crack depth
τ	Bond strength
C_{cl}	Chloride ions concentration in mortar
t	Diffusion time
D_{cl}	Chloride diffusion coefficient in mortar
C_{cl}^s	Surface chloride concentration
C_{cl}^{crit}	Critical chloride threshold
C_{O_2}	Oxygen concentration in mortar
D_{O_2}	Diffusion coefficient of oxygen in mortar
∇	nabla, the mathematics operator that is used for the gradient calculations
J_i	Mass flux of ions i
D_i	Diffusion coefficient of ions i

C_i	Concentration of ions i
z_i	Valency of the charged ions i
R	Universal gas constant, 8.314 J/(mol·K)
F	Faraday's constant, 96485 C/mol
\emptyset	Electric potential in mortar
\mathbf{u}	Flow velocity of electrolyte
\mathbf{i}	Electric current density
ρ	Electric resistance
\mathbf{n}	Normal factor
i_{mac}	Macrocell current density
i_{mic}	Microcell current density
i_{Fe}	Anodic electric current densities
i_{O_2}	Cathodic electric current densities
i_{Fe}^0	Anodic corresponding exchange current densities under the equilibrium condition
$i_{\text{O}_2}^0$	Cathodic corresponding exchange current densities under the equilibrium condition
ϕ_{Fe}	Anodic equilibrium potential
ϕ_{O_2}	Cathodic equilibrium potential
z_{O_2}	Valency of O_2 of cathodic reduction
$C_{\text{O}_2}^s$	Surface oxygen concentration
L	Shortest distance from the mortar surface to steel surface
C	Cover thickness
D	Steel bar diameter
i_L	Limiting current density
i_{total}	Total electric current density
$R(\theta, t)$	Radials loss around the circumference of steel bar at the anode region
M_{Fe}	Atomic weight of iron
z_{Fe}	Valency of anodic reaction
ρ_{Fe}	Density of steel
$\delta(\theta, t)$	Corrosion rust layer thickness
α	Expansion ratio

1 Introduction

1.1 Background

Concrete, composed of ordinary Portland cement (OPC), sand, and coarse aggregate, is the most widely used construction material worldwide. It offers exceptional mechanical properties, including high compressive strength, excellent durability, and good fire resistance. Among its components, OPC plays a significant role as the binding material, governing the overall performance of concrete, which is essential for meeting the growing demand for construction materials. Over the past few decades, the rising demand for cement production has been driven by global population growth [1], as illustrated in Figure 1. This trend was particularly pronounced between 2000 and 2010, primarily due to infrastructure development [2], which significantly accelerated cement production. However, this increasing demand has led to a corresponding rise in carbon dioxide (CO₂) emissions.

Cement manufacturing involves the calcination of raw materials, a mixture of limestone, clay, aluminium, and iron ore [3], a stage that requires substantial energy consumption and results in substantial CO₂ emissions. Currently, this process accounts for approximately 7% of global CO₂ emissions [4]. The rise in CO₂ emissions leads to severe climate issues, such as global warming, which poses a critical challenge worldwide. To address these issues, various strategies have been proposed globally, including the UK's Net Zero Strategy [5]. This strategy aims to mitigate the impact of carbon emissions on climate change while promoting sustainable development.

Moreover, as limestone is a non-renewable resource, finding low-carbon alternatives for concrete has become an emerging concern. In recent decades, alkali-activated materials (AAMs), such as fly ash (FA) and ground granulated blast slag (GGBS, termed as slag (SA) hereafter), have gained increasing attention from both commercial and research perspectives. These materials are recognised as environmentally friendly because they are industrial by-

products or wastes. FA is a by-product of coal-fired thermal power plants, while SA is a waste product from ironworks. Unlike OPC, which requires a calcination process, AAMs do not require this stage, thereby significantly reducing carbon emissions and energy consumption [6,7].

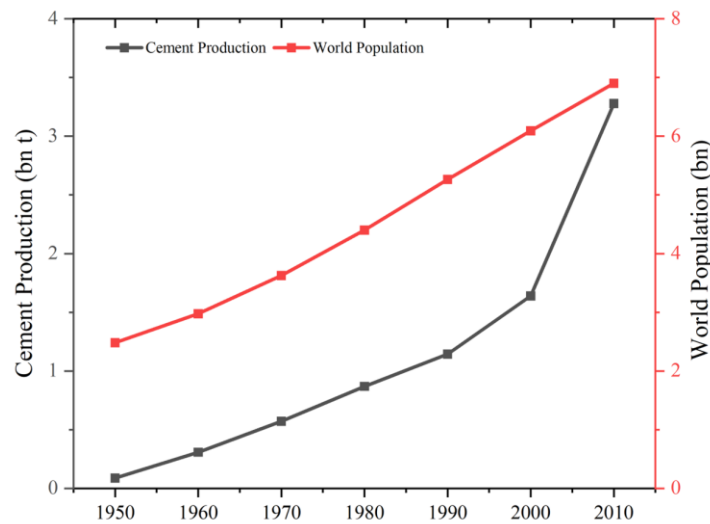


Figure 1. The correlation between world cement production consumed (left) and world population (right), adapted from Scrivener et al. [1]

Beyond AAMs' low-carbon characteristics, another key distinction between AAMs and OPC lies in their activation processes. AAMs are chemically activated using alkaline solutions, whereas OPC is hydrated with water. This specific activation method of AAMs results in varying gel microstructures. In principle, the microstructure of AAMs can be classified into two primary categories: calcium aluminium silicate hydrate (C-A-S-H) and sodium aluminosilicate hydrate (N-A-S-H). This classification is important because the microstructure significantly influences the mechanical properties of AAMs' products. For example, the C-A-S-H structure is similar to the calcium silicate hydrate (C-S-H) found in OPC but is more compact and tortuous [8]. In contrast, the N-A-S-H structure exhibits a ring-like formation and tends to be more porous [9]. These microstructural differences making AAMs exhibits mechanical properties that are superior or comparable to those of OPC [10-12], demonstrating their significant potential to replace or partially replace OPC in modern construction [13].

Steel reinforcement plays an important role in concrete structures, since concrete is naturally weak in tension, reinforcement enhances the durability and service life of concrete structures. However, the corrosion of embedded reinforcement deteriorates the concrete structure, reducing its performance. In reinforced concrete corrosion, chloride ions play a primary role in corrosion initiation. Once they accumulate on the steel surface and exceed a critical threshold, they destroy the passive film formed on the reinforcement surface, ultimately leading to corrosion [14,15].

The corrosion of reinforced OPC concrete has been extensively studied over the past few decades, including aspects such as the critical chloride threshold, corrosion mechanisms [16-20]. In contrast, research on reinforced AAMs corrosion remains limited, despite studies indicating that AAMs exhibit superior chloride resistance compared to OPC [21-23]. Moreover, the long-term durability and structural performance of reinforced AAMs after corrosion initiation remains uncertain, posing a significant challenge to their widespread application in construction.

1.2 Research Significance

According to the Royal Academy of Engineering [24], as reported by the National Engineering Policy Centre, the UK's construction sector currently contributes approximately 40% of the UK's carbon emissions and is estimated to account for up to 11% of global carbon emissions. To meet the ambitious decarbonisation goals outlined in the UK Government's Net Zero Strategy [25] by 2050, reducing carbon emissions to minimal level offset by natural absorption and durable storage through carbon dioxide removal measures, achieving net-zero impact, the Royal Academy of Engineering [24] emphasised that the construction sector must align with the national carbon reduction targets of 68% by 2030 and 78% by 2035.

AAMs represent a promising alternative to traditional OPC. These materials not only have a significantly reduced carbon footprint but also exhibit superior mechanical properties, making

them an ideal choice for construction purposes. However, before AAMs can be widely adopted in construction and infrastructure, their long-term performance in reinforced systems, particularly the corrosion behaviour, must be thoroughly understood. Corrosion-induced deterioration of reinforced concrete structures not only weakens the structural durability but also results in sustainable financial losses. Stewart and Bastidas-Arteaga [26] estimated that the global cost of maintaining and replacing deteriorated reinforced concrete structures exceeds £2.3 trillion annually.

Common on-site measurement techniques for reinforced OPC concrete include half-cell potential and linear polarisation resistance [27]. The half-cell potential method maps the potential of embedded reinforcement to locate corrosion [28], while the linear polarisation resistance method calculates the instantaneous corrosion current density to evaluate reinforcement condition. These techniques are widely used to assess corrosion status, optimise maintenance strategies, and enable the early actions to extend structural service life. However, the applicability of these methods to reinforced AAMs remains uncertain. Studies have shown that parameters obtained using these techniques deviate significantly from those used for reinforced OPC concrete [29-31], leading to inaccurate assessments of the actual condition of embedded reinforcement. For instance, extremely low half-cell potential values may falsely suggest a high corrosion risk, even no corrosion is present [28,32,33]. This discrepancy arises due to significant differences in materials and microstructures between AAMs and OPC structures. Considering these issues, a practical corrosion determination method for reinforced AAMs is essential to support engineers and asset managers in making informed decisions regarding their long-term performance.

1.3 Aim and Objectives

This research is focused on understanding the chloride-ingress-induced corrosion mechanisms and structural implications in reinforced alkali-activated fly ash and slag (AAFS) mortar and

concrete. By comprehensively and systematically exploring corrosion-related electrochemical parameters, this study aims to propose a tailored corrosion assessment method for reinforced AAFS mortar and concrete. The investigation of reinforced AAFS in this study is divided into four objectives as follows:

- To examine and analyse the mechanical properties of AAFS concretes and mortars, along with the fracture properties of AAFS concretes.
- To investigate the electrochemical behaviour of reinforced AAFS mortars subjected to wetting-drying cyclic corrosion (salt fog spray and dry cycles).
- To explore the corrosion behaviour of reinforced AAFS mortar/concrete, including the corrosion mechanism, the spatiotemporal evolution of corrosion at steel-mortar interface, and the bond properties at steel-concrete interface
- To employ numerical simulations to interpret the obtained experimental data and to explain complex phenomena that cannot be directly observed in experiments.

1.4 Scope of Thesis

This section outlines the scope of the thesis, highlighting the key focus areas and presenting the main findings. The following is a detailed overview of each chapter.

Chapter 2 presents a comprehensive literature review, structured into five sections. The first section introduces AAMs, covering the characteristics of raw materials, the mechanical and fracture properties of the final products, and associated practical challenges. The second section provides a brief overview of corrosion theory and the corrosion characteristics of reinforced AAFS concretes and mortars. The third section focus on the electrochemical behaviour of reinforced AAFS concretes and mortars under corrosion conditions. The fourth section analyses the influence of corrosion at the steel-mortar/concrete interface from both macro- and micro-level perspectives. The final section provides a concise overview of numerical simulations.

Chapter 3 outlines the methodologies employed in this research. It begins with an overview of the raw materials, followed by the sample preparation process. Subsequent sections provide detailed descriptions of the test methods, including mechanical testing, electrochemical measurements, SEM-EDS analysis, and X-CT analysis. The chapter concludes with an in-depth introduction to the principles and processes of numerical simulations.

Chapter 4 presents the mechanical and fracture test results for AAFS concrete and mortar. The findings indicate that an AAFS mix with 50%SA and 50%FA show the closest match to OPC samples for both concrete and mortar.

Chapter 5 focuses on the electrochemical measurement results for reinforced AAFS mortars. Corrosion potential and polarisation resistance values are analysed, and Tafel constant values for reinforced AAFS mortars with different mix ratios are studied. In addition, the chloride threshold, defined as the chloride ion concentration required to initiate reinforcement corrosion, is determined. Finally, a practical method for determining corrosion initiation in reinforced AAFS mortar is proposed.

Chapter 6 presents the results on the influence of corrosion on interface properties at both macroscopic and microscopic levels. The morphological characteristics and spatiotemporal evolution of corrosion at the steel-mortar interface are thoroughly investigated. Two corrosion mechanisms, microcell and macrocell corrosion, are identified. In addition, a phenomenon is observed in which micro-gap thickness influences the corrosion initiated at the steel-mortar interface of AAFS mortars. Furthermore, pull-out results indicate that bond strength at the steel-concrete interface initially increases after reinforcement corrosion, remains high for some time, and then gradually declines.

Chapter 7 presents the numerical simulation results for steel bars positioned both centrally and eccentrically within the mortar samples. The findings indicate that cover thickness significantly

influences corrosion initiation time, whereas the effect of isolated pores is comparatively minor. In addition, the results are further validated by the von Mises model, a model based on ductile failure mechanisms, where yielding occurs due to shear (distortion energy), demonstrating its effectiveness in simulating corrosion evolution. However, the model has inherent limitations, particularly in accounting for the distribution of corrosion rust and its sensitivity to multiple peaks along the steel circumference.

Chapter 8 summarises the key findings and discussions from Chapters 4 to 7. Detailed recommendations for future research are also outlined.

2 Literature Review

2.1 Precursors, Activators and Microstructural Characteristics of AAMs

AAMs is a generic term used to describe materials rich in aluminosilicate sources, commonly referred to as “precursors” in casting samples. These materials primarily originate from industrial wastes or by-products. For example, SA is a waste product that comes from the activities of iron works, while FA is a by-product of coal-fired thermal power plants. However, not all AAMs are obtained from the industrial residues; a small proportion come from processed materials, such as metakaolin (MK), which is produced through the thermal treatment of clay. In contrast, the production of OPC involves the calcination of a mixture of raw materials, including limestone, clay, aluminium, and iron ore [3]. This fundamental difference in production processes highlights the variations in raw material compositions between AAMs and OPC: AAMs are characterised by a high content of solid aluminosilicate salts, whereas OPC primarily consists of calcium-silicate salts [34,35]. Due to these compositional differences, AAMs requires alkaline solutions, such as the sodium hydroxide (NaOH), to dissolve the aluminosilicate salts and enhance reactions with other cations [36]. Additionally, sodium silicate (Na_2SiO_3), also known as the waterglass solution, is often combined with NaOH to improve the mechanical strength of AAMs’ mortar or concrete [37,38]. In contrast, OPC requires only water for hydration.

Due to these differences, the gel structure of AAMs can be broadly classified into two gel types based on calcium content: (1) calcium-aluminium-silicate-hydrate (C-A-S-H) for high calcium AAMs, and (2) sodium-aluminosilicate-hydrate (N-A-S-H) for low-calcium AAMs [8,39,40]. A 2D schematic drawing of these gels are shown in Figure 2. Provis et al. [8] state that the structure of C-A-S-H is similar to the calcium-silicate-hydrate (C-S-H) gel in OPC but is denser and more tortuous due the partial replacement of silicate by the aluminium. In contrast, N-A-S-H forms circular structures, resulting in a more porous microstructure [9].

According to Duxson et al. [10], three primary oxides in precursors, silicon dioxide (SiO_2), aluminium oxide (Al_2O_3), and calcium oxide (CaO), govern the microstructure formation. SiO_2 and Al_2O_3 from the hybrid precursors influence microstructure homogeneity, while CaO determines gel type. Additionally, SiO_2 and Al_2O_3 from activators also contribute to the microstructure formation. The relationship between gel types and these three oxides can be explained using the SiO_2 - Al_2O_3 - CaO ternary system [10,41,42], which has garnered significant research interest. This system is based on the proportional relationship among the three oxides and its influence on gel formation will be introduced first.

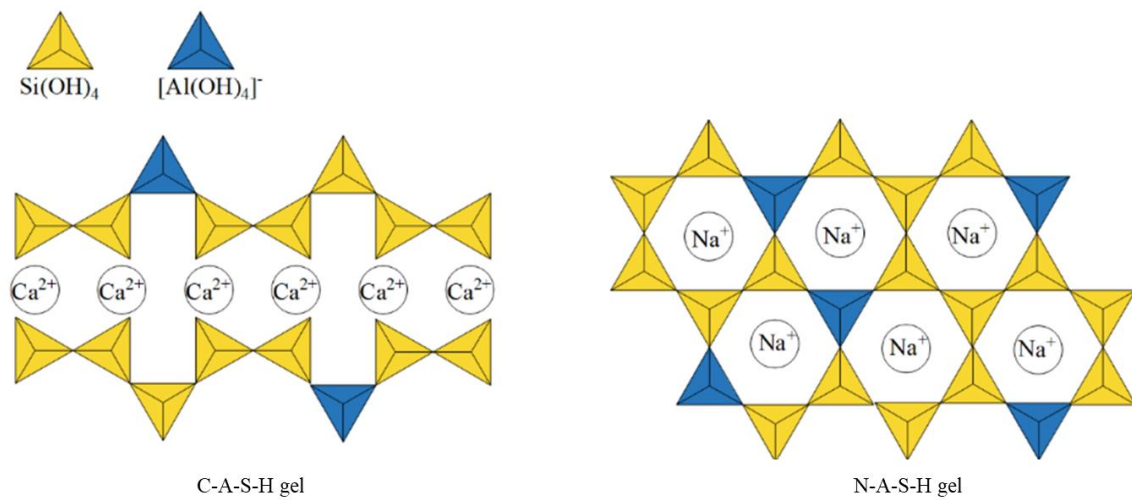


Figure 2. 2D schematic of C-A-S-H gel and N-A-S-H gel, adapted from Zhang et al. [43]

Duxson et al. [10] studied the effect of Si/Al ratios on the morphology and microstructural properties of alkali-activated metakaolin using SEM analysis and nuclear magnetic resonance (NMR) spectroscopy. Various Si/Al ratios were tested in their study. When the Si/Al ratio was below 1.40, unreacted material and large interconnected pores were observed in the binder matrix. In contrast, a homogeneous binder phase with partially unreacted particles and smaller isolated pores appeared when the Si/Al ratio above 1.65. The maximum compressive strength and lowest porosity were achieved at a Si/Al ratio of 1.9. These findings can be found in their subsequent studies [44,45].

Criado et al. [46] investigated the influence of Si/Al, Ca/Si, and Al/Ca ratios on gel formation in AAFS concrete. Their samples consisted of six mix proportions, with FA replaced by SA at 0, 20%, 40%, 60%, 80% and 100%. All groups were subjected to the same curing environment and alkaline activator dosage. They found that the gels formed in the AAFS concrete with 40% and 60% FA replacement were significantly different from samples made with 100% SA and 100% FA. Specifically, hybrid precursors led to the formation of C-(N)-A-S-H gel, demonstrating the coexistence of N-A-S-H gel and C-A-S-H gel. In addition, they reported that higher mechanical strength was achieved with increased Si/Al and Ca/Si ratios and a decreased Al/Ca ratio [46].

Nath and Kumar [47] also observed C-(N)-A-S-H gel in AAFS paste when the FA replacement ratio was over 30%. They noted that only N-A-S-H gel was present when the Ca/Si ratio was below 0.1. Similarly, Ye and Radlinska [48] reported that N-A-S-H gel played a dominant role in the microstructure of AAFS paste, with a small amount of C-A-S-H gel coexisting when $0 < \text{Ca/Si} < 0.3$ and $2 < \text{Si/Al} < 12.5$.

Regarding the influence of alkaline activators on gel formation, Reddy and Subramaniam [49] studied the effect of activator's alkali and silica content on the properties of AAFS paste. They prepared samples with a ratio of 50FA:50SA, and samples were activated using the mix of NaOH and Na₂SiO₃ solutions with varying alkali and silica contents. They found that silica provided by the Na₂SiO₃ solution promotes the long-term SA reaction, while alkali ions enhance early polycondensation process by reducing the silica polymerisation, thereby increasing the reactivity between dissolved calcium ions (Ca²⁺) and silicate ions (SiO₃²⁻). Besides, the Ca/Si ratio required for the formation of C-A-S-H gel ranged from 0.6 to 0.8 [49].

Based on the available literature [46,48-56], the evolution of gel phases in AAFS with respect to the Ca/Si ratio are summarised below and with a SiO₂-CaO-Al₂O₃ ternary diagram illustrating the gel phases, as shown in Figure 3.

- (1) For $0 < \text{Ca/Si ratio} \leq 0.1$, only N-A-S-H gel is present in the binder matrix.
- (2) For $0.1 < \text{Ca/Si ratio} \leq 0.3$, N-A-S-H gel gradually transitions into N-(C)-A-S-H gel, coexisting with C-A-S-H gel as the calcium content increase. Consequently, the microstructure evolves from a loose to a denser state.
- (3) For $0.3 < \text{Ca/Si ratio} \leq 0.6$, N-(C)-A-S-H gel gradually transforms into C-(N)-A-S-H gel as the calcium content continues to increase, with the C-A-S-H gel becoming the dominant phase.
- (4) For $\text{Ca/Si ratio} > 0.6$, C-A-S-H gel plays the dominant role, significantly increasing the tortuosity and compactness of the binder matrix.

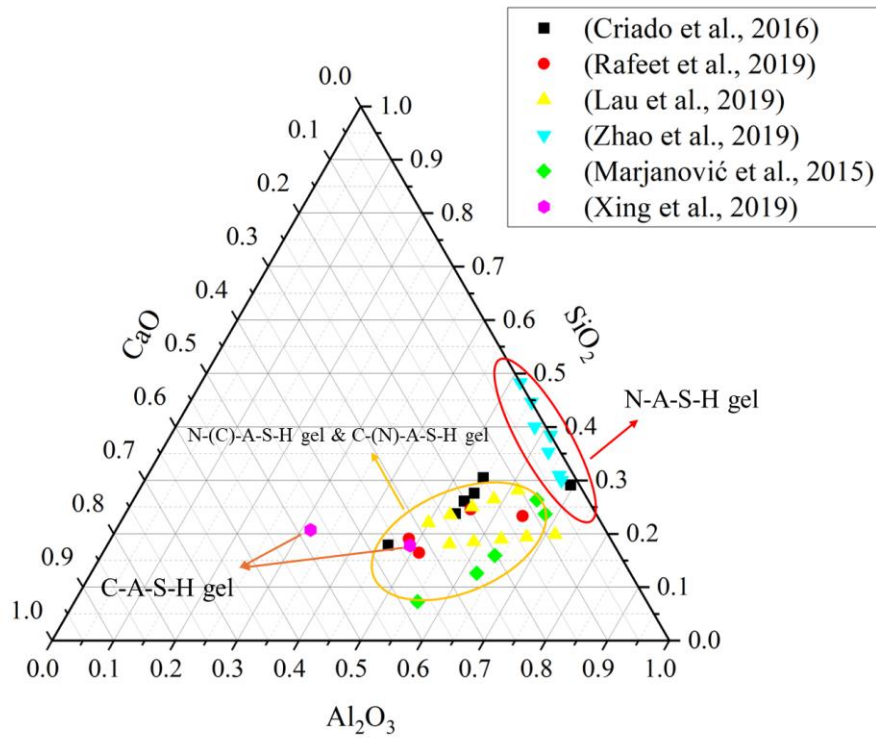


Figure 3. Ternary diagram of gel phases evolution trends, derived from various studies [46,50-54]

2.2 Mechanical Strength and Key Issues of AAFS

2.2.1 Compressive Strength

For OPC concrete, compressive strength is one of the most important mechanical properties, as it determines the load-bearing capacity of a structure. For AAFS concrete, the compressive strength depends on various factors, including the mix proportions of hybrid precursors, curing methods, and the dosage of alkaline activator. Ruengsilapanun et al. [57] reported that using only FA as precursor results in a low reaction rate under ambient curing environment, leading to low compressive strength. Conversely, using only SA can achieve sufficient compressive strength in hardened binders. However, this may cause issues, such as poor workability and rapid setting times [58-60]. Employing hybrid precursors (a combination of FA and SA) mitigates these issues. The following sections provide a detailed review of the primary factors that influences the compressive strength of AAFS samples, including the SA content in hybrid precursors, curing regimes, and alkaline activator dosage.

2.2.1.1 Effect of SA Content

As stated in Section 2.1, a denser microstructure of AAFS can be achieved by the increasing the calcium content. Generally, higher SA content in the FA-SA hybrid precursors results in higher compressive strength. Nath and Sarker [61] investigated the effect of SA content on the early strength properties of FA-based AAFS mortar and concrete, employing three FA replacement ratios with SA of 0%, 10%, 20%, and 30%. They reported that compressive strength increased with SA content for both AAFS mortar and concrete, which were activated and cured under the same conditions. The highest compressive strength was achieved when the FA replacement ratio of 30%. This conclusion was also supported by Fang et al. [62].

Mallikarjuna Rao and Gunneswara Rao [63] conducted a comprehensive study on the influence of SA content on the compressive strength of AAFS mortar. They prepared 10 mix ratios (FA:SA), ranging from 0:10 to 10:0, with incremental increase of 1 in FA content for each ratio.

The NaOH solution was prepared in concentrations of 8M, 12M, and 16M and combined with Na_2SiO_3 solution in a fixed mass ratio ($\text{Na}_2\text{SiO}_3/\text{NaOH}$) of 2.5. Besides, two curing regimes were employed: one at 35 °C (outdoor curing) for 28 days, and the other at 60 °C (oven curing) for 24 h, followed by outdoor curing for 28 days.

Figure 4 exhibits the 28-day compressive strengths of AAFS mortars, as adapted from Mallikarjuna Rao and Gunneswara Rao [63]. It can be observed that compressive strength increased with higher SA content, greater alkali concentration, and elevated curing temperature. Among these factors, curing temperature has a more significant effect on compressive strength than other two factors. This is because higher temperature improves the reaction rate between precursors and activator.

Regarding NaOH solution concentration, its effect on compressive strength is minimal in low-calcium group (e.g., the 100FA group). However, with increasing SA content, the 16 M NaOH solution dissolves more CaO, achieving higher compressive strength at lower temperatures compared to the other concentrations. Under high-temperature curing, the difference in compressive strength between 12 M and 16 M solutions becomes less significant. Further discussion on the effect of curing temperature and alkaline activators will be provided in the following sections.

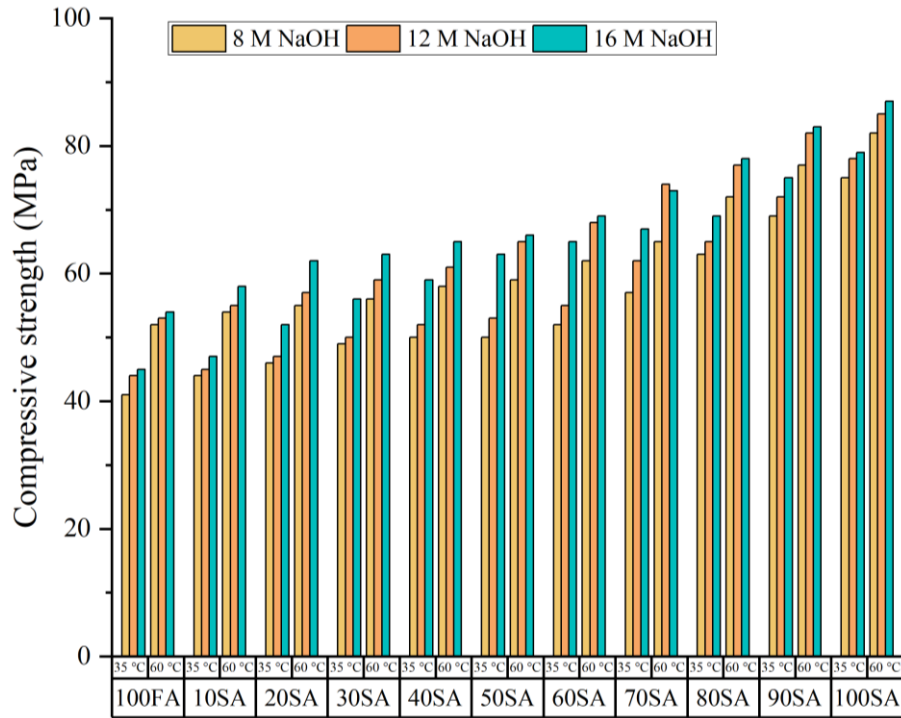


Figure 4. The effect of alkali concentration, curing temperature and SA content on 28-day compressive strength of AAFS mortar, adapt from Mallikarjuna Rao and Gunneswara Rao [63]

2.2.1.2 Effect of Curing Regimes

The commonly used curing regimes for cementitious materials include water curing, ambient curing, high temperature curing, and steam curing. For OPC, curing typically involves water immersion or exposure to a humid environment to promote the hydration, thereby improving the mechanical strength and durability of the final product. However, the curing regime for AAFS differs from OPC because water does not directly participate in the reaction but instead enhances the workability of AAFS [64]. In addition, due to the issue of alkali leaching [65], which dilutes the alkaline concentration in the pore solution (reducing pH) and consequently weakens the strength of hardened AAFS [66]. As a result, water curing is rarely used for AAFS. The effects of alkali leaching are discussed in Section 2.2.3.2.

Ambient temperature curing, typically in the range of 20 to 25 °C [59,67-69], is commonly applied to AAFS due to practical limitations of large curing facilities for on-site construction [70]. This curing regime is suitable for high calcium-based AAFS because the characteristics

of C-A-S-H gel is like the C-S-H gel in OPC [13,39]. In contrast, low calcium-based AAFS typically requires high temperature curing due to the high activation energy needed to initiate chemical reactions [70].

The high temperature curing regime typically ranges between 50 and 80 °C [71,72]. This method is commonly used to enhance early-age strength in AAFS. Elevated temperatures accelerate the reaction rate between alkaline activator and precursors by providing thermal energy, which promotes gel development and enhances the mechanical strength of hardened AAFS. Sindhunata et al. [73] reported that increasing the curing temperature improves the homogeneity of N-A-S-H gel networks formed in alkali-activated fly ash (AAFA) paste. Wang et al. [74] investigated the effects of curing temperature (20, 40, 60, 80, and 100 °C) and curing time (6, 12, and 24 h) on the compressive strength of AAFS concrete with FA:SA mix ratios of 75%:25%, 50%:50%, and 25%:75%. They reported that increasing both temperature and curing time enhanced the compressive strength of AAFS concrete. However, a slight reduction in compressive strength was observed at 100 °C compared to 80 °C for the same duration, which was attributed to microcracks caused by drying shrinkage [75,76]. The effect of drying shrinkage-induced microcracks on sample's strength will be further discussed in Section 2.2.3.1. In addition to high temperature curing, other methods, such as steam curing, autoclave curing, CO₂ curing, and microwave curing, can also be employed for AAFS.

The steam curing method utilises high-temperature vapour to provide thermal energy, accelerating the chemical reaction between precursors and activators [77]. Besides, vapour creates and maintains high humidity levels, preventing moisture evaporation from pore solutions [78]. Wu et al. [79] studied the effects of steam curing on FA-dominated AAFS and reported that shrinkage was significantly reduced, and higher early-age strength was achieved compared to specimens cured under ambient conditions. Similarly, Xue et al. [80] found that steam curing decreases the drying shrinkage in SA-based AAFS also. Aydın and Baradan [81]

suggested that steam curing improves the reaction of SA and leading to a finer pore size distribution due to continuous polycondensation process. Moreover, the autoclave curing method, which curing samples in a sealed vessel by pressurizing steam. This method significantly reducing shrinkage creep and refines the pore network, leading to higher compressive strength compared to steam curing [81-83]. However, these methods are only suitable for pre-cast components because equipment size limitations in on-site construction.

In addition to the aforementioned curing methods, CO₂ curing and microwave curing are two emerging techniques. CO₂ curing utilises the carbonation effect on AAFS, which transforms C-A-S-H gel into C-S-H gel [84] and precipitates calcium carbonate (CaCO₃) within the pores. This reduces porosity and resulting in a denser microstructure, therefore, preventing the ingress of aggressive ions [85,86]. However, it should be noted that high CO₂ concentration can lead to the formation of metastable bicarbonate ions (HCO₃⁻) from carbonate ions (CO₃²⁻). The relationship between these two ions in pore solution and CO₂ concentration is illustrated in Figure 5. These ions dissolve in pore solutions, creating a weakly acidic environment that decreases pH values [43,87-89]. This pH reduction can decrease compressive strength [90] and cause depassivation of the passive film on steel reinforcement surfaces [91].

Microwave curing is an innovative thermal curing technique that converts electromagnetic energy into heat energy through microwave radiation. This process rapidly increases the internal temperature of the material, thereby accelerating the reaction process of AAFS [70,92,93]. Unlike conventional oven curing, which uses temperature gradient, microwaves interacts directly with water molecules in pore solutions, ensuring uniform heating [94,95]. El-Feky et al. [96] compared microwave curing with other curing methods for the strength development of SA-based AAFS paste. Their results revealed that microwave-cured specimens reached up to 90% of their 28 days strength within just 7 days, with fewer shrinkage cracks. Although microwave curing is more efficient in strength development and effectively

eliminates issues such as shrinkage cracks, its practical application is limited by the size and capacity of available facilities.

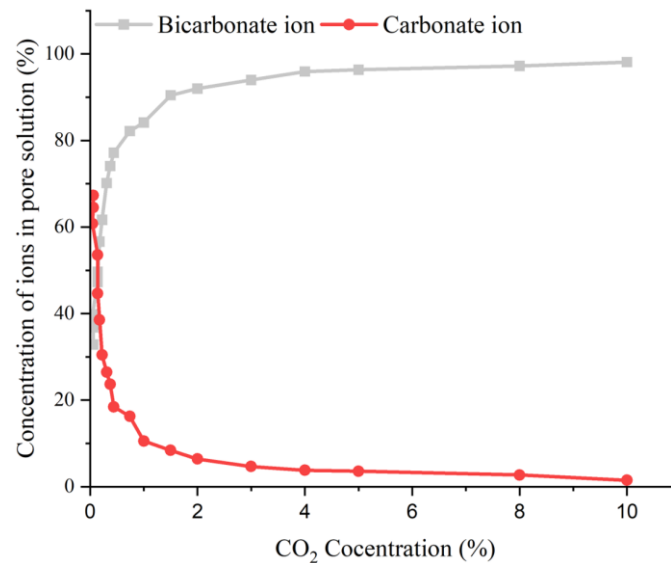


Figure 5. Relationship between carbonate ions and bicarbonate ions in pore solution under different CO₂ concentration, adapted from Bernal et al. [97]

2.2.1.3 Effect of alkaline activator

The alkaline activator plays a crucial role in the development of mechanical strength of AAFS by influencing its microstructure homogeneity and, consequently, its mechanical performance. The combined use of NaOH and Na₂SiO₃ solutions leads to superior properties in AAFS, particularly in terms of strength, compared to using either solution alone. NaOH solution establishes an alkaline environment for AAFS binder, while Na₂SiO₃ solution enhances precursors reactivity by contributing additional silica content [98]. Several factors associated with alkaline activators that affect the strength properties of hardened AAFS are introduced below.

The alkaline solution to binder (S/B) ratio, expressed as a mass ratio, generally ranges from 0.3 to 0.6 [99-101]. This ratio determines the total amount of activator used in casting AAFS. Increasing S/B ratio not only raises the alkali and hydroxide ions concentration but also increases the water content. However, an excessively high concentration of alkaline solution

can hinder the reactions in AAFS binder [102]. Ruiz-Santaquiteria et al. [103] investigated the effect of S/B ratios (0.5, 0.75, and 1.25) on the strength properties of AAFA paste using 8 M NaOH solution. They indicated that a lower S/B ratio resulted in higher compressive strength, while excess NaOH solution inhibited gel polymerisation. Similarly, Fang et al. [62] studied S/B ratios of 0.35 and 0.4 in AAFS concrete with five mix proportions and demonstrated that a lower S/B ratio led to higher compressive strength. For AAFA mortar, Hadi et al. [101] examined the effect of S/B ratios from 0.4 to 0.7 (in 0.1 increments) in AAFA mortar and found the optimal S/B ratio range to be between 0.5 and 0.6. In contrast, Chi [104] reported that an S/B ratio of 0.35 achieved higher compressive strength for AAFA mortar when studying the influence of S/B ratios of 0.35, 0.5, and 0.65. This discrepancy could be attributed to differences in alkaline solution concentration, even though similar S/B ratios were used in the experiment.

Aside from S/B ratio, two other expressions are commonly used. The alkaline solution concentration and the silica modulus ($M_s = \text{SiO}_2/\text{Na}_2\text{O}$) are expressed as the percentage of sodium oxide (Na_2O) content relative to the binder mass (generally 4% to 7%) [105-110] and the molar ratio of SiO_2 to Na_2O [111], respectively. Krizan and Zivanovic [106] studied the effect of NaOH and Na_2SiO_3 mixtures on alkali-activated slag (AASA) mortar with various Na_2O concentrations (3%, 4%, and 6%) and M_s ratios (0.6, 0.9, 1.2, and 1.5). They found that the AASA mortar's compressive strength increased with the M_s ratio at a fixed Na_2O concentration. Similarly, compressive strength increased with the Na_2O concentration at a fixed M_s ratio [107,108].

Furthermore, the Na_2SiO_3 to NaOH mass ratio, generally ranges from 0.5 to 3 [99,112-114]. This ratio represents the macroscopic relationship between Na_2SiO_3 and NaOH masses. In contrast, M_s ratio describes it at the microscopic level. Hadi et al. [101] assessed the influence of $\text{Na}_2\text{SiO}_3/\text{NaOH}$ ratios (1.5, 2.0, and 2.5) for AAFA mortar using NaOH solutions of 12 M, 14 M, and 16 M. They reported that higher $\text{Na}_2\text{SiO}_3/\text{NaOH}$ ratios increased compressive

strength at a fixed NaOH solutions due to higher silica content [98]. However, compressive strength tends to decrease when the $\text{Na}_2\text{SiO}_3/\text{NaOH}$ ratio exceeds a certain value. Ibrahim et al. [114] evaluated $\text{Na}_2\text{SiO}_3/\text{NaOH}$ ratios (2.0, 2.25, 2.5, and 2.75) for natural-pozzolan-based concrete and reported that maximum compressive strength at a ratio of 2.5. Similarly, several studies recommend maintaining the $\text{Na}_2\text{SiO}_3/\text{NaOH}$ ratio at or below 2.5 for optimal mechanical strength [99,112,115].

2.2.2 Fracture Properties

Fracture properties, refer to the material characteristics that describe how a material behaves when subjected to stress leading to crack initiation and propagation, of concrete structures are equally important as their strength properties, as they reflect the material's resistance to crack initiation and propagation. Although OPC concrete exhibits good compressive strength, it is recognised as a brittle material due to its low tensile strength and fracture toughness. As an emerging material, AAFS concrete has been extensively studied for its strength properties, demonstrating comparable or even superior performance to OPC concrete [59,67-69]. However, research on the fracture properties of AAFS concrete remains relatively limited.

2.2.2.1 Influence of Precursors

Focusing on low-calcium-based AAFS concrete, Nath and Sarker [116] studied its fracture properties using ambient-curing method. They employed the three-point bending test on notched beams and compared the results with OPC concrete. They reported that FA-based AAFS concretes exhibited similar load-deflection behaviour to OPC concretes, along with comparable fracture toughness and compressive strength. Besides, they found that the fracture energy increased proportionally with SA content, which was attributed to the refined microstructure in concrete matrix. Rooholamini et al. [117] investigated the influence of pozzolanic material proportions on the fracture properties of AAFS concrete. They reported

that a higher proportion of pozzolanic materials (over 70%) resulted in the lower mechanical strength and poorer fracture properties compared to OPC concrete.

Regarding the high-calcium AAFS concrete, Zhang et al. [118] explored the strength and fracture properties in AAFS pastes using two FA:SA ratios (3:7 and 5:5) and various Ms ratios. They found that increasing SA content improved both compressive strength and fracture toughness. Ding et al. [119] compared the fracture properties between AASA and OPC in both mortar and concrete across three compressive strength levels (30, 50, and 70 MPa). They reported that the AASA samples exhibited higher fracture energy than OPC samples, even at a compressive strength of 30 MPa, due to a denser microstructure. In addition, they also found that AASA samples were more brittle than OPC samples due to pre-existing microcracks in the AASA matrix.

2.2.2.2 Influence of Temperature

As mentioned in Section 2.2.1.2, curing temperature significantly influences the mechanical strength of AAFS mortar or concrete. Pan et al. [120] investigated the influence of high temperature curing (60 °C) on the fracture properties of AAFA concrete with varying curing times. They found that curing time over 72 h were less effective in improving the mechanical and fracture properties of AAFA concrete. Furthermore, they reported that AAFA concrete exhibited greater brittleness than OPC concrete at a similar strength level, with lower compressive strength and fracture energy. For a short curing duration, Sarker et al. [121] found that AAFA concrete exhibited higher fracture energy than OPC concrete when cured at 60 °C for 6 hours.

2.2.2.3 Influence of Specimen size

Apart from precursors and curing temperature and time, specimen size also affects the fracture properties. Zhang et al. [122] investigated the fracture properties of AASA and OPC concrete cast with seawater coral aggregate using the three-point bending test on notched beams. They

prepared samples with varying notched crack-depth ratios (0.2, 0.3, 0.4, and 0.5) and alkalinity levels (3, 4, and 6 wt.%). They reported that higher crack-depth ratios increased sample's brittleness due to reduced effective load-bearing capacity. Besides, they found that the higher alkalinity promotes formation of a compact microstructure.

2.2.2.4 Fracture model

Moreover, for OPC concrete, several models have been proposed to describe its fracture behaviour, including the double-K model [123] and the CEB-FIP model [124], among others. Nevertheless, these models have not been validated for AAFS concrete. Ding et al. [125] evaluated the fracture properties of ambient-cured AAFS concrete and validated their findings using predictive models. They reported that Bažant and Becq-Giraduon model [126] provided better predictions for the fracture energy compared to the CEB-FIP model [124].

Currently, research on the fracture properties of AAFS mortar and concrete remains limited, particularly regarding microstructural aspects. Furthermore, the fracture behaviour of AAFS concrete in conjunction with reinforcing bars, both before and after corrosion, represents an area that has yet to be thoroughly explored. Although some studies have examined the fracture properties of fibre-reinforced AAFS concrete [127-129], these topics fall outside the scope of this research and are therefore not discussed here.

2.2.3 Key Issues

Despite AAFS mortar and concrete exhibit mechanical properties that are comparable to, or even superior to, those of OPC mortar and concrete, they face notable durability challenges—particularly shrinkage-induced cracking and efflorescence. Understanding the mechanisms and interrelationship of shrinkage and efflorescence is essential for optimizing mix design, curing conditions, and the long-term performance of AAFS mortar and concrete.

2.2.3.1 Shrinkage-Induced Cracks

Shrinkage is one of the critical engineering properties of concrete, as it involves volume reduction, which may lead to crack formation and consequently affect concrete's durability. In AAFS binders, the extent and type of shrinkage are influenced by various factors, with curing temperature being a significant contributor. According to previous studies, research on AAFS shrinkage has primarily focused on two aspects: (1) autogenous shrinkage [68,130,131], which refers to the volume reduction within hardened concrete caused by ongoing polymerisation between gels; and (2) drying shrinkage [80,132,133], which refers to moisture loss from the pore solution to the surrounding environment. Compared to autogenous shrinkage, drying shrinkage is more likely to cause microcracks.

Under ambient curing conditions, previous studies [134,135] have reported that drying shrinkage in AAFA binders is greater compared to those cured under high temperature. This difference is attributed to high temperature curing promotes the growth of N-A-S-H gel, resulting in a more uniform gel distribution and finer pores [70]. Ma and Ye [136] investigated the autogenous and drying shrinkage of AAFA pastes with varying Na_2SiO_3 contents. They observed that autogenous shrinkage primarily occurred within the first 1-3 days. Specimens with higher Na_2SiO_3 contents exhibited greater autogenous shrinkage, but no visible cracks were detected during this stage. Conversely, drying shrinkage was more significant and associated with higher weight loss [137,138].

AASA binders exhibit greater drying and autogenous shrinkage compared to AAFA binders [137-139]. This behaviour is attributed to the C-A-S-H gel, which is more compact and tortuous than the N-A-S-H gel [140,141], as described in Section 2.1. According to Neto et al. [142], drying shrinkage in AASA paste and mortar occurs in two distinct stages: (1) extensive water loss upon the exposure environment and temperature, and (2) ongoing polymerisation among gels and polycondensation among different phases, which squeezes out moisture. Based on

these, compared to AAFA binders, which rarely exhibit shrinkage-induced cracks [136], AASA binders are more prone to microcrack formation due to drying shrinkage [143].

Humad et al. [144] studied the shrinkage properties of AAFS pastes and concretes. They reported that incorporating FA into SA reduced autogenous shrinkage, thereby limiting the microcrack formation in the binder matrix, but had less impact on drying shrinkage. In addition, they observed the formation of hydrotalcite in the binder matrix, which reduced susceptibility to microcracking. Li et al. [145] and Fang et al. [146] reached similar conclusions, reporting that a higher SA content in AAFS pastes resulted in greater autogenous shrinkage. Furthermore, while compressive strength increases with a higher activator content, the likelihood of shrinkage-induced cracks also rises [147,148]. Therefore, an optimal mix proportion between FA and SA, along with the appropriate alkaline activator concentration, should be considered to balance strength and shrinkage behaviour.

2.2.3.2 Efflorescence

Efflorescence refers to the recrystallisation of leached alkali ions on the surface [149,150], as shown in Figure 6. This phenomenon occurs when alkali ions migrate from the pore solution to the surface in a humid environment. Continuous leaching can deplete the alkalinity of the AAFS samples, reducing pH and potentially weakening the binder matrix [56]. Solids formed on the sample surface can cause surface spalling and microcracks due to volume expansion during the transition from the liquid to the solid phase, ultimately leading to an uneven surface.



Figure 6. Efflorescence in AAFS mortar

Srinivasamurthy et al. [56] studied the influence of efflorescence on the compressive strength of AAFS paste (100FA, 90FA/10SA, and 70FA/30SA). They indicated that the N-A-S-H gel in the 100FA sample underwent slight degradation, forming a carbonate phase after early-age efflorescence, which reduced compressive strength. In contrast, samples containing SA exhibited a slight increase in compressive strength following efflorescence, attributed to a slow, ongoing polymerisation process [149]. However, excessive alkali concentration hinders the reaction between SA and alkaline solution [102,151]. Leaching behaviour diluted the pore solution concentration, allowing previously hindered reactions to continue. Although its compressive strength increased at early ages, long-term behaviour showed a reduction in compressive strength [149]. Furthermore, white deposits caused surface spalling, which increased the porosity [152,153]. Fernando et al. [154] assessed the long-term durability properties of AAFA concrete over 1-year. They reported that efflorescence led to the deterioration of the AAFA concrete, coarsening the pore network and causing cracks. Increased porosity and cracks made the sample more susceptible to aggressive ions, such as chloride [155].

To reduce efflorescence, various additives have been explored, such as zeolite powder [156] and nano-silicate [157]. Zeolite powder inhibits leaching behaviour by binding alkali ions due to its unique structure, while nano-silicate accelerates the alkali ion consumption to form more gel phases. Besides, calcium hydroxide ($\text{Ca}(\text{OH})_2$) [158] and red mud [159] have been found to mitigate efflorescence. Optimising mix design [160] and applying surface coating [161] have also shown potential in reducing efflorescence in AAFS sample.

2.3 Corrosion of Reinforced AAFS

In this section, the corrosion mechanism in concrete will be introduced firstly, followed by a review of chloride-induced reinforcement corrosion in AAFS samples. The overall corrosion process of embedded reinforcement can be divided into three stages [162]:

- **Passivation stage:** In the absence of chloride contamination, embedded reinforcement is protected by a dense passive film composed mainly of iron oxides or hydroxides. This film forms in the highly alkaline environment of concrete and prevents corrosive agents such as oxygen and water from reaching the steel surface.
- **Depassivation stage:** This stage begins when aggressive ions, such as chloride ions from de-icing salts or seawater fog splashes, penetrate the concrete via capillary pores or diffusion driven by concentration gradients [163]. When the chloride concentration at the reinforcement surface exceeds a critical threshold, the passive film deteriorates, exposing the steel to corrosion.
- **Corrosion stage:** Once the passive film is disrupted, and both moisture and oxygen are present, corrosion initiates. In reinforced OPC concrete, localized pitting corrosion is the most common form. Over time, these pits expand, accelerating deterioration and compromising structural integrity.

2.3.1 Microcell and Macrocell corrosion

A schematic representation of reinforcement corrosion in concrete is illustrated in Figure 7, showing two scenarios: microcell and macrocell corrosion.

- Microcell corrosion occurs when different areas of the same steel bar act as the anode and cathode. The exposed steel area becomes anodic, while the surrounding passive zones act as the cathode. In the presence of sufficient electrolyte and oxygen, this leads to localized corrosion, such as pitting.
- Macrocell corrosion occurs when electrolyte or oxygen availability is uneven. In this case, the anode and cathode are spatially separated. Electrons released at the anode travel to a distant cathodic area with sufficient oxygen and moisture. As a result, corrosion spreads over a broader region of the reinforcement.

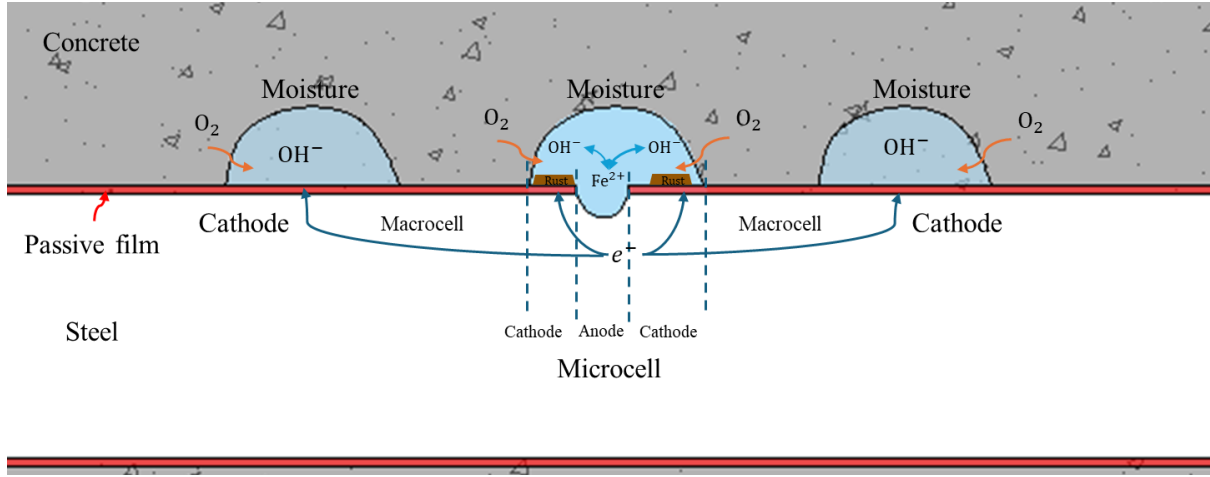


Figure 7. Sketch of microcell and macrocell corrosion in reinforced concrete

2.3.2 Electrochemical (Half-Cell) Reactions

To understand the underlying processes driving both microcell and macrocell corrosion, it is essential to examine the electrochemical reactions occurring at the steel–concrete interface. Once the passive film on the steel surface is disrupted, primarily by chloride ions (Cl^-), as depicted in Eq. 1.



Once the passive film is compromised, the underlying metallic iron (Fe) is exposed to a corrosive environment, initiating a redox (oxidation-reduction) reaction. This redox process consists of two half-cell reactions:

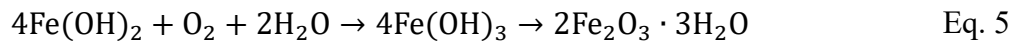
- **Anodic reaction (oxidation):** metallic iron is converted into ferrous ions (Fe^{2+}), releasing electrons (e^-).



- **Cathodic reaction (reduction):** oxygen (O_2) and water (H_2O) (Eq. 3) react with the released to form hydroxide ions (OH^-).



During this process, Cl^- play a critical role by facilitating the transport of dissolved Fe^{2+} away from the corrosion site. The Fe^{2+} then reacts with OH^- to form ferrous hydroxide ($\text{Fe}(\text{OH})_2$), a greenish compound. With continued exposure to oxygen and water, $\text{Fe}(\text{OH})_2$ further oxidises ferric hydroxide and eventually into rust (hydrated ferric oxide, $\text{Fe}_2\text{O}_3 \cdot n\text{H}_2\text{O}$), a brownish compound.



2.3.3 Chloride-Induced Reinforced AAFS Concrete Corrosion

2.3.3.1 Chloride resistance of AAFS samples

For low-calcium AAMs, Kupwade-Patil and Allouche [164] investigated the chloride resistance of reinforced AAFA concrete (Class F FA) cured at 80 °C for 3 days. They conducted a cyclic wetting/drying corrosion test (14 days in a 7.5% NaCl solution followed by 14 days of air drying) over a period of 12 months and compared the results with reinforced OPC concrete. They found that reinforced AAFA concrete exhibited lower porosity and chloride diffusion coefficients, but also a lower chloride threshold for corrosion initiation compared to reinforced OPC concrete. Monticelli et al. [21] studied the corrosion behaviour of reinforced AAFA mortar with three Ms ratios (6.25, 7.14, and 8.33). Samples were cured at ambient environment (25 °C and 35% relative humidity (R.H.)) for 28 days, with reinforced OPC mortar as the reference group. Both samples were exposed to a 3.5% NaCl solution after curing. They reported that higher Ms ratio increased porosity and reduced mechanical strength in AAFA mortar compared OPC mortar. However, they found that the chloride threshold value in AAFA mortar was higher than OPC mortar, indicating better resistance to corrosion initiation, which contradicts the findings of Kupwade-Patil and Allouche [164]. The discrepancy may be attributed to differences in curing method, as heat curing produces a more homogenous binder matrix in AAFA samples, as discussed in Section 2.2.1.2.

Pasupathy et al. [165] reported that of AAFA concrete exhibited lower durability than OPC concrete in a saline lake environment over 6 years. Steam-cured (60 °C) AAFA concrete showed chloride content and chloride diffusion coefficient were approximately 2.5 times higher than ambient-cured OPC concrete. In a follow-up study, Pasupathy et al. [166] found that the chloride diffusion coefficient of AAFA concrete was approximately 1.5 times higher than OPC concrete after 4 years, with pH values between 7 to 8 compared to 12-12.5 for OPC concrete. Ma et al. [167] observed higher permeability in AAFA paste than OPC paste, which suggests a higher porosity.

Chindaprasirt and Chalee [168] reported that the chloride diffusion coefficient in AAFA (Class C FA) concrete decreased as increased NaOH concentration. Thomas et al. [140] evaluated AAFA (Class C FA), AASA and OPC concrete using rapid chloride permeability (RCP), the 90-day salt ponding, and chloride permeability tests. They found that AAFA concrete had a chloride diffusion coefficient more than three times higher than OPC concrete, highlighting poor chloride resistance. In contrast, AASA concrete showed a diffusion coefficient 0.5 to 0.67 times that of OPC concrete, demonstrating the highest chloride resistance. Similarly, Noushini et al. [169] reported that AAFA concrete exhibited lower chloride resistance than OPC concrete, even when cured at high temperatures (60, 70, and 90 °C). Based on these studies, it can be concluded that AAFA mortar and concrete generally exhibit lower chloride resistance than OPC binders.

The fine pore network and tortuosity of AASA microstructure, characterised by the C-A-S-H gel, provide excellent chloride resistance. Roy et al. [170] reported that the chloride diffusion coefficient of AASA binders was approximately half that of OPC binders. Ismail et al. [171] studied the influence of FA on AASA mortar and concrete on chloride permeability using the RCP and salt ponding tests. They prepared mortar samples with FA content ranging from 100% to 0% and concrete samples with FA content from 100% to 50%. Their findings indicated that

chloride diffusion coefficient increased as the SA content decreased, with AAFA mortar and concrete showing the highest diffusion coefficients and AASA binder the lowest. Ma et al. [22] and Runci and Serdar [23] also reported significantly lower chloride diffusion coefficient in AASA binders compared to OPC binders. However, despite its superior chloride resistance, AASA binders remain susceptibility to shrinkage cracks, as stated in Section 2.2.3.1, limiting their application in construction purpose.

AAFS binders combine the benefits of reduced shrinkage crack risk (compared to AASA) and higher compressive strength (compared to AAFA), as mentioned in Section 2.2.1. Babaee and Castel [172] investigated the chloride diffusivity of AAFS mortars with three mix proportions (75%FA/25%SA, 50%FA/50%SA, and 25%FA/75%SA) activated with the different Na_2O concentrations (3%, 5%, and 8%) and cured at the ambient temperature ($23\text{ }^{\circ}\text{C} \pm 2\text{ }^{\circ}\text{C}$). They reported that chloride diffusivity decreased as SA content increased, with a nearly tenfold reduction when the SA content increased from 25% to 75%. This improvement is attributed to the dominant role of C-A-S-H gel, which cross-links with N-A-S-H gel, resulting in the finer porosity [32]. Tennakoon et al. [30] also reported that the AAFS concrete exhibited lower chloride diffusion coefficient than OPC concrete. In summary, the chloride resistance capacity increases in the order: AAFA < OPC < AASA.

2.3.3.2 Chloride Binding Capacity

The chloride resistance of concrete is related to the microstructure of binder matrix and the chloride binding capacity of the hydration phases. Chloride binding refers to the process by which hydration products in the binder matrix fix Cl^- ions through physical adsorption or chemical reactions, reducing their penetration rate and extending the service life of reinforced concrete structures. In OPC systems, the AFm phases (Alumina Ferrite Monosulfate) and C-S-H gel are the primary hydration products with chloride binding capacity [173]. The AFm phases bind chloride ions through chemical reactions, forming Friedel's salt

($3\text{CaO}\cdot\text{Al}_2\text{O}_3\cdot\text{CaCl}_2\cdot 10\text{H}_2\text{O}$), a relatively stable precipitate under natural environmental conditions [174].

For AAFS binders, the chemical composition of raw materials and the activation method differ from OPC, resulting in different gel phases (C-A-S-H and N-A-S-H gels) and secondary hydration phases. In low-calcium AAMs, characterised by N-A-S-H gel, secondary hydration products are almost absent due to lack of calcium content in the precursors. Ismail et al. [171] reported that chloride binding in AAFA binders occurs through physical adsorption by the N-A-S-H gel, which has a large surface area due to its ring-shaped structure, as shown in Figure 2. This process leads to the precipitation of chloride salts upon solution evaporation. However, these precipitates re-dissolve when moisture re-enters the binder matrix. Gunasekara et al. [32] pointed out that the chloride binding capacity of AAFS binders depends on calcium content in the precursor, which promotes the formation of a more compact C-N-A-S-H gel. In addition, Noushini et al. [169], identified the absence of AFm phases and the Friedel's salt in AAFA binders using X-ray diffraction (X-RD) analysis,

In high-calcium AAMs, the higher calcium content in the precursor leads a denser microstructure compared to low-calcium AAMs (Section 2.1), and influences chloride binding capacity. In AASA binders, the tortuous and less porous microstructure binds chloride ions through both physical and chemical methods [173,175]. Secondary hydration phases, such as hydrotalcite-like phases (Mg-Al layered double hydroxide (LDHs)), play a role in chloride binding through anion exchange in the interlayers [176]. The high aluminium and calcium content in SA also supports the formation of AFm phases, which bind chloride ions as Friedel's salt [174]. Although both LDHs and Friedel's salt are present in AASA binder, the amount of Friedel's salt is five times lower than the amount of LDHs [177]. Zhang et al. [178] further pointed out that hydrotalcite-like phases play a more important role in chloride binding than Friedel's salt in AAFS binder.

2.3.3.3 Chloride Threshold

There are two types of chloride ions in concrete: free chloride and bound chloride. Free chloride ions can migrate freely within concrete, whereas bound chloride ions are restricted due to physical or chemical binding to the gel or secondary hydration phases. The chloride threshold, also known as the critical chloride content (C_{crit}), is defined as the minimum chloride concentration required to accumulate on the steel surface to breakdown the passive film [14,15].

Multiple ways are used for expressing C_{crit} , as shown in Table 1. It is commonly represented as a weight percentage (wt.%) of free chloride content to the binder weight [14,179,180]. In some cases, total chloride content is used instead of free chloride content due to the significant lower amount of bound chloride [14,181]. Another expression is the molar ratio of free chloride to hydroxide ions ($[Cl^-]/[OH^-]$), which reflects the balance between free chloride ions and the alkalinity of the pore solution surrounding the reinforcement [182].

Table 1. Different expression for the chloride thresholds

Class	Expression
Free chloride	wt.%, by weight of binder
Total chloride	wt.%, by weight of binder
Molar concentration of chloride ions in pore solution	The molar ratio of $[Cl^-]/[OH^-]$

Over the past few decades, numerous studies [15,182-188] have reported varying C_{crit} values for de-passivating reinforcement, as shown in Table 2. These values depend on raw materials and the corrosion environment. For reinforcement immersed in simulated pore solutions contaminated with chloride, the $[Cl^-]/[OH^-]$ ratio ranges from 0.6 to 0.83 [183,184]. In contrast, reinforcement embedded in OPC mortar exhibits a higher range of 1.17 to 3.98 [182]. This difference is attributed to the absence of chloride binding hydration phases in simulated pore solution, which provides a more uniform environment. Furthermore, Manera et al. [15] reported that the addition of 10% silica fume, significantly increases the C_{crit} values, compared to results from Morris et al. [188]. This increase is attributed to the improved concrete matrix,

which forms a more uniform microstructure and enhances the passive film stability [189]. Moreover, the CEB-FIP model [124] and RILEM recommendations [190] suggest a C_{crit} value of 0.4 wt.% of cement for OPC concrete, a commonly used threshold corrosion initiation.

Table 2. C_{crit} values obtained from the published literature

Reference	Material/System	C_{crit}		
		Free chloride (wt.%)	Total chloride (wt.%)	[Cl-]/[OH-]
[183]	Simulated pore solution with chloride	N/A	N/A	0.6
[184]	Simulated pore solution with chloride	N/A	N/A	0.83
[185]	OPC concrete	0.14 – 0.22	N/A	N/A
[186]	Blended OPC and FA concrete	N/A	N/A	0.20 – 0.70
[182]	OPC mortar	0.39 – 1.16	1.24 – 3.08	1.17 – 3.98
[187]	OPC mortar	N/A	N/A	1.76
[188]	OPC concrete	N/A	0.4 – 1.3	N/A
[15]	OPC + 10% silica fume concrete	N/A	1.1 – 2.0	N/A

For AAFS binders, C_{crit} values are not well-defined due to complex chloride transport and binding mechanisms, as well as the differences in microstructural characteristics. Monticelli et al. [21] examined the influence of activator dosage on the chloride resistance of AAFA mortar, reporting C_{crit} values of approximately 1-1.7 wt.%, significantly higher than the 0.5 wt.% observed for OPC mortars. The increase in soluble silicate of the activator enhances the dissolution of FA, resulting in a more homogeneous N-A-S-H gel, which contributes to higher C_{crit} values. However, despite these higher values, AAFA mortars exhibit lower chloride resistance than OPC mortars due to the large surface area of the ring-shaped N-A-S-H gel and the lack of chloride-binding hydration phases, as discussed in Section 2.3.3.1 and 2.3.3.2.

Babae and Castel [172] studied C_{crit} values in AAFS mortars with three FA/SA ratios (75%/25%, 50%/50%, and 25%/75%) and varying alkali concentrations (3%, 4%, 5%, 6%, and 8% Na₂O). They used total chloride content as C_{crit} value due to the significantly lower bond chloride content. They found that C_{crit} values decreased with increasing SA content and decreasing alkali concentrations. The lowest C_{crit} value (0.19 wt.%) was found in AAFS mortar

with 25%FA/75%SA and 3% Na₂O, while the highest (0.69 wt.%) was observed in the sample with 75%FA/25%SA and 8% Na₂O. This variation was attributed to the sulphate contained in SA precursor, which destabilise the passive film [29,191,192].

Mundra et al. [193] investigated depassivation mechanism of passive film in simulated pore solutions of low-calcium AASA binder using three NaOH concentrations: 0.8 M, 1.12 M, and 1.36 M. They indicated that C_{crit} ($[Cl^-]/[OH^-]$) values of 0.9, 1.70, and 2.40, respectively, which could be expressed as a constant value of 1.25 using the ratio $[Cl^-]/[OH^-]^3$. However, due to the limited literature, the depassivation mechanism in reinforced AAFS mortar and concrete remains unclear.

2.4 Electrochemical Properties Measurement

The corrosion of reinforcement embedded in concrete structures poses a serious challenge to their service life and safety. As mentioned in the introduction, repairing corroded reinforced concrete structures is extremely costly. Therefore, detecting corrosion in reinforced concrete structures before the propagation stage can significantly reduce maintenance costs and extend their service life. In this section, electrochemical techniques for corrosion detection, including open circuit potential, linear polarisation resistance, and the Tafel extrapolation, will be introduced.

2.4.1 Open Circuit Potential

The open circuit potential (OCP), also known as the half-cell potential, represents the corrosion potential (E_{corr}) when the measured object is in equilibrium state. At this state, the reaction rates at the anode and cathode are dynamically equal, and no external current is generated [194]. This method is widely used to determine the corrosion probability of reinforcement in OPC concrete structures due to its speed and non-destructive nature. According to ASTM C876 [195], the corrosion probability of embedded reinforcement can be determined based on E_{corr} values,

as outlined in Table 3. Reference electrodes, such as the CSE (copper/copper sulphate electrode) and SCE (saturated calomel electrode), are commonly used in these measurements.

Table 3. The E_{corr} values and related corrosion probability of reinforcement embedded in concrete [195]

(mV vs. CSE)	(mV vs. SCE)	Corrosion probability
$E_{\text{corr}} > -200$	$E_{\text{corr}} > -127$	Low probability (10% corrosion risk)
$-200 < E_{\text{corr}} < -350$	$-127 < E_{\text{corr}} < -277$	Intermediate condition
$E_{\text{corr}} < -350$	$E_{\text{corr}} < -277$	High probability (90% corrosion risk)

For the measurement of E_{corr} for embedded reinforcement, as depicted in Figure 8, a high-impedance voltmeter is connected to the reinforcement (positive terminal) as the working electrode (WE) and to a reference electrode (RE, negative terminal). A suitable electrolyte layer, such as a sponge soaked in electrolyte solutions, is placed between the RE and the concrete surface to enhance electrical conductivity. The potential difference between reinforcement and the RE is measured by the voltmeter, allowing the corrosion probability of the reinforcement to be determined based on the corrosion potential, as exhibited in Table 3.

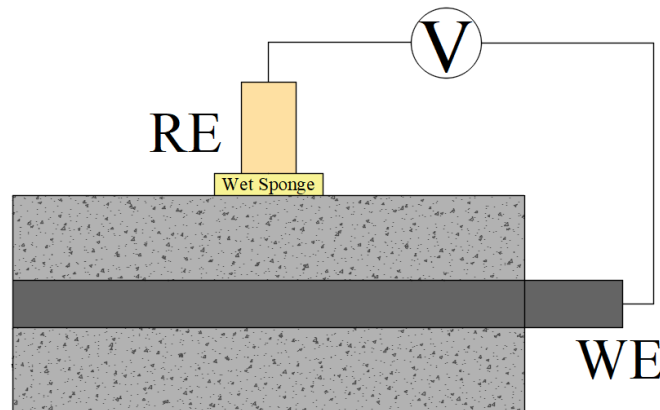


Figure 8. Setting up the OCP measurement of embedded reinforcement

Despite being a widely used and non-destructive tool for assessing corrosion probability, the accuracy of the OCP method can be influenced by various external and material factors. Measured E_{corr} values are affected by concrete cover thickness, contamination by aggressive ions, moisture content, and oxygen availability [28,33,196]. An increase in concrete cover

thickness leads to significant differences in E_{corr} values, particularly for depths exceeding 75 mm, which hinders the accurate corrosion assessment [196].

Aggressive ions, such as Cl^- , can break the passive film on the steel surface once their concentration exceeds the C_{crit} . Before the passive film breaks down, Cl^- accumulation shifts E_{corr} to more negative values [33]. According to Elsener et al. [28], E_{corr} of reinforcement in a wet and chloride-contaminated environment ranges from -400 to -600 mV_{SCE}. Gunasekara et al. [32] tested the effect of chloride-contaminated concrete on E_{corr} using different chloride content levels: 0%, 0.25%, 0.5%, 1%, 2%, 3%, and 5%. They reported that higher chloride content resulted in more negative E_{corr} values: -100 to -300 mV_{CSE} for chloride levels between 0% to 0.25%, -300 to -450 mV_{CSE} for 1% to 2%, and below -450 mV_{CSE} for 3% to 5%.

Moisture content also significantly affects E_{corr} values, as shown in Table 4. E_{corr} shifts to more negative values as moisture content increases, closely related to the oxygen availability around the reinforcement. In saturated concrete, oxygen content in the pores decreases due to the restricted substance transport [197]. Consequently, E_{corr} values become extremely low because oxygen is essential for cathodic reduction in redox reactions, as shown in Eq. 3. A lack of oxygen disrupts the balance of the half-cell reaction, leading to these shifts.

Table 4. E_{corr} values for reinforcement embedded in concrete with different moisture content, data adapt from Elsener et al. [28]

Moisture content in concrete	E_{corr} (mV _{CSE})
Dry	0 to +200
Humidity	-400 to -100
Saturation	-900 to -1000

For reinforced AAFS mortar and concrete, determining corrosion probability through E_{corr} values using ASTM C876 [195] may not be suitable. Several studies [29-31] have reported no corrosion on the reinforcement surface, even when E_{corr} values (around -600 mV_{SCE}) fall within the 90% corrosion risk range, as outlined in Table 3. The presence of sulphide is hypothesised to contribute to these low E_{corr} values. Sulphide can react with O_2 to form a layer of a sulphide

film on the reinforcement surface, which affects the stability of passive film and reduces the redox potential [198].

2.4.2 Linear Polarisation Resistance and Tafel Extrapolation Method

Linear polarisation resistance (LPR) is another commonly used electrochemical technique for evaluating corrosion condition in reinforced concrete. This non-destructive method measures the instantaneous corrosion current density of embedded reinforcement by applying a small overpotential (typically ± 5 to ± 20 mV) around the E_{corr} [111,199]. The polarisation resistance (R_p) is calculated from the linear portion of the potential-current plot during the transition from negative to positive potential, as shown in Eq. 6. More detailed guidance on employing the LPR method for on-site measurements to determine the corrosion rate of reinforced concrete structures is provided by Andrade et al. [27]. They also proposed a criterion for determining corrosion probability based on corrosion current densities, as shown in Table 5. However, a limitation of the LPR method is that it provides information about the overall corrosion of the reinforcement but cannot identify the exact corrosion zone.

$$R_p = \left(\frac{\eta}{\Delta i}\right)_{\Delta E \rightarrow 0} \quad \text{Eq. 6}$$

where R_p is the polarisation resistance; η is overpotential; Δi is the corresponding current density to η .

The Stern-Geary equation [200] is used to calculate the corrosion current densities, as shown below:

$$i_{\text{corr}} = \frac{B}{R_p} \quad \text{Eq. 7}$$

where i_{corr} is the corrosion current density; B is the Tafel constant value.

Table 5. Ranges of i_{corr} values related to corrosion probability of the reinforcement, adapted from [27].

i_{corr} ($\mu\text{A}/\text{cm}^2$)	Corrosion probability
≤ 0.1	Negligible
$0.1 - 0.5$	Low
$0.5 - 1$	Moderate
>1	High

The Tafel constant B is calculated using the extrapolation method, which employs a similar technique to the LPR method but with a larger polarisation potential range (± 200 mV) [194]. Andrade and Gonzalez [201] introduced the potential-logarithmic current (E vs. log i) curve identifying linear sections in both anodic and cathodic polarisation curves. From these, the anodic (β_a) and cathodic (β_c) Tafel slopes and can be determined, enabling the calculation of the Tafel constant B using:

$$B = \frac{\beta_a \cdot \beta_c}{2.303(\beta_a + \beta_c)} \quad \text{Eq. 8}$$

An example of a Tafel plot is shown in Figure 9. By extrapolating the linear regions of the anodic and cathodic branches, the critical i_{corr} value can be determined at the intersection point. However, this technique is considered destructive when a large polarisation potential range is employed, as this can cause irreversible changes to the reinforcement's surface properties [202,203].

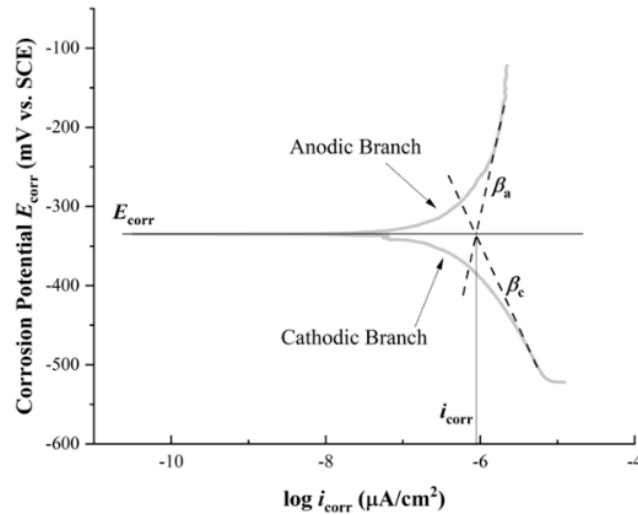


Figure 9. Example of the Tafel plot

For reinforced OPC concrete structures, widely accepted B values are 26 mV (active condition) and 52 mV (passive condition), as proposed by Andrade and Gonzalez [201]. For reinforced AAFS mortar and concrete, B values were reported deviate significantly from those used for OPC concrete [111,204,205]. Babae and Castel [111] reported B values for AAFS (85%FA-15%SA) concrete ranging from 45 mV and 58 mV, in active conditions, while 13 mV and 20 mV in passive conditions. Robayo-Salazar et al. [205] studied carbonation effects on low-calcium AAMs (70% natural volcanic pozzolan and 30% SA) over 360 days, finding specimen still in passive, B values ranges from 16 mV to 20 mV. Runci et al. [204] assessed B values of reinforced AAFS mortars using the Tafel extrapolation. They reported that these values were 15 mV to 25 mV for passive conditions, and 55 mV to 63 mV for active conditions.

These findings indicate that the B values for reinforced AAFS mortar and concrete deviate significantly from the empirical values used for reinforced OPC concrete. Using a B value of 26 mV could underestimate the actual corrosion rate in reinforced AAFS systems. However, due to limited data, appropriate B values for reinforced AAFS mortar and concrete remain unclear.

2.5 Bond Properties, Morphology and Spatiotemporal Evolution of Corrosion at SMI/SCI

2.5.1 Bond Properties for Reinforced AAC

The bond performance between reinforcement and concrete is an important characteristic for reinforced concrete, as it ensures that the reinforcement remains in position and effectively transfers tensile forces. Bond strength depends on several forces, including interface adhesion, friction, and mechanical interlocking (e.g., coarse aggregate interlock) [206]. Corrosion, particularly chloride-induced corrosion, as described in Section 2.3, can deteriorate bond strength. While the early-stage corrosion may temporarily increase the bond strength by filling micro-gaps at the steel-concrete interface (SCI) with corrosion rust, prolonged corrosion ultimately reduces bond strength. For reinforced AAFS concrete, bond strength characteristics are reviewed in the literature regarding the following aspects: (1) material types and exposure environments, and (2) the influence of reinforcement corrosion.

For the influence of material types, as described in Section 2.2.1, the compressive strength of high-calcium and low-calcium AAFS concrete varies due to differences in microstructure, which also affects the bond strength. Albitar et al. [207] reported that reinforced AAFA concrete exhibits stronger bond strength than reinforced OPC concrete. This finding aligns with Adak and Mandal [208], who studied the bond strength of reinforced AAFA concrete under different curing environments (elevated and ambient temperatures). They found that shorter periods of elevated temperature curing improve bond strength. Al-Azzawi et al. [209] observed that the bond strength of reinforced AAFA concrete increases with higher FA content (from 300 to 500 kg/m³) and SiO₂ content in activators but decreases with higher Na₂O content. Increased FA content promotes a more homogeneous and compact binder matrix, while higher SiO₂ content enhances the skeleton structure of N-A-S-H gel. In contrast, excessive Na₂O content may hinder chemical reaction by forming a compact hydroxide layer around the FA particles [102].

Zhang et al. [210] examined the influence of curing temperature (25, 100, 300, 500, and 700 °C) on the bond strength of blended MK and FA concrete. Pull-out test results showed specimens cured below 300 °C exhibit similar bond behaviour, however, bond strength significantly decreases by half when the curing temperature is over 500 °C.

Ramagiri et al. [211] studied the bond performance of ambient-cured, low-calcium-based reinforced AAFS concrete under high temperature. They found that bond strength increased with higher SA content under ambient curing but decreased after high-temperature exposure. Notably, samples with an FA:SA ratio of 7:3 exhibited the best mechanical performance at temperature exceeding 760 °C. This improvement was attributed to the formation of new crystalline phases, such as akermanite ($\text{Ca}_2\text{MgSi}_2\text{O}_7$) and gellenite ($\text{CaSO}_4 \cdot 2\text{H}_2\text{O}$), which reduced porosity. Liu et al. [212] investigated the bond performance of ambient-cured, high-calcium-based reinforced AAFS concrete under high temperatures (up to 800 °C). They found that bond strength decreased with increasing temperature. Based on their results, high-calcium AAFS concrete exhibited superior bond performance compared to low-calcium samples under ambient conditions [211] and similar bond performance under high-temperature conditions.

To understand the bond behaviour of AAFS concrete under non-elevated temperature conditions, Castel and Foster [213] investigated the bond properties of low-calcium reinforced AAFS concretes cured at 80 °C, using reinforced OPC concretes as a control group. Both ribbed and smooth bars were tested. They reported higher bond strength in reinforced AAFS concrete than in reinforced OPC concrete, however, they concluded this was not due to better chemical adhesion in AAFS concrete, as similar bond stress-slip behaviour was observed in samples with smooth bars.

Regarding the effects of corrosion, Cui et al. [214] studied the influence of corrosion on the bond properties of reinforced AASA concrete with 16 mm rebar, using OPC concrete a

reference. The impressed current method, with a current density of $200 \mu\text{A}/\text{cm}^2$, was applied to samples to accelerate reinforcement corrosion. They pointed out that the ultimate bond stress increased at a corrosion degree reached of 0.5% but decreased thereafter. AASA specimens exhibited slightly higher bond strength than OPC specimens at a corrosion degree of approximately 1%. Similarly, Albitar et al. [207] reported that reinforced AAFA concrete exhibited stronger bond strength than OPC concrete after corrosion.

Although studies on the bond properties at the SCI for reinforced AAFS concrete using glass fibre-reinforced polymer rebars have been conducted [215], they are not included here as they fall outside the scope of corrosion. Due to limited studies on the effects of corrosion on bond properties in reinforced AAFS concrete, its characteristics remain insufficiently understood.

2.5.2 Morphology at the steel-mortar/concrete interface

The SCI or steel-mortar interface (SMI), refers to the contact zone between rebar and concrete or mortar, playing an important role in reinforced concrete/mortar structures, particularly in influencing the corrosion behaviour of embedded reinforcement in corrosive environments. This is due to the inhomogeneity and porous structures around the reinforcement [216], as shown in Figure 11, which increase the risk of reinforcement corrosion. The “wall effect” refers to the tendency of coarse aggregates to be excluded or less densely packed near the formwork or mould walls, resulting in a paste-rich or aggregate-deficient zone near the boundaries, as shown in Figure 10. A similar packing inefficiency occurs in the interfacial transition zone (ITZ)—the region surrounding the aggregate particles—where the accumulation of fine particles leads to higher porosity and weaker mechanical properties. This effect also explains the porous structure found around reinforcement, which can be regarded as a special type of aggregate in concrete [216,217]. As the SCI or SMI, the presence of rebar disrupts the uniform packing, leading to a locally paste-rich zone with elevated porosity. Referring to downward casting direction, Chen et al. [218] observed that the porous zone around a horizontally

embedded rebar is significantly thicker on the lower side than on the upper side after hardening. This asymmetry results from the combined effects of bleeding water rising, vibration-induced particle rearrangement, and gravity-driven settlement of solid particles, which are more pronounced on the underside of the steel bar during casting [219].

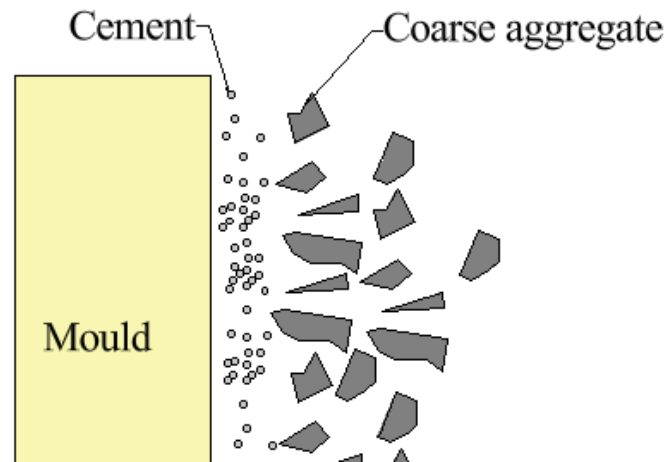


Figure 10. Sketch of wall effect

Bleed water refers to the water that migrates upward and accumulates on the upper side of the transversely placed rebar in freshly poured reinforced concrete [220,221]. This behaviour results in a more porous and coarser region in the concrete matrix on the upper side of the reinforcement, weakening the bond between the rebar and the concrete. The application of vibration further accelerates this effect, as air bubbles trapped beneath the rebar during the vibration lead to voids around the rebar [222]. These phenomena are collectively referred to as the “top bar effect” [216,219]. In addition, concrete settlement beneath the rebar can cause these voids to expand, increasing their thickness [223].

To better characterise the SCI, techniques such as scanning electron microscopy (SEM) are commonly employed [217]. SEM enables high-resolution imaging of the SCI and operates in two primary modes: secondary electron (SE) mode and backscattered electrons (BSE) mode. SE mode captures morphological and topographic features of the sample’s surface, while the

BSE mode distinguishes material phases within the sample [218,224-226], as illustrated in Figure 12. SEM is often coupled with energy dispersive spectroscopy (EDS). EDS provides element distribution maps by scanning specific lines or areas [227].

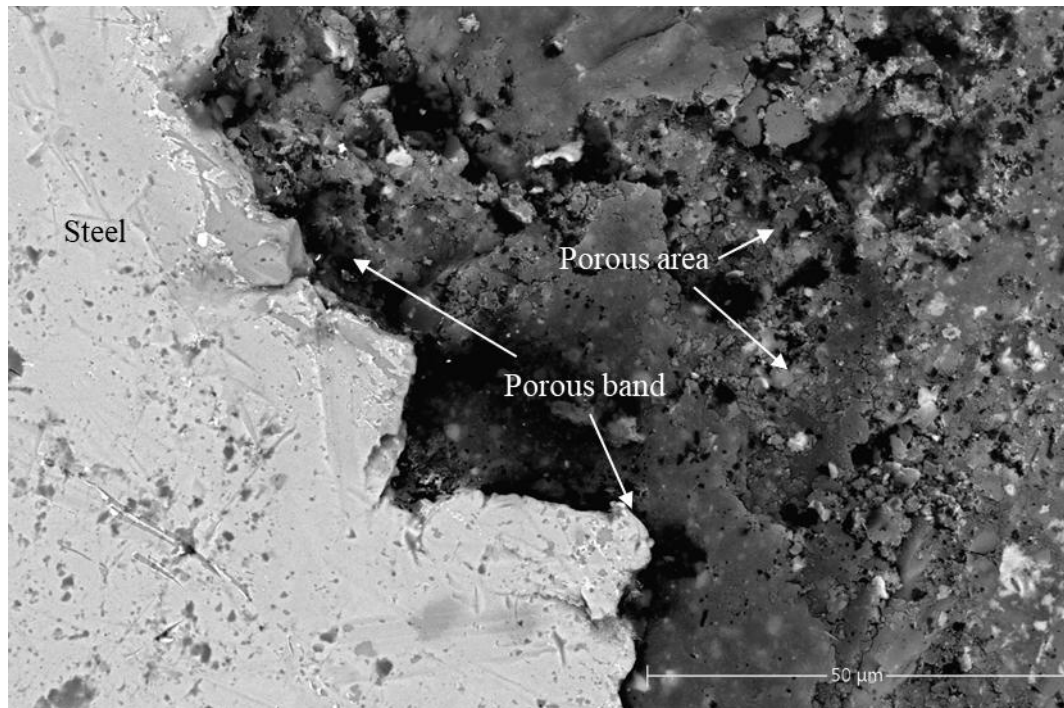


Figure 11. BSE image for porous structure around the steel

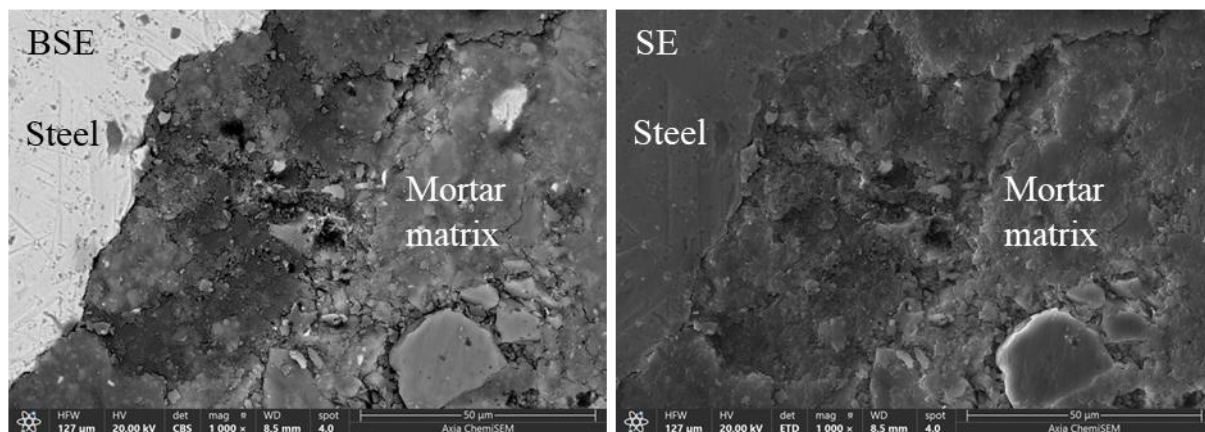


Figure 12. Examples of SEM images in BSE mode (left) and SE mode (right)

These techniques are widely used to study the morphology and the corrosion of reinforcing bar in reinforced concrete structures. Shi et al. [228] studied the corrosion behaviour of 2304 duplex stainless steel embedded in OPC and AASA mortars. Using BSE-EDS analysis, they characterised the SMI and found that the SMI in OPC mortar was less compact and more porous

than that in AASA mortar after 360 days of accelerated corrosion. Shi et al. [91] investigated the long-term corrosion resistance of reinforced AASA mortar in marine environments over 54 months. They examined two corrosive environments: 3.5% saltwater immersion and atmospheric exposure. Results indicated that corrosion resistance of reinforced AASA mortar was lower under atmospheric exposure than in saltwater immersion, evidenced by differences in corrosion rust layer thickness observed in BSE-EDS images. This difference was attributed to the low carbonation resistance of AASA mortar due to the absence of portlandite in the pore solution, which acts as a buffer against carbonation [229-232].

Chen et al. [233] and Wang et al. [234] studied the composition of the passive film on steel rebar immersed in simulated AAFA and AASA pore solutions, respectively, using SEM-EDS analysis and other analytical techniques. In AAFA pore solution, the passive film consists of a bilayer structure with an FeOOH-rich outer layer and an FeO-rich inner layer, along with a firm, zeolite-like layer outside the passive layer [233]. In AASA pore solution, an adsorption aluminate/silicate layer was observed on the passive film, and a less compact FeS layer was detected in the inner passive film using X-ray photoelectron spectroscopy (XPS) [234]. However, simulated pore solutions cannot fully represent the actual characteristics of the passive film on reinforcement embedded in mortar or concrete. This limitation because the simulated pore solution provides a uniform environment with unrestricted substance transport, however, this is restricted in AAFS mortar and concrete due to the complex pore network. Due to limited studies on the SCI or SMI in reinforced AAFS concrete, the relationship between corrosion mechanism and interface characteristics remains unclearly.

2.5.3 Spatiotemporal Evolution of Corrosion at SCI and SMI

Although SEM coupled with EDS enables the study of morphological and topographic characteristics at the SCI in reinforced concrete and the SMI in reinforced mortar, these techniques require destructive sample preparation steps, such as slicing. These treatments only

reveal surface information at a specific moment, leaving the temporal evolution of surface characteristics unknown. To study the spatiotemporal evolution of corrosion characteristics at the SCI or SMI over time, X-ray computed tomography (X-CT) technique can be utilised. X-CT is a non-destructive method that provides high-resolution 3D images of a sample's internal structure without causing physical damage [235]. This technique offers valuable insights into the durability of reinforced concrete structures by illustrating how corrosion initiation and progression affect overall structural performance. For instance, X-CT can reveal the spatial distribution of corrosion rusts at the SCI [226,236] and the cracks induced by internal tensile forces resulting from the accumulation of corrosion rusts. These insights enable the development of numerical models that simulate the expansion of corrosion products and crack propagation [18,237,238], therefore, facilitating more accurate predictions of the service life of reinforced concrete structures.

Beck et al. [239] were among the first to study the corrosion process of reinforcing steel in chloride-contaminated mortar cylinder ($\varnothing 40$ mm x 90 mm) using X-CT analysis. Their results demonstrated that X-CT analysis is a suitable technique for investigating pitting corrosion in rebar embedded within mortar samples. Šavija et al. [240] highlighted the value of X-CT analysis in studying the fracture behaviour of hardened cementitious materials. They employed X-CT to monitor the formation of corrosion-induced cover cracking in reinforced mortar cylinder samples using subjected to impressed current method. Dong et al. [241] used X-CT to track the evolution of corrosion products over time, from the initiation of corrosion in reinforcement embedded in the cement paste to the propagation of corrosion-induced cracks. Their work provided detailed observations of the morphology at rebar-cement paste interface, including pits cavities, the spatial distribution of corrosion rust, and crack formation. In further research, Dong et al. [242] investigated the performance of corrosion inhibitors in reinforced

concrete using X-CT analysis. They reported that corrosion inhibitors delay rust formation at the SCI, thereby extending the service life of reinforced concrete structure.

In addition to providing morphological information on corrosion at the SCI or SMI, X-CT analysis can also help determine corrosion mechanisms within hardened cementitious materials. Itty et al. [243] conducted in-situ monitoring of corrosion on different types of rebars (carbon steel and ferritic stainless steel) embedded in cement paste by coupling galvanostatic corrosion with X-CT analysis. Their results revealed that carbon steel exhibits more homogeneous corrosion, whereas ferritic stainless steel shows localised corrosion.

However, most studies, including those mentioned above, used the impressed current method to accelerate corrosion [244-247]. This approach can weaken or eliminate the effects of the concrete matrix, such as the buffering action of portlandite in the pore solution. In contrast, the corrosion process of reinforced concrete in natural environment differs significantly from that induced by the impressed current method. In natural settings, no external electric field drives the migration of corrosive ions. Instead, ion transport in concrete is primarily governed by diffusion and capillary suction, as introduced in Section 2.3.1.

To address the limitations of the impressed current method, Xi and Yang [235] employed an alternative wetting-drying cyclic corrosion process (salt fog spray and high-temperature drying) using a corrosion chamber to accelerate corrosion in corner-located smooth steel bars embedded in OPC concrete. They utilised X-CT analysis to study the spatial distribution of corrosion and reported the presence of a transverse crack extending from outer surface towards the smooth steel bar. This finding is significant because transverse cracks in reinforced concrete were previously not well-identified and were often attributed to load-induced cracking rather than cracking caused by the accumulation of corrosion rusts [235]. Compared to the impressed

current method, the use of a corrosion chamber allows for more precise control of parameters when simulating marine environments, providing a closer approximation to natural conditions.

Current literature on the study of AAFS mortar and concrete using X-CT analysis has primarily focused on analysing microstructural characteristics, such as pore structure. Guha and Ouellet-Plamondon [248] utilised X-CT analysis to study the porosity of blended FA with bauxite residue. Similarly, Brakat and Zhang [249] studied the dispersion and pore structure of the AASA paste reinforced with natural cellulose fibres. By reconstructing 3D images from X-CT data, they observed a well-dispersed distribution of fibre in the AASA paste, which effectively mitigated shrinkage. Ling et al. [250] used X-CT analysis to examine the distribution of corrosion rust and crack behaviour in reinforced AAFA paste containing fibres. They applied the impressed current method to accelerate the corrosion in the samples, using two different setups: one wrapped in a sponge and the other in stainless steel mesh. Results revealed that cracks caused by the accumulation of corrosion rust grew faster in the stainless-steel wrapped sample compared to the sponge wrapped sample.

Based on the reviewed literature, a significant research gap exists in the study of corrosion in reinforced AAFS mortar or concrete, particularly regarding the spatiotemporal evolution of corrosion at the SCI or SMI.

2.6 Numerical simulations of corrosion in reinforced concrete or mortar

As computer technology continues to evolve rapidly, numerical simulation has become an increasingly powerful tool for analysing, predicting, and optimising the performance of complex systems. In the context of reinforced concrete structures, numerical simulations provide valuable insights into predicting the service life by simulating corrosion behaviour. Over the past two decades, numerous corrosion models [16-20,251,252], both uniform and non-uniform, have been developed to simulate the corrosion of reinforcement embedded in concrete and its impact on structural performance. For instance, Dekoster et al. [20] employed

finite element analysis (FEA) to study the flexural behaviour of corroded concrete beams under uniform corrosion conditions. They indicated that a good agreement between FEA results with experimental data. Similarly, Chen and Mahadevan [252] proposed a uniform corrosion model to simulate the three stages of chloride-induced corrosion in reinforced concrete.

In the past decade, numerical models for chloride-induced corrosion in reinforced concrete have gradually shifted from uniform to non-uniform. This transition is driven by the ability of non-uniform models to more accurately represent corrosion behaviour under natural conditions. Zhao et al. [19] compared the damage caused by uniform and non-uniform corrosion in reinforced concrete. They proposed a Gaussian model to describe the distribution of non-uniform corrosion and demonstrated that non-uniform corrosion causes greater damage to concrete cover than uniform corrosion. Beyond Gaussian models, alternative approaches have been developed to characterise the fracture behaviour of concrete cover under corrosion. Xi et al. [18] introduced a meso-scale von Mises model to simulate the fracture behaviour of concrete cover under non-uniform corrosion. Their simulations revealed that microcracks formed on the surface of concrete cover before the development of discrete cracks, consistent with their X-CT results [235].

The corrosion mechanisms of reinforcement in concrete were introduced in Section 2.3.1. To comprehensively evaluate corrosion behaviour under varying conditions and the role of individual material phases, such as coarse aggregate [253], multi-physics coupling simulations have gained significant attention for their ability to capture complex interactions. Environmental conditions, such as the freeze-thaw cycles in cold regions [254] and wetting-drying cycles in marine environments [255], exert distinct effects on chloride transport in concrete. Chen et al. [254] investigated chloride transport using multi-phase coupling, considering factors such as coarse aggregate, the ITZ, and freeze-thaw cycles. Their results, validated against experimental data, revealed that coarse aggregate exhibits a buffering effect

on chloride diffusion, while the ITZ accelerates chloride transport. Additionally, they observed that freeze-thaw cycles enhance chloride transport, with this effect becoming more pronounced as the number of cycles increases. Van der Zanden et al. [255] proposed a model coupling water and chloride ions diffusion in concrete while accounting for wetting-drying cycles. They reported that chloride ion transport primarily occurs through the large pores, fully saturated pores, with smaller pores contribute minimally to this process.

Electrochemical theory-based simulations of corrosion in reinforced concrete and mortar [194] have also garnered increasing attention. This approach incorporates the Nernst-Planck equations (thermodynamics) and activation polarization equations (kinetics) to describe ion diffusion and the corrosion process. Bentz et al. [256] modelled the influence of transverse cracks on chloride penetration using Fick's second law. By comparing experimental data with simulation results, they found strong agreement between each. Cao [257] simulated localised corrosion in chloride contaminated reinforced concrete, incorporating both microcell corrosion and macrocell corrosion mechanisms through polarisation equations. Jones et al. [258] investigated the chloride-induced corrosion in reinforced concrete, evaluating corrosion resistance methods such as crack fillers and epoxy-coated steel bars through numerical simulations. They pointed out that the continuum model might underestimate chloride concentration and overestimate the service life of reinforced concrete structures. However, their simulation lacked the experimental validation. Samson et al. [259] used 3D simulations to evaluate a newly developed probe for assessing the corrosion state of reinforced concrete structures. Michel et al. [260] simulated the corrosion propagation in reinforced concrete using electrochemical parameters derived from their experimental works. Fu et al. [251] proposed a non-uniform corrosion model based on experimental results obtained from the impressed current method applied to rebars embedded in mortar samples.

In simulation of reinforced AAFS concrete and mortar, Liu et al. [253] investigated chloride transport in AAFS concrete. They found that SA content refines pore structures, which delays the corrosion initiation, while coarse aggregate provides limited benefits in mitigating chloride transport. Ling et al. [250] studied corrosion in reinforced FA mortar combined with polyvinyl alcohol (PVA) fibre using both experimental and numerical methods. Employing a non-uniform corrosion model, they observed that the distribution of rust thickness followed a Gaussian distribution. Yang et al. [261] studied the influence of chloride diffusion on the service life of AAFA and LC³ (limestone-calcined clay) concrete, considering variations in pore tortuosity. Their simulation results revealed that LC³ concrete exhibited the highest pore tortuosity compared to AAFA concrete, indicating a stronger buffer effect against chloride ingress.

The microstructure characteristics of AAFS concrete or mortar vary significantly depending on mix ratios, precursor types, activator concentration, and curing environments. However, these parameters are not yet fully understood, resulting in limited advancements in simulation research in this area.

2.7 Summary

This chapter provides a comprehensive review of AAMs' products, focusing on their fundamental characteristics, mechanical properties, corrosion resistance, electrochemical performance, and interfacial behaviour. However, current studies lack a clear understanding of corrosion behaviour in reinforced AAFS mortar and concrete, particularly regarding the spatiotemporal evolution at the steel–concrete interface. In addition, the commonly used B value from OPC systems may not be suitable for AAFS, reliable data are currently limited. Furthermore, despite their strong mechanical performance, AAFS materials face durability challenges such as shrinkage-induced cracking and efflorescence.

Therefore, this research focuses on evaluating the long-term performance of reinforced AAFS mortar and concrete under corrosive conditions, aiming to support their practical application.

3 Methodology

3.1 Materials, Sample and Experiment Preparation

3.1.1 Precursors, Alkaline Activator and Casting Procedure

In this research, two primary types of AAMs were utilised: Class F FA sourced from CEMEX, UK, and GGBS provided by Hanson cement, UK. In addition, metakaolin (MK) and limestone powder (LSP) were incorporated as supplementary materials. MK was used to examine the effect of alternative cementitious materials in the AAFS system, while LSP was introduced to evaluate the influence of inert mineral additions. The chemical compositions of these materials were analysed using X-ray fluorescence analysis and are presented in Table 6.

Table 6. Chemical composition of precursors determined by X-Ray fluorescence analysis [wt.%]

Element	SiO ₂	Al ₂ O ₃	CaO	MgO	SO ₃	Fe ₂ O ₃	Na ₂ O	K ₂ O	TiO ₂	MnO	P ₂ O ₅	SrO	BaO	Loss on ignition (L.O.I)
Class F FA	52.7	19.7	8.4	1.76	0.08	8.24	1.01	1.66	0.9	0.06	0.42	0.11	0.18	4.33
GGBS	33.6	13.9	40.2	8.02	0.62	1.12	0.22	0.56	0.71	0.28	0.03	0.04	0.07	0.72
MK	62.22	30.43	0.07	0.15	0.06	1.30	0.04	0.73	1.62	<0.01	0.05	0.01	0.04	3.28
LS	8.95	0.12	51.5	0.22	0.03	0.14	<0.01	0.02	0.01	0.03	0.06	0.07	<0.01	40.02

The formulation and preparation of the alkaline activators, which play a key role in initiating the polymerisation reaction, are detailed as follows:

Preparation of alkaline activator:

- The alkaline activator was prepared by combining a 12 M NaOH solution with a Na₂SiO₃ solution, maintaining a total equivalent Na₂O of 7% relative to the binder mass (FA+SA). The Na₂O contribution was proportioned between the two components at a fixed mass ratio of 1:2.5 (NaOH:Na₂SiO₃). This combination was designed to achieve high early-age mechanical strength in the specimens [262].

Solution preparation:

- The 12 M NaOH solution was prepared by dissolving 480 g of NaOH pellets (\geq 98%purity) into 1 litre of deionised water in a beaker, using a magnetic stirrer to

facilitate dissolution. After cooling to room temperature, the solution was transferred to a 1-litre volumetric flask and stored in the chemical storage cabinet until sample casting. The Na_2SiO_3 solution contained 13.5% Na_2O , 26.5% SiO_2 , and 60% H_2O by mass. Both solutions were sourced from Fisher Scientific, UK.

Water to solid (binder + dissolved solid in alkaline solution) ratio:

- A water to total solids ratio of 0.3 was adopted (including both added free water and the water contributed by the alkaline solutions) to optimise sample performance. Trial tests demonstrated that higher ratios introduce excess free water, leading to prolonged setting times and reduced mechanical strength.

Additionally, sand with a fineness modulus of 2.75 was used as the fine aggregate. Two types of coarse aggregates were utilised in this research, which were the 10 mm gravel and 20 mm limestone. At the beginning of this research, 10 mm gravel was used for sample casting to evaluate the mechanical properties of AAFS concrete; however, the gravel was later replaced with 20 mm limestone due to its lower mechanical strength and less favourable interfacial properties, which resulted in low strength of the cast samples and failed to meet the expected performance.

To comprehensively investigate the corrosion behaviour of reinforced AAFS mortar and concrete, five basic mix proportions of Class F FA and SA were designed, ranging from high-calcium systems (C-A-S-H gel) to low-calcium systems (N-A-S-H gel), as detailed in Table 7. In addition, two supplementary groups were included within the 70SA-30FA mix. In these groups 20% of the FA was replaced with MK and LSP, respectively. These substitutions were applied only for samples using limestone aggregate to study the influence of these materials on the strength properties of AAFS concrete. For comparison, a reference OPC group with a water-

to-cement ratio of 0.4 was prepared, this ratio is commonly used in cement studies as it balances hydration efficiency, mechanical performance, and practical workability.

Table 7. Mix proportions for AAFS samples (Unit: kg/m³).

Group ID and name	OPC	Class F FA	GGBS	LS	MK	NaOH	Na ₂ SiO ₃	Free water	Sand	Coarse Aggregate
1 100SA	-	-	400	-	-	44.06	110.15	43.09	640	1152
2 70SA-30FA	-	120	280	-	-					
3 50SA-50FA	-	200	200	-	-					
4 30SA-70FA	-	280	120	-	-					
5 100FA	-	400	-	-	-					
6 70SA-20LSP-10FA	-	40	280	80	-	-	-	160	640	1152
7 70SA-20MK-10FA	-	40	280	-	80					
8 OPC	400	-	-	-	-	-	-	-	-	-

To ensure consistent mixing and uniformity across all test groups, appropriate mixing equipment and procedures were employed. As shown in Figure 13, two different types of Hobart mixers were used: one for AAFS mortar and another for concrete. The mortar mixer features three speed levels, the low, medium, and high, designed for different mixing requirements. The low-speed setting was used to achieve the uniform distribution of raw materials, including precursors and sand, while the medium-speed setting ensured thorough mixing of the alkaline activator with the raw materials. Using medium-speed mixing will promote mortar formation between the alkaline activator and solid precursors. This approach prevents premature hardening of the mixture, which typically occurs under low-speed mixing conditions. The high-speed mode was not utilised during the casting process. In contrast, the concrete mixer operates at a single fixed speed.

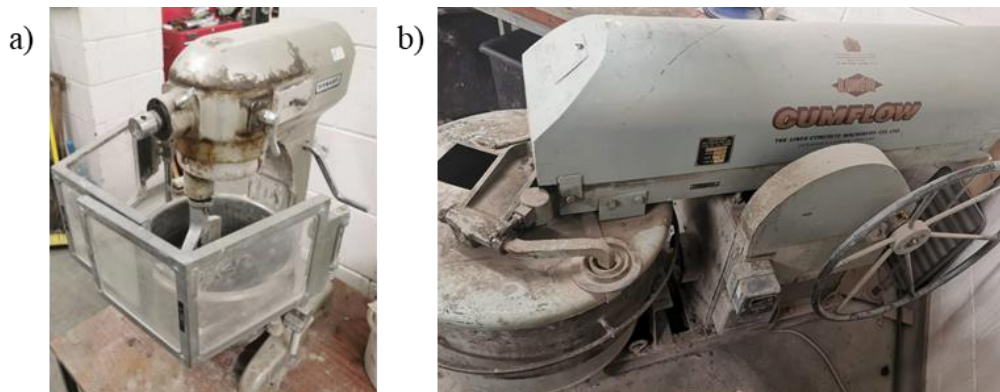


Figure 13. Two different types of Hobart mixers: a) mortar mixer; b) concrete mixer



Figure 14. The alkaline solution mixed using a magnetic stirrer

The alkaline solution, consisting of a 12 M NaOH solution, Na_2SiO_3 solution, and free water, was pre-prepared and thoroughly mixed using a magnetic stirrer to ensure uniformity, as shown in Figure 14. After preparing the alkaline activator, the mixing and casting process were carried out. The casting procedure for AAFS mortar and concrete samples followed the same initial steps, with the only difference being addition of coarse aggregate for concrete samples. The detailed steps are outlined below:

1. The precursors were poured into the mixer container and mixed at a low speed to ensure even distribution.
2. Concrete sand was then added to the container and mixed at the same speed until evenly distributed.

3. The alkaline activator was gradually added while mixing continued. Low speed mixing was initially used to roughly combine the activator and precursors, followed by medium speed mixing to achieve a thorough mix.
4. For AAFS concrete samples, limestone was then added to the mortar and mixed until a uniform consistency was achieved.

After the mixing, the mortar or concrete was poured into various moulds. Following initial setting, the moulds were wrapped in plastic film to prevent excessive moisture loss and then placed in the oven for curing. The specimens were cured at 60 °C to promote early strength development. This elevated curing temperature was necessary because the presence of FA in the precursors tends to slow strength gain due to the high energy required for initiating chemical reaction [39].

3.1.2 Sample Preparation

In this research, samples of various sizes were cast to facilitate different studies:

- 100 x 100 x 100 mm³ cubes to assess the compressive strength of AAFS concrete
- Ø100 x 200 mm³ cylinders to evaluate the split tensile strength of AAFS concrete
- 150 x 150 x 600 mm³ beams to investigate the fracture properties of AAFS concrete
- 150 x 150 x 150 mm³ cubes to explore the bond properties of reinforced AAFS concrete under different corrosion conditions
- 40 x 40 x 160 mm³ prisms to study the flexural strength and compressive strength of AAFS mortar
- 40 x 40 x 80 mm³ prisms to quantify the electrochemical behaviour of reinforced AAFS mortar and analysis morphological and topographic features after the corrosion initiation.

- Ø20 mm x 20 mm cylinders to explore the spatiotemporal evolution of corrosion inside reinforced AAFS mortar

The types and dimensions of the samples are outlined above, and a detailed description of the specimen preparation is provided below. The procedures for basic strength tests, including the compressive strength test for concrete cubes, split tensile strength test for concrete cylinders, and flexural and compressive strength tests for mortar prisms, are not described here, as they are detailed in BS EN 12390-1 [263], BS EN 12390-6 [264], and BS EN 196-1 [264], respectively. Table 8 provides detailed information for each sample type, including the heat curing conditions, sample sketches (excluding the standard cube, cylinder, and prism specimens), and the mix groups selected for each experimental setup.

To investigate the electrochemical behaviour of reinforced AAFS mortars, from the passive state to corrosion initiation, five basic mix groups (1-5, as shown in Table 7) and an OPC reference group were selected. The specimens were designed as 40 x 40 x 80 mm³ mortar prisms with a Ø6 mm rebar embedded at the centre. To facilitate electrical connection, a small hole was drilled into one side of the rebar's cross-section, and a copper wire was inserted and soldered with lead to act as a conductor. Both ends of the rebar were then sealed with epoxy resin before embedding it in the mortar prism. A sketch of the sample is exhibited in Table 8.

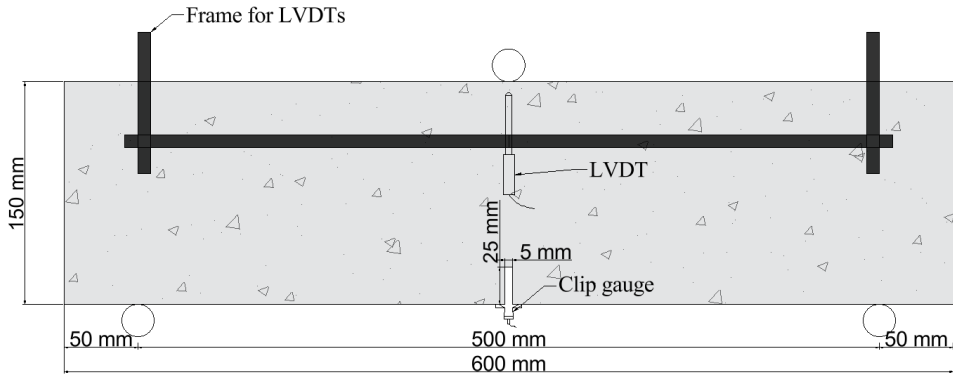
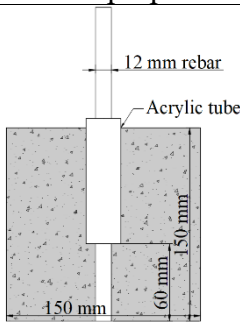
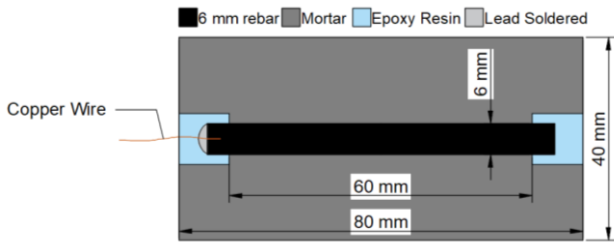
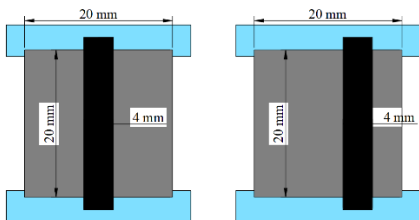
X-CT was used to study the spatiotemporal evolution of corrosion at the SMI, high resolution for phase analysis was crucial. Therefore, a Ø20 mm x 20 mm mortar cylinder, adapted from Xi and Yang [235], was selected with mix group 3. A Ø4 mm smooth steel bar was positioned in two configurations: one centred within the cylinder and the other offset by 4 mm from the centre. Both ends of the cylinder were coated with epoxy resin to prevent the corrosion of the exposed steel bar. These configurations were designed to investigate corrosion in both relatively uniform and non-uniform environments. A sketch of samples is shown in Table 8.

The sample used to study the bond properties between reinforcement and concrete was designed in accordance with RILEM recommendations [265], which specify a bond length of at least five times the rebar diameter. Accordingly, a bond length of 60 mm was selected for a Ø12 mm rebar. The non-bond section of the rebar was covered with an acrylic tube to prevent direct contact between the rebar and the concrete. The sketch of sample is illustrated in Table 8.

Referring to BS EN 14651 [266], a notched crack with the size of 5 mm x 25 mm (width x depth) was cut on the bottom side of the concrete beam (150 mm x 150 mm x 600 mm) to control the formation and propagation of cracks in region above the it. The test methods for theses samples will be detailed in the following sections.

Besides, considering the influence of high temperature curing on the drying shrinkage, where over-curing may lead to irreversible changes to the specimen microstructure (as described in Section 2.2.3.1), different oven curing durations were applied depending on the specimen sizes, as presented in Table 8. After oven curing, AAFS samples were stored under laboratory conditions, whereas OPC samples were kept in a water tank until the test date.

Table 8. Samples information including oven curing time, sketches, and selected mix proportions (as per Table 7)

Mix	Sample Type	Study	Oven curing hours
1-8	Concrete	Compressive strength	24
2-4, 8	Concrete	Split tensile strength	24
2-4, 6, 7	Concrete	Fracture properties	24
			
3	Reinforced Concrete	Bond properties	24
			
1-5, 8	Mortar	Flexural and compressive strength	24
1-5, 8	Reinforced Mortar	Electrochemical behaviour	16
			
3	Reinforced Mortar	Spatiotemporal evolution of corrosion	4
			

3.1.3 Exposure Environments

Following curing, the corrosion resistance evaluation was conducted through two distinct accelerated testing regimes:

1. Alternative wetting/drying (w/d) cyclic corrosion:
 - a. Applicable samples: electrochemical samples and X-CT samples.
 - b. Equipment: Environmental chamber (Figure 15)
 - c. Environment simulation: Marine exposure conditions
 - d. Cycle parameters:
 - i. 3 complete w/d cycles per 24-hour period,
 - ii. each cycle consisting of the following steps:
 1. 2 hours salt fog (3.5% sodium chloride) spray at 25 °C, 98% RH.
 2. 3.5 hours drying stage at 50 °C.
 3. 0.5 hours buffer stage to allow the chamber temperature to cool from 50 °C to 25 °C before the next cycle starts.
2. Impressed current accelerated corrosion:
 - a. Applicable samples: Pull-out test specimens.
 - b. Equipment: 30 V DC power supply (Figure 16)

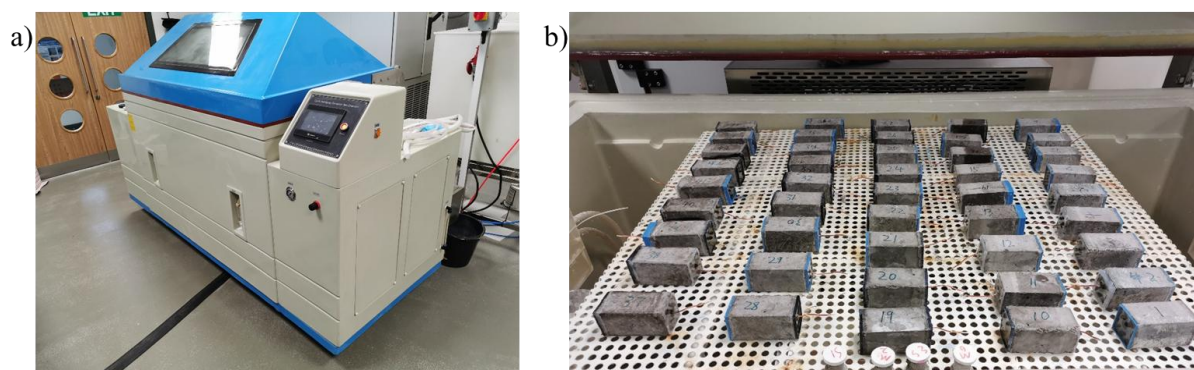


Figure 15. a) Corrosion environment chamber; b) the placement of electrochemical and X-CT samples in the corrosion environment chamber

The second method employed was the impressed current method, which allows faster corrosion of reinforced concrete compared to natural corrosion processes. This method was essential for studying the bond properties of reinforced AAFS concrete, as the large concrete cover thickness slows chloride penetration in w/d conditions. In this method, an external current density of $100 \mu\text{A}/\text{cm}^2$ was applied to the sample (steel rebar works as WE) using a 30 V DC power supply [267-269]. Under the influence of an external potential field, chloride ions migrate rapidly through the concrete via electric migration, significantly accelerating corrosion process compared to diffusion alone. The setup for impressed current method is shown in Figure 16. To ensure consistent corrosion current density across the whole samples, a joint electrical circuit was utilised, as illustrated in Figure 16 (b).

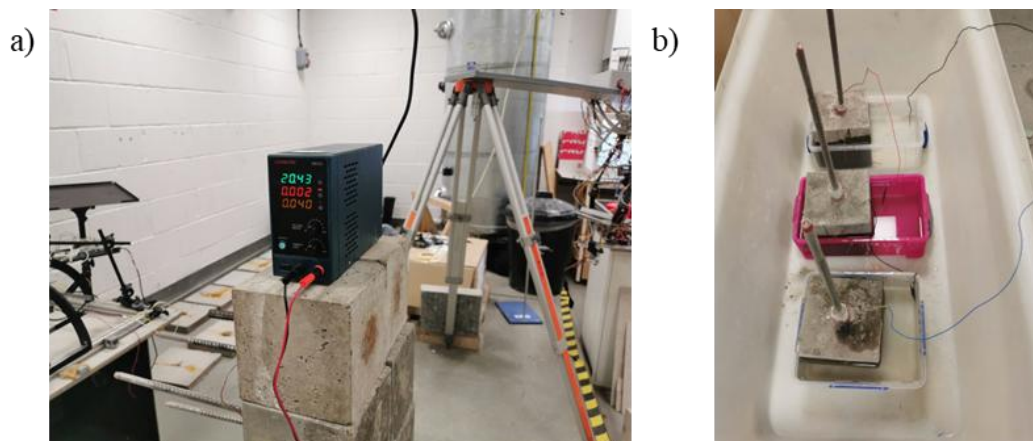


Figure 16. Setup for the impressed current method for pull-out test samples: (a) a 30 V power supply; (b) a joint electric circuit to ensure that the corrosion current density remains consistent for a group of three samples

3.2 Mechanical Test

3.2.1 Compressive Strength Test

For the compressive strength test of AAFS concrete, standard 100 mm cubes were used in accordance with BS EN 12390-1 [263]. Following BS EN 12390-3 [270], the loading rate was set to 0.6 MPa/s. The compressive strength of the AAFS concrete was calculated using the following equation:

$$f_c = \frac{F}{A_c} \quad \text{Eq. 9}$$

where f_c is the compressive strength, in MPa; F is the maximum load at failure, in N; A_c is the cross-section area of the specimen on which the compressive force acts, in mm².

Initially, compressive strength tests were conducted on AAFS-gravel concrete, in which gravel was used as the coarse aggregate. Four mix ratios (70SA–30FA, 50SA–50FA, 30SA–70FA, and OPC) were examined at 28 days of curing. The 100SA and 100FA groups were excluded due to the high shrinkage risk of the former and the low compressive strength of the latter. For each mix ratio, three cubes were prepared and tested at 28 days.

Subsequently, gravel was replaced with limestone as the coarse aggregate, and compressive strength was evaluated at two curing ages (14 and 28 days). Specimens of all mix ratios listed in Table 7 were prepared, with a total of six cubes cast for each mix ratio—three cubes were tested at each curing age. The average values at each curing age were calculated based on the results of three specimens.

This test was performed using a Controls 2000 kN compression frame, as shown in Figure 17, a machine designed for testing concrete and other construction materials under compressive loads. This machine is compatible with various test types, including compressive strength, flexural strength, and splitting tensile strength. Its adaptability makes it suitable for a wide range of experimental requirements.



Figure 17. Setup for compressive strength test of AAFS concrete cube

3.2.2 Tensile Splitting Strength Test

The tensile splitting strength test is a widely used method for determining the split tensile strength of concrete. This indirect test applies a compressive load to the specimens, as directly applying tensile loads to concrete is challenging due to equipment limitations. The test was conducted following the guidance of BS EN 12390-6 [271], using cylinder concrete specimens with the dimensions of Ø100 mm x 200 mm. The test setup, shown in Figure 18, utilised the same compression frame (Figure 17), equipped with a specialised accessory designed specifically for this purpose. After completing the test, the tensile splitting strength was calculated using the equation below:

$$f_{ct} = \frac{2 \cdot F}{\pi \cdot L \cdot d} \quad \text{Eq. 10}$$

where f_{ct} is the tensile splitting strength, in MPa; L is the length of the specimen, in mm; d is the diameter of the cylinder specimen, in mm.

In this test, only AAFS-gravel concrete cylinders were tested, using the same mix ratios as those adopted in the compressive strength tests for AAFS-gravel concrete. The average tensile splitting strength at 28 days was calculated. AAFS-limestone samples were not tested due to

material limitations, as there was insufficient material available to cast additional specimens at that time.



Figure 18. Setup for tensile splitting strength test of AAFS concrete cylinder

3.2.3 Three-Point Bending Test for Mortar Samples

In accordance with BS EN 196-1 [264], both flexural strength (three-point bending test) and compressive strength of mortar can be measured using the same mortar prism (40 mm x 40 mm x 160 mm). During testing, the mortar prism is first subjected to the flexural strength test, which causes it to break into two halves, each approximately 80 mm in length. The compressive strength test is then conducted on these two halves using a specific loading cell, with a 40 mm x 40 mm cross-section for both top and bottom platens. The loading rates were set to 50 N/s for the three-point bending test and 2400 N/s for the compressive strength test. The flexural strength and compressive strength of the mortar samples were calculated by using following equations:

$$R_f = \frac{1.5 \cdot F_f \cdot l}{b^3} \quad \text{Eq. 11}$$

$$R_c = \frac{F_c}{1600} \quad \text{Eq. 12}$$

where R_f is the flexural strength, in MPa; b is the side length of the square section of the prism, in mm; F_f is the load applied to the middle of the prism at failure, in N; l is the distance between

the support, in mm; R_c is the compressive strength, in MPa; F_c is the maximum load at failure, in N.

In this test, the 350 kN frame from Controls was used for the flexural strength test due to its higher sensitivity to loading force, ensuring accurate data recording. In contrast, the 2000 kN frame, while suitable for compressive strength tests that require the application of large loads, lacks the sensitivity of the 350 kN frame and may not accurately record data for the three-point bending test. The setup for these two tests, including the specific accessories used, is presented in Figure 19.

In this test, AAFS mortars with mix ratios corresponding to Groups 1–5 and 8, as listed in Table 7, were prepared. A total of six samples were cast for each mix ratio—three samples were tested at 14 days and the other three at 28 days.

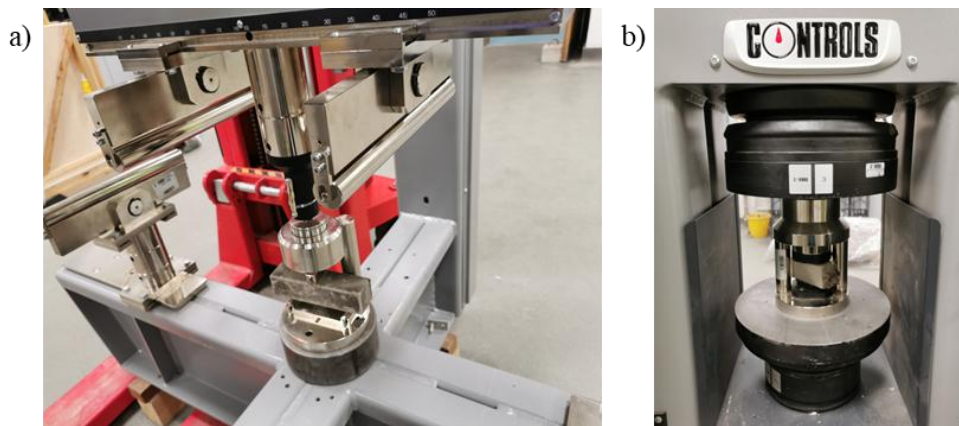


Figure 19. Setup for three-point bending test for AAFS mortar: a) The flexural strength test; b) The compressive strength test for the halves of the mortar prism

3.2.4 Three-Point Bending Test for Notched AAFS Concrete Beams

Fracture properties are equally as important as mechanical strength in ensuring the safe application of AAFS concrete structures in real-world conditions, as discussed in Section 2.2.2.

To evaluate the fracture properties of AAFS concrete, a three-point bending test was performed on notched beams. In accordance with BS EN 14651 [266], beams with dimensions of 150 mm x 150 mm x 600 mm were used, featuring a pre-cut notch (5 mm x 25 mm, width x depth) on the bottom side of beam. A clip gauge was installed at the notched crack, while two 10 mm

linear variable differential transducers (LVDTs) were positioned on both sides of the beam, as illustrated in Figure 20. The testing machine utilised a Controls' 350 kN frame, as depicted in Figure 20 (b). The clip gauge was employed to control the crack mouth opening displacement (CMOD) rate at 0.05 mm/min. Simultaneously, the LVDTs measured the mid-span deflection of the beam. To improve measurement accuracy and account for potential deviations when using a single LVDT, the average of deflection from the two LVDTs was calculated.



Figure 20. The experimental setup for the three-point bending test of notched beam: (a) the installation of knife edge (b) Setup of clip gauge (c) Setup of LVDTs

To gain a clear understanding of the fracture properties of AAFS concrete, various mix ratios were utilised, as illustrated in Table 8. After completing the tests, the Load-CMOD and Load-Deflection graphs were plotted using the recorded data. The fracture energy (G_F , J/m²) was calculated following the RILEM guidelines [272], as expressed in Eq. 13:

$$G_F = \frac{W_0 + mg\delta_0}{A_{lig}} \quad \text{Eq. 13}$$

where W_0 is the area under the Load-Deflection curve, in J; m is the mass of the beam between two supports, in kg; g is the gravity acceleration (9.81 m/s²); δ_0 is the deflection at the final failure position of the beam, in m; A_{lig} is the area of the ligament, in m².

The fracture toughness K_{IC} was calculated using Eq. 14, based on the method described by Peterson and research [273] and Nath and Sarker [116]:

$$K_{IC} = \frac{3P_{max}l}{2bd^2} \sqrt{a_0} (1.93 - 3.07A + 14.53A^2 - 25.11A^3 + 25.8A^4) \quad \text{Eq. 14}$$

where P_{max} is the maximum load of recorded data, in kN; l is the span of beam, in mm; b and d are the width and depth of beam, in mm; a_0 is the notched crack depth and $A = a_0/d$.

For the mortar test, mix ratio Groups 1-5 and 8, as listed in Table 7, were prepared. A total of six samples were cast for each mix ratio and divided into two groups, with three samples tested at 14 days and the remaining three at 28 days.

3.2.5 Pull-Out Test

Understanding the bond performance between reinforcement and concrete is essential for ensuring the quality and durability of reinforced concrete structures. The bond strength significantly influences the serviceability [274] and shear resistance [275] of such structures. However, reinforcement corrosion can deteriorate this bond by accumulating corrosion products, ultimately reducing the service life of reinforced concrete structures.

The pull-out test can be divided into two stages based on the load-slip curve: the pre-peak stage and the post-peak stage. The pre-peak stage represents the slip behaviour of the rebar prior to reaching the peak load, while the post-peak stage describes the slip behaviour of the rebar under the residual bond strength after bond failure. Two testing methods were employed: the load control method and the displacement control method. The load control method was used to investigate the relationship between the peak bond strength and reinforcement slip during the pre-peak stage, while the displacement control method examined the relationship between residual bond strength and rebar slip in the post-peak stage.

For the load control method, a loading rate of 72 N/s was calculated based on the diameter of the rebar, following the RC6 guideline from RILEM Technique Recommendations [265]. The

test setup is illustrated in Figure 21 (a). This test was performed using an Instron 8802 universal test machine (UTM) with a load capacity of 250 kN. A steel cage was constructed to constrain the reinforced AAFS concrete, securely fastened to the bottom holder with screws and bolts. A strain gauge was attached to the rebar to monitor strain variations during the test. For the displacement control method, a tensile test frame from Controls was utilised, as shown in Figure 21 (b). A loading rate of 1 mm/min was applied, and a 50 mm gauge LVDT was used to measure the reinforcement slip. Both tests were conducted until the complete bond failure occurred. After the test, bond strength was calculated using the following formula:

$$\tau = \frac{P}{\pi \cdot d \cdot l} \quad \text{Eq. 15}$$

where τ is the bond strength, in MPa; P is the maximum load from pull-out test, in N; d is the diameter of the reinforce bar, in mm; l is the bonded length of the steel bar, in mm.

For this test, only the mix ratios corresponding to Groups 3 and 8, as listed in Table 7, were prepared, a total of 18 samples, which were divided into six groups. Initially, only the AAFS-gravel concrete specimens were tested. However, due to the absence of clear post-peak region caused by splitting failure at the peak load, the coarse aggregate was replaced with limestone. In addition, OPC specimens were also prepared for comparison. As the primary focus of this test is the bond performance of reinforced AAFS concrete under corrosions. 21 AAFS-limestone samples (divided into four groups) and 12 OPC samples (divided into four groups) were prepared. All samples were cured for 28 days before testing.

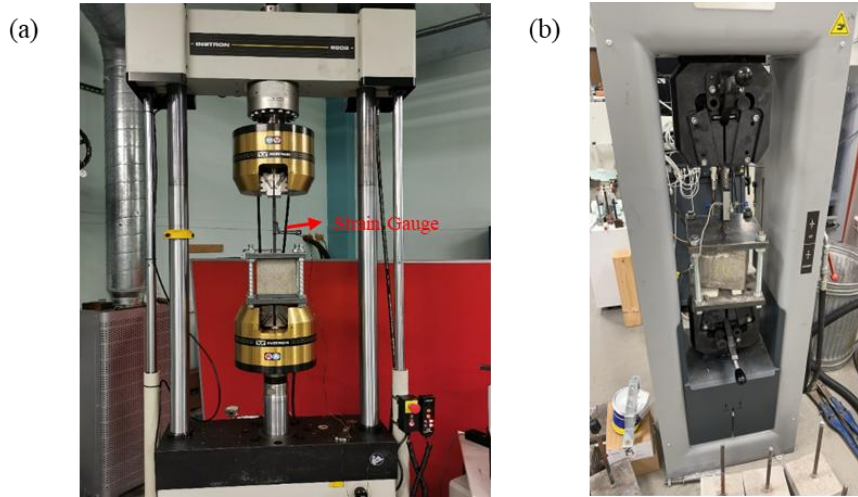


Figure 21. Setup for the reinforced AAC pull-out test: (a) Load control method; (b) Displacement control method

3.3 Electrochemistry Measurements

As described in Section 2.4, OCP and LPR are the most commonly used electrochemical techniques for non-destructive monitoring of the corrosion state of embedded reinforcement in concrete structures. To perform these electrochemical measurements, a potentiostat (Gamry Interface 1010B) with a three-electrode system was utilised, as shown in Figure 22. The electrochemical sample was partially immersed in the 3.5% saltwater solution to minimise the effects of concentration polarisation [111]. Concentration polarisation occurs when ions accumulate near the electrode during an electrochemical reaction, causing a concentration gradient. By limiting the immersion, it was possible to reduce the stagnant layer thickness near the electrode and enhance natural convection, thereby decreasing ion build-up and maintaining a more uniform ion distribution. Additionally, the use of a 3.5% saltwater solution aimed to enhance the conductivity of the sample throughout the circuit.

In this setup, the rebar connected to the copper wire served as the working electrode (WE), while a titanium mesh functioned as the counter electrode (CE), completing an electrical circuit between the WE and CE. A saturated calomel electrode (SCE), combined with a Luggin capillary, was used as the reference electrode (RE). The RE is inherently stable and does not participate in the redox reactions of iron corrosion. Instead, it provides a consistent potential,

which the potentiostat uses as a reference to monitor and record the potential changes in the WE. During OCP measurements, it is assumed that no electric current flows between the WE and RE, ensured by the high impedance resistance incorporated into the potentiostat between these two electrodes.

The Luggin capillary was employed to mitigate the impact of ohmic drop (IR-drop) [276]. It consists of a glass tube with a body section and a gradually narrowing tube ending in a capillary tip. Agar gel, acted as a salt bridge, fills the Luggin capillary, with the RE inserted into the agar gel within the body section, as illustrated in Figure 22. The capillary tip is positioned close to the specimen surface to enhance measurement accuracy by minimising the path length for ionic current, therefore, reducing ohmic resistance in the system. For reinforced AAFS mortar, resistance changes occur due to ion transport between the mortar matrix and the electrolyte. Positioning the Luggin capillary tip near the sample surface ensures that the influence of resistance changes due to phase transitions is negligible. However, the tip must not be placed too close to the sample surface, as this may cause “shielding”, where the Luggin capillary interferes with electrolyte flow, electric field distribution, or ion diffusion near the WE. To avoid this, the distance between the sample surface and the Luggin capillary tip should be at least twice the outer diameter of the capillary tip [276].

While Luggin capillary mitigates the influence of IR-drop, it cannot fully eliminate it. Therefore, the IR-drop was measured using the potentiostat’s built-in function, and 80% of the measured IR drop was compensated within the system. This level of compensation was selected to avoid overcompensation, which could potentially cause oscillations in the measured data [27,277].

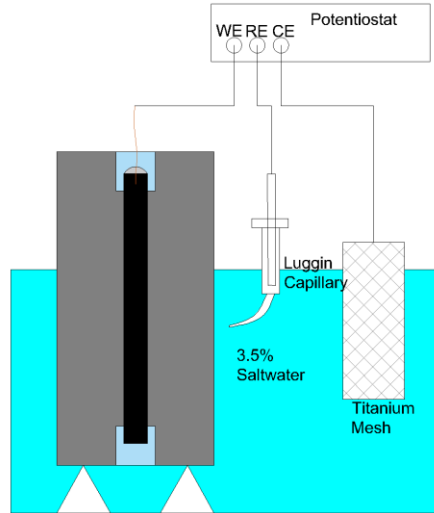


Figure 22. Setup for the three-electrode system

For these measurements, a total of 9 samples corresponding to Groups 1-5 and 8 were prepared. During the accelerated corrosion period, as stated in Section 3.1.3, OCP and LPR measurements were conducted daily to monitor the corrosion condition of the electrochemical samples in the environmental chamber. The OCP was measured first, with readings recorded once the value stabilised to fluctuations of less than 1 mV/min. This was performed after the samples were partially immersed in the electrolyte, allowing the internal condition of the sample to stabilise. Following the OCP measurement, the LPR measurement was conducted. A small polarised potential range (± 10 mV) was applied to the WE, with the potential scanned from negative to positive at a scan rate of 0.167 mV/s [111,204]. After the measurement, the R_p for each sample was calculated using Eq. 7. The evolution of E_{corr} and R_p over time was then plotted for analysis.

For the Tafel extrapolation method, as stated in Section 2.4.2, a large polarised potential range (± 200 mV) was applied to the steel rebar, using the same scan rate and direction as in the LPR measurement. Since this technique is considered destructive and may cause irreversible changes to the surface properties of the rebar [27], it can affect the measurement accuracy by reducing the E_{corr} . Therefore, Tafel extrapolation method was performed only twice: once

before the accelerated corrosion process began and once when the corrosion initiation was detected. After the measurement, the anode and cathode Tafel slopes, β_a and β_c , were determined from the potential-logarithmic plot of the anodic and cathodic regions. Subsequently, the Tafel constant B value for each sample was calculated using Eq. 8.

3.4 Interface Characterisation at the SMI

3.4.1 Free and Bound Chloride Content at the SMI

The chloride threshold (C_{crit}), as stated in Section 2.3.3.3, refers to the critical chloride concentration at which the accumulation of Cl^- on the reinforcement leads to the breakdown of the passive film [14,15]. Understanding C_{crit} is crucial for assessing the durability and service life of reinforced concrete structures. After corrosion initiation was detected in the electrochemical samples, a portion of the corroded samples was split to enable visual inspection of the corrosion. The mortar matrix surrounding the embedded rebar was carefully extracted from the areas where corrosion was observed. The extracted binder matrix was then analysed to determine the water-soluble chloride (free chloride) and acid-soluble chloride (bound chloride) contents in the reinforced AAFS mortars. Since copper was inserted into the rebar, there was a potential risk of galvanic corrosion due to the differing electrochemical potentials of the two metals, even though the rebar was coated with epoxy resin. To ensure accurate results, any sample showing corrosion at the epoxy resin-sealed zone was excluded from the analysis.

The Ion Chromatography Professional (ICP) 850 was employed for this analysis, as shown in Figure 23. This instrument is designed for precise and efficient analysis of anions and cations and was chosen to address the interference caused by the presence of sulphides in the SA, which can compromise the accuracy of traditional titration methods. In the traditional titration method, a silver nitrate solution is used to titrate Cl^- from the treated sample solution, forming a precipitate of $AgCl$, as described in Eq. 18. However, dissolved sulphide ions (S^{2-}) are strong reducing agents that can react with the silver ions (Ag^+), forming a secondary precipitate of

Ag₂S. This additional reaction increases the consumption of silver nitrate solution, potentially leading to an overestimation of the actual free chloride content.



Figure 23. Ion Chromatography Professional (ICP) 850

The test samples were prepared in accordance with guidelines from ASTM C1218 [278] and ASTM C1152 [279], which provide detailed procedures for measuring the free and bound chloride content in mortar and concrete using the titration method. The adapted procedure, modified for analysis with the ICP 850, is as follows:

1. Powdered Sample Preparation:

- a. Grinding and Sieving: The mortar matrix extracted from the corrosion area was ground into a fine powder and passed through an 850 μm sieve. This step ensured uniform particle size, enhancing the dissolution of chloride ions during the next step.
- b. Mixing with deionised water: The sieved powder was mixed with the deionised water at a mass ratio of 1:8 (powder:water). Deionised water was used to eliminate interference from external ions present in tap water, ensuring accurate chloride ion measurement.

2. Free chloride ions extraction:

- a. Hot water treatment: The mixture of powdered samples and deionised water was subjected a 15-minute hot water treatment at 60 °C. This step promoted the release of free chloride ions from the solid matrix into the deionised water.
- b. Shaking: The mixture was then subjected to 6 hours of continuous shaking using a mechanical shaker, as shown in Figure 24 (a). This step accelerated the release of physically bound chloride ions, enhancing the extraction efficiency.

3. Filtration and dilution for free chloride content measurement

- a. Centrifugation: After shaking, the suspension was centrifuged at 10,000 r/min to separate the liquid and solid phases, as shown in Figure 24 (b) and (c).
- b. Filtration: The supernatant was filtered using a syringe fitted with a 0.45 µm pore-size membrane filter to remove fine particles invisible to the naked eye.
- c. Dilution: The filtered solution was diluted to 100 times its original concentration to ensure compatibility with the detection limits of the ICP 850. The diluted samples were then analysed using the ICP 850 (Figure 23).

4. Bound Chloride content measurement:

- a. Oven drying: To measure bound chlorides ions, the residual solids from Step 3 were oven-dried to remove moisture. The dried solid was then powdered to loosen it, as it had become compressed during the centrifugation process.
- b. Acid treatment: The powdered solid was treated with 1:1 nitric acid, following the procedure outlined in ASTM C1152 [279]. This treatment dissolved the chemically bound chlorides into the solution by breaking down the solid's microstructure.
- c. Centrifugation and filtration: This step followed the same procedure as described in Step 3.

- d. Dilution: The filtered solution was diluted to 10 times its original concentration, as previous trial tests showed relatively lower concentration of bound chlorides.

After that, the diluted samples were analysed using ICP 850 (Figure 23).

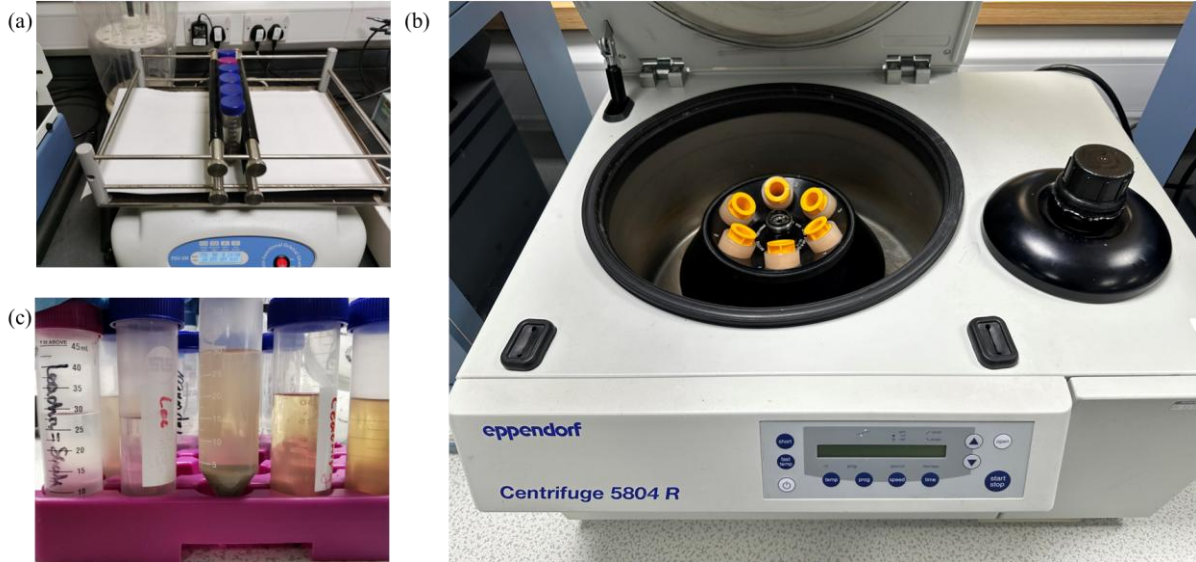


Figure 24. Experimental setup for chloride content analysis (a) shaking process (b) centrifuge (c) separation of liquid and solid phases after centrifugation

3.4.2 SEM-EDS Sample Preparation and Analysis at SMI

SEM-EDS analysis is a powerful technique for investigating the morphological and topographic characteristics of a material's microstructure. It provides detailed examination of surface features and element distribution map, which is important for understanding the corrosion process, as introduced in Section 2.5.2. To characterise corrosion in reinforced AAFS mortars, particularly at the SMI region, samples were prepared from five basic groups of electrochemical samples (as illustrated in Table 8) after corrosion initiation was detected. One slice containing the corrosion zone was extracted for analysis. The preparation procedure, including slicing, oven drying, epoxy resin coating, surface grinding and polishing, is outlined below:

1. Slicing:

Electrochemical samples were sliced into 5 mm sections using the ATM Brilliant 220 precision cutter, as shown in Figure 25 (a). The cutting process was performed sequentially on the same

sample. After the first cut, the diamond cutting disc was precisely moved 5 mm to prepare for the next cut, ensuring consistent section thickness across all slices. To minimise damage to the cross-sectional interface during the cutting [280], a rotation speed of 1000 rpm and a feed rate of 0.03 mm/s were selected.

2. Ethanol treatment and drying:

After the cutting, the sliced samples were immersed in ethanol to remove water absorbed during the cutting process, as water cooling was employed with the diamond cutting disc. This step was necessary to prevent further corrosion damage during batch-processing and before oven drying. Following ethanol immersion, the samples were oven dried for at least 24 h to ensure complete drying for epoxy resin coating. Insufficient drying could leave moisture in the sample, hindering epoxy resin penetration, leading to incomplete coverage or the formation on the sample surface, which would affect the subsequent SEM-EDS analysis.

3. Epoxy resin coating and vacuum degassing:

After drying, the samples were transferred into silicon moulds and filled with epoxy resin. The samples and moulds were then placed in a vacuum chamber for vacuum degassing, as shown in Figure 25 (b). This step aimed to fully infiltrate the pores with liquid epoxy resin and remove air bubbles from the microstructure. The degassing process was repeated several times until no bubbles were observed. After degassing, the samples and moulds were set aside until the epoxy resin to fully hardened.

4. Surface grinding and polishing:

After the epoxy resin had fully hardened, surface grinding and polishing were conducted. Surface grinding removed the excess epoxy resin coating, which could interfere with SEM-EDS measurements, particularly in EDS analysis. Residual epoxy resin on the sample surface can weaken the energy source signal and introduce unexpected elements, compromising the

accurate element detection. Grinding was carried out progressively using grinding paper with the grit sizes of 60, 120, 240, 600, and 800 mesh. After grinding, polishing was performed using polishing paper with mesh sizes of 1200, 2000, 4000, 6000, and 10000, to achieve a smooth and even surface. Finally, the polished samples were gold-coated to enhance conductivity during SEM-EDS measurements.

The Axia ChemiSEM was employed for SEM-EDS analysis at the SMI. The operation interface, sample setup, and live images are shown in Figure 26. The dual SE and BSE modes facilitate the analysis process by eliminating the need to switch between imaging modes or machines. Furthermore, the Axia ChemiSEM can simultaneously process SEM and EDS signals, providing detailed morphological information alongside elemental mapping within the measured zone. For the SEM-EDS measurements, an acceleration voltage of 20 kV and a spot size of 4.0 nm were used to ensure high-resolution observation of the interface properties.

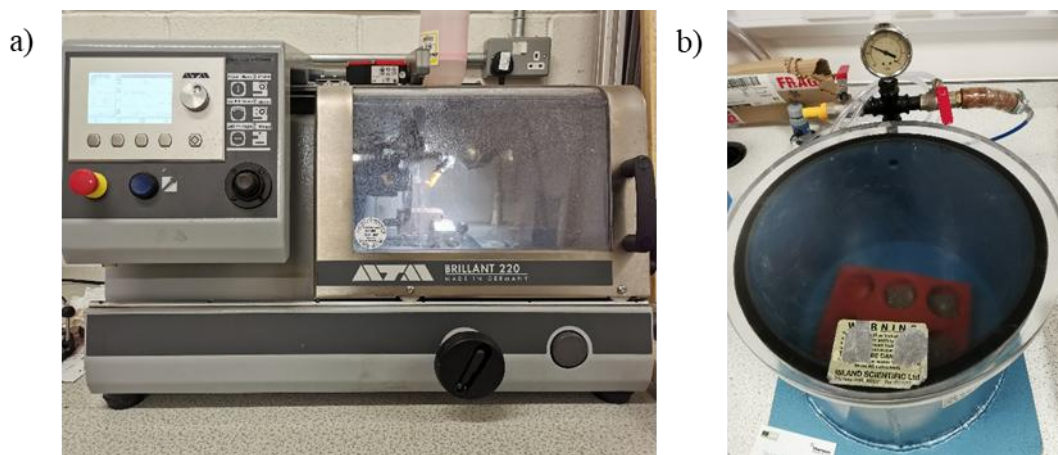


Figure 25. (a) The ATM Brilliant 220 precision cutter; (b) using vacuum chamber to eliminate the air bubbles from samples pore structure

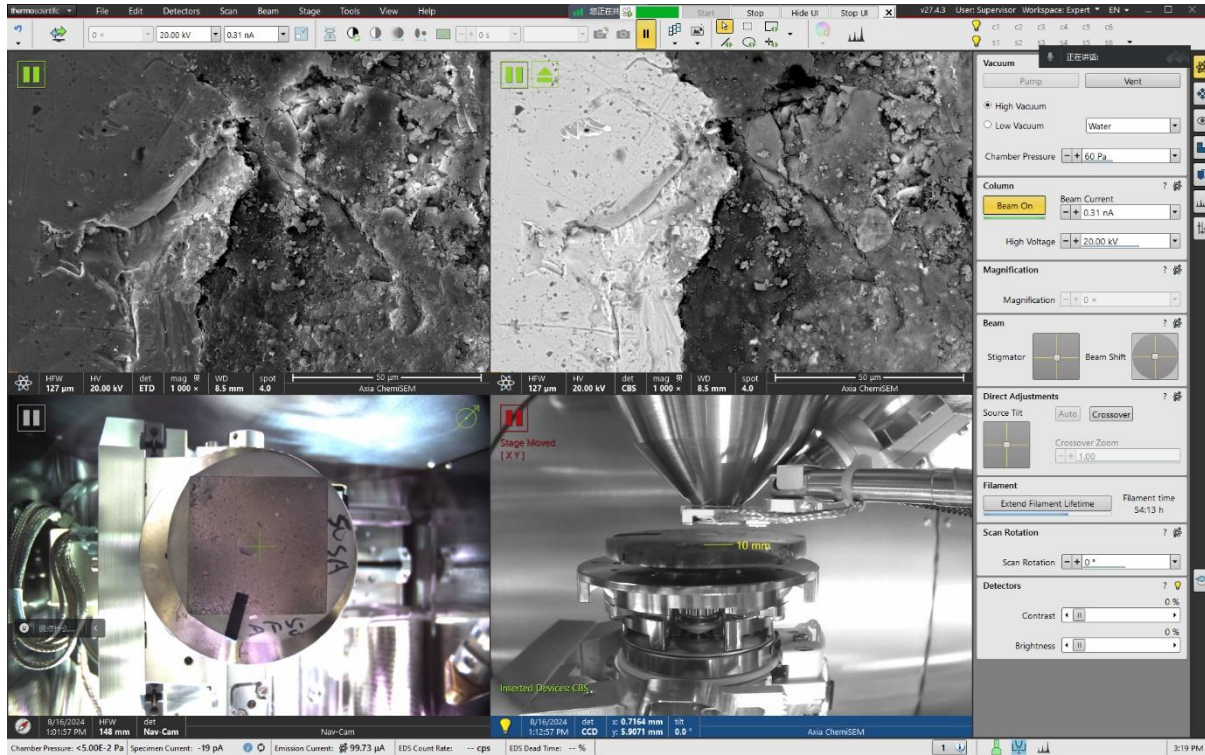


Figure 26. Sample setup in the Axia ChemiSEM for SEM-EDS measurement (the bottom left and right); with synchronized graphical view for SE mode (top-left) and BSE mode (top-right)

3.4.3 X-CT analysis

3.4.3.1 Introduction

As introduced in Section 0, X-CT analysis is a valuable tool for non-destructive evaluation of the internal structure of reinforced concrete, as well as for exploring the spatial distribution and temporal evolution of corrosion rust. In this research, X-CT analysis was employed to investigate the spatiotemporal evolution at SMI in 50SA-50FA AAFS mortar. One sample was prepared for each steel bar position—centre and side.

For this measurement, the “NiKon XT H 320” machine, equipped with a 225 kV X-ray source, was used for X-ray and CT inspection, as shown in Figure 27. The sample was securely taped onto the scanning plate within the scanning cabinet to prevent small vibrations that could compromise data quality. Beam hardening, an artifact caused by X-ray passing through dense materials such as steel, was mitigated by applying a 0.25 mm copper filter. The scanning

parameters were set to 3141 projections (angular step 0.1146°), 150 kV, 77 μA , and 1 s exposure, as chosen from Xi and Yang [235].

The X-CT specimens were initially scanned in their passive condition, non-corrosion condition, which works as the control group. After scanning, the raw X-CT data was reconstructed into visible 3D images using the machine's built-in algorithm. Image processing and analysis were then performed using the software Avizo. In the following, the standard applications used in the image processing and analysing, all of which are built-in function of in Avizo, will be introduced.

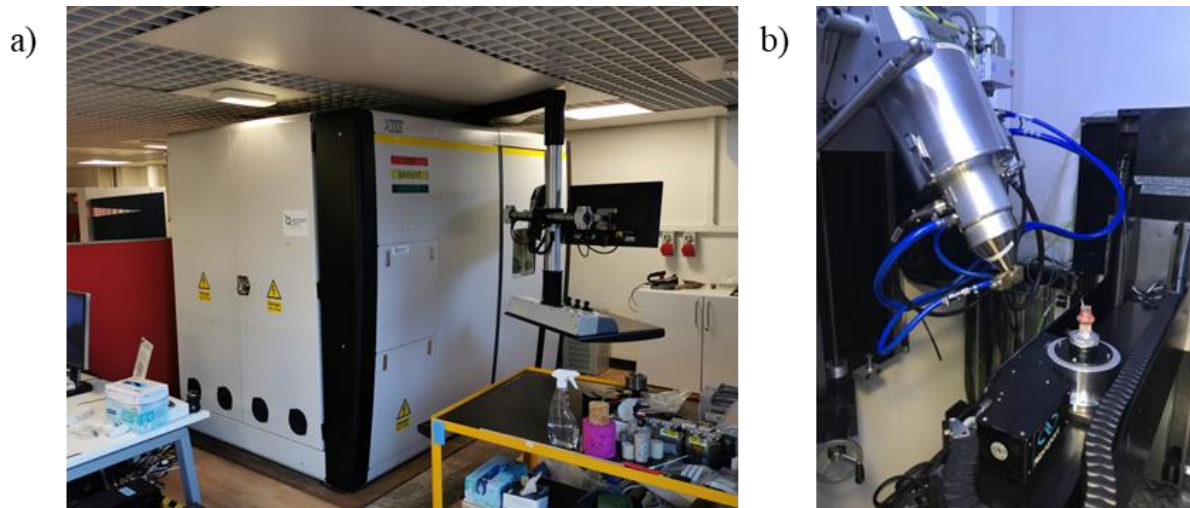


Figure 27. a) NiKon XT H 320 for X-ray and CT inspection; b) test sample setup

3.4.3.2 Pre-Processing

Figure 28 (a) shows the reconstructed 3D structure of the specimen along the x-z axis in its passive condition. The image reveals that the specimen is inclined slightly, and the presence of ring artifacts on both top and bottom sides. The inclination results from a slight tilt of the sample during scanning, which becomes magnified in the reconstruction. The artifacts are attributed to beam hardening effects inherent to the X-CT machine.

To align the sample parallel to the z-axis and eliminate the artifacts, two applications were utilised: image registration and the crop editor. Image registration was used to geometrically

transform and align the specimen correctly along the spatial orientation. The crop editor removed the volume containing ring artifacts by cropping the affected regions from both the top and bottom of the image, as these zones contained unreliable data [235]. Figure 28 (b) displays the corrected 3D structures after applying these adjustments.

In the following, advanced processing was performed on the reconfigured 3D images to enhance the features of each material phases. Two primary tools were utilised for this purpose: the imaging filter and volume edit. The imaging filter incorporates multiple smoothing algorithms, such as Gaussian filter, which reduces noise while preserving edges and fine details, hence, enhancing overall image quality. The volume edit tool was employed for interactive editing and manipulation of volumetric datasets within the 3D image structure. This function allows customisation of threshold values and border positions to refine the dataset. It is important to note that volume editing must be completed prior to phase segmentation. An example of this process is shown in Figure 29, illustrating the effect of the volume edit tool on pore segmentation. The left image shows segmentation results without volume editing, where noise (irrelevant information) is visible outside the sample body, leading to inaccuracies. After volume editing (right image), the threshold border is redefined, and noise outside the sample body is successfully removed, improving image quality.

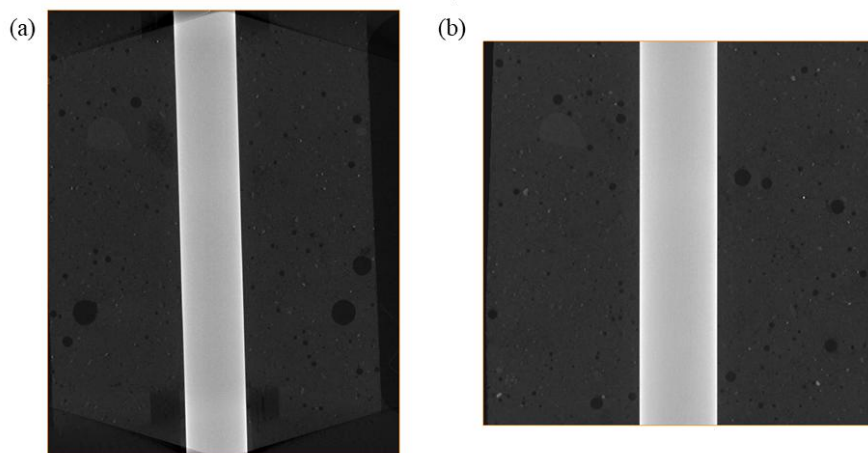


Figure 28. Reconstructed 3D structure from the initial scanning at x-z axis view, (a) non geometrically processed image, (b) image after correction

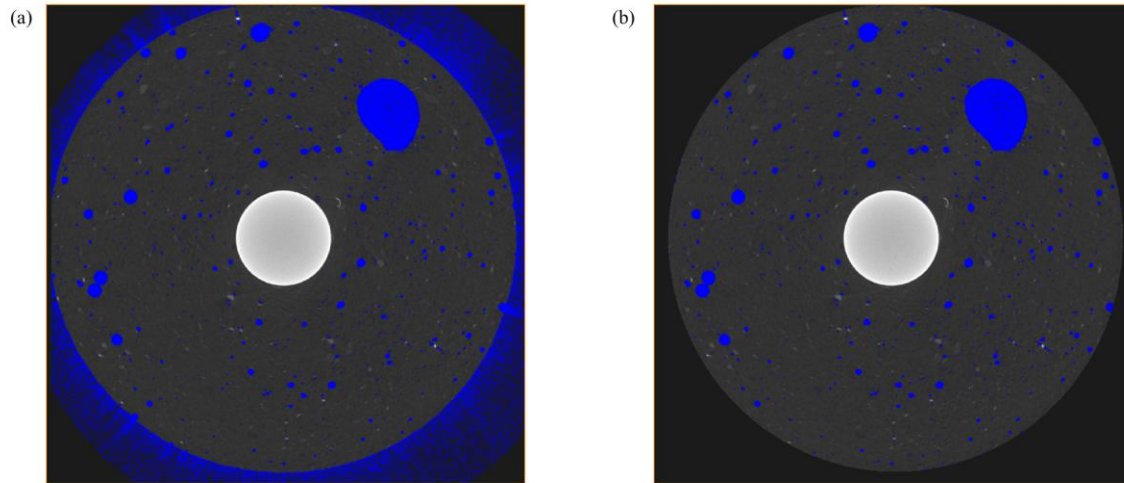


Figure 29. Volume edit treatment on images (a) before treatment (b) after treatment

3.4.3.3 Material Phases Segmentation

The segmentation of material phases, including pores, cracks, steel bar, and corrosion rust, was performed using the thresholding method. This method distinguishes material phases based on their grey values, which correspond to variations in the material density. Figure 30 shows a plot of the grey values along a probing line passing through the mortar matrix, corrosion rusts, steel bar, cracks, and pores. Using these thresholds, the segmentation of these phases was successfully extracted. However, it should be noted that this method provides a rough determination, and the density in certain zones may be underestimated due to the high density of the steel bar. Consequently, a manual review was employed in at suspicious points to ensure accuracy.

After the initial segmentation of each material phase, advanced processing was performed on the segmented dataset using 3D morphological analysis and label analysis. These methods extract material phases information, such as geometry and shape. Using the analysis filter function, the segmented image data was further refined to ensures the accuracy of the results.

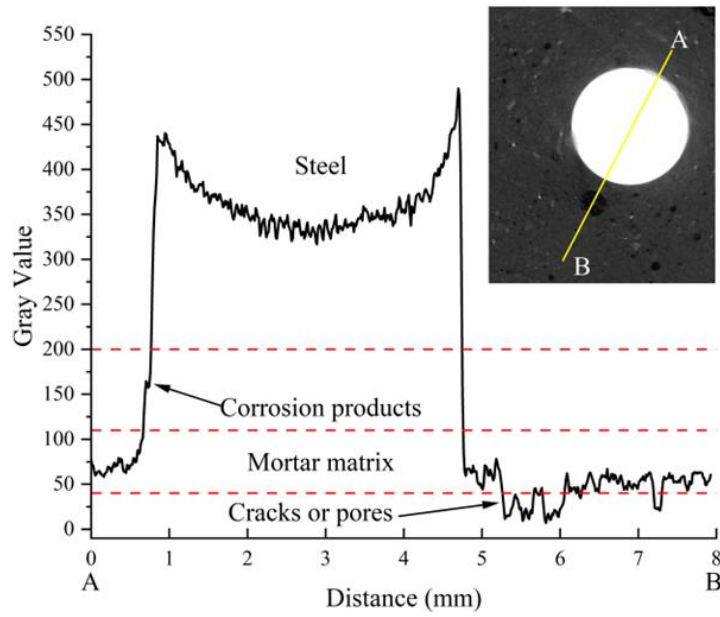


Figure 30. Phase identification in X-CT image through using grey values

3.4.3.4 Data processing

To analysis the spatiotemporal corrosion evolution of the embedded steel bar and corrosion rusts, their segmented phases (3D images) under different corrosion conditions were sliced along the longitudinal direction of the sample to obtain individual images. An example of corrosion rust and corroded steel bar from slice 369, taken from the sample with middle-positioned steel bar, is shown in Figure 31.

These sliced images were first converted into 8-bit format, with grey values ranging from 0 to 255. This conversion facilitated the identification of corrosion rust and corroded steel within the image, which are represented by distinct grey tones. Additionally, the 8-bit format reduced the file sizes, improving the processing efficiency.

Python was used to perform batch processing of the sliced images. The processing progress included the following:

1. Shape identification: The shape and position of the corrosion rust and the steel bar were identified first in each image.

2. Centre determination and establish coordinate axes: The centre of the identified shape was determined and marked with a red dot. Then, the x-y axes were established at this point.
3. Border scanning: The right side of the x-axes work as the starting point, and the border of the shape was scanned at intervals of 1° , capturing pixel data along the perimeter. After that, the pixel data were converted to the thickness measurements (in mm) for further analysis.

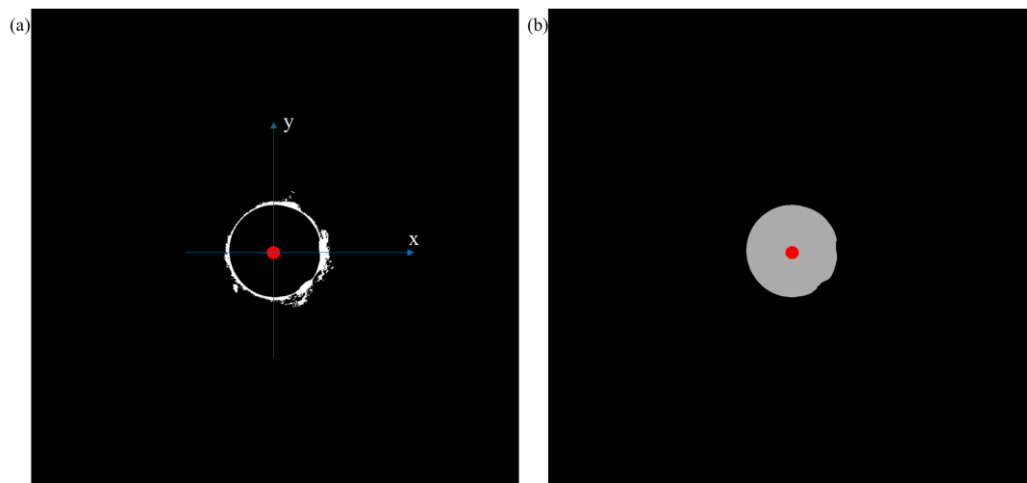


Figure 31. Processing on (a) corrosion rusts and (b) corroded steel

3.5 Numerical simulations

The numerical simulations of chloride ingress-induced corrosion in reinforced AAFS mortar were conducted based on X-CT measurement results. In this research, 2D models were employed to simulate the corrosion process for the two samples configurations. The simulation was performed using COMOSOL Multiphysics, a software capable of coupling multiple physics interfaces to simulate complex process and providing visualisation tool to track the changes over time.

3.5.1 Geometric Configuration

The geometric configuration for these 2D models is presented in Figure 32. The geometric parameters are consistent with the real X-CT samples, as described in Section 3.1.2. The

distribution of pores was extracted from the segmented pore phase obtained from X-CT measurement data using AVIZO software, as discussed in previous sections. In the simulation, these pores are considered to buffer chloride diffusion process because they are isolated.

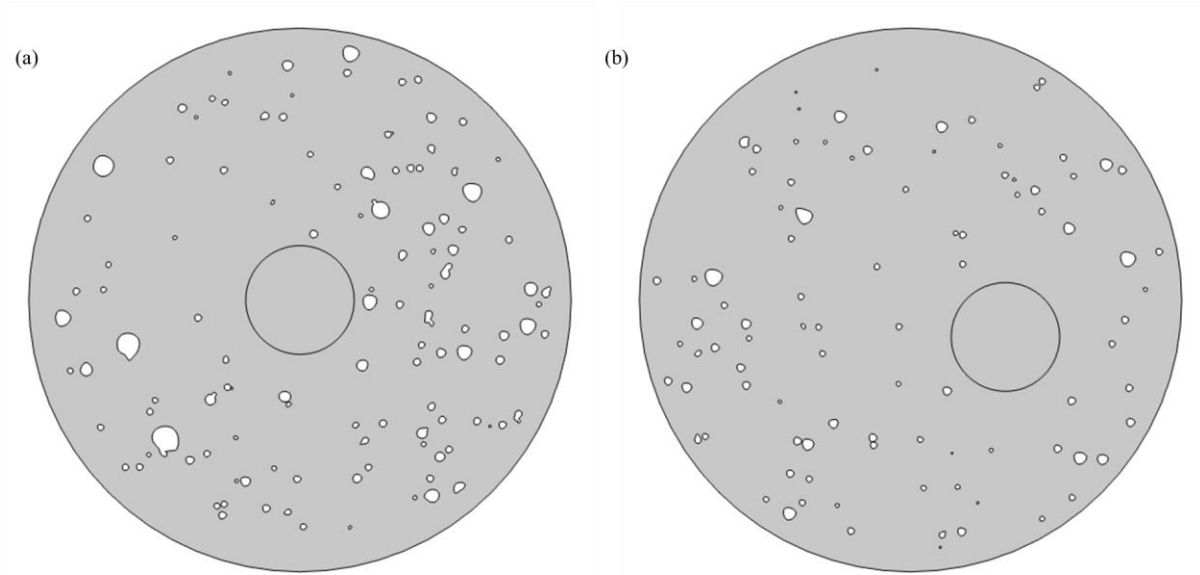


Figure 32. Geometric configuration for middle positioned steel bar and side positioned bar

3.5.2 Chloride Diffusion and Oxygen Transport in Mortar

As mentioned in Section 2.3.1, the presence of chloride ions on the reinforcement surface can cause pitting corrosion by locally breaking down the passive film, hence, exposing the underlying steel to corrosive environments. Therefore, it is assumed that the concentration of chloride ions governs the depassivation process of the passive film formed on the steel bar.

The transport of ions in the electrolyte occurs through three mechanisms: diffusion, electric migrate, and convection [194]. However, due to the complex microstructure of the AAFS mortar, only the diffusion process of chloride transport is considered in this simulation. This process is described by Fick's second law:

$$\frac{\partial C_{cl}}{\partial t} = \nabla \cdot (D_{cl} \nabla C_{cl}) \quad \text{Eq. 18}$$

where C_{cl} is defined as the chloride ions concentration in mortar, in mol/m³. D_{cl} is the chloride diffusion coefficient in mortar, in m²/s. t is the diffusion time, in s. $\nabla = (\frac{\partial}{\partial x}, \frac{\partial}{\partial y})$ for 2D, nabla, the mathematics operator that is used for the gradient calculations.

Under realistic conditions, the X-CT samples are subjected to the w/d cyclic corrosion in an environmental chamber. Although the chamber is saturated with salt fog during the wetting cycle, the actual amount chloride adsorbed on the sample surface is limited. In this simulation, a surface chloride concentration (C_{cl}^s) of 1.38 wt.% of mortar is used to represent the adsorbed chloride on the sample surface, as selected from previous studies [281,282].

Furthermore, the critical chloride threshold (C_{cl}^{crit}), which marks the transition of steel reinforcement from a passive to an active state, is determined based on ICP analysis, as shown in Table 17. A mean value of 0.36 wt.% is adopted for the 50SA-50FA mortar in this simulation.

Although chloride diffusion may continue during transition from the wetting to the drying stage, this effect is considered negligible due to the small sample size and a bit longer drying duration at high temperatures. Therefore, it is assumed that no chloride diffusion occurs during the drying stage. Therefore, in the simulation, chloride diffusion is assumed to occur only during the wetting phase.

According to Babae and Castel [172], the chloride diffusion coefficient in 50SA-50FA mortar ranges from 3×10^{-12} m²/s to 10.4×10^{-12} m²/s. Hence, the average value of 6.7×10^{-12} m²/s is selected as D_{cl} .

Oxygen transport in mortar can also be described by Fick's second law:

$$\frac{\partial C_{O_2}}{\partial t} = \nabla \cdot (D_{O_2} \nabla C_{O_2}) \quad \text{Eq. 19}$$

where C_{O_2} is defined as the oxygen concentration in mortar, in mol/m³. D_{O_2} is the diffusion coefficient of oxygen in mortar, in m²/s.

In the natural environment, the oxygen constitutes 21% of the total air, resulting in the oxygen concentration ($C_{O_2}^{air}$) of 9.68 mol/m³. Since steel corrosion requires both water and oxygen, gaseous oxygen in the mortar must first dissolve into the pore solution. According to Henry's law [234,283], the concentration of dissolved oxygen at the mortar surface is $C_{O_2}^s = 0.267 \text{ mol/m}^3$, attributed to the presence of adsorbed salt solution on the sample surface. During the drying stage, oxygen can still diffuse into the mortar at a faster rate than in saturated samples and redissolves into the pore solution during the wetting stage [284,285]. Therefore, it is assumed that the oxygen continuously diffuses through the mortar in the form of dissolved oxygen.

From Figure 34, the 50SA-50FA mortar samples demonstrate results comparable to OPC mortar samples, suggesting similar microstructures. Due to the lack of specific data on the oxygen diffusion coefficient in AAFS concrete or mortar, the oxygen diffusion coefficient is assumed to be $D_{O_2} = 6 \times 10^{-9} \text{ m}^2/\text{s}$, based on values reported by Cao and Cheung [281]. The parameters mentioned above are summarised in Table 9.

Table 9. Geometric and materials parameters

Parameters	Values	Source
Concrete cover, C	20 mm	Experimental Results
Steel bar diameter, D	4 mm	
Surface chloride concentration, C_{cl}^s	1.38 wt.% of mortar	
Critical chloride threshold, C_{cl}^{crit}	0.36 wt.% of mortar	
Surface oxygen concentration, $C_{O_2}^s$	0.267 mol/m^3	[172]
Chloride diffusion coefficient, D_{Cl}	$6.7 \times 10^{-12} \text{ m}^2/\text{s}$	
Oxygen diffusion coefficient, D_{O_2}	$6 \times 10^{-9} \text{ m}^2/\text{s}$	

3.5.3 Potential Distribution in Mortar

To simulate the potential distribution in mortar sample, the Nernst-Planck equation was employed. This equation describes the movement of charged ions under the influence of concentration gradients (diffusion), electric fields (electric migration), and convection, expressed as:

$$\mathbf{J}_i = \underbrace{-D_i \nabla C_i}_{\text{Diffusion}} - \underbrace{\frac{z_i F}{RT} D_i C_i \nabla \phi}_{\text{Migration}} + \underbrace{C_i \mathbf{u}}_{\text{Convection}} \quad \text{Eq. 20}$$

where \mathbf{J}_i is the mass flux of charged ions i , in mol/(m²·s). D_i is the diffusion coefficient, in m²/s, and C_i is the concentration. z_i represents the valency of the charged ions. F is the Faraday's constant, 96485 C/mol. R is the universal gas constant, 8.314 J/(mol·K). T is the absolute temperature, in K. ϕ is the electric potential, in V. \mathbf{u} is the flow velocity of electrolyte, in m/s.

In this simulation, convection within the mortar is assumed to be negligible due to the limitations of its pore structure. Under quiescent conditions, concentration gradients are negligible, and ion transport is dominated by migration [281]. Therefore, after neglecting the diffusion and convection terms, the simplified Nernst–Planck equation is expressed as:

$$\mathbf{J}_i = -\frac{z_i F}{RT} D_i C_i \nabla \phi \quad \text{Eq. 21}$$

According to the Faraday's law, the electric current density \mathbf{i} (A/m²) can be expressed as

$$\mathbf{i} = F \sum_i z_i \mathbf{J}_i = \frac{F^2}{RT} \nabla \phi \sum_i z_i^2 D_i C_i \quad \text{Eq. 22}$$

In the mortar, the electrolyte is considered to maintain electroneutrality, as both chloride ions and sodium ions (Na⁺) penetrate mortar matrix. Hence, the electric current density in the mortar matrix can be expressed as

$$\nabla \cdot \mathbf{i} = 0 \quad \text{Eq. 23}$$

The electric potential distribution in the mortar is obtained by combining the simplified Nernst–Planck equation (Eq. 21) with Faraday's law (Eq. 22) and the assumption of local electroneutrality (Eq. 23). Treating the mortar as an ohmic conductor (Eq. 24) [281,286], the resulting expression (Eq. 25) governs the spatial variation of potential in the domain. This equation is a steady-state form of the Poisson equation and can be numerically solved using

appropriate boundary conditions to determine the electric field and current distribution within the mortar.

$$\mathbf{i} = -\frac{1}{\rho} \nabla \phi \quad \text{Eq. 24}$$

$$\nabla \cdot \left(\frac{1}{\rho} \nabla \phi \right) = 0 \quad \text{Eq. 25}$$

For boundary conditions:

1. At the steel-mortar boundary, the macrocell current density (i_{mac}) flows outward from the active region toward the more distant passive region. The macrocell current flux must equal the total current flux at the interface, which flows through the boundary, as shown below:

$$i_{mac} = -\mathbf{n} \cdot \left(\frac{1}{\rho} \nabla \phi \right) \Big|_{interface} \quad \text{Eq. 26}$$

where i_{mac} denotes macrocell corrosion current density in A/m², and \mathbf{n} is the unit normal vector to the boundary surface.

2. At the boundary of the mortar surface, where no current flow occurs, it is defined as a boundary with zero current flux:

$$\mathbf{n} \cdot \left(\frac{1}{\rho} \nabla \phi \right) = 0 \quad \text{Eq. 27}$$

With these two boundary conditions, the spatial potential distribution can be solved numerically by using the finite element method (FEM).

3.5.4 Microcell and Macrocell electric current densities

In this simulation, the combination of the microcell and macrocell corrosion mechanisms were employed. In the microcell corrosion, exposed steel acts as the anode, where oxidation occurs, while the adjacent zone covered by passive film serves as the cathode, where reduction takes

place. In contrast, macrocell corrosion, involves the development of a potential field across the mortar, with the anode and cathode located farther apart within the specimen.

When the anode and cathode undergo activation polarization, their electrode potentials shift from the original values associated with the material phases to a new equilibrium potential. This shift creates an overpotential, which drives the electrochemical reactions and generates an electric current. Using polarization equations, the anodic current density (Eq. 28) and cathodic current density (Eq. 29) can be calculated:

$$i_{Fe} = i_{Fe}^0 \exp\left(2.303 \frac{\phi - \phi_{Fe}}{\beta_a}\right) \quad \text{Eq. 28}$$

$$i_{O_2} = i_{O_2}^0 \exp\left(2.303 \frac{\phi - \phi_{O_2}}{\beta_c}\right) \quad \text{Eq. 29}$$

where ϕ_{Fe} and ϕ_{O_2} are the anodic and cathodic equilibrium potentials (mV vs. SCE), in V. i_{Fe}^0 and $i_{O_2}^0$ are the anodic and cathodic corresponding exchange current densities under the equilibrium potentials, in A/m². i_{Fe} and i_{O_2} are the anodic and cathodic electric current densities, in A/m².

In addition to activation polarisation, concentration polarisation also affects the cathodic reaction due to the delayed replenishment of consumed oxygen. To account for this, the limiting current density is introduced in this simulation. Assuming a linear distribution of oxygen concentration from the mortar surface to the steel surface [194], the limiting current density i_L (A/m²) can be calculated as:

$$i_L = \frac{D_{O_2} z_{O_2} F C_{O_2}^s}{L} \quad \text{Eq. 30}$$

where z_{O_2} is the valency of O₂ of cathodic reduction, which is 4. F is the Faraday's constant, 96485 C/mol. L is the oxygen diffusion distance from mortar surface to the steel surface, in m.

For the centrally placed steel bar, L is fixed at a value of 8 mm. For the side-placed steel bar, the distance L can be calculated as the shortest distance from the mortar surface to steel surface using Eq. 31.

$$L = C + \frac{D}{2}(1 - \cos\theta) \quad \text{Eq. 31}$$

According to Perez [194], the cathodic electric current (Eq. 29) transitions to a modified form when the limiting current density is incorporated.

$$i_{O_2} = \frac{i_{O_2}^0 \exp\left(2.303 \frac{\phi - \phi_{O_2}}{\beta_c}\right)}{1 + \frac{i_{O_2}^0}{i_L} \exp\left(2.303 \frac{\phi - \phi_{O_2}}{\beta_c}\right)} \quad \text{Eq. 32}$$

In the active region during microcell corrosion, the electrons released from the anode are consumed at the cathode. The electric current density of microcell (i_{mic}) is equal to the cathodic electric current density, as shown in Eq. 33. In macrocell corrosion, the electrons generated at the anode surface are partially consumed by the cathodic reactions within adjacent microcells. The remaining electrons are transported through the pore solution to the cathode, which is located farther from the anode. Consequently, the electric current density of macrocell (i_{mac}) can be expressed in Eq. 34. A sketch drawing is shown in

$$i_{mic} = i_{O_2} = \frac{i_{O_2}^0 \exp\left(2.303 \frac{\phi - \phi_{O_2}}{\beta_c}\right)}{1 + \frac{i_{O_2}^0}{i_L} \exp\left(2.303 \frac{\phi - \phi_{O_2}}{\beta_c}\right)} \quad \text{Eq. 33}$$

$$i_{mac} = i_{Fe} - i_{O_2} = i_{Fe}^0 \exp\left(2.303 \frac{\phi - \phi_{Fe}}{\beta_a}\right) - \frac{i_{O_2}^0 \exp\left(2.303 \frac{\phi - \phi_{O_2}}{\beta_c}\right)}{1 + \frac{i_{O_2}^0}{i_L} \exp\left(2.303 \frac{\phi - \phi_{O_2}}{\beta_c}\right)} \quad \text{Eq. 34}$$

Furthermore, it should be noted all the electrons are released from the anodic reactions.

Therefore, the total corrosion current can be expressed as:

$$i_{total} = i_{Fe} = i_{Fe}^0 \exp\left(2.303 \frac{\phi - \phi_{Fe}}{\beta_a}\right) \quad \text{Eq. 35}$$

The values for the parameters mentioned in this section are summarised in Table 10.

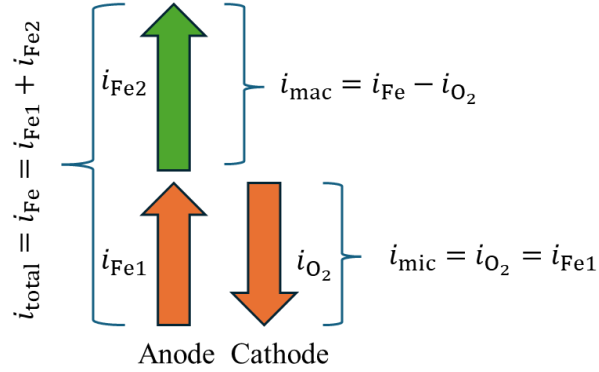


Figure 33. The sketch of microcell and macrocell electric current density

Table 10. Electrochemical parameter used in numerical modelling simulations

Parameters	Values	Source
Faraday's constant, F	96485 C/mol	Constant values
Universal gas constant, R	8.314 J/(mol·K)	
Anodic Tafel slope, β_a	246.8 mV/dec	
Cathodic Tafel slope, β_c	-255.6 mV/dec	Experiment results
Mortar resistivity, ρ	200 $\Omega \cdot m$	
Anodic equilibrium potential, ϕ_{Fe}	-780 mV	[281]
Cathodic equilibrium potential, ϕ_{O_2}	160 mV	
Anodic Exchange Current Density, i_{Fe}^0	3×10^{-4} A/m ²	
Cathodic Exchange Current Density, $i_{O_2}^0$	1×10^{-5} A/m ²	

3.5.5 Corrosion of Steel Bar and Rust Expansion

The anode current density, resulting from the half-cell reactions of iron corrosion (Eq. 2), can be used to quantify the amount of the dissolved steel through Faraday's law [194], as shown below:

$$R(\theta, t) = \frac{\int_{t_i}^t i_{total}(\theta, t) dt \cdot M_{Fe}}{Z_{Fe} \cdot F \cdot \rho_{Fe}} \quad \text{Eq. 36}$$

where $R(\theta, t)$ represents the radials loss around the circumference of steel bar at the anode region, in m. M_{Fe} is the atomic weight of iron, equal to 55.845 g/mol. ρ_{Fe} is the density of steel,

which is 7850 kg/m³. z_{Fe} denotes the valency of anodic reaction, which is 2. t_i and t represent the corrosion initiation time and corrosion finish time, respectively.

The rust expansion ratio (α) can be defined as the ratio of the volume of the corrosion product to the volume of the original steel bar [162,282]. Consequently, the thickness of corrosion rust layer ($\delta(\theta, t)$) around the circumference of the steel bar can be expressed as:

$$\delta(\theta, t) = (\alpha - 1) \times R(\theta, t) \quad \text{Eq. 37}$$

In this research, the corrosion expansion ratio α of the corrosion product is taken as 2.96, as reported by Suda et al. [287]

4 Mechanical Properties of AAFS Concretes

4.1 Introduction

In this chapter, the results of mechanical tests, excluding the pull-out test, for AAFS mortar and concrete samples were analysed and compared with OPC reference groups. The pull-out test will be presented in Chapter 6. Factors influencing the mechanical properties of AAFS concretes, including the mix proportions of precursors and the aggregate types (gravel and limestone) were detailed analysed. The three-point bending test for mortar samples will be introduced first, followed by the compression test, tensile splitting tests, and fracture test for AAFS concretes.

4.2 Flexural Strength and Compressive Strength of Mortar Samples

Figure 34 shows the histogram of (a) flexural strength and (b) compressive strength results for five kinds of AAFS mortars (Groups 1-5, as detailed in Table 7) and OPC mortar, obtained from the three-point bending test and the compressive strength test on mortar prisms, as described in Section 3.2.3. Detailed results are provided in Table 11. From Figure 34, it is observed that both flexural strength and compressive strength for AAFS mortars increase with higher SA content. The 100FA samples exhibit the lowest values in both flexural strength and compressive strength, while the 100SA samples show the highest.

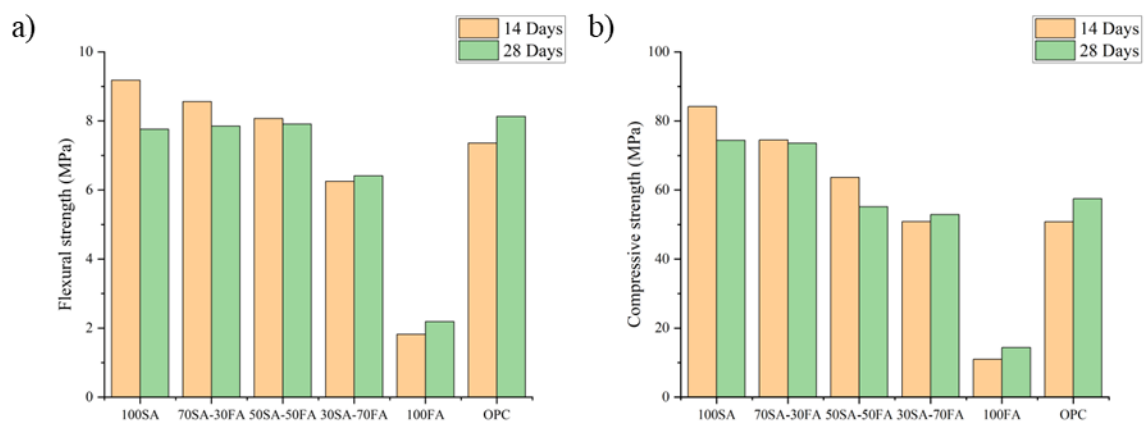


Figure 34. Histogram of the three-point bending test and compression test: (a) Flexural strength and (b) compressive strength for AAFS mortars and OPC reference mortar

Table 11. Average flexural strength (MPa) and compressive strength (MPa) of AAFS mortars at 14 days and 28 days

Groups	14 Days	28 Days	Percentage of improvement	14 Days	28 Days	Percentage of improvement
	Flexural Strength (MPa)			Compressive Strength (MPa)		
100SA	7.73	9.18	18.76%	84.15	74.38	-11.61%
70SA-30FA	8.59	7.85	-8.61%	74.44	73.56	-1.18%
50SA-50FA	8.09	7.92	-2.10%	63.64	55.16	-13.32%
30SA-70FA	6.25	5.67	-9.28%	50.87	44.89	-11.76%
100FA	1.82	2.19	20.33%	11.01	14.38	30.61%
OPC	7.36	8.13	10.46%	50.82	57.48	13.11%

At 28 days, AAFS mortar samples containing 50% or more SA content show a reduction in both flexural strength and compressive strength compared to their 14-day strengths. For flexural strength, the reduction increases with higher SA content. For compressive strength, the 70SA-30FA samples exhibit the smallest reduction, while the reductions in the 100SA and 50SA-50FA samples are similar and significantly greater than in the 70SA-30FA samples. In contrast, the 30SA-70FA and 100FA samples show an increase in their 28-day strengths compared to their 14-day strengths.

The observed differences in strength evolution between 28-day and 14-day samples are attributed to the combined effects of drying shrinkage and the polycondensation process within the mortar matrix. The reduction in strength is primarily due to the high SA content, which promotes the formation of C-A-S-H gel. The continuous polycondensation process contributes to the formation of microcracks within the mortar matrix. Additionally, drying shrinkage, as described in Section 2.2.3.1, also contributes to microcracks formation due to the moisture loss [288]. Consequently, the strength of the samples decreases at 28 days. The slight drop in compressive strength of the 70SA-30FA samples might be due to the optimal mix proportion, which results in a more uniform mortar matrix.

For the 30SA-70FA and 100FA samples, the characteristics of N-A-S-H gel include high porosity, which is refined as the evolution progresses to N-(C)-A-S-H gel through C-A-S-H gel participation. Due to these characteristics, the polycondensation process tends to refine the

overall porosity of the mortar matrix, thereby enhancing the strength of the mortar samples. Comparing these results with samples containing 50% or more SA content reveals differences in the effect of the polycondensation process. This variation arises from the differences in porosity characteristics between C-A-S-H gel and N-A-S-H gel, as stated in Section 2.1.

Compared to the OPC reference samples, AAFS mortar samples containing more than 30% SA content exhibit comparable or even superior flexural strength and compressive strength at the same curing age. However, their strength development from 14 to 28 days shows a negative growth trend, as reflected by the percentage change in Table 11. The reason for this has been discussed in the above context. For the 30SA-70FA samples, the flexural strength is lower than that of OPC samples, while the compressive strength is comparable. The 100FA samples show the lowest flexural strength and compressive strength. This is due to the N-A-S-H gel, which is more porous.

4.3 Mechanical Strength Properties for AAFS Concretes

4.3.1 AAFS Gravel Concretes

At the initial stage of the research, the 100SA and 100FA groups were excluded due to their highest and lowest strengths, respectively. Only AAFS samples with compressive strength comparable to the OPC reference were selected, based on the findings from the literature review, as outlined in Section 2.2.1.

Figure 35 shows the average 28-day compressive strength and tensile splitting strength for three AAFS concrete groups (30SA-70FA, 50SA-50FA, and 70SA-30FA) and the OPC reference group, all utilising 10 mm gravel as the coarse aggregate. As shown in Figure 35 (a), the average compressive strength of AAFS samples decreases with a reduction in SA content in the precursors, consistent with the trend observed in mortar samples. Furthermore, the results for 70SA-30FA and 50SA-50FA concretes are closely aligned. All three AAFS groups demonstrate higher compressive strength than the OPC reference group.

From Figure 35 (b), it is evident that the average tensile splitting strength of AAFS concrete follows a similar trend to the compressive strength results, with strength increasing as the SA content in the precursors rises. Compared to the OPC reference group, the 70SA-30FA and 50SA-50FA concretes exhibit higher tensile splitting strengths, whereas the 30SA-70FA samples show lower tensile splitting strength. A detailed analysis of the related parameters will be presented in the following section.

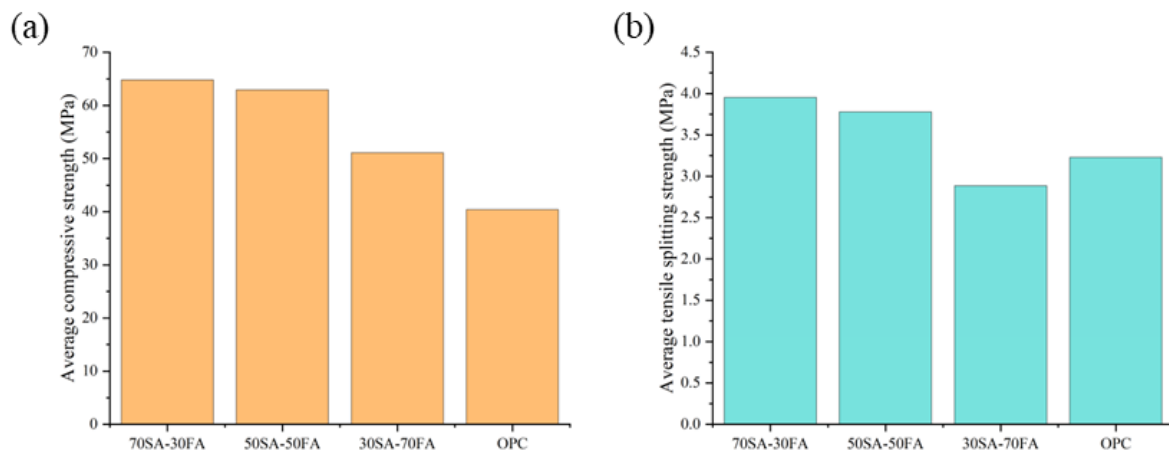


Figure 35. The 28-day strength results for three types of AAFS concretes and OPC reference concrete with gravel aggregate: (a) average compressive strength and (b) average splitting tensile strength

4.3.2 AAFS Limestone Concretes

In this section, the results of the compressive strength test for AAFS concretes and OPC concrete, with limestone used as a replacement for gravel aggregate, are presented. Unlike the groups selected for AAFS gravel concretes, the 100SA and 100FA groups were also included in the AAFS limestone concretes. Additionally, two supplementary materials, MK and LSP, were employed to investigate the influence of precursors on the mechanical properties of AAFS concretes. These materials were added to the 70SA-30FA group by replacing 20% of the FA content in the precursor.

Figure 36 presents the average compressive strength results for AAFS and OPC concrete samples at 14 and 28 days, with detailed data provided in Table 12. From the histogram plot, it

is observed that at 14 days, the average compressive strength of AAFS concrete samples (using only FA and SA as precursors) generally increases with higher SA content, except for the 30SA-70FA concrete group. Among these groups, the 100FA concrete samples exhibit the lowest strength, while the 100SA concrete samples show the highest. The strength difference between these two groups is attributed to variations in the chemical composition of the precursors, specifically the CaO content, as shown in Table 6. The mix proportions (Table 7) further amplify these compositional differences, resulting in the formation of distinct gels: C-A-S-H gel in 100SA samples and N-A-S-H gel in 100FA samples [8,9]. The characteristics of these gels and their influence on compressive strength have been described in Section 2.1 and Section 2.2.1 and will not be repeated here. These differences ultimately lead to the observed variation in compressive strength between the two groups.

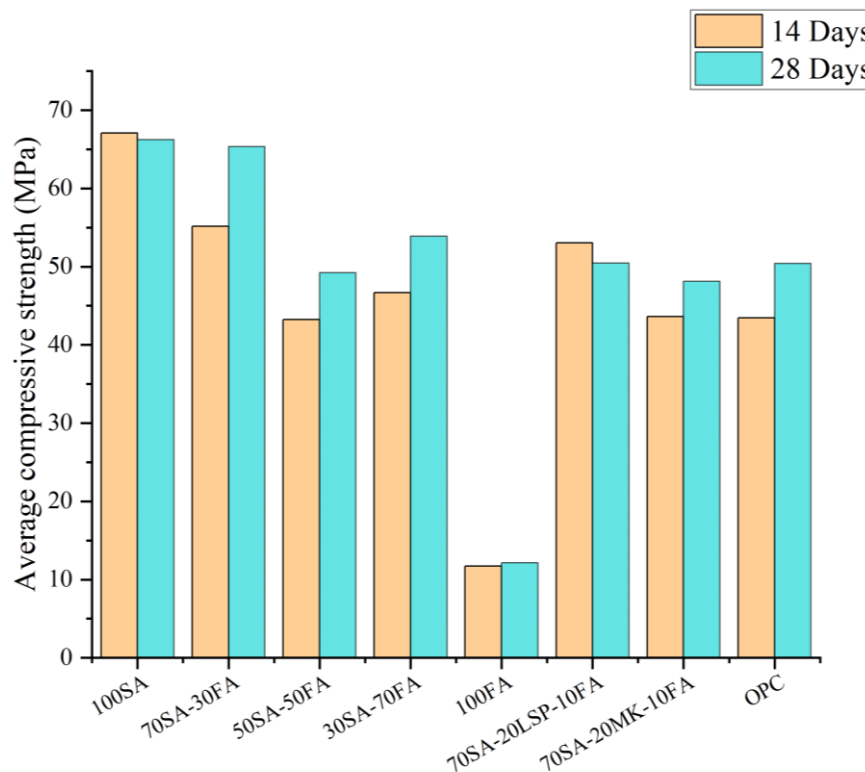


Figure 36. The average compressive strength of AAFS and OPC concretes at 14 days and 28 days

Table 12. Average compressive strength for concrete samples at 14 days and 28 days

Group	AAC	
	14 Days	28 Days
	Average compressive strength (MPa)	Average compressive strength (MPa)
1	100SA	67.08
2	70SA-30FA	66.24
3	50SA-50FA	65.34
4	30SA-70FA	49.26
5	100FA	46.68
6	70SA-20MK-10FA	53.92
7	70SA-20LSP-10FA	11.71
8	OPC	12.15
		50.47
		48.12
		50.41

The 30SA-70FA concrete samples exhibit higher compressive strength than the 50SA-50FA concrete samples but lower than the 70SA-30FA samples. This phenomenon, which contrasts with observations for the same group in AAFS mortars and AAFS gravel concretes, can be attributed to two factors: the “wall effect” caused by the coarse aggregate and the physical properties of the aggregate. The “wall effect”, as mentioned in Section 2.5.2, causes a non-uniform distribution of the alkaline activator and precursor grains around the coarse aggregate [216,217]. leading to variations in the density of the ITZ [289,290]. To better understand the influence of the “wall effect” on compressive strength, an in-depth analysis was conducted. Figure 37 compares the compositional distribution of Groups 1-7 on a CaO-SiO₂-Al₂O₃ ternary diagram, as described in section 2.1. The corresponding ratios for all AAFS groups are quantitatively summarized in Table 13, calculated from both solid precursors and alkaline activator.

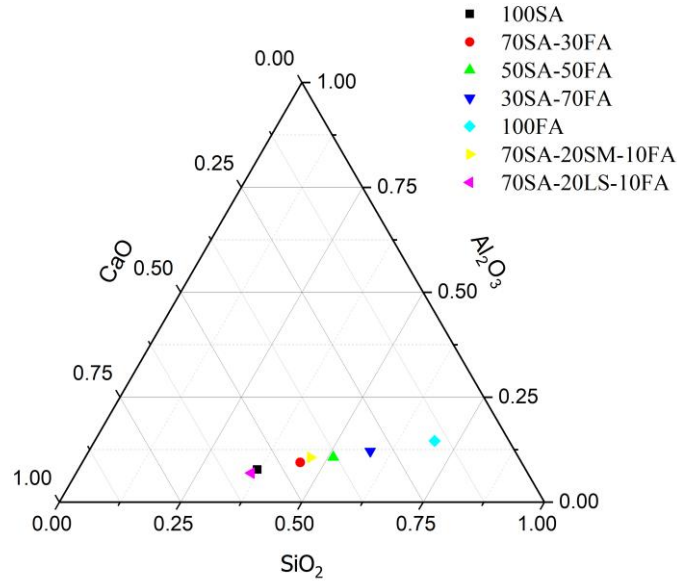


Figure 37. Ternary diagram illustrating the composition distribution of Groups 1-7.

Table 13. The ratios of main elements for AAFS concrete groups

	Group	Ca/Si	Si/Al	Al/Ca
1	100SA	1.50	4.72	0.14
2	70SA-30FA	1.01	4.75	0.21
3	50SA-50FA	0.75	4.76	0.28
4	30SA-70FA	0.51	4.77	0.41
5	100FA	0.22	4.79	0.96
6	70SA-20MK-10FA	0.92	4.34	0.25
7	70SA-20LSP-10FA	1.58	5.22	0.12

From Table 13, the 50SA-50FA group has a higher Ca/Si ratio than the 30SA-70FA group, suggesting the formation of more C-A-S-H gel. However, the Al/Ca ratio in the 50SA-50FA group is lower than in the 30SA-70FA group. These variations influence the hydration process at the ITZ in AAFS concretes. According to Fang and Zhang [289], the hydration of FA occurs first at the ITZ, releasing Al^{3+} and Si^{4+} ions, which results in the formation of N-A-S-H gel. Subsequently, Ca^{2+} ions gradually released from SA grains lead to the formation of C-A-S-H gel, which combines with N-A-S-H gel through the polycondensation process to produce N-(C)-A-S-H gel. However, the release of Ca^{2+} ions from SA grains can be hindered by the formation of a compact hydroxide film caused by the high concentration of alkaline activator [103]. As a result, the 30SA-70FA samples show higher average compressive strength due to

their higher SiO_2 and Al_2O_3 content (Figure 37), which reduces the activator concentration and facilitates the release of Ca^{2+} ions. In contrast, the lower SiO_2 and Al_2O_3 content in the 50SA-50FA group may hinder the release of Ca^{2+} ions, as it does not reduce the activator concentration as effectively. Additionally, the compressive strength of the 30SA-70FA group is lower than that of the 70SA-30FA group due to differences in the dominant gel types and their microstructural characteristics, as introduced in Section 2.1.

For 30SA-70FA groups, regarding the influence of aggregate types, limestone has angular shapes, and a larger surface area compared to gravel, which has a smaller, smoother surface. Limestone is also stronger than gravel. Therefore, the 30SA-70FA limestone aggregate concrete show a distinct difference in compressive strength compared to the 30SA-70FA gravel aggregate concrete. For mortar samples, the compressive strength for the same mix proportion is lower than in the other groups, as mortar is more homogeneous and not affected by the “wall effect”.

An interesting observation is that both the 30SA-70FA mortar and limestone concrete samples exhibit an average compressive strength approximately four times higher than that of the 100FA samples, despite only 30% of the FA being replaced by SA, as illustrated in Figure 34 and Figure 36. Although the 100FA group has a Ca/Si ratio of 0.22 (Table 13), meeting the lower limit for C-A-S-H gel formation, as described in Section 2.1, the higher Al/Ca ratio makes the formation of this gel negligible. Instead, a large quantity of N-A-S-H gel is generated. The porous, ring-shaped structure of the N-A-S-H gel (Figure 2) in the 100FA group results in a weaker binder skeleton compared to other groups. Replacing part of the FA with SA compensates this shortcoming, as SA contains approximately five times more CaO than FA (Table 6). The increased CaO content in the 30SA-70FA group promotes the formation of C-A-S-H gel, which combines with N-A-S-H gel through the polycondensation process to form

N-(C)-A-S-H gel, refining the porosity and compacting the matrix. As a result, the 30SA-70FA group achieves higher compressive strength than the 100FA group.

At 28 days, AAFS groups (Groups 2 to 5, Table 7) show an increase in average compressive strength compared to their 14-day strength, as shown in Figure 36. Among these groups, the 100FA group exhibits the lowest rate of increase, while the 70SA-30FA group shows the highest. The former is attributed to the lack of CaO content, which limits further microstructure refinement, while the latter is due to the gradual release of Ca^{2+} ions from the compact hydroxide film as hydration reactions continue. The 50FA-50FA and 30SA-70FA groups exhibit a similar rate of increase, likely due to their similar element ratios (Table 13). However, for the 100SA group, a slight decrease in average compressive strength is observed at 28-day compared to their 14-day strength. This decrease is attributed to the combined effects of drying shrinkage and polycondensation of gels within the concrete matrix, which may result in the formation of microcracks, as discussed in Section 2.2.3.1. This phenomenon is more pronounced in mortar samples, where the 28-day average compressive strength of AAFS mortars with SA content above 50% is lower than their 14-day strengths, as illustrated in Figure 34. This is due to the more homogenous properties of mortar compared to concrete.

For the 70SA-20LSP-10FA group, as shown in Table 7, where 20% of the FA content is replaced with LSP, the average compressive strength varies, as shown in Figure 36. At 14 days, the 70SA-20LSP-10FA group is comparable to the 70SA-30FA group. From Table 6 and Table 13, raw LSP contains high CaO content but low Al_2O_3 content, resulting in higher Ca/Si and Si/Al ratios, which fall between 100SA and 70SA-30FA groups. However, although X-RF analysis indicates high CaO content in LSP (51.5%), it predominately exists as CaCO_3 (calcium carbonate), as evidenced by the high loss of ignition (L.O.I). At early reaction stages, CaCO_3 acts as a pore filler in the 70SA-20LSP-20FA group, reducing porosity and increasing early strength. This contributes to maintaining a compressive strength similar to the 70SA-30FA

group. At 28 days, the compressive strength of the 70SA-20LSP-10FA samples decreases compared to their 14-day strength. This decrease is attributed to chemical stability of CaCO_3 , which is minimally reactive with the alkaline activator (e.g., NaOH), meaning that only a small portion participates in the hydration process [291]. Consequently, at later ages, microcracks may develop around these solid grains due to polycondensation process between gels, reducing the overall properties of concrete.

For the 70SA-20MK-10FA group, with 20% of the FA content is replaced by MK, the average compressive strength is comparable to the 50SA-50FA group. From Table 6, MK contains very little CaO but has higher Al_2O_3 and SiO_2 contents, resulting in higher Al/Ca and Ca/Si ratios, which fall between the 30SA-70FA and 50SA-50FA groups, as illustrated in Table 13. Consequently, the 70SA-20MK-10FA samples show similar compressive strength to the 50SA-50FA samples. In contrast to LSP, although MK lacks CaO content, its SiO_2 and Al_2O_3 contents actively participate in the hydration process, contributing to the increased compressive strength of the 70SA-20MK-10FA samples at 28 days, as shown in Table 12.

When comparing the AAFS concretes to the OPC reference concrete, AAFS concretes with 30% SA content in the precursors exhibit compressive strength comparable to OPC concrete. Particularly, AAFS groups with SA content above 50% demonstrate the compressive strength superior to the OPC group. Conversely, the 100FA samples show the lowest compressive strength among all groups. For groups where FA content is partially replaced by LSP and MK, the compressive strength is also comparable to the OPC reference group.

4.4 Fracture Properties of AAFS Concrete

In this section, the results of the three-point bending test on notched concrete beams with CMOD control are analysed and discussed. The load-deflection behaviours of the test, along with the derived fracture properties, including fracture energy (G_F) and fracture toughness (K_{IC}) are calculated using Eq. 13 and Eq. 14. Two types of concrete beams with different dimensions

were prepared: the first type, made with 10 mm gravel, had dimensions of 100 mm x 100 mm x 500 mm, while the second type, cast with 20 mm limestone, had dimensions of 150 mm x 150 mm x 600 mm.

4.4.1 AAFS Gravel Concrete beams

The representative load-CMOD and load-deflection curves for AAFS gravel concrete beams are shown in Figure 38, while the mean G_F and K_{IC} values are presented in Table 14. From Figure 38 (a), it is observed that the AAFS concrete beams show a similar rate of increase in the linear region (before reaching peak load), while the rate for the OPC reference concrete beam is slightly higher. This difference may be due to defects present within the OPC concrete, such as high porosity, which accelerates cracks propagation. In the post-peak region, the evolution of each curve varies, and hysteresis loops are observed, particularly in the 30SA-70FA sample. These hysteresis loops are likely caused by the sudden breakage of gravel aggregates within the concrete beam during loading, which partially dissipates the applied energy [292]. Additionally, the 70SA-30FA concrete sample stops at approximately 0.5 mm of CMOD, with some residual force remaining, due to sudden brittle failure.

From Figure 38 (b), the load-deflection curve, it is observed that the load evolution in the elastic stage (linear portion) for AAFS gravel concrete beams is similar to their load-CMOD curves before reaching the peak load. In contrast, the OPC gravel concrete beam exhibits a deviation compared to its load-CMOD curve. By comparing the slopes of these curves in the linear region, the deflection stiffness of AAFS gravel concrete beams is observed to be higher than that of the OPC gravel concrete beam. In the post-peak region, the curve of the OPC sample drops rapidly from the peak load compared to the AAFS samples, where the decline is smoother. This behaviour indicates that the OPC gravel concrete beam exhibits higher brittleness. The significant deviation in the linear portion between load-CMOD and load-deflection curves for

OPC gravel concrete will be discussed in comparison with OPC limestone concrete in the next section.

Although the curve behaviours for AAFS gravel concrete beams and OPC gravel concrete beam are different, the mean G_F and K_{IC} values are consistent among the 30SA-70FA group, 70SA-30FA group, and OPC group, as illustrated in Table 14. This indicates these groups have the comparable the fracture energy and toughness despite differences in curve behaviour. Furthermore, the 50SA-50FA group shows the lowest values for these two parameters, indicating poor in fracture resistance compared to other groups.

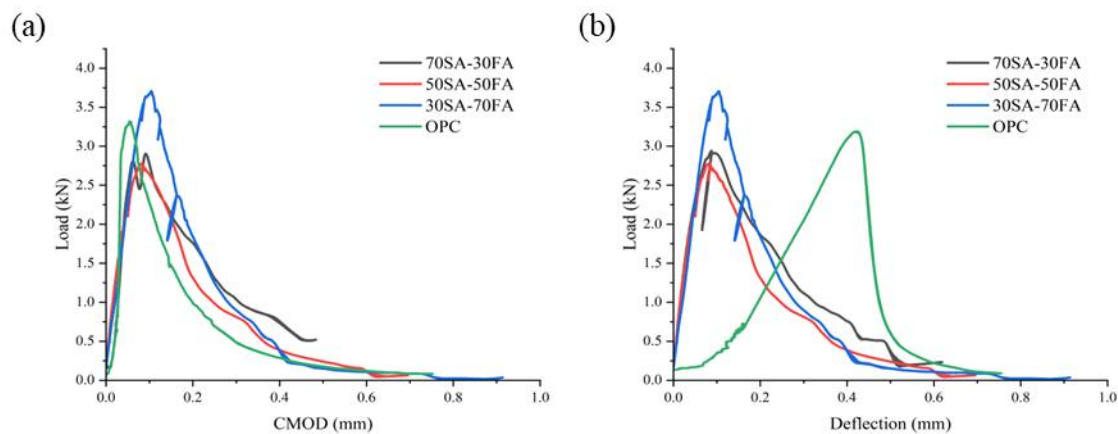


Figure 38. Representative Load-CMOD curve (a) and Load-Deflection curve (b) for AAFS concrete beams (100 mm x 100 mm x 500 mm)

Table 14. Mean fracture energy and fracture toughness of gravel type AAFS concrete beams

Group	Mean G_F (J/m ²)	Mean K_{IC} (MPa·mm ^{1/2})
70SA-30FA	134.03	18.90
50SA-50FA	107.33	17.36
30SA-70FA	128.40	18.83
OPC	135.78	19.13

4.4.2 AAFS Limestone Concrete beams

For AAFS limestone concrete beams, the 70SA-20MK-10FA and 70SA-20LSP-10FA groups were also included. Figure 39 shows the load-CMOD and load-deflection curves for representative AAFS concrete beams cast with limestone, while Table 15 lists their mean G_F and K_{IC} . From Figure 39 (a), the load-CMOD curves for all groups exhibit similar behaviour

in their linear elastic region, followed by a transition from elastic to plastic stage before reaching the maximum load (P_{\max}). Beyond P_{\max} , the curves enter a softening stage, characterised by the propagation of crack above the notched region, as shown in Figure 40. This process leads to a gradual reduction in the sample's load-bearing capacity and stiffness. For instance, in the 30SA-70FA sample, a hysteresis loop is clearly observed at the peak load. Additionally, for the OPC group, sudden brittle failure occurs in all samples after reaching P_{\max} (represented by the yellow curve), leading to the absence of a post-peak region.

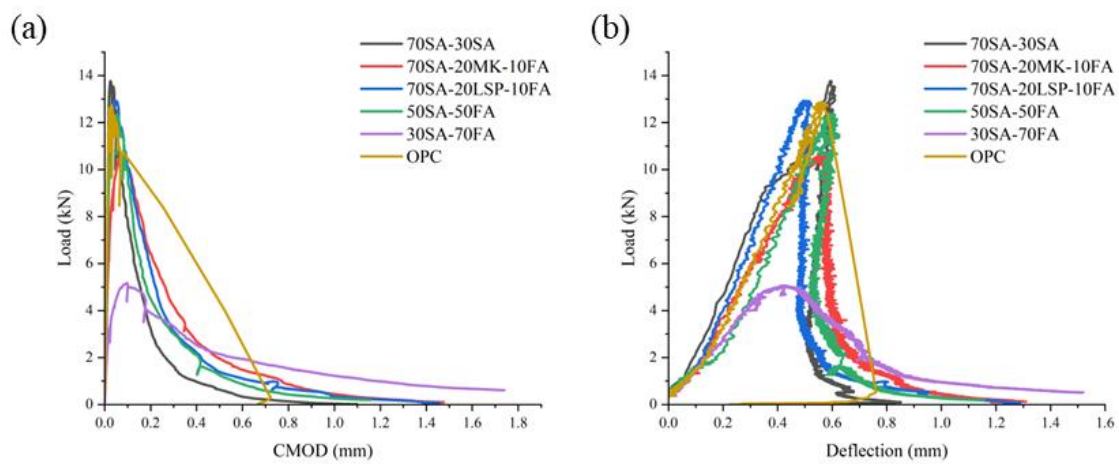


Figure 39. Representative Load-CMOD curve (a) and Load-Deflection curve (b) for AAFS concrete beams (150 mm x 150 mm x 600 mm)



Figure 40. Failure of the AAFS limestone concrete beam

From Figure 39 (b), it is observed that the evolution trend of the load-deflection curves differs from that of the load-CMOD curves. Specifically, the slope of the linear region in the load-deflection curves is smaller than that of the load-CMOD curves, requiring a larger deflection to reach the peak load. This difference arises due to the distinct measurement objectives of the

two methods. The load-CMOD curve is controlled by a clip gauge at a constant rate, capturing the relationship between the load and the opening distance of the notched zone. In contrast, the load-deflection curve reflects the deflection of the beam at the midspan between the two supports. As a result, the linear slopes are different for these two plots.

From both plots in Figure 39, it is noticed that the 30SA-70FA beam exhibits the lowest P_{max} . In addition, in the softening stage, the 30SA-70FA beam shows a smoother drop in load, indicating better ductility compared to the other beam groups. As the SA content in the precursors increases to 50%, the P_{max} for the 50SA-50FA beam nearly doubles compared to the 30SA-70FA beam. However, the mean G_F values for these two groups are quite similar, as listed in Table 15. This similarity is attributed to the better ductile characteristic of the 30SA-70FA beam, which increases the distance required for failure. Despite having comparable fracture energy, the significantly smaller mean K_{IC} value ($10.79 \text{ MPa}\cdot\text{mm}^{1/2}$) of the 30SA-70FA group, nearly 50% lower than other groups (above $20 \text{ MPa}\cdot\text{mm}^{1/2}$), highlights its poor fracture resistance.

For the remaining groups (excluding the 30SA-70FA group), Figure 39 (b) shows that the 70SA-20MK-10FA beam exhibits a smaller P_{max} compared to the 50SA-50FA beam, but their mean G_F and K_{IC} values are quite similar. This similarity is attributed to their comparable element ratios, as shown in Table 13. The effects of replacing FA with MK and LSP on concrete strength properties have already been discussed in Section 4.3.2 and will not be repeated here. Furthermore, the addition of MK enhances the ductile properties of the beam to some extent, as evidenced by the smoother reduction in load during the softening stage, as seen in Figure 39 (b). For the AAFS concrete beam with LSP, as stated in Section 4.3.2, this can lead to the formation of microcracks around the solid particles, increasing the sample's brittleness. This brittleness is evident in the post-peak curve (Figure 39 (b)), where the most rapid drop is observed.

For the OPC reference group, the mean G_F value is not available due to the sudden brittle failure, and only the mean K_{IC} value is present in Table 15. The load-deflection curve of the OPC limestone concrete beam in the linear region shows similar behaviour to that of the OPC gravel concrete beam, as shown in Figure 38 (b). Additionally, in the limestone concrete beams, the load-deflection curves across groups are almost consistent. In contrast, for the gravel concrete beams, the AAFS groups show distinct differences compared to the OPC group. This variation may be attributed to the physical properties of the aggregate types and the size effects of the beam. The larger beam size and stronger aggregate contribute to better fracture resistance.

Table 15. Mean fracture energy and fracture toughness of AAFS concrete beams

Group	Mean G_F (J/m ²)	Mean K_{IC} (MPa·mm ^{1/2})
70SA-30FA	188	27.44
70SA-20LS-10FA	230.12	22.32
70SA-20MK-10FA	227.3	25.08
50SA-50FA	206.28	25.48
30SA-70FA	194.23	10.79
OPC	-	27.01

4.5 Discussion

From these mechanical test results, it is evident that aggregate types significantly influence the mechanical properties of concrete. To better understanding this effect, a comparison of the 28-day compressive strength between mortar and concrete samples with the same mix proportions is presented in Figure 41. It is observed that the compressive strength of concrete samples generally decreases compared to their corresponding mortar samples, except for the 50SA-50FA gravel concrete and 30SA-70FA limestone concrete. The former exhibits a significant increase in compressive strength, while the latter shows a slight increase. The higher compressive strength of the 30SA-70FA limestone concrete has been analysed in relation to the effects of aggregate and precursor composition, as presented in Section 4.3.2. This can also explain the higher compressive strength of the 50SA-50FA gravel concrete. However, its higher value compared to the limestone aggregate concrete may be attributed to the more uniform

distribution of the smaller gravel particles, combined with the "wall effect," ultimately leading to greater strength.

Figure 42 shows images of the failure of concrete samples made with these two types of aggregates after the compression test and three-point bending test. By comparison, it is evident that gravel splits in both tests, whereas limestone remains relatively intact, particularly after compression testing. For the fracture test, the characteristics of gravel result in it splitting during the test, with cracks propagating along the aggregate, leading to a short post-peak phase (Figure 38). This behaviour provides evidence that gravel exhibits lower strength than limestone and is unable to dissipate energy effectively. Limestone, on the other hand, significantly mitigates this issue. Its angularity and high strength enhance the overall properties of the concrete, as reflected in the higher fracture energy values observed (Figure 39).

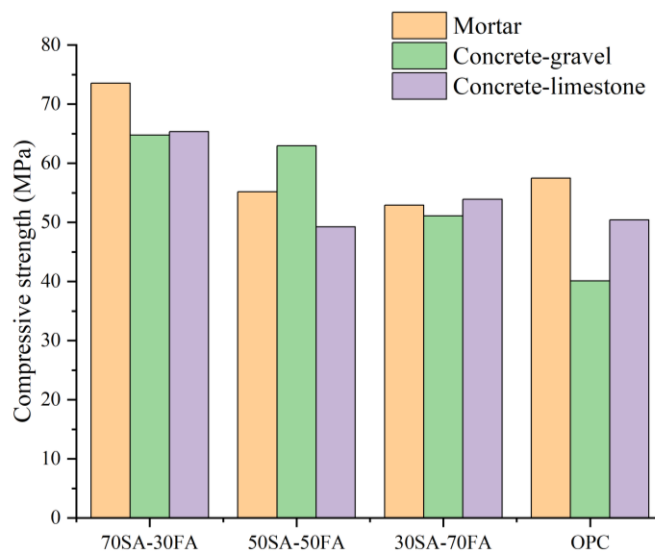


Figure 41. Comparison of compressive strength among mortar and concretes

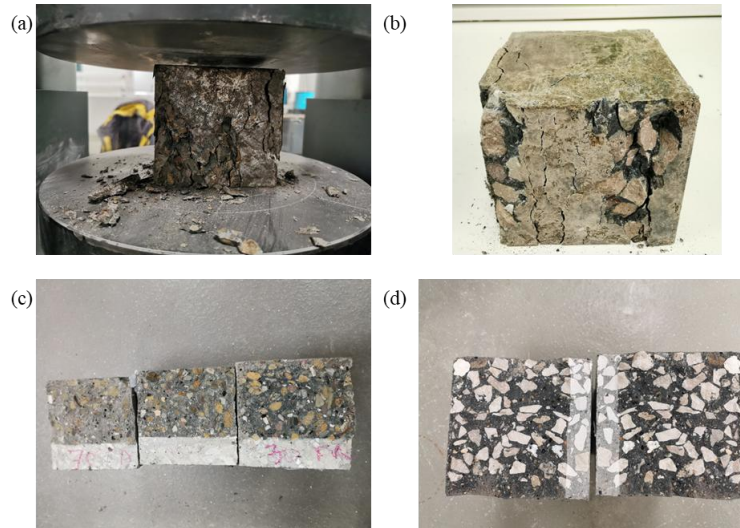


Figure 42. The condition of the gravel and limestone after tests were finished, (a) and (b) the compression test, (c) and (d) the three-point bending test

4.6 Summary

In this chapter, the mechanical properties and the fracture properties of both AAFS concrete and mortar samples have been systematically evaluated. The compressive and flexural strengths of AAFS binders are generally enhanced with increasing slag (SA) content in the precursor mix, especially at early ages. This trend, as illustrated in Figure 34, highlights the high initial reactivity of slag, which accelerates polymerisation and densifies the matrix.

The observed discrepancy in strength development between mortar and concrete samples is attributed to the “wall effect” at the ITZ, where aggregate alters the local distribution of activators and precursors. This uneven distribution leads to distinct reaction kinetics in the ITZ compared to the bulk matrix. Moreover, the presence of coarse aggregates in concrete provides a confinement effect that mitigates microcrack formation during polycondensation, partially explaining the continued strength gain in concrete from 14 to 28 days. This is contrary to the strength reduction observed in mortars.

Regarding the fracture properties, AAFS limestone concrete beams with the low-calcium content (30SA-70FA) exhibit fracture energy comparable to the high-calcium samples, but

significantly lower fracture toughness, indicating a higher susceptibility to crack propagation. Although higher SA content improves fracture toughness, this enhancement is accompanied by increased brittleness, as indicated by the sharper post-peak drop in load during softening stage (Figure 39). This toughness-brittleness trade-off represents a critical consideration for structural design.

From experiment results, replacing 10 mm gravel with 20 mm limestone enhanced matrix densification and ITZ quality, yielding more reliable mechanical performance. Among all mix proportions, the 50SA-50FA group (Group 3 in Table 7) showed most balanced performance, matching OPC in both compressive and flexural strength for mortar and concrete. While 30SA–70FA concrete achieved compressive strength comparable to OPC, its poor tensile resistance limits its applicability in load bearing or crack-sensitive applications (Figure 34). Therefore, the 50SA-50FA group was selected as representative AAFS composition for advanced durability tests, including pull-out test and X-CT measurements. These findings highlight the importance of optimizing precursor composition and aggregate type in achieving balanced mechanical performance in AAFS systems.

5 Electrochemical Properties of AAFS

This chapter is based on a manuscript currently under review: **Feng Zhang**, Shangtong Yang, Xun Xi, Guijie Sang, Chun-Qing Li, ‘Chloride-Ingress Induced Corrosion in Reinforced Alkali-Activated Mortars: Electrochemical Behaviour and Interface Properties’, submitted to Construction and Building Materials.

5.1 Introduction

The electrochemical measurement results, including the evolution of E_{corr} values from OCP measurements and R_p values from LPR measurements over time, are presented and analysed in this chapter. These two parameters provide valuable insights into the corrosion behaviour of reinforced AAFS mortars and serve as indicator for corrosion assessment. Based on these parameters, the free and bound chloride content in the corrosion zone is measured once corrosion initiation is detected. Additionally, the Tafel constant B values, determined using the Tafel extrapolation method, are calculated and analysed for samples under both passive and active conditions.

To gain a deeper understanding of the factors influencing the electrochemical behaviour of reinforced AAFS mortars, the effects of calcium content, efflorescence caused by alkali leaching, and sulphide products on E_{corr} values are analysed and discussed. Finally, based on the electrochemical data obtained, a corrosion determination criterion is proposed for reinforced AAFS mortars.

5.2 Corrosion Potential (E_{corr}) and Polarisation Resistance (R_p)

Due to the absence of a fully established criterion for corrosion assessment in AAFS system, the interpretation of E_{corr} values based on ASTM C876 [195], which was originally developed for OPC concrete, as shown in Table 3, may be unreliable. Therefore, manual inspection was conducted on some specimens to verify the actual condition of the embedded steel, despite their E_{corr} values fell within the low-corrosion-risk range. In addition, a few specimens failed

due to poor electrical connection, likely caused by insufficient soldering of the copper wire onto the rebar. As a result, the actual number of valid samples was lower than the total samples initially described in Section 3.3. Therefore, the remaining samples were re-labelled, as shown below:

Table 16. Re-label of samples for each mix group

Group	Sample number
100SA	S1, S2, S3, S4, S5
70SA-30FA	S6, S7, S8, S9, S10
50SA-50FA	S11, S12, S13, S14, S15
30SA-70FA	S16, S17, S18, S19, S20
100FA	S21, S22, S23, S24
OPC	S25, S26, S27, S28, S29, S30

Figure 44 to Figure 49 illustrate the evolution of E_{corr} and R_p values over time for five groups of reinforced AAFS mortars and the reinforced OPC mortar reference group. These figures provide insights into the influence of material properties, particularly microstructure, on these parameters. In addition, images of the steel rebar's surface condition, obtained from split samples after corrosion initiation, are presented alongside the graphs to provide a visual correlation with the electrochemical results.

From these figures, the average passive E_{corr} values for reinforced AAFS mortars on day 0 are as follows (Figure 44 to Figure 48): approximately $-153 \text{ mV}_{\text{SCE}}$ for the 100SA samples, $-129 \text{ mV}_{\text{SCE}}$ for the 70SA-30FA samples, $-115 \text{ mV}_{\text{SCE}}$ for the 50SA-50FA samples, $-110 \text{ mV}_{\text{SCE}}$ for the 30SA-70FA samples, and $-123 \text{ mV}_{\text{SCE}}$ for the 100FA samples. The increasing trend in E_{corr} values from high-calcium to low-calcium samples (except for 100FA samples), as shown in Figure 43, is attributed to the progressive evolution of samples' microstructure. As the SA content decreases, the gel transitions from a more compact form to a more porous one ($\text{C-A-S-H} \rightarrow \text{C-(N)-A-S-H} \rightarrow \text{N-(C)-A-S-H}$), increasing the porosity, as described in Section 2.1. This transition facilitates the movement of electrolytes within the binder, reducing binder resistivity and increasing conductivity, thereby changing the E_{corr} values [293,294].

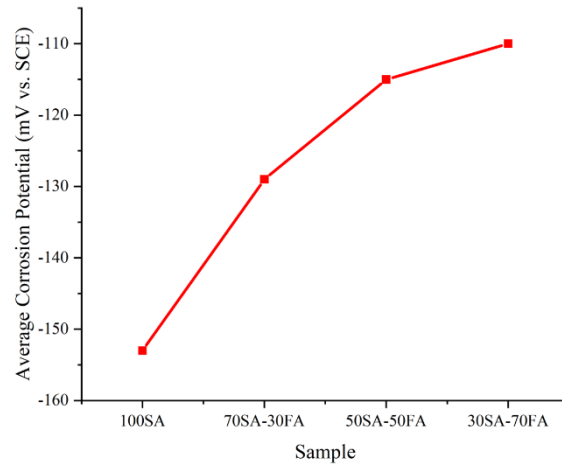


Figure 43. Increasing trend in E_{corr} from high-calcium to low-calcium samples

While most samples exhibit a trend correlating SA content with E_{corr} values, 100FA samples deviate from this pattern, displaying an E_{corr} value slightly more negative than those of 30SA-50FA and 50SA-50FA samples. This difference can be attributed to the dominance of N-A-S-H gel in the 100FA samples, characterised by its more porous microstructure. This porous structure allows aggressive ions, such as Cl^- ions, to penetrate the binder more easily than in the denser N-(C)-A-S-H gel. During the stabilisation period for the sample in the three-electrode system, the ingress of aggressive ions increases local electrochemical activity, ultimately resulting in the more negative E_{corr} value observed [30,295,296].

The average E_{corr} value for the reinforced OPC reference mortar group on day 0 is approximately $-160 \text{ mV}_{\text{SCE}}$, as depicted in Figure 49. As stated in Section 2.1, the C-S-H gel formed in OPC has properties similar to C-A-S-H gel in high-calcium AAFS samples, though it is slightly less dense, which may affect ion mobility of [13,175]. Furthermore, the pore solution chemistry in OPC ($\text{Ca}(\text{OH})_2$) differs significantly from that in AAFS (NaOH) [141]. Specifically, the presence of $\text{Ca}(\text{OH})_2$ in OPC could react with Cl^- ions to form Friedel's salt during the equilibrium stage in the three-electrode system, thereby reducing the mobility of free Cl^- ions [174]. The less dense microstructure and unique pore solution chemistry together

contribute to the more negative E_{corr} values observed in reinforced OPC mortars by enhancing ion mobility and electrochemical activity.

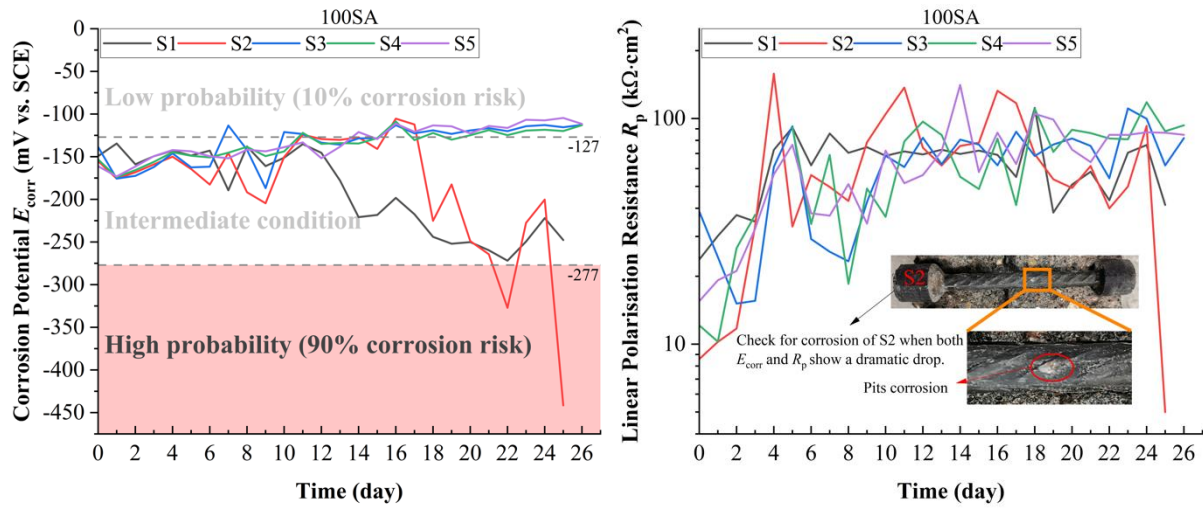


Figure 44. Evolution of E_{corr} and R_p values over time for 100SA samples

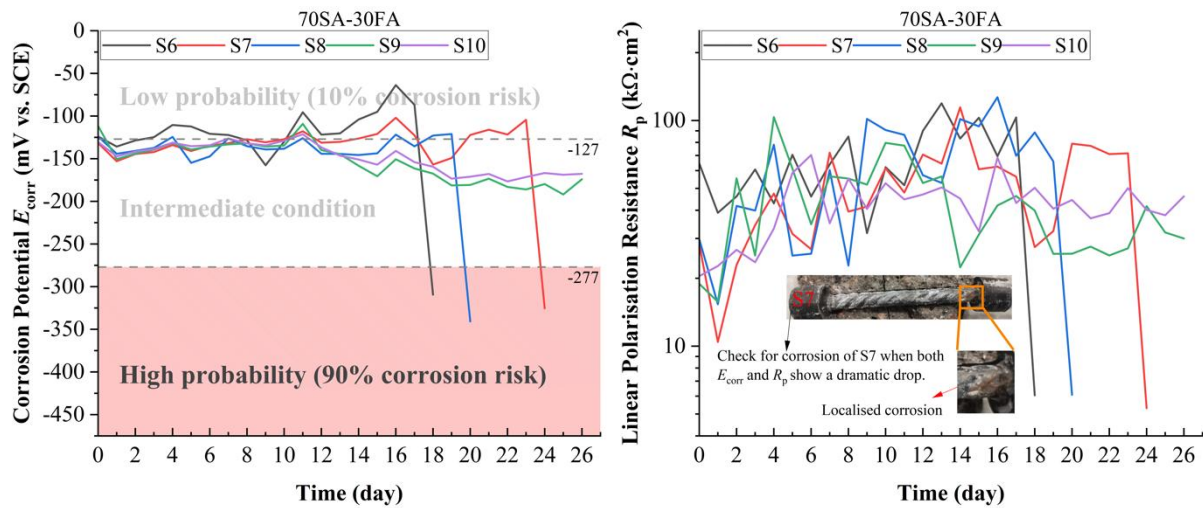


Figure 45. Evolution of E_{corr} and R_p values over time for 70SA-30FA samples

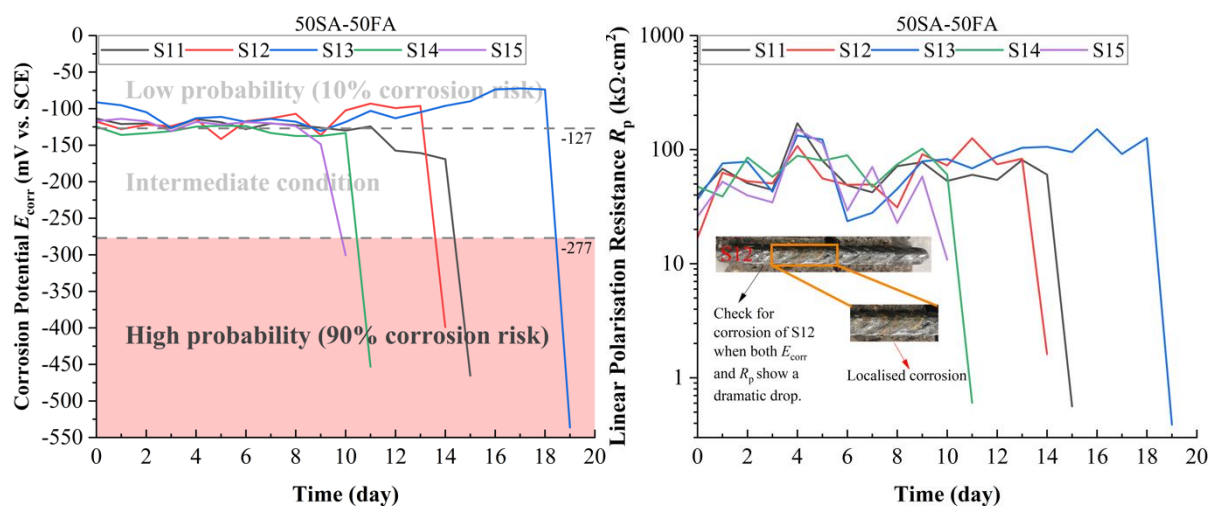


Figure 46. Evolution of E_{corr} and R_p values over time for 50SA-50FA samples

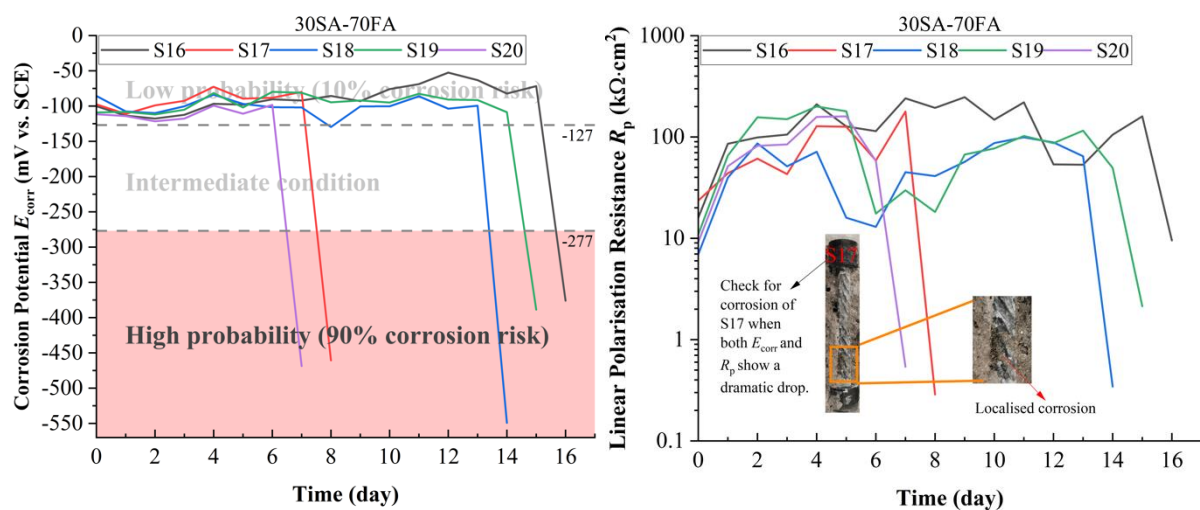


Figure 47. Evolution of E_{corr} and R_p values over time for 30SA-70FA samples

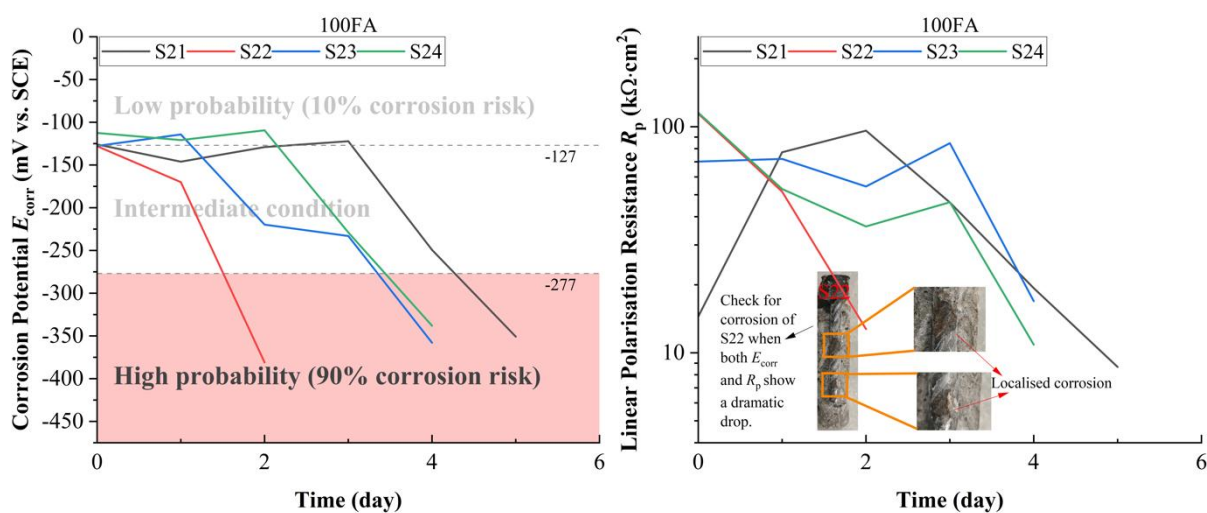


Figure 48. Evolution of E_{corr} and R_p values over time for 100FA samples

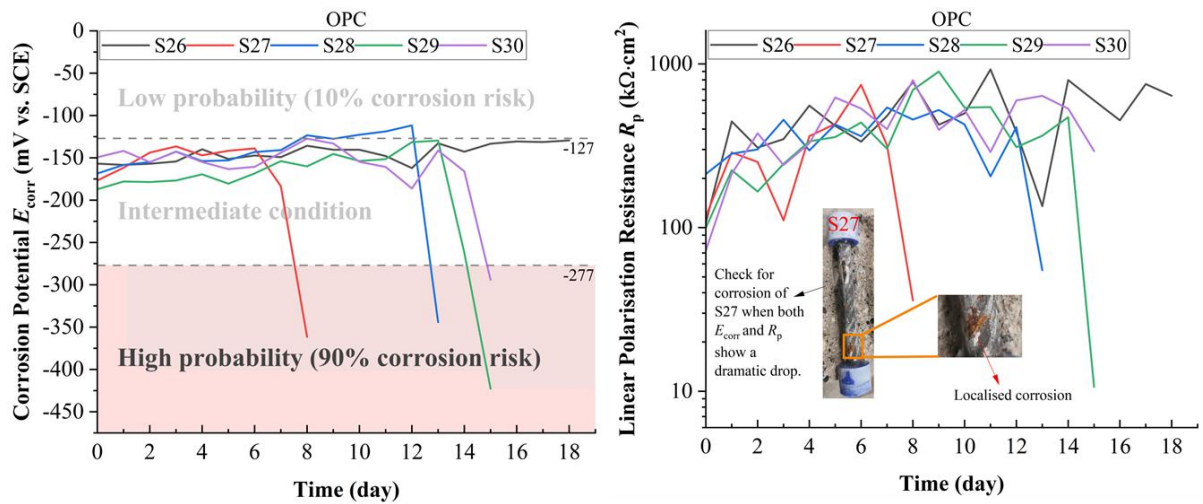


Figure 49. Evolution of E_{corr} and R_p values over time for OPC samples

After the accelerated corrosion process begins, the overall E_{corr} values for specimens in each group remain relatively stable throughout the test period, indicating that the samples maintain a sound electrochemical condition. The evolution of E_{corr} values over time, particularly their sharp drop from the low to high corrosion risk zone, will be further analysed in the next section in relation to corrosion initiation.

For the evolution of R_p values, significant oscillations are observed, as illustrated in Figure 44 to Figure 49. An increase in R_p values is observed in all groups except the 100FA group during the initial days of the w/d cyclic accelerated corrosion process. This increase is attributed to the reaction of unreacted particles in the binder matrix, driven by the thermal energy during the drying stage of the w/d cycles [71,72]. The drying process at 50 °C acts as a short-duration elevated temperature curing step, promoting polycondensation and integration of newly formed gel into the binder matrix. This results in a more homogenous matrix [297,298], limiting ions mobility within the sample. Consequently, an increase in R_p values is observed.

In contrast, the 100FA samples, composed solely of N-A-S-H gel, lack SA content and therefore have lower calcium content in the precursors. This absence inhibits the formation of C-A-S-H gel, which significantly reduces porosity during the polycondensation process. The effect of C-A-S-H gel is evident in compressive strength, as shown in Figure 34, where the 30SA-70FA

mortars exhibit significantly higher compressive strength than the 100FA mortars. As a result, R_p values in 100FA samples show minimal change, reflecting the limited influence of the polycondensation process.

The subsequent oscillation in R_p values after the initial increase during the first few days can be attributed to sample deterioration. During the accelerated corrosion process, frequent alternation between wetting and drying environments introduces several issues that deteriorate the samples' properties. These issues are detailed in Section 2.2.3. The first issue is the development of shrinkage cracks, which result from both autogenous shrinkage [68,130,131] and drying shrinkage [80,132,133], as detailed in Section 2.2.3.1. These cracks significantly accelerate the ingress and diffusion of Cl^- ions into the mortar, compromising the material's durability [155]. The second issue is the leaching of alkali ions [56,154], as described in Section 2.2.3.2. This leaching causes recrystallisation of alkali ions on the mortar surface (efflorescence) and their precipitation within pores (subflorescence) [152]. These behaviours damage the pore network and cause surface spalling, compromising the integrity and altering the conductivity of the mortar samples, as shown in Figure 50.

These behaviours ultimately reduce the conductivity of the mortar matrix. Additionally, the ingress of Cl^- ions modifies the conductivity by increasing the ionic concentration within the pores, which changes the electrochemistry balance of the pore solution and impacts the overall matrix behaviour. The combined effect of these factors explains the significant oscillations observed in the R_p values during the accelerated corrosion process.

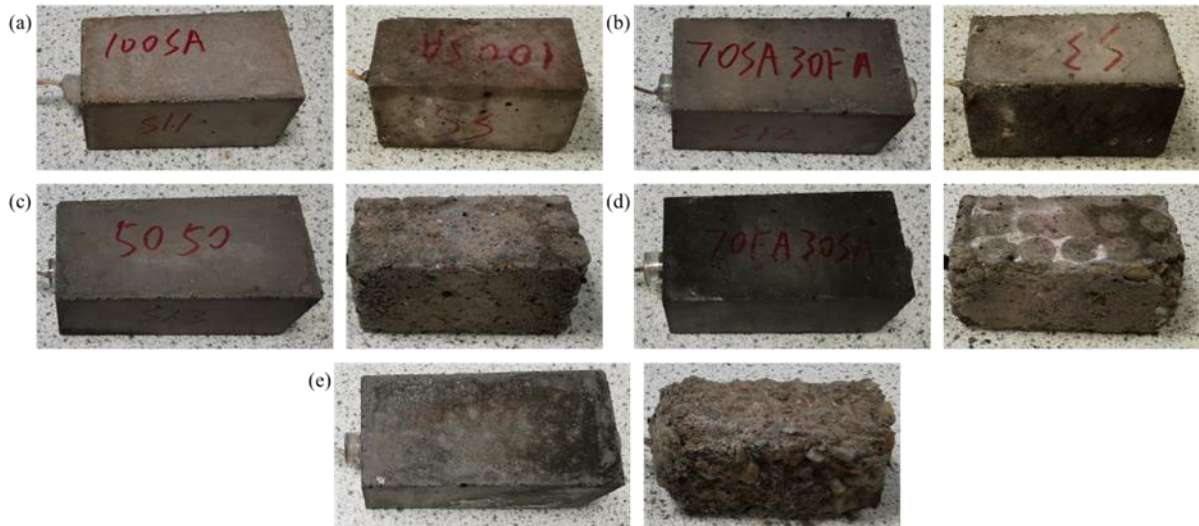


Figure 50. Effect of efflorescence for electrochemical sample before (left) and after (right) w/d cyclic accelerated corrosion under the same time: a) 100SA sample; b) 70SA-30FA sample; c) 50SA-50FA sample; d) 30SA-70FA sample; e) 100FA sample

5.3 Corrosion Initiation and Chloride Threshold (C_{crit})

5.3.1 Corrosion Initiation Determination

This section is focused on the corrosion initiation of reinforced AAFS mortars, particularly in relation to E_{corr} values. Figure 44 to Figure 49 indicate that the E_{corr} values for the five reinforced AAFS mortar groups initially remained within the low corrosion risk zone, according to the corrosion determination criterion from ASTM C876 [195], as shown in Table 3. A few days after the start of the accelerated corrosion procedure, the 100FA group exhibited a dramatic drop in E_{corr} values, transitioning from the low to high corrosion risk zone, accompanied by a corresponding decline in R_p values. These decreases in both E_{corr} and R_p values resulted from the breakdown of the high-resistance passive film on the rebar surface, which exposes the rebar to a corrosive environment and causes more negative E_{corr} values and lower R_p values. Subsequently, Tafel extrapolation measurements were conducted, and then the samples were split to visually inspect the embedded steel rebar. Figure 48 shows clear evidence of pitting and localised corrosion on the rebar surface. As the accelerated corrosion process continued, the same procedure was applied to the other groups, all of which revealed corrosion on the rebar surface.

These observations confirm that the corrosion determination criterion in the ASTM C876 [195] is applicable for assessing corrosion in reinforced AAFS mortars. Furthermore, the timing of the sudden drop in E_{corr} and R_p values during the accelerated corrosion period suggests that corrosion resistance improves with increasing SA content in the precursors. This improvement is attributed to the formation of a more compacted and tortuous microstructure and the increased chloride-binding phases associated with higher SA content, as described in Section 2.3.3. Specifically, the 50FA-50SA group demonstrated corrosion resistance comparable to the OPC reference group (Figure 46 and Figure 49), as evidenced by the similar trends in E_{corr} and R_p value reductions. Moreover, the compressive strengths of these two types of mortars are also comparable, as shown in Table 11. Therefore, AAFS mortar with approximately 50% SA content in the precursors demonstrates significant potential as a replacement for OPC mortar. Although higher SA content (above 50%) enhances corrosion resistance (Figure 44 and Figure 45) and compressive strength (Table 11), the increased risk of shrinkage cracks, as described in Section 2.2.2, may limit its practical application.

5.3.2 Chloride Threshold

As described in Section 3.4.1, both free and bound chloride contents were measured in the region surrounding the corrosion site at the time of corrosion initiation. Table 17 presents the results for free and bound chloride contents for five types of reinforced AAFS mortars. Due to the relatively small bound chloride content in these samples, the total chloride content is considered as the C_{crit} . Results for reinforced OPC mortars are not included in this study, as extensive research has already been established a critical chloride threshold of approximately 0.4 wt.% for OPC, as detailed in Section 2.3.3.3.

From Table 17, it is observed that the 100SA samples exhibit lowest values for both free and bound chloride contents among all groups. The free chloride content ranges from 0.06 to 0.10 wt.%, while the bound chloride content ranges from 0.01 to 0.03 wt.%. This suggests that the

passive film formed on the steel surface is unstable, making it more vulnerable to Cl^- attack. In contrast, the 100FA samples exhibit the highest free and bound chloride contents, nearly nine times higher than those of 100SA group. The free chloride content ranges from 0.53 to 0.98 wt.%, and the bound chloride content ranges from 0.05 to 0.07 wt.%, indicating the formation of a compact passive film on the steel surface. However, these observations contrast with the corrosion behaviour shown in Figure 44 to Figure 49. The trend indicates that both free and bound chloride contents increase as the SA content decreases, which is inversely related to chloride resistance, as discussed in Section 5.2.

Table 17. Free and Bound Chloride for five kinds of AAFS mortars

AAFS Mortar	Free Chloride	Bound Chloride	Total Chloride (C_{crit})
100SA	0.06 - 0.10	0.01 - 0.03	0.07 - 0.13
70SA-30FA	0.10 - 0.16	0.02 - 0.05	0.12 - 0.21
50SA-50FA	0.21 - 0.42	0.02 - 0.07	0.23 - 0.49
30SA-70FA	0.38 - 0.61	0.03 - 0.04	0.53 - 0.65
100FA	0.53 - 0.98	0.05 - 0.07	0.58 - 1.05

The variation in chloride content within the binder matrix is primarily attributed to the microstructure differences between C-A-S-H gel and N-A-S-H gel, particularly in terms of porosity and tortuosity. As described in Section 2.1 and 2.3.3, the tortuous, compact microstructure of C-A-S-H gel [8,39], combined with secondary phases such as Mg-Al LDHs in high-calcium AAFS mortars [299,300], enhances chloride resistance through physical adsorption and chemical binding. Consequently, the migration rate of chloride ions in high-calcium AAFS mortars is significantly lower than in low-calcium AAFS mortars, as reported by Babaee and Castel [111].

Moreover, this tortuous and compact microstructure also limits the transport of other substances, such as O_2 . As reported by Balcikanli and Ozbay [301] and Bondar et al. [302], the oxygen permeability in AASA concrete ranges from $1.56 \times 10^{-17} \text{ m}^2$ to $5.33 \times 10^{-17} \text{ m}^2$, compared to $1.5 \times 10^{-17} \text{ m}^2$ to $5 \times 10^{-17} \text{ m}^2$ in natural pozzolan (NP) concrete. Both are significantly lower than the $7.4 \times 10^{-16} \text{ m}^2$ reported for OPC concrete [303]. Additionally, sulphides in SA precursors

(e.g., 0.62% in SA, as shown in Table 6) react with oxygen more effectively than iron, reducing oxygen availability at the SMI and affecting the formation of the passive film [198]. Reaction products formed between sulphides and oxygen can precipitate on the rebar surface and integrate with the passive film [191,234], resulting in a porous and non-compact structure that decreases its protective capability. Consequently, the passive film in high-calcium reinforced AAFS mortars becomes less protective, resulting in a lower C_{crit} value, as evidenced by the experimental findings (Table 17).

5.4 Tafel Constant B Values

Table 18 presents the Tafel constant B values for five types of reinforced AAFS mortars under both passive and active conditions. It is observed that B values increase as the SA content decreases in the precursors under both conditions. Under passive conditions, B values range from 16 to 25 mV, aligning with the trends reported by Babae and Castel [111] and Runci et al. [204], although differences in specific ranges are observed:

- For the 100SA samples and 50SA-50FA samples, passive B values range from 16-18 mV and 19-24 mV, respectively. This contrasts with the findings of Runci et al. [204], who reported B values of 25 mV for the 100SA samples and 14-16 mV for 50SA-50FA samples.
- For the low-calcium groups, including the 100FA and 30SA-70FA samples, passive B values range from 21-25 mV, which are higher than the 14-20 mV range reported by Babae and Castel [111] for FA-dominated samples.

Under active conditions, the 100SA samples exhibit the lowest B values, ranging from 39-41 mV, while samples in the other groups fall within a range of 52-64 mV. Although the active B values for the 100SA samples are higher than those in the passive condition, they remain the lowest among all groups. This is primarily attributed to the limited oxygen concentration at the SMI. The Tafel extrapolation method involves polarising the rebar out of equilibrium in the

redox reaction by applying an external voltage, allowing either the anodic or cathodic reaction to dominate. Since the reduction reaction at the cathode requires oxygen, as shown in Eq. 3, however, the compact and tortuous microstructure significantly hinders oxygen diffusion within the sample [301]. Consequently, the cathodic reduction reaction quickly shifts to the anodic oxidation due to the insufficient oxygen at the SMI. The SEM-EDS results at the SMI, discussed in Section 6.2.2, further support this conclusion regarding the impact of limited oxygen on electrochemical behaviour.

To better illustrate this behaviour, Figure 51 shows an example of the Tafel curve under both passive and active conditions. Under passive conditions, the cathodic region is smaller than the anodic region, even during the cathodic scan. This behaviour indicates that the anodic oxidation reaction dominates due to insufficient oxygen for the cathodic reduction reaction. The lack of oxygen gradually decreases the rate of the reduction reaction, eventually making it slower than the anodic rate. As a result, the cathodic Tafel slope (β_{c-p}) is significantly smaller than the anodic Tafel slope (β_{a-p}), resulting in low B values, which reflect the anodic reactions. Additionally, the polarisation scan is controlled by the potentiostat, ensuring current balance throughout the system. Therefore, even if the cathodic current density decreases, the system's overall current remains balanced due to the potentiostat's effect.

Under active conditions, the cathodic region becomes larger than in the passive condition, as shown in Figure 51. Several factors contribute to this phenomenon:

- The breakdown of the passive film lowers the electrical resistance at the SMI, facilitating electron flow.
- Shrinkage and efflorescence effects, as described in Section 2.2.3, result in microcracks and connected pores. These structural changes facilitate oxygen transport in the mortar compared to the passive condition.

All these factors contribute to the observed increase in B values for samples in active conditions.

Table 18. Tafel constant B values for five kinds of steel-reinforced AAFS groups

Group	Passive Condition			Active Condition		
	β_a , mV/decade	β_c , mV/decade	B (mV)	β_a , mV/decade	β_c , mV/decade	B (mV)
100 SA	312.66	42.33	16.19	450.33	113.18	39.27
	182.19	82.13	24.58	322.41	109.99	35.61
	145.26	52.03	16.63	219.42	164.75	40.86
	168.78	55.91	18.24	440.54	167.45	52.68
70 SA-30 FA	109.11	70.34	18.57	226.66	282.46	54.60
	119.58	67.84	18.79	259.59	232.20	53.22
	121.41	70.92	19.44	276.23	251.91	57.21
	106.48	68.15	18.04	306.49	288.63	64.54
	110.33	65.41	17.83	273.42	181.64	47.39
50 SA-50 FA	141.60	74.33	21.17	247.25	274.54	56.49
	163.11	87.30	24.69	230.56	249.27	52.01
	129.77	69.42	19.64	134.17	267.27	38.79
	129.92	77.40	21.06	427.84	172.08	53.29
	159.17	81.00	23.31	183.37	302.57	49.58
30 SA-70 FA	144.91	79.96	22.37	177.48	407.81	53.70
	123.34	85.09	21.86	209.13	376.91	58.40
	126.86	81.87	21.61	269.38	277.25	59.33
	132.07	87.31	22.82	261.75	262.65	56.93
	139.66	85.81	23.08	177.69	331.37	50.22
100 FA	153.68	89.20	24.51	291.82	217.14	54.06
	113.50	101.30	23.24	368.01	262.50	66.53
	113.18	69.92	18.77	241.14	261.71	54.50

Since the widely accepted empirical B values for OPC are 26 mV under active conditions and 52 mV under passive conditions, OPC samples were not included in this research. To better understand the distribution of B values for reinforced AAFS mortars, Figure 52 presents a histogram showing B values across five AAFS groups under both passive and active conditions. The distribution peak for B values in the passive condition falls within the range of 20-22 mV, while the peak in the active condition lies between 50-55 mV. These values deviate significantly from the empirical values for OPC, as originally proposed by Andrade and Gonzalez [201]. This deviation can be attributed to differences in the test environments. Specifically, the saturated calcium hydroxide solution used in their tests creates a homogeneous environment with relatively higher oxygen availability. In contrast, the complex microstructure of the AAFS mortar matrix restricts oxygen transport. Consequently, the limited oxygen

availability at the SMI is considered the primary factor causing the variation in B values between reinforced OPC and AAFS mortars.

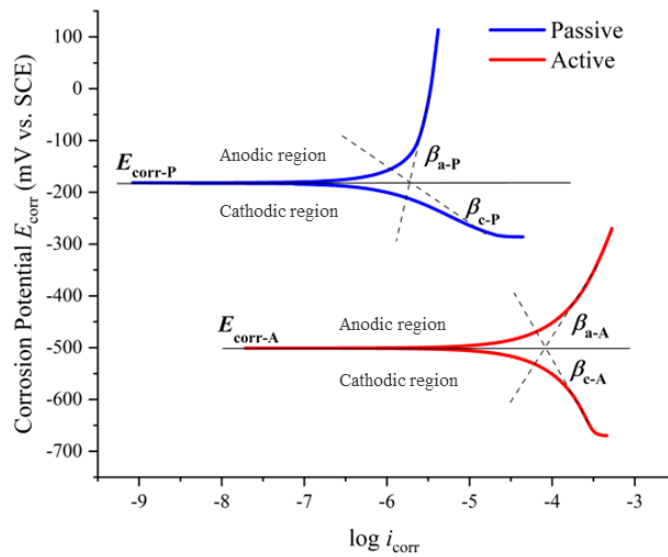


Figure 51. Difference in the Tafel plot for steel-reinforced AAFS mortar under passive and active conditions

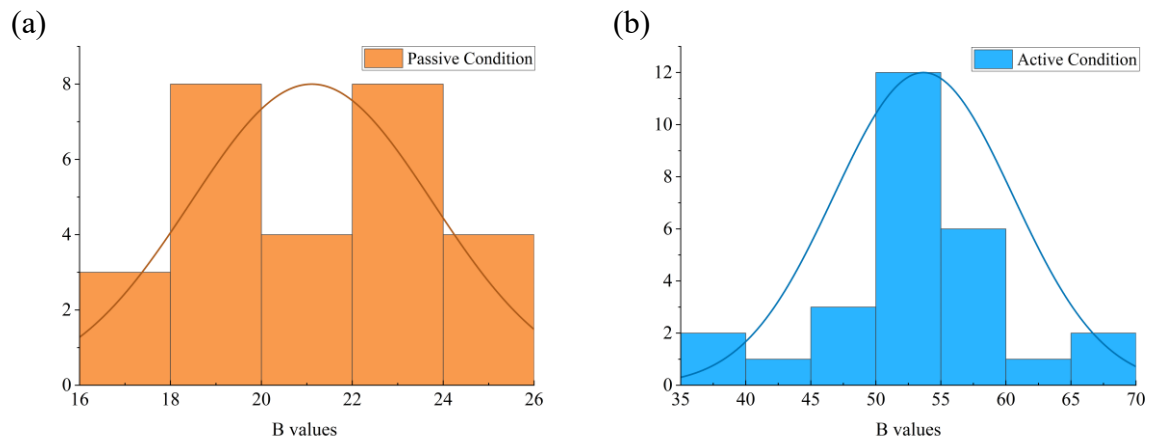


Figure 52. Distribution of Tafel constant B values for steel-reinforced AAFS mortars at (a) passive condition; (b) active condition

5.5 Discussion

Based on the experimental results of this study, the corrosion determination criterion from ASTM C876 [195] for E_{corr} values, originally designed to distinguish between passive and active conditions in reinforced OPC concrete, has been adapted to suit reinforced AAFS mortars. This adaptation is made in conjunction with the Tafel constant B values, as shown in Table 19. For passive conditions, a E_{corr} value of $-300 \text{ mV}_{\text{SCE}}$ was selected based on previous

studies (as listed in Section 2.4), along with R_p values exceeding $60 \text{ k}\Omega\cdot\text{cm}^2$, considering the variations in precursor chemistry and mix proportions.

Table 19. An adaption from ASTM C876 for corrosion determination to suit for steel-reinforced AAFS mortars measured under non-saturated condition

E_{corr} (mV vs. SCE)	R_p ($\text{k}\Omega\cdot\text{cm}^2$)	Corrosion Risk	Tafel constant B (mV)
$E_{corr} > -300$	$R_p > 60$	Passive condition	$20 < B < 22$
$-300 < E_{corr} < -350$	$10 < R_p < 60$	Uncertainty corrosion	
$E_{corr} < -350$	$R_p < 10$	Active condition	$50 < B < 60$ (SA < 70%)
			$35 < B < 40$ (SA \geq 70%)

For active conditions, most E_{corr} and R_p values for corroded reinforced AAFS mortars were below -350 mV_{SCE} and $10 \text{ k}\Omega\cdot\text{cm}^2$, as illustrated in Figure 44 to Figure 48. Consequently, these thresholds were selected as the corrosion line, where regions below this line correspond to a 90% corrosion risk. Based on the distribution of Tafel constant B values (Figure 52), B values ranging from 20 to 22 mV for passive conditions and 50 to 60 mV for active conditions were reasonably selected. However, for reinforced AAFS mortar with a high SA content (over 70%), these ranges should be adjusted downward to approximately 35 to 40 mV.

Regarding E_{corr} values, several studies have reported they dropping to approximately -600 mV_{SCE} within a few days of exposure to saltwater, tap water, or other solutions, indicating a 90% corrosion risk according to the determination criterion [21,198,304]. These extremely low E_{corr} values have been attributed to the presence of sulphide in precursors, which consumes oxygen and disrupts the stability of the passive film on the rebar surface. However, it is worth noting that sulphide films (e.g., FeS) on the steel surface have only been observed in controlled experiments where the rebar was immersed in simulated pore solutions of AAMs [191,234]. Such simulated environments are relatively homogeneous and oxygen-rich, which contrast sharply with the complex and heterogeneous microstructure of AAFS mortar or concrete, where the transport of substances, particularly oxygen, is significantly restricted [301,302].

This raises concerns about the direct applicability of sulphide-related mechanisms observed in idealised systems to actual AAFS materials.

To evaluate the practical relevance of the E_{corr} values-based corrosion criterion, comparative experiments were conducted with samples exposed to two conditions: immersion in 3.5% saltwater and tap water. For simplicity, only three mix ratios were selected: 100SA, 50SA–50FA, and 100FA, representing the transition of gel types from C-A-S-H to N-A-S-H, with 50SA–50FA as the intermediate C-(N)-A-S-H system.

As shown in Figure 53, immersed samples are compared with those stored in the environmental chamber. The results show that immersed samples exhibited a sharp drop in E_{corr} , falling between $-600 \text{ mV}_{\text{SCE}}$ to $-700 \text{ mV}_{\text{SCE}}$ within just a few days. In contrast, samples exposed to w/d cycles maintained significantly higher E_{corr} values. Importantly, visual inspection of the steel rebar after 10 days revealed no visible corrosion on the rebar surface, despite their extremely negative E_{corr} values.

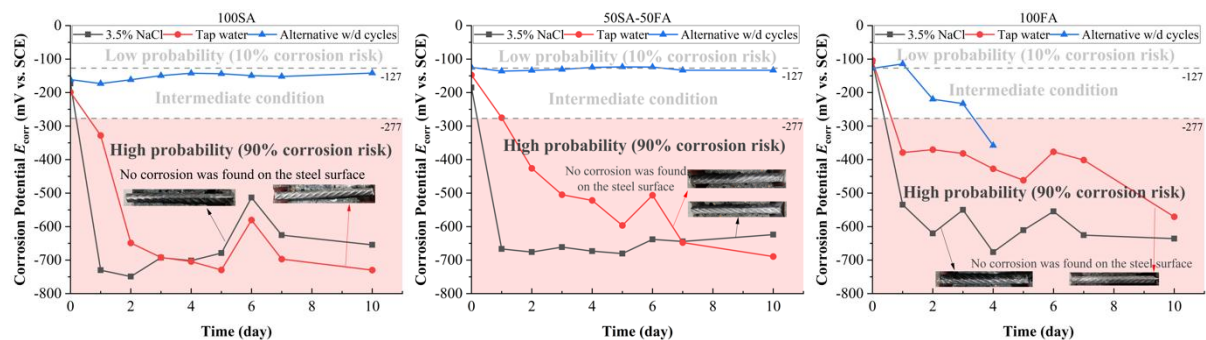


Figure 53. Comparison of the E_{corr} values for samples under different exposure conditions

These results suggest that low E_{corr} values observed under saturated conditions may not truly reflect the corrosion state of the embedded steel. In fact, the discrepancy points to differences in oxygen availability. Since the only variable between the two test conditions was the moisture state, it is reasonable to attribute the variation in E_{corr} values to oxygen concentration at the SMI. Figure 53 further confirms this: although the materials and mix proportions remained identical, immersed samples, which remained saturated, exhibited much lower E_{corr} values than

dried specimens. This supports the conclusion that oxygen transport, not sulphide reaction, is the dominant factor influencing E_{corr} values under these conditions [28,33,196]. Accordingly, the proposed corrosion criterion should be applied with caution and only under dry measurement condition, where oxygen transport is not impeded. Otherwise, E_{corr} value-based assessments may significantly overestimate corrosion risk in AAFS mortars.

Furthermore, limited O_2 availability at the SMI affects not only E_{corr} , but also other properties, such as the C_{crit} . As shown in Figure 44, pitting corrosion was observed in the 100SA sample, despite their low C_{rite} values (0.07 to 0.13 wt.%, Table 17) were significantly lower than the widely accepted C_{crit} value of 0.4 wt.% for reinforced OPC concrete [190]. This suggests that although the dense microstructure of 100SA samples offers high chloride resistance, it also restricts oxygen transports, weakening the stability of the passive film. As discussed in Section 5.3, decreasing SA content leads to a more porous matrix, improving oxygen diffusion to the steel surface and thereby increasing C_{crit} . Therefore, C_{crit} appears to be inversely proportional to chloride resistance, as it is governed by a trade-off between oxygen availability and microstructural compactness.

5.6 Summary

In this chapter, the electrochemical performance of steel-reinforced AAFS mortars subjected to the w/d cyclic corrosion in an environmental chamber was systematically analysed. The corrosion assessment criterion based on E_{corr} , originally developed for OPC systems, was found to be unreliable in AAFS systems, particularly under saturated conditions. Although previous hypotheses attributed E_{corr} reductions to sulphide reactions, experimental evidence from immersion tests and morphology analysis (as described in Section 6) revealed that oxygen availability at the SMI is the dominant factor affecting E_{corr} response. The study further demonstrated that low E_{corr} values may occur without steel bar corrosion due to oxygen deficiency rather than material degradation. This has significant implications for corrosion

assessment in AAFS structures, where dense microstructures may hinder oxygen transport despite high chloride binding capacity. As such, corrosion criteria for AAFS must be adapted to account for environmental factors, particularly saturation condition, rather than relying solely on E_{corr} -based thresholds. Therefore, an adapted corrosion criterion, valid under dry conditions, was proposed, offering improved reliability for interpreting E_{corr} results in AAFS systems.

6 Interfacial Behaviour Between Steel and AAFS

6.1 Introduction

This chapter begins with an analysis of the morphological and topographic features at the SMI for five types of AAFS mortars subjected to accelerated corrosion, using SEM-EDS analysis. This evaluation identifies two distinct corrosion mechanisms: microcell corrosion and macrocell corrosion. These findings are further supported by the X-CT measurements, which illustrate the spatiotemporal evolution of corrosion rusts and the associated deterioration of steel bars under identical accelerated corrosion conditions. Finally, the relationship between the bond strength of reinforced AAFS concrete and influencing factors, such as aggregate types and precursor materials, is thoroughly assessed.

6.2 SEM-EDS Analysis

6.2.1 Morphology and topographic analysis at the SMI

As described in Section 3.4.2, the morphological and topographic characteristics of SMI in five types of reinforced AAFS mortars were studied using SEM-EDS measurements. Two key features were investigated: the porous zone and the micro-gap. The porous zone refers to a discontinuous, loosely packed band with high porosity surrounding the reinforcement, which facilitates the diffusion of aggressive ions towards the steel surface. In contrast, the micro-gap is a narrow, dis-continuous gap formed primarily due to phenomena such as water bleeding, as introduced in Section 2.5.2. The thickness of micro-gap plays a crucial role in determining oxygen availability at the SMI, thereby influencing localised electrochemical reactions and corrosion behaviour.

BSE images of the analysed samples were used, including an overview image of the rebar and detailed images captured at four specific points to provide a comprehensive analysis of the SMI. For instance, in Figure 56, the overview image, the darker areas around the steel rebar represent the porous zone, which has high porosity. To quantify these regions, the software ImageJ was

employed to extract the porous zones and micro-gap around the rebar using grey value and thresholding methods. This process involved a fixed-size selection box to ensure consistency and precision in morphological quantification. However, in certain cases, the box size was adjusted to better accommodate the morphology of the SMI.

Figure 54 presents BSE images of the morphology at the SMI for the 100SA sample. From the overview image, porous band are visible at these points (A1 to A4), and the mortar matrix surrounding the rebar appears uniform. The formation of these porous zone may be attributed to drying shrinkage and the polycondensation process of the binder, as the sample underwent w/d cyclic accelerated corrosion in an environmental chamber. Points A1, A2 and A4 display morphological details at the SMI, including the rebar (white phase), the porous band (dark phase), and the mortar matrix (light grey phase), as labelled in A1. In addition, micro-gaps are visible between the porous band and the rebar surface. Since A2 and A4 show similar characteristics to A1, only A1 is labelled ensure clarity and avoid redundancy. Point A3 marks the boundary between the porous band and the surrounding mortar matrix, where distinct microcracks are observed. Microcracks are very fine cracks, typically ranging from a few micrometres to a few hundred micrometres in length, and are usually formed due to mechanical stress, thermal shrinkage, or chemical reactions. Unlike micro-gaps, which are discontinuities at the SMI primarily caused by water bleeding and poor interfacial bonding, microcracks propagate within the mortar matrix itself and may serve as pathways for ion ingress, potentially accelerating degradation. Furthermore, some microcracks are also visible within the porous band itself, likely resulting from the polycondensation process of newly formed binder gels in this region.

Figure 55 illustrates the porous band and micro-gap extracted from the BSE images using the ImageJ. Due to the irregular shape of the rebar, the porous bands are not perfectly straight, which adds complexity to the thickness measurement. As a result, some marked lines were

inclined to align with the porous bands' position, ensuring accurate thickness quantification. As shown in Figure 55, the thickness of the porous band varies significantly, ranging from 17 μm at its narrowest to 43 μm at its widest. This variation is attributed to the casting direction and vibration during the preparation process, which induced water bleeding and mortar settlement, leading to uneven distribution of mortar at the SMI, as described in Section 2.5.2. Additionally, the w/d cyclic accelerated corrosion may have further contributed to this variation by promoting the polycondensation process and localised shrinkage. The thickness of the micro-gap ranges from 388 nm to approximately 2.515 μm .

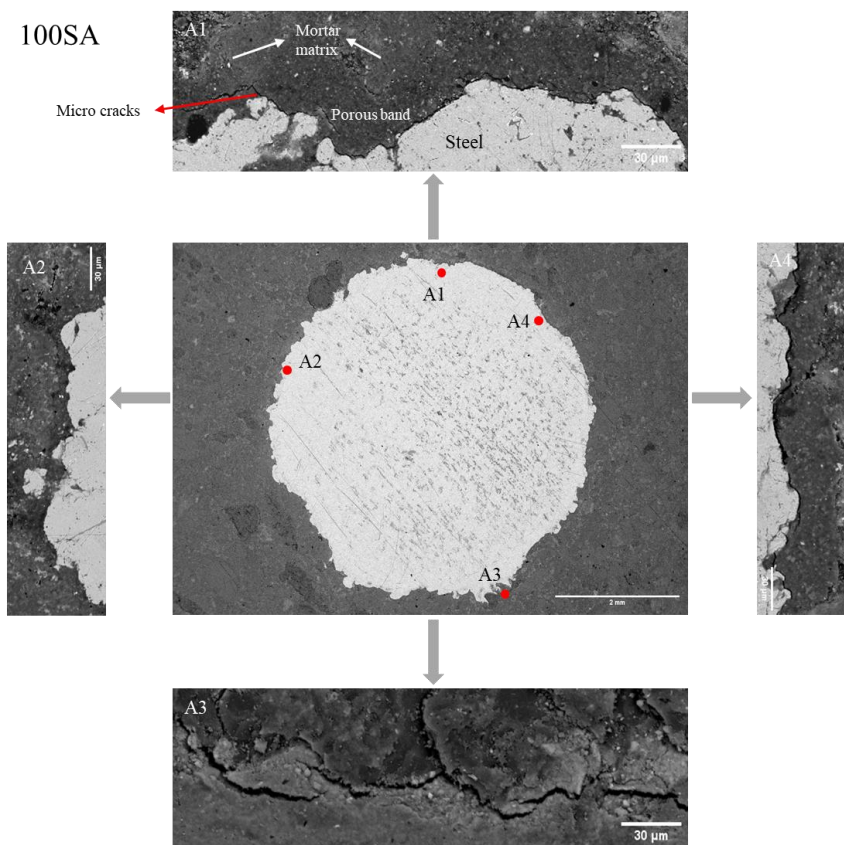


Figure 54. Morphology at the SMI for 100SA sample

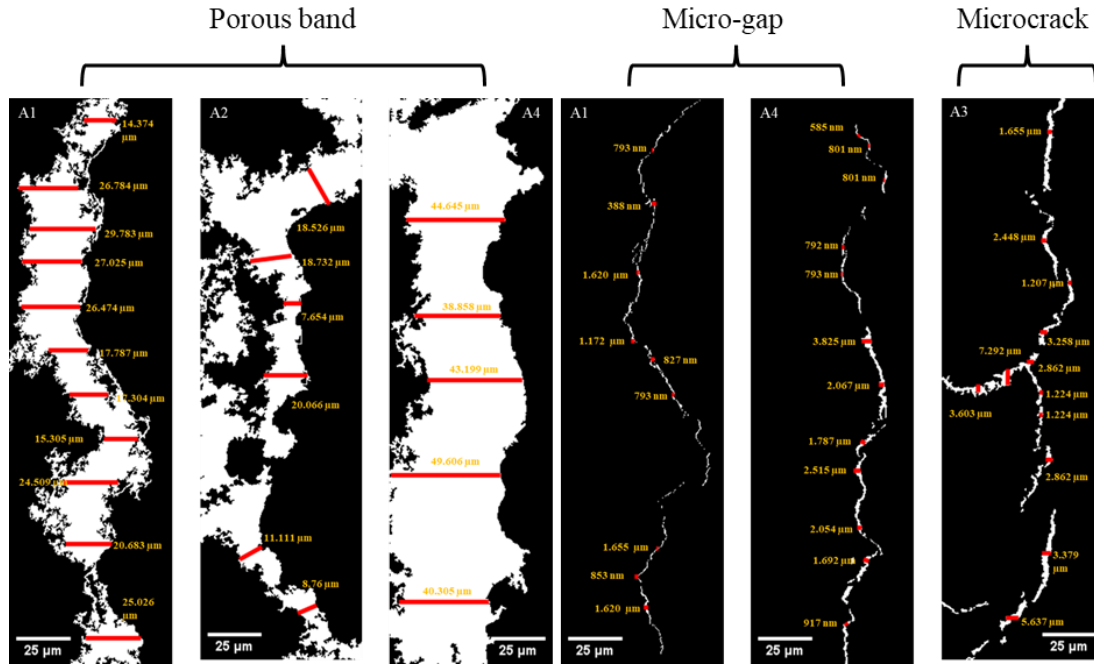


Figure 55. BSE images of porous band and micro-gap for 100SA sample after ImageJ processed

Figure 56 displays the BSE images of the 70SA-30FA sample, featuring an overview image of the rebar and detailed images captured at four specific points. From the overview image, the porous zones appear larger and more pronounced than those observed in the 100SA sample. This observation is further supported by Figure 57, which shows that the porous bands in the 70SA-30FA sample are thicker than those in the 100SA sample. The maximum thickness of the porous band in the 70SA-30FA sample is measured at 57 µm, which exceeds the largest value observed in the 100SA sample (43 µm).

Additionally, several large darker regions (porous region) around the reinforcement are observed. These regions may result from incomplete hydration caused by the uneven distribution of the alkaline activator and particle grains due to the “wall effect”. This phenomenon is evident at point B4, where an unreacted fly ash grain is observed within the porous band, clearly demonstrating the influence of the "wall effect".

Moreover, at point B2, a wide micro-gap measuring approximately 10 µm in thickness is observed between the large porous area and the rebar. This can be attributed to the

polycondensation process of the binder gel and the influence of the "wall effect", which leads to poor bonding between the binder and the rebar surface. In contrast to point B2, no micro-gaps or microcracks are observed at the SMI at the other presented points, indicating good bonding between the rebar and the AAFS mortar matrix.

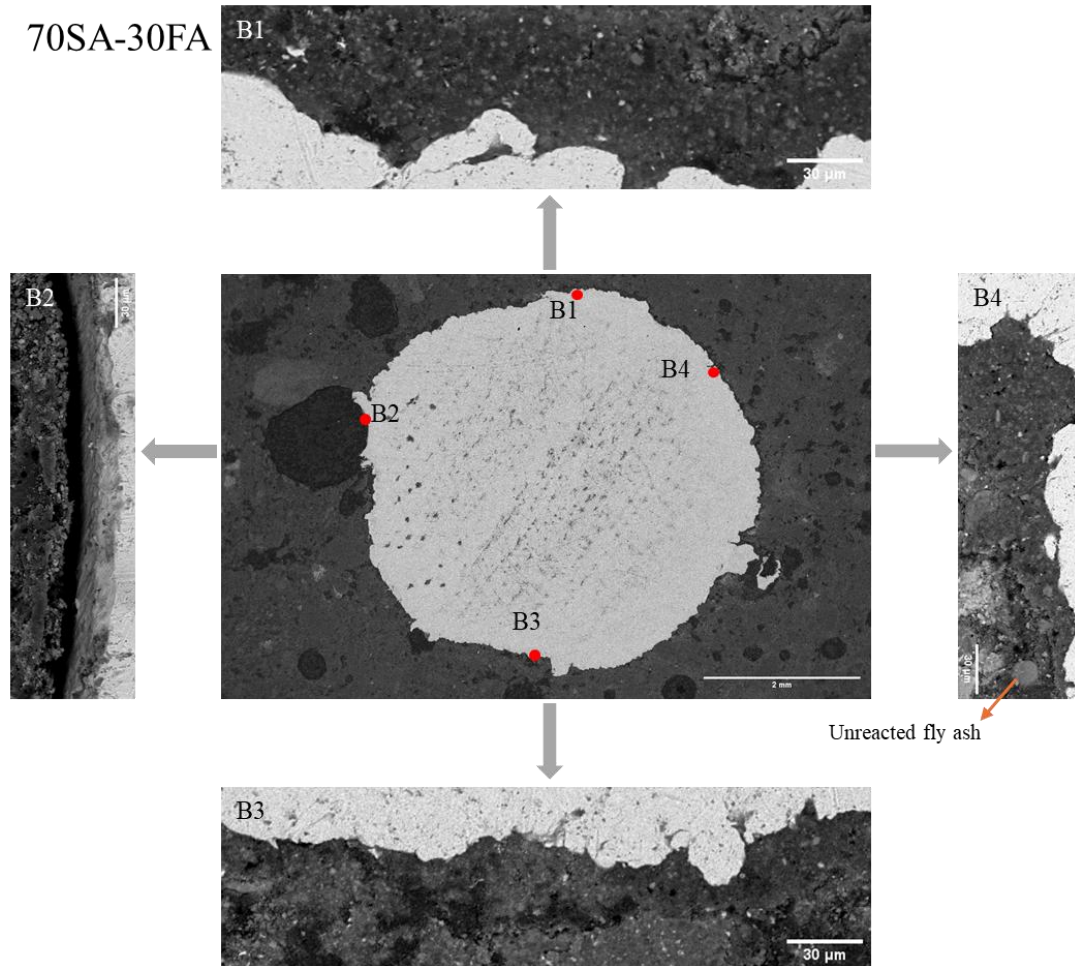


Figure 56. Morphology at the SMI for 70SA-30FA sample

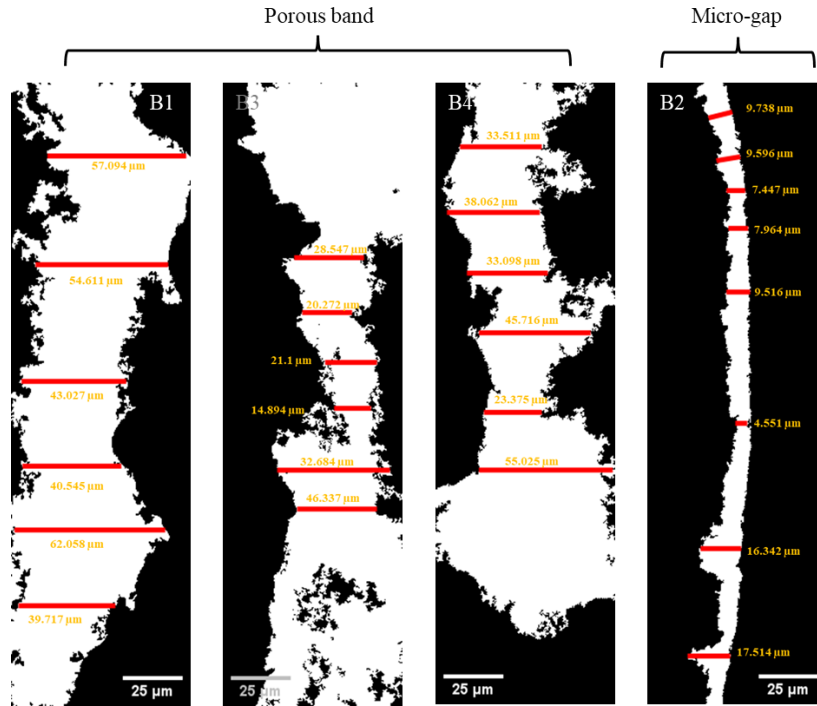


Figure 57. BSE images of porous band and micro-gap for 70SA-30FA sample after ImageJ processed

Figure 58 illustrates the BSE images of the 50SA-50FA sample, including an overview image of the rebar and magnified views at four specific points. From the overview image, the porous regions appear less distinct compared to those in the two previously discussed samples. At points C1 to C4, relatively few micro-gaps are observed at the interface between the porous band and the rebar, similar to the trend seen in the 70SA-30FA sample. However, microcracks are noticeable within the porous band, particularly at point C3. Additionally, a clear boundary line between porous band (dark phase) and mortar matrix (light-grey phase) is observed, with several microcracks present at this interface. Rough regions are observed around this boundary line, suggesting localised heterogeneity in this region. Figure 59 shows the extracted thickness of the porous band in the 50SA-50FA sample, as no visible micro-gaps are present. For point C1, C2, and C4, the porous band thickness is relatively uniform, ranging between 25 µm and 38 µm. However, at point C3, the maximum thickness for the porous bands increases significantly to 99 µm, nearly double that observed in the 70SA-30FA sample. This is likely a

result of the localised settling of the mortar matrix after casting, which leads to increased porosity and thickness in this region, as described in Section 2.5.2.

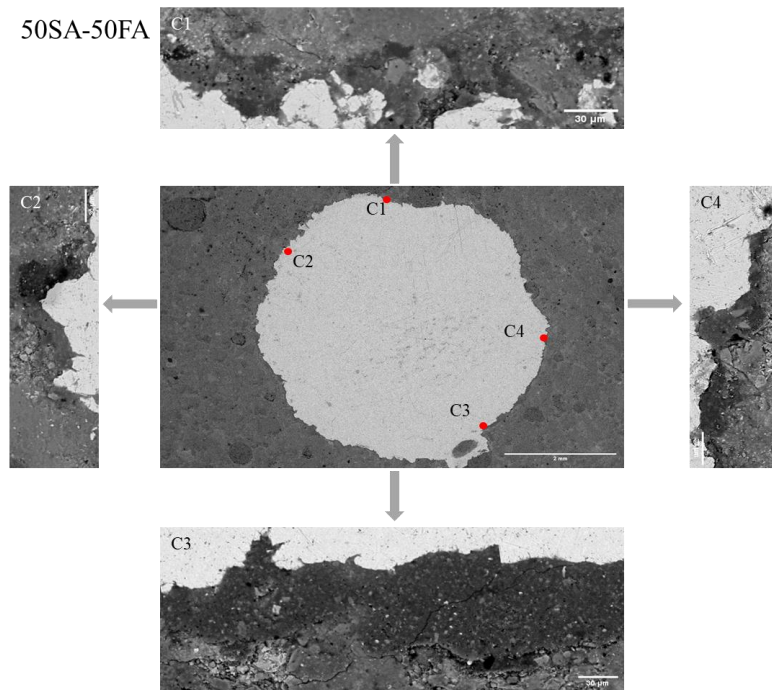


Figure 58. Morphology at the SMI for 50SA-50FA sample

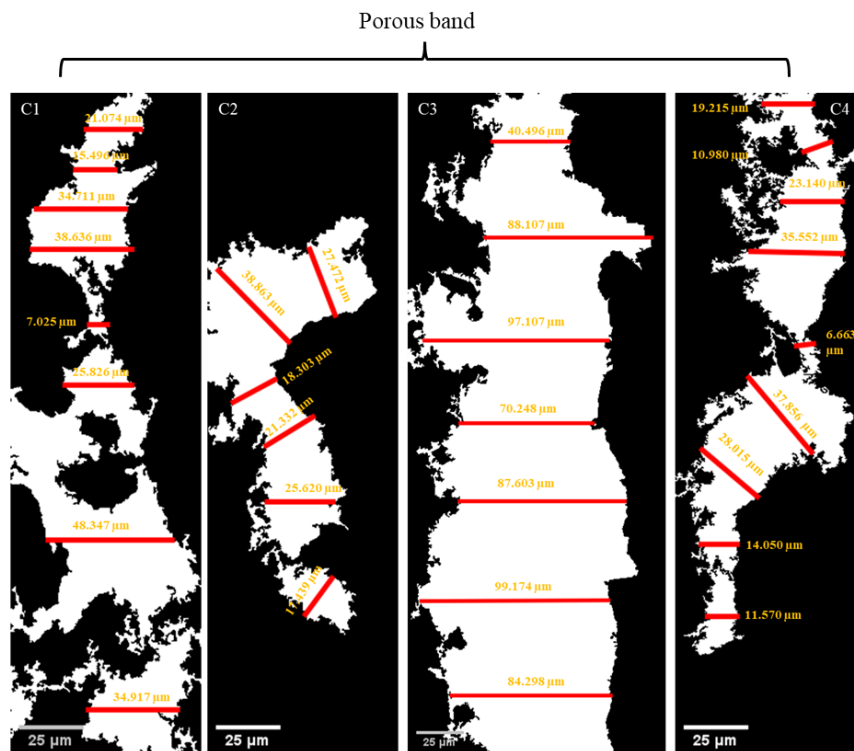


Figure 59. BSE images of porous band and micro-cracks for 50SA-50FA sample after ImageJ processed

Figure 60 presents the BSE images of the 30SA-70FA sample, consisting of an overview image of the rebar and detailed images at four specific points. In the overview image, the mortar matrix on the left side of the rebar appears significantly rougher, and the porous band surrounding the reinforcement has expanded compared to those in the previously discussed samples. The cause of this expansion will be discussed later in conjunction with the 100FA sample, as both samples exhibit similar surface morphology characteristics. At these four points, the micro-gap is clearly visible at the SMI. Points D1 and D2 exhibit larger micro-gap thicknesses, whereas the micro-gap at D3 is smaller. At D4, microcracks are observed within the porous bands.

The porous bands and micro-gaps at the SMI are extracted and displayed in Figure 61. The micro-gap at D3 is not included due to its minimal thickness, which is below the resolution limit for extraction. From this figure, the smallest thicknesses of the porous band and micro-gap are approximately 12 μm and 414 nm, respectively, while the largest thicknesses reach 86.5 μm . Compared to the other samples with higher SA content, the increased thickness of the porous band and micro-gap is attributed to the less compact microstructure, which arises from the low-calcium content and the dominance of N-A-S-H gel.

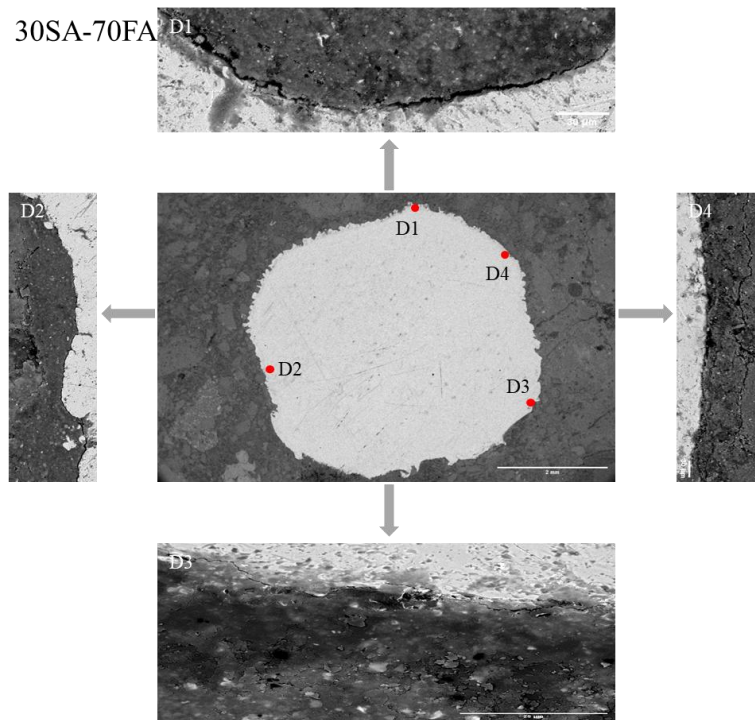


Figure 60. Morphology at the SMI for 30SA-70FA sample

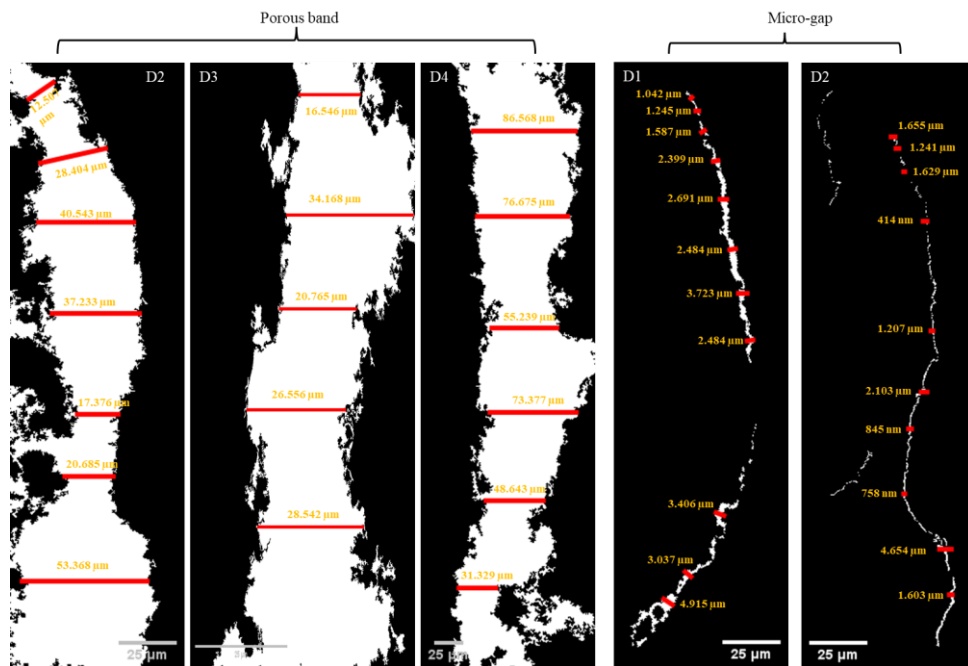


Figure 61. BSE images of porous band and micro-cracks for 30SA-70FA sample after ImageJ processed

Figure 62 exhibits the BSE images of 100FA sample. From the overview image, the rebar is surrounded by a rough mortar matrix, a condition similar to that observed in the 30SA-70FA sample. This deterioration is attributed to efflorescence during the accelerated corrosion period, caused by alkali leaching, as described in Section 2.2.3.2. This process causes surface spalling

and damage to the pore network, as shown in Figure 50, ultimately leading to the formation of the rough mortar matrix. At these four points, pronounced micro-gaps around the reinforcement are observed. The porous band is not visible in this sample because the increased roughness of the mortar matrix. From Figure 63, the thickness of the micro-gap in the 100FA sample varies, with an average thickness of approximately 5 μm .

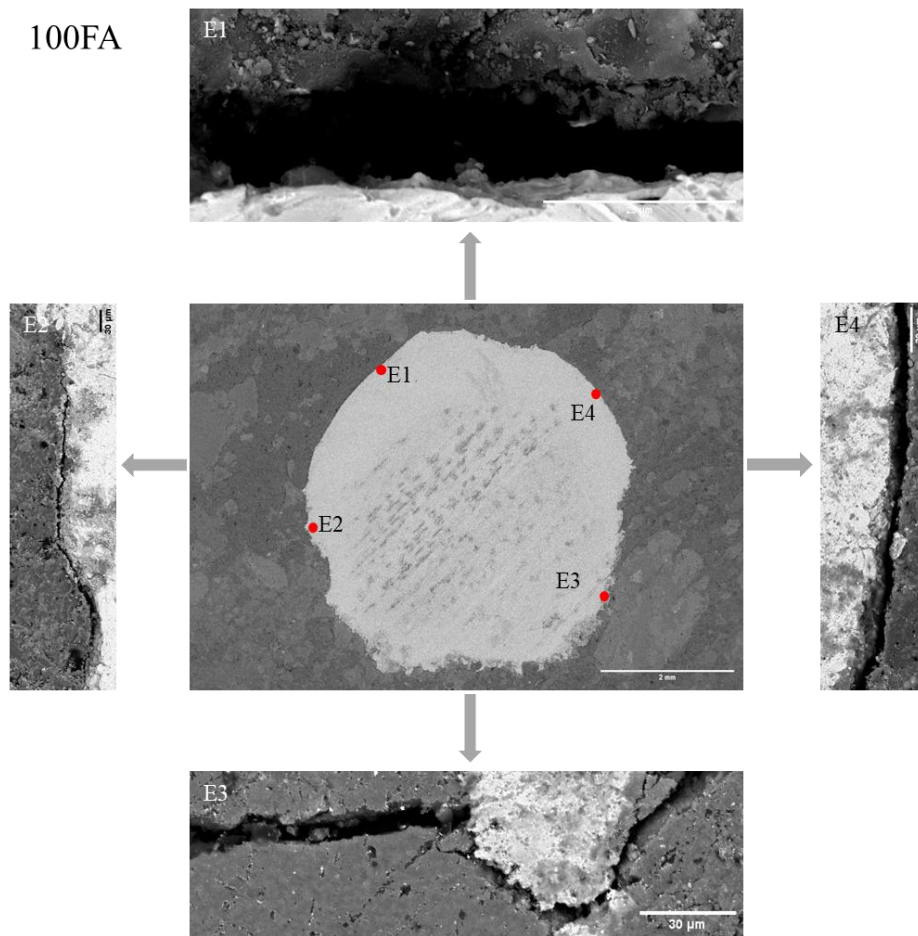


Figure 62. Morphology at the SMI for 100FA sample

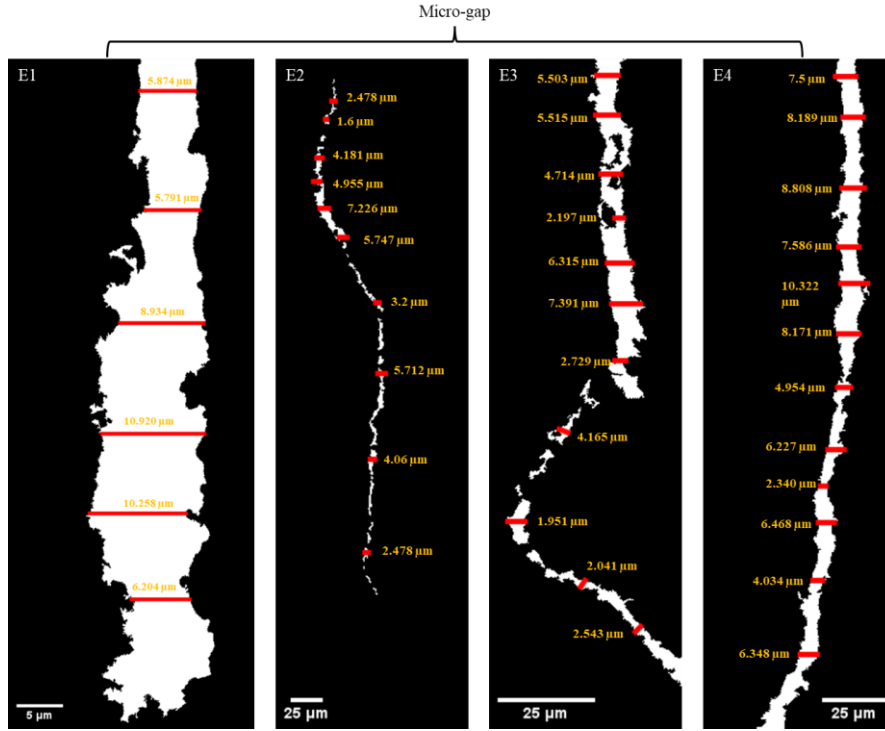


Figure 63. BSE images of porous band and micro-cracks for 100FA sample after ImageJ processed

To better understand of the porous band and micro-gap in these samples, all recorded BSE images, beyond those displayed above, were analysed to assess their thickness and the evolution trends with the change in SA content. A statistical analysis was conducted using Student's t-distribution [305] at a 95% confidence level, as defined by the following equation:

$$t_{0.95,n-1} = \frac{\bar{x} - u}{S/\sqrt{n}} \quad \text{Eq. 38}$$

where \bar{x} is the mean value of the recorded measurements, u is the actual mean value of the porous band but unknown, S is the standard deviation of the recorded measurements, n is the number of measurements, $t_{0.95,n-1}$ is the t-value with the confidence level of 95% and $n-1$ means degree of freedom used to find t value from the t-distribution chart.

Following the suggestion from Chen et al. [218], 20 measurements of the porous band and micro-gap were taken per section to ensure statistical significance. The results, calculated using Eq. 38, are plotted in Figure 65, and the data are summarised in Table 20. The 100SA and

70SA-30FA samples show a similar range for both porous band and micro-gap thickness, reflecting comparable microstructural characteristics. In contrast, the 50SA-50FA sample shows a significant increase in the top limit of the porous band thickness. For the 30SA-70FA sample, the porous band thickness (top limit) is approximately four times greater than that of the 70SA-30FA and 100SA samples. In the 100FA sample, the micro-gap thickness reaches the highest value; however, the porous band could not be measured due to the highly rough mortar matrix. These variations align with the expected evolution of microstructure characteristics as the SA content decreases, transitioning from high-calcium to low-calcium samples.

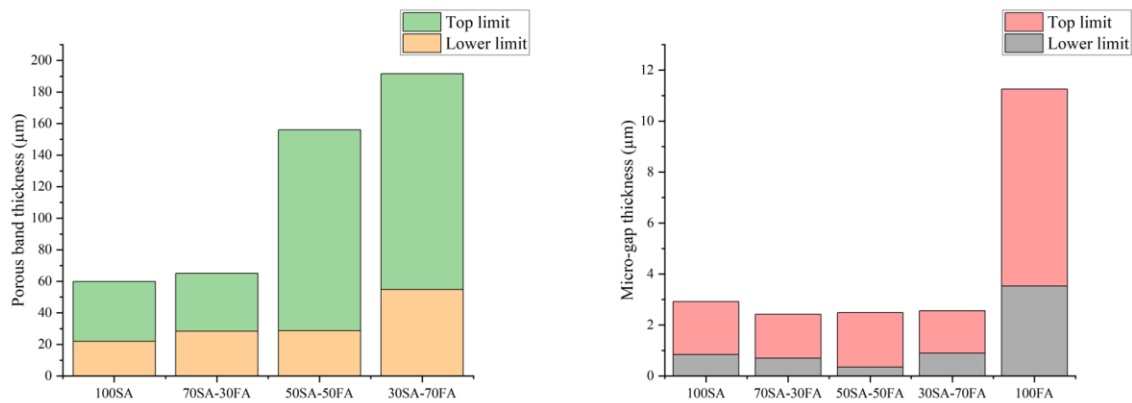


Figure 64. Thickness range of porous band and micro-gap for each sample

Table 20. Thickness range of porous band and micro-gap for each sample

Sample	Porous band thickness (μm)		Micro-gap thickness (μm)	
	Lower limit	Top limit	Lower limit	Top limit
100SA	21.97	37.96	0.84	2.08
70SA-30FA	28.41	36.74	0.7	1.72
50SA-50FA	28.81	127.19	0.35	2.14
30SA-70FA	54.73	136.86	0.9	1.66
100FA	N/A	N/A	3.53	7.73

6.2.2 Corrosion Mechanisms at SMI

BSE images clearly reveal the morphological information at the observed interface. When SEM analysis is coupled with EDS technology, the element of each component can be accurately identified. The integration of these two techniques allows for detailed mapping of corrosion rust distribution and provides valuable insight into the corrosion mechanisms in reinforced AAFS mortars.

Figure 65 shows the BSE-SE-EDS images for the 100SA sample, highlighting the initiation of corrosion at a micro-gap within the SMI. The BSE images reveal a distinct material phase in light grey at the SMI, distinguishable from the reinforcement (white) and the mortar matrix (dark). The maximum thickness of the microcrack is measured at approximately 11.94 μm .

EDS analysis identifies this light-grey phase as corrosion rust at the SMI. The element distribution of corrosion rust (Fe and O) and corrosive salt (Cl and Na) is displayed below the BSE-SE images. From the EDS images, enrichment of element Fe and Cl is observed at the micro-gap, as highlighted by red ellipses. Simultaneously, the presence of element O at this location confirms the formation of corrosion rust. This type of corrosion is classified as microcell corrosion, as stated in Section 2.3.1.

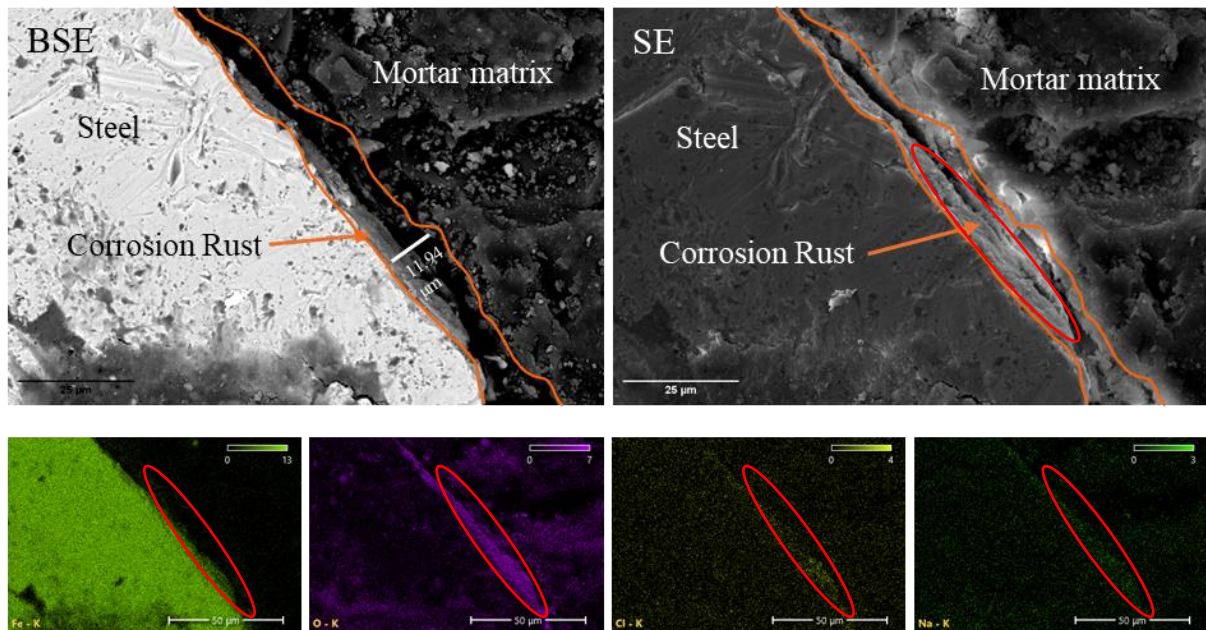


Figure 65. BSE-SE-EDS images for corrosion in 100SA sample

Figure 66 presents the BSE-SE images depicting the corrosion in the 70SA-30FA sample, along with the corresponding EDS analysis results. In both the BSE and SE images, no longitudinal micro-gap is observed at the SMI; however, a transverse microcrack is present. The origin of this transverse microcrack may be attributed to the accumulation of corrosion rust within the mortar matrix, coupled with drying shrinkage during the accelerated corrosion period.

Additionally, the mortar matrix and porous zone exhibit a coarse and rough surface. Based on the EDS results, the corrosion process at this location involves the migration of ferrous ions (Fe^{2+}) from the corroded iron (Fe) into the mortar matrix, driven by the potential field associated with macrocell corrosion. Within the mortar matrix, these ions undergo oxidation. The resulting volume expansion of corrosion rust fills pores and disrupts the pore network, thereby contributing to the coarse and rough mortar matrix. Furthermore, the formation of macrocell corrosion is attributed to the lack of oxygen at the steel surface, which inhibits reduction reaction near the corroded steel.

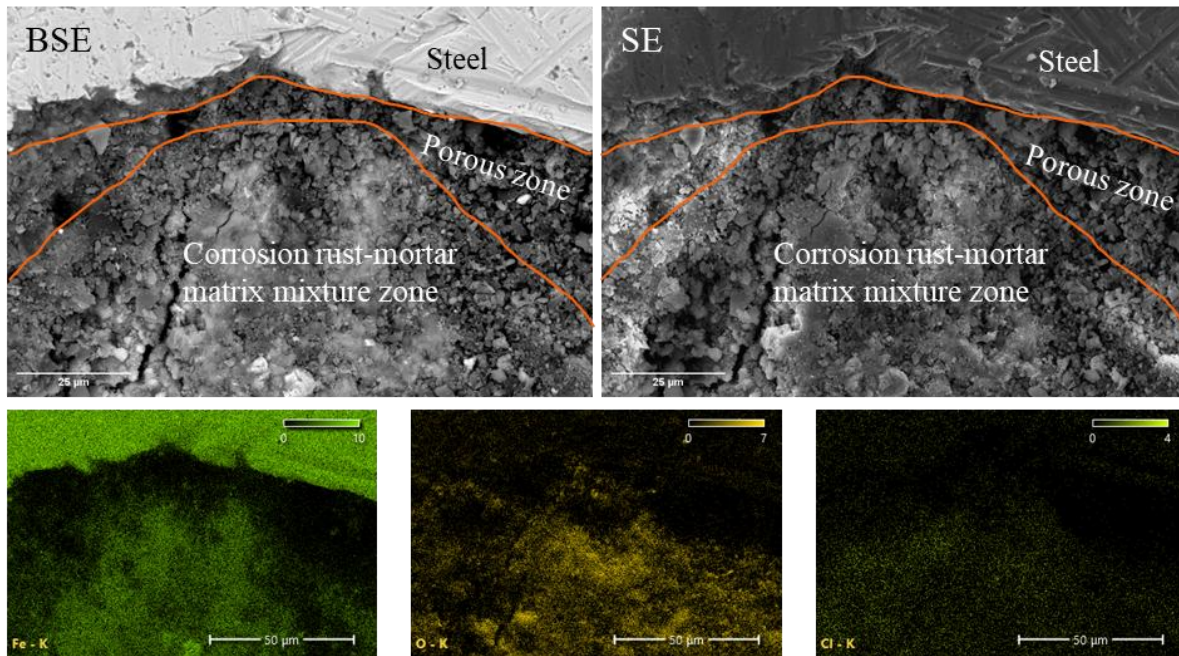


Figure 66. BSE-SE-EDS images for corrosion in 70SA-30FA sample

Compared to the macrocell corrosion observed in 70SA-30FA sample, Figure 67 provides clear evidence of macrocell corrosion in the 50SA-50FA sample. The BSE and SE images reveal a longitudinal micro-gap at the SMI, with a thickness of approximately $1.45\ \mu\text{m}$. EDS analysis indicates the presence of element Fe within the mortar matrix, with sporadic occurrences detected in the porous band extending from the steel surface into the mortar matrix. Additionally, an enrichment of the element Cl is observed in the mortar matrix. These findings suggest that the accumulation of Fe^{2+} primarily occurs in the mortar matrix rather than around

the reinforcement surface, despite the presence of micro-gap at the SMI. This is attributed to the small thickness of the microcrack, which restricts oxygen availability due to the limited volume, making it insufficient to initiate microcell corrosion.

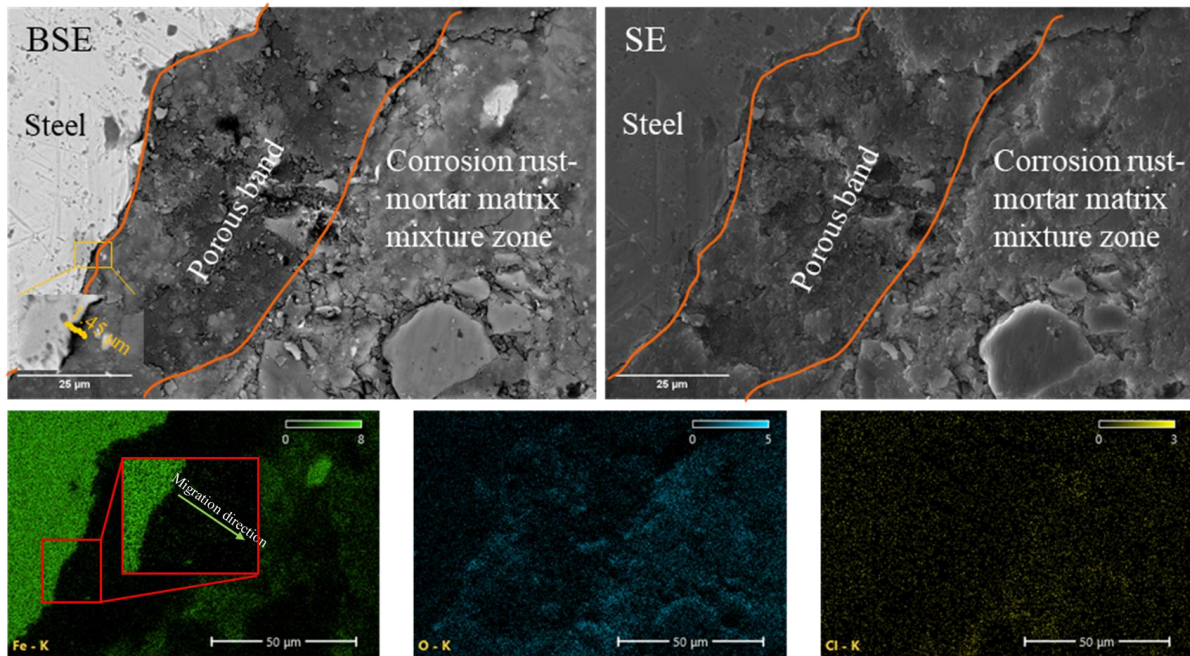


Figure 67. BSE-SE-EDS images for corrosion in 50SA-50FA sample

In the 30SA-70FA sample, a smaller micro-gap (approximately 635 nm) is observed at the SMI, which is notably smaller than the micro-gap in 50SA-50FA sample, as shown in Figure 68. Based on the BSE and SE images, no corrosion rust is detected within the micro-gap, despite the presence of element Fe identified through EDS measurements. This behaviour may be attributed to the limited amount of Fe^{2+} , which has not yet migrated to the mortar matrix, as element O is not detected in the micro-gap.

In the 100FA sample, as shown in Figure 69, a micro-gap with varying thicknesses is observed at different locations along the steel surface at the SMI. The maximum thickness of the micro-gap is approximately 10.382 μm , while the general thickness is around 2.134 μm , as shown in SE image. From the EDS images, element Fe is detected within the micro-gap, revealing a situation similar to that observed in the 30SA-70FA sample regarding the presence of element Fe. However, the distribution the element O suggests that corrosion rust is absent in most of

the micro-gap, except at locations where the thickness is greater than 10 μm (highlighted in a red circle). At these positions, detection of element Fe and O confirms the formation of corrosion rust.

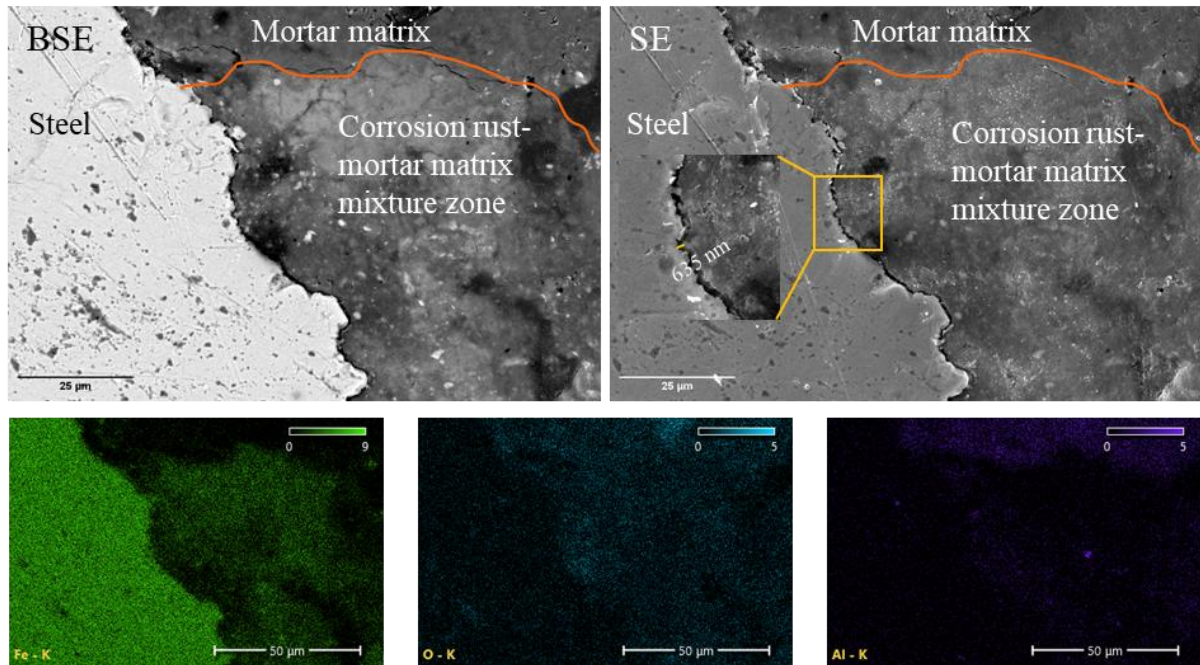


Figure 68. BSE-SE-EDS images for corrosion in 30SA-70FA sample

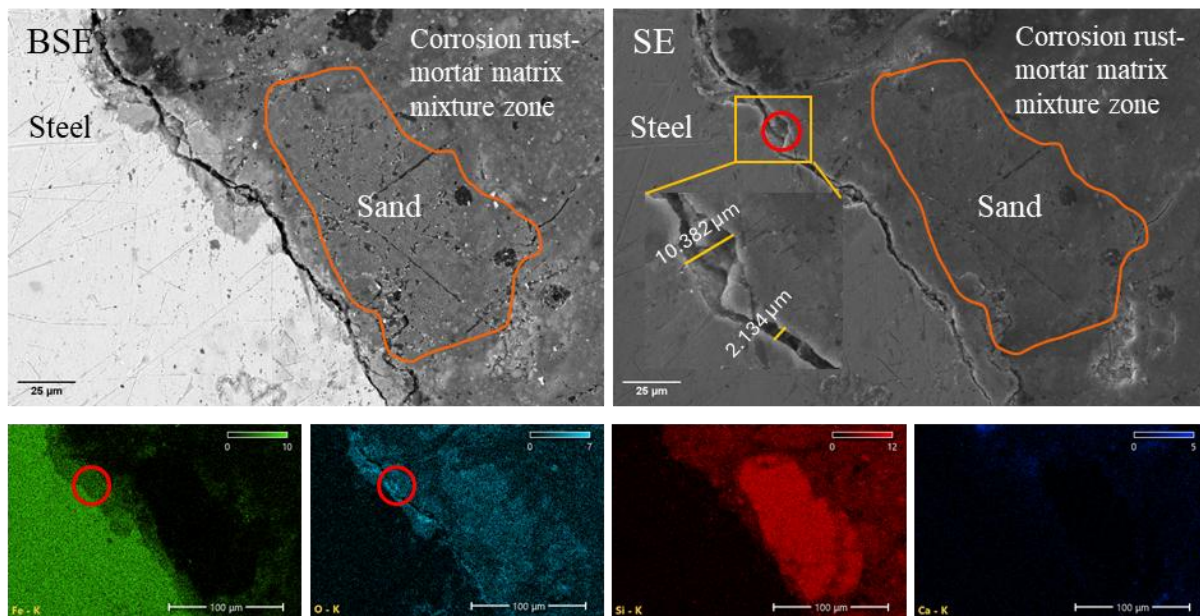


Figure 69. BSE-SE-EDS images for corrosion in 100FA sample

Based on the results above, it can be concluded that both microcell and macrocell corrosion mechanisms occur in reinforced AAFS mortars. The specific type of corrosion mechanism, however, is determined by the characteristics of the SMI, particularly the thicknesses of the micro-gap, which governs oxygen availability at the steel interface. The corrosion type relates to the micro-gap is listed below:

- **Microcell corrosion:** This occurs on the steel surface when the micro-gap thickness at the SMI exceeds 10 μm , providing sufficient O_2 to support the cathodic reaction adjacent to the corroded steel.
- **Macrocell corrosion:** This initiates when the micro-gap thickness at the SMI is below or around 2 μm , or when no micro-gap is present, as insufficient O_2 availability inhibits the cathodic reduction near the corroded zone. Fe^{2+} ions generated by anodic oxidation migrate into the mortar matrix, driven by the potential field established between the anode and the non-adjacent cathode, leading to ions diffusion away from the corroded steel surface.

6.3 X-CT Analysis

6.3.1 X-CT Image Processing and Spatiotemporal Evolution of Corrosion

SEM-EDS analysis is a valuable tool for characterising the corrosion behaviour of reinforced AAFS mortars at both the microstructural and element levels, providing detailed insights into interfacial properties between steel rebar and the mortar matrix. However, its ability to track the progression of reinforcement corrosion is limited by the destructive nature of sample preparation. This limitation is effectively addressed by the X-CT technique, which allows continuous, non-destructive observation of the corrosion process within the sample. In this study, the spatiotemporal evolution of corrosion was investigated using X-CT for two configurations of 50SA-50FA mortar samples: one with a smooth steel bar positioned centrally (named as M1) and the other eccentrically (named as S2) within the mortar.

Using the segmentation method described in Section 3.4.3, the evolution of material phases within the samples was effectively traced, enabling detailed analysis of phases changes over time. For the M1 sample, Figure 70 shows 3D views of the segmented components after the initial scan, including (a) mortar, (b) steel bar before corrosion, (c) pores, and (d) cracks. These images clearly reveal the spatial distribution of each material phase within the specimen. Specifically, Figure 70 (c) highlights a few large pores alongside numerous smaller ones, while Figure 70 (d) identifies two types of microcracks: one as a small gap at the bottom and the other originating from the internal defects within the sand.

Three X-CT scans were performed at different stages of accelerated corrosion: after 97 cycles, 137 cycles, and 186 cycles. These scans captured the initiation and progression of corrosion on the steel bar and the deterioration of material phases. Figure 71 provides an illustrative example from M1, highlighting the deterioration of the mortar surface during the accelerated corrosion process. Initially, the sample exhibited a smooth outer surface characteristic of its passive state. After 97 cycles of w/d cyclic corrosion, the outer surface became rough, with thin microcracks visible (Figure 72 (a)). After 137 cycles, further deterioration was observed, including spalling of the outer layer and increased surface roughness. By 186 cycles, extensive spalling had occurred, leaving only a small portion of the top surface intact. The actual surface condition of the sample after 186 cycles is shown in Figure 72 (b). A significant reduction in the mortar matrix volume is evident, primarily attributed to spalling caused by alkali leaching and efflorescence, which damage surface and disrupt the pore network within the mortar matrix. The influence of these factors has already been discussed in Chapter 5 and will not be repeated here.

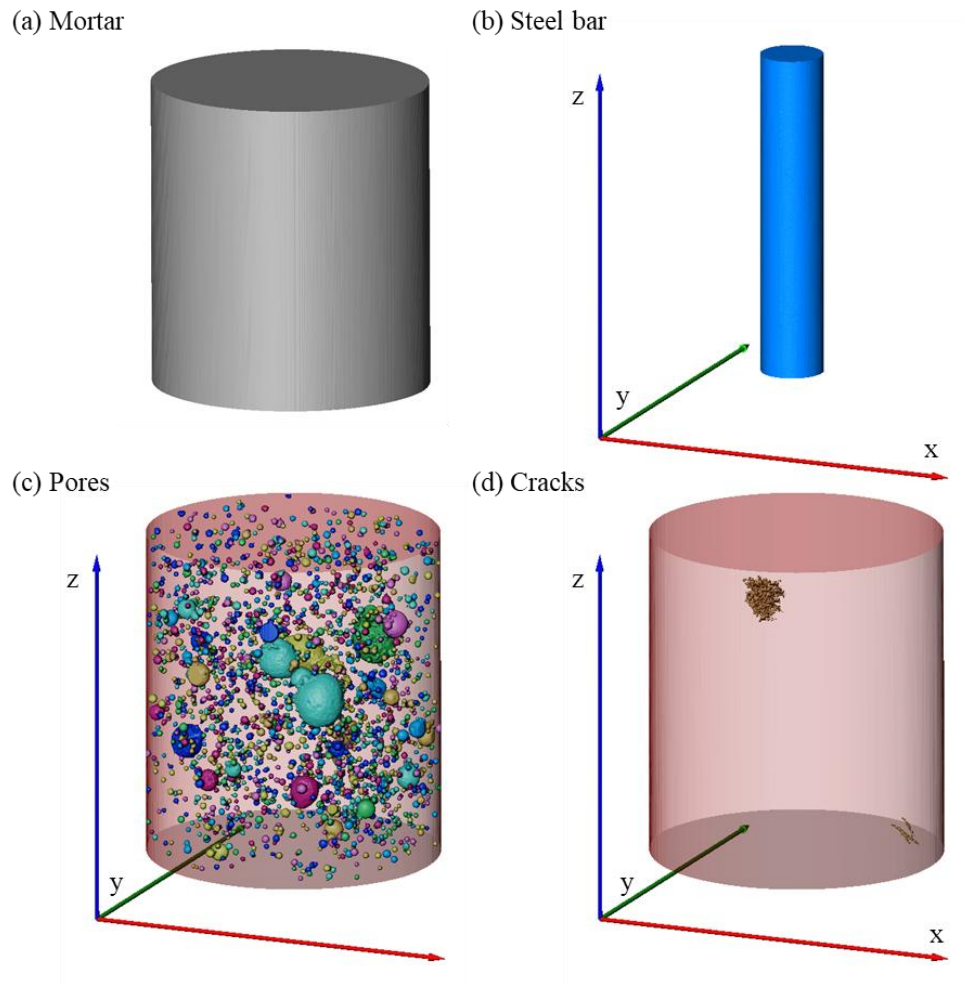


Figure 70. Three-dimensional views of (a) mortar, (b) steel bar, (c) pores and (d) cracks and voids

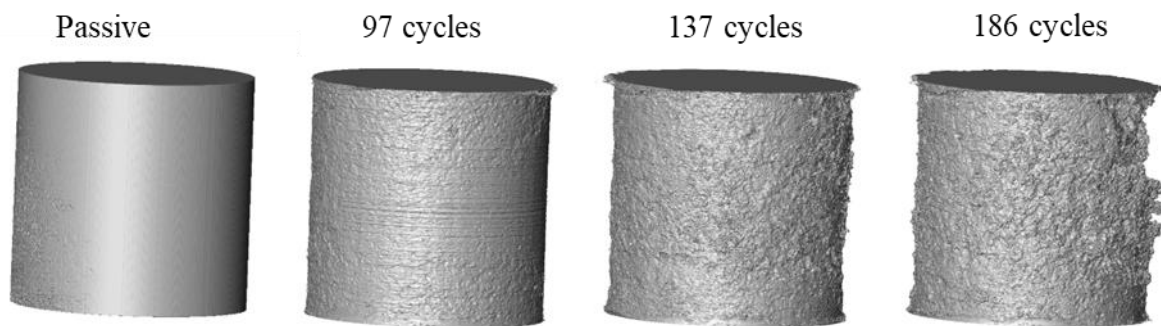


Figure 71. Change of outer surface for specimen during the accelerated corrosion period

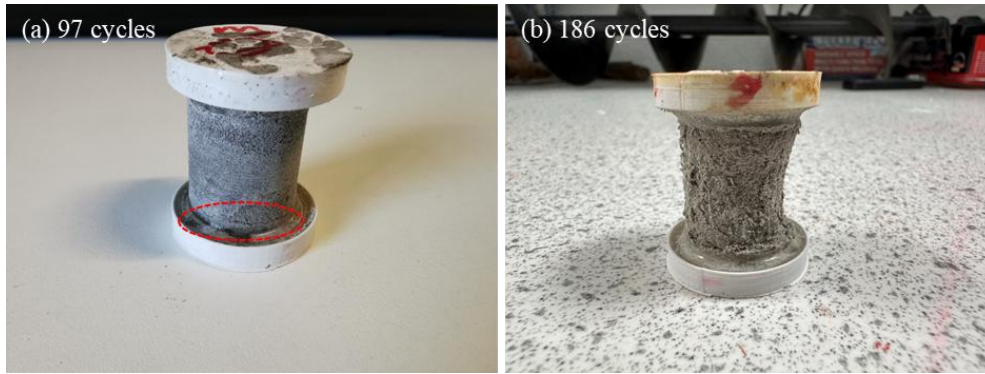


Figure 72. Surface change of sample at (a) 97 cycles and (b) 186 cycles

The initiation and subsequent evolution of steel bar corrosion and corrosion rust are depicted in x-z view images of the steel bar and rust in sample M1 and S2 at different stages, as shown in Figure 73 and Figure 74, respectively. In Figure 73, after 97 cycles of accelerated corrosion, pits are visible on the steel bar surface in both samples, but they are located in different regions, as highlighted by the red dashed ellipses. Figure 74 further reveals that, at 97 cycles, pitting corrosion in the centrally positioned sample M1 is relatively uniform across the entire steel bar, whereas in the eccentrically positioned sample S2, corrosion is more concentrated in specific regions. As accelerated corrosion progresses, the corrosion zone gradually spreads across the rebar surface, with pit cavities becoming deeper and larger. The quantification of steel bar corrosion will be discussed in detail in Section 6.3.2.

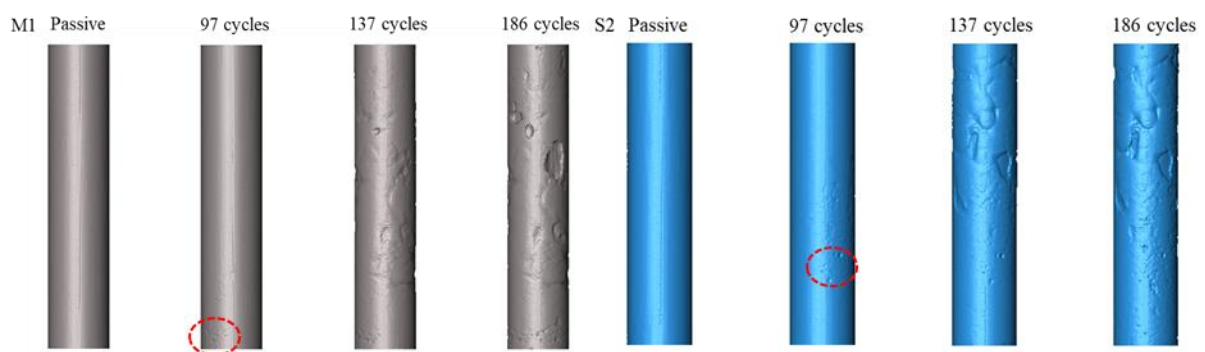


Figure 73. Evolution of corrosion of on the steel surface for M1 (left) and S2 (right)



Figure 74. Evolution of steel corrosion rust for M1 (left) and S2 (right)

Figure 75 presents cross-sectional images of the same slice around the steel bar at different stages of corrosion in samples S2. Several key phenomena regarding the evolution of corrosion were observed. First, corrosion initiates around a pore, as shown in Figure 75 (b) within the red dashed circle. The pre-existing oxygen and moisture within the pores promote the corrosion initiation at the steel-pore contact point, forming a microcell. Additionally, corrosion rust was observed to accumulate within the pores and gradually fill them, causing cracks in the mortar matrix, as illustrated in Figure 75 (d) within the red dashed rectangle. Furthermore, corrosion was detected away from the main corrosion zone, as depicted in Figure 75 (d) within the orange dashed circle. Notably, no pore was present at this location, suggesting that macrocell corrosion had formed.

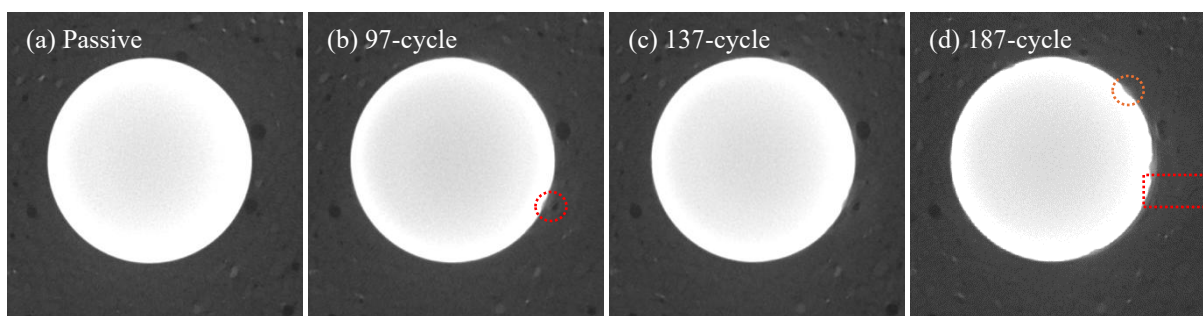


Figure 75. Reconstructed X-CT data for corrosion evolution on the steel surface

During the accelerated corrosion process, in addition to the previously described corrosion evolution, a transverse crack initiated from the mortar surface and propagated toward the steel

bar. The evolution of this crack and its corresponding 3D images are shown in Figure 76. The initial condition of the sample, where the crack begins to form, is shown in Figure 72 (a). Using the M6 samples as an example, Figure 76 shows x-z view images of the cross-section, revealing a small transverse crack on the lower-left side of the sample after 97 cycles. The corresponding 3D image at this stage indicates that the transverse crack almost encircles the mortar.

In Figure 76 (b), the transverse crack progresses further toward the steel, and an additional crack is observed on the lower-right side of the sample, which was not previously present. In addition, longitudinal cracks (middle-left) and another transverse crack extending from the steel bar toward the outer surface of the mortar are observed. The corresponding 3D image shows that the longitudinal cracks occupy one-third of the mortar's perimeter. By the end of 186 cycles, the longitudinal and transverse cracks have connected, as shown in Figure 76 (c).

Previous studies [235,244,245,306] have explored the impact of transverse cracks on the reinforced concrete or mortar corrosion, focusing on aspects such as chloride penetration rates, corrosion-induced transverse cracks, and load-induced transverse cracks. However, the transverse cracks observed in this research, originating from the outer surface of the sample and propagating toward the steel bar, have been rarely reported in the literature [235]. This may be attributed to the lack of effective methods for tracking the internal corrosion evolution in reinforced concrete or mortar, which limits the observation of such cracks. Additionally, such transverse cracks are often considered to form under load conditions and are thus typically ignored in studies of corrosion-induced cracks. However, as no load was applied in this study, the observed phenomenon suggests that corrosion-induced cracking can also initiate from the mortar surface rather than solely from the steel surface.

Considering the role of alkali leaching in reinforced AAFS mortar, the formation mechanism of transverse cracks may be summarised as follows:

- Tensile stress development: Under the influence of unbalanced pressure along the longitudinal direction of the steel bar, tensile stress develops on the mortar surface, beginning from the maximum corrosion zone. This stress leads to initial surface cracking.
- Efflorescence-induced damage: Efflorescence and subflorescence resulting from alkali leaching damages the mortar's pore network, causing surface spalling. This degradation accelerates the propagation of transverse crack.

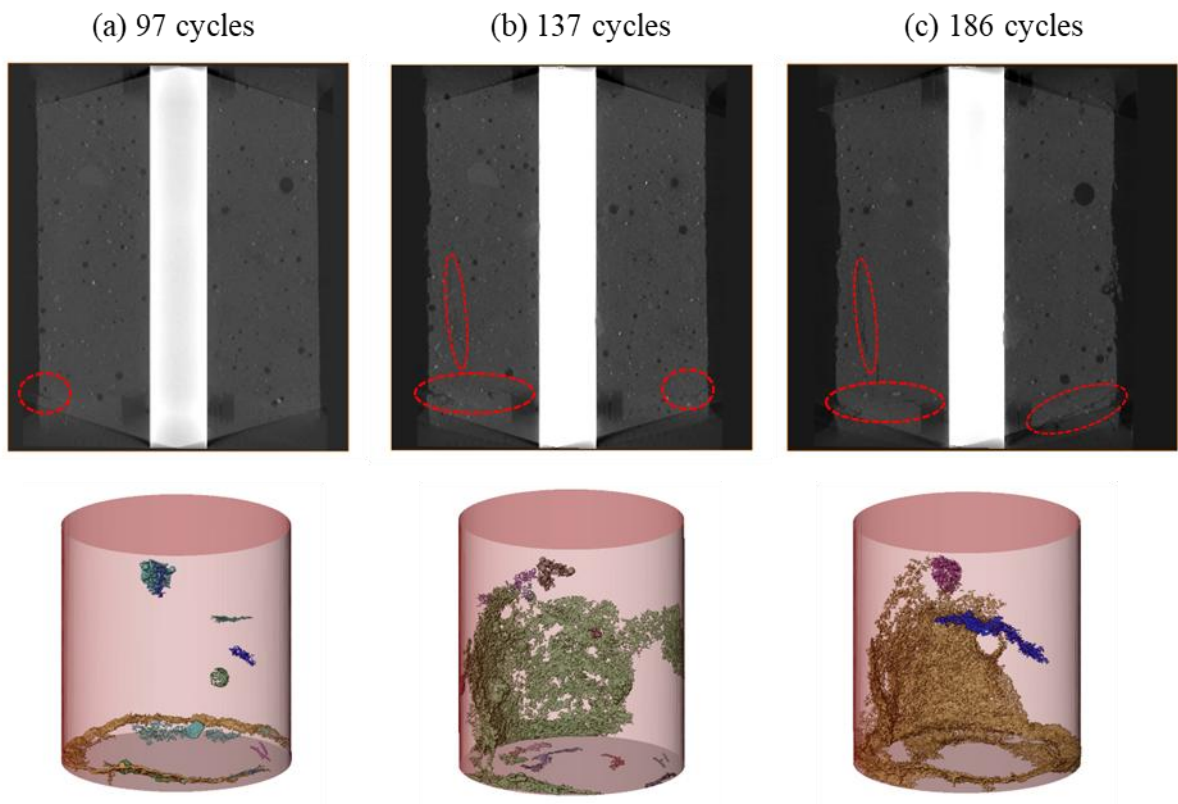


Figure 76. Evolution of cracks in mortar along with the accelerated corrosion progression

6.3.2 Spatiotemporal Evolution of Corrosion of Reinforced AAFS Mortar

6.3.2.1 Corrosion degree

After segmenting the material phases, Python was employed to quantify the corrosion of reinforced AAFS mortar, as described in Section 3.4.3. The corrosion degree of the steel bar in both samples, calculated along its longitudinal direction, was determined using the following equation [235]:

$$\eta_s = \frac{W_0 - W_r}{W_0} \times 100\% \quad \text{Eq. 39}$$

where η_s is the corrosion degree of the steel; W_0 and W_r are the original mass and the residual mass of the steel bar for any given slice.

Figure 77 illustrates the corrosion degree along the longitudinal direction of the steel bar, calculated from 1468 slices in sample M1 and 1379 slices in sample S2. The results clearly show that the corrosion degree varies along the reinforcement. After 97 cycles, corrosion initiation in M1 is concentrated on the top and bottom sides of the steel, whereas in S2, it is concentrated in the middle zone. Additionally, the corrosion degree in both samples remain below to 0.5%. After an additional 40 cycles of accelerated corrosion, the corrosion degree in both samples increased, exhibiting distinct distribution patterns across the steel bar. In sample M1, the corrosion distribution is concentrated between slice 200 to slice 1000, consistent with the observed condition of the steel bar, as shown in Figure 73. Furthermore, the corrosion distribution in M1 is relatively uniform compared to the more irregular distribution observed in sample S2.

In sample S2, a significant increase in corrosion, reaching up to 5%, was observed between slice 800 and slice 1000. In the remaining sections of the steel bar, the corrosion degree is generally lower than 1%. This is due to the presence of pores around the steel bar, which provide the oxygen and moisture necessary for corrosion initiation and progression. By the end of 186 cycles of accelerated corrosion, the corrosion degree for M1 showed a significant increase between slices 800 and 1000, while the other regions exhibited only a modest increase in corrosion degree. Additionally, the increase in peak corrosion degree at 186 cycles is less pronounced compared to 137 cycles, while the corrosion degree in the other regions displayed a significant rise.

The accumulation of corrosion rust on the steel surface fills the pore first. However, if the pores around the steel bar become fully filled, macrocell corrosion may initiate, as observed in Figure 75 (d). Overall, there is a significant increase in corrosion degree in the non-peak regions. The highest corrosion degree in sample S2 reached nearly 7%, exceeding the maximum value of approximately 5% observed in sample M1. This difference can be explained by the position of steel bar and the deterioration of mortar matrix:

- Steel bar position: In M1, the centrally placed steel bar has a uniform cover thickness, whereas the eccentrically placed steel bar in S2 experiences a non-uniform cover thickness. This uneven cover makes one side of steel bar in S2, with a thinner cover, more exposed to the oxygen and moisture compared to the centrally placed steel bar in M1.
- Mortar deterioration: The deterioration of mortar matrix, including surface spalling as shown in Figure 72 (b), reduces the cover thickness, particularly around the eccentrically placed steel bar in S2. This reduction in cover thickness facilitates the penetration of oxygen, moisture, and aggressive ions, significantly increasing the corrosion rate compared to sample M1.

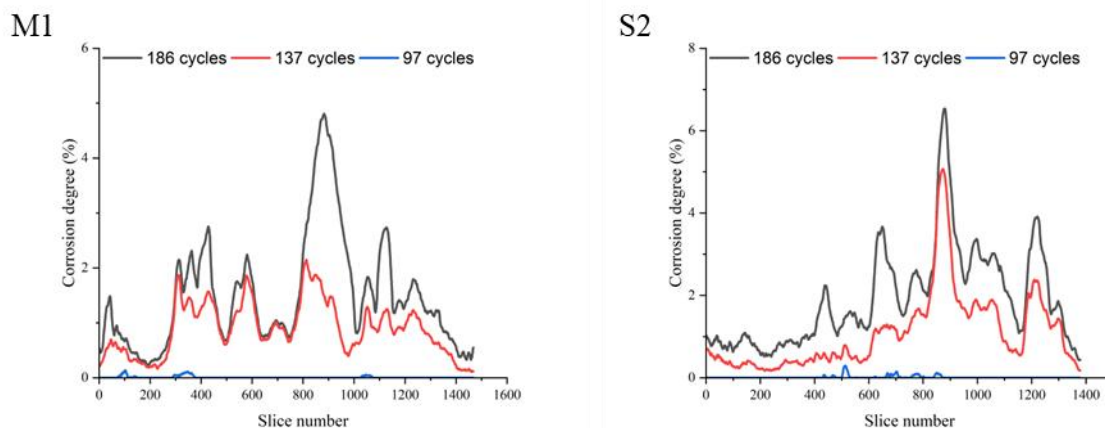


Figure 77. Corrosion degree of the steel bar along the longitudinal direction.

6.3.2.2 Radial loss of steel bar

The residual cross-section area of a corroded steel bar significantly influences the service life and structural properties of corroded reinforced structures. The maximum and average radial losses of the steel bar at any given slice are critical indicators used to characterise non-uniform or pitting corrosion patterns along the longitudinal direction of the steel bar. To quantify these patterns, the maximum and average radial loss, as well as their ratio, are calculated using the following equations [235]:

$$R_{avg} = \frac{\sum_0^{2\pi} R_r(\theta)}{2\pi} \quad \text{Eq. 40}$$

$$R_m = \max_{\theta \in [0, 2\pi]} R_r(\theta) \quad \text{Eq. 41}$$

$$\beta = \frac{R_m}{R_{avg}} \quad \text{Eq. 42}$$

where R_{avg} and R_m is the average and maximum radial loss of the steel bar and $R_r(\theta)$ is the radial loss of the steel bar at the angle θ in the range of 0 to 2π , for any given cross-section. β is the ratio between the maximum and the average radial losses.

Figure 78 and

Figure 79 depict the maximum and average radial loss of the steel bar for both samples after corrosion initiation. At the onset of corrosion, the maximum radial loss is below 0.1 mm, while the corresponding average radial loss is below 0.05 mm. As accelerated corrosion progresses, both the maximum and average radial losses of the steel bar increase. By the end of 137 cycles of accelerated corrosion, the maximum radial loss of the steel bar in sample S2 reaches approximately 0.2 mm, nearly double that of sample M1, where the value is approximately 0.1 mm. Similarly, the average radial loss for both samples show a strong correlation with maximum radial loss, with the maximum value in S2 and M1 also exhibiting a ratio of 2.

As shown in Figure 80, the ratio β between maximum and average radial loss is higher at the end of 97 cycles of accelerated corrosion, marking the initiation of corrosion where pitting

corrosion is observed. This phenomenon is further confirmed through the 3D structural image of the steel bar (Figure 73). As the corrosion degree increases, the β ratio gradually decreases, falling within a range of 5 to 20, which aligns well with previous studies [235,307-309]. Although β shows exceptionally high values in certain regions, for instance, ranging from 20 to 65 for S2 between slices 1 and 100, these high-value areas correspond to newly emerging corrosion regions. This observation is further supported by the 3D image of the rebar, as shown in Figure 73, which shows the distribution of corrosion regions on the rebar surface. Thus, the β ratio in newly formed corrosion areas is significantly higher than in regions that have already experienced corrosion. Furthermore, the distribution of this ratio effectively highlights the non-uniform nature of corrosion in reinforced AAFS mortar.

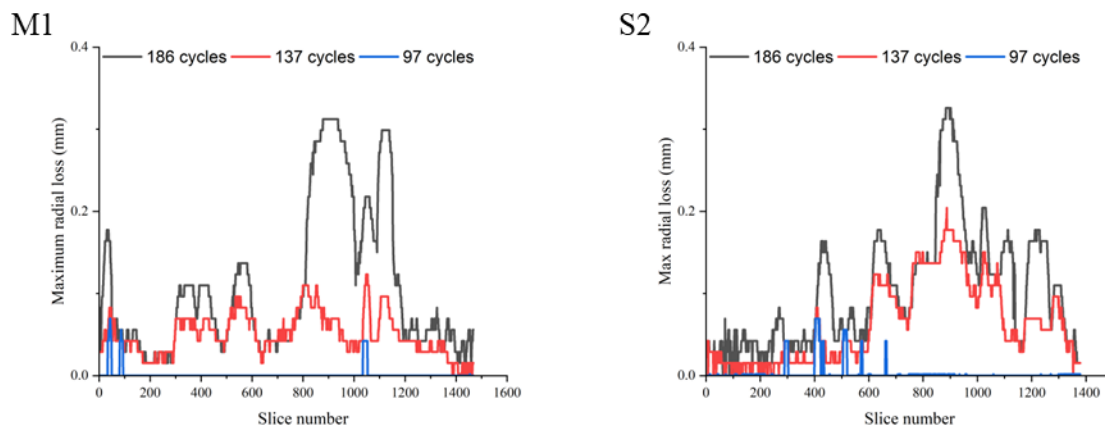


Figure 78. Maximum radial loss of steel bar in sample M1 and S2 along the longitude direction

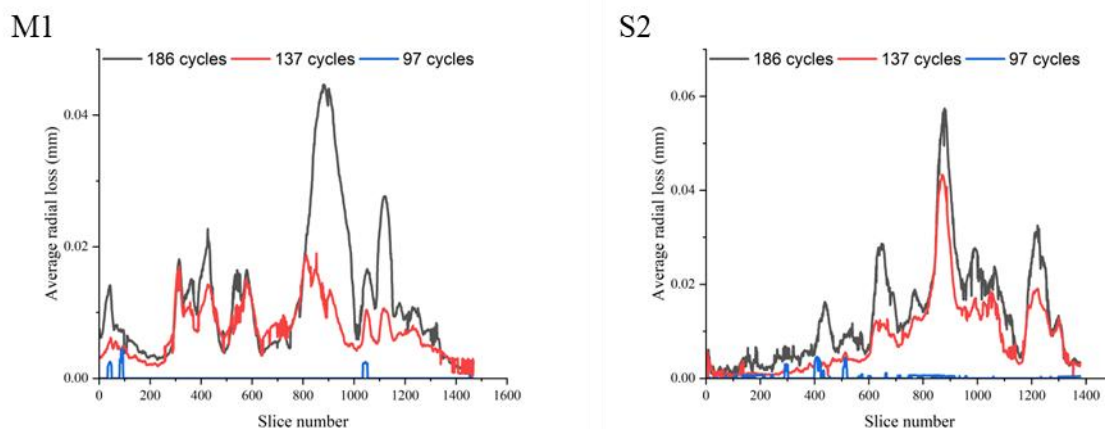


Figure 79. Average radial loss of steel bar in sample M1 and S2 along the longitude direction

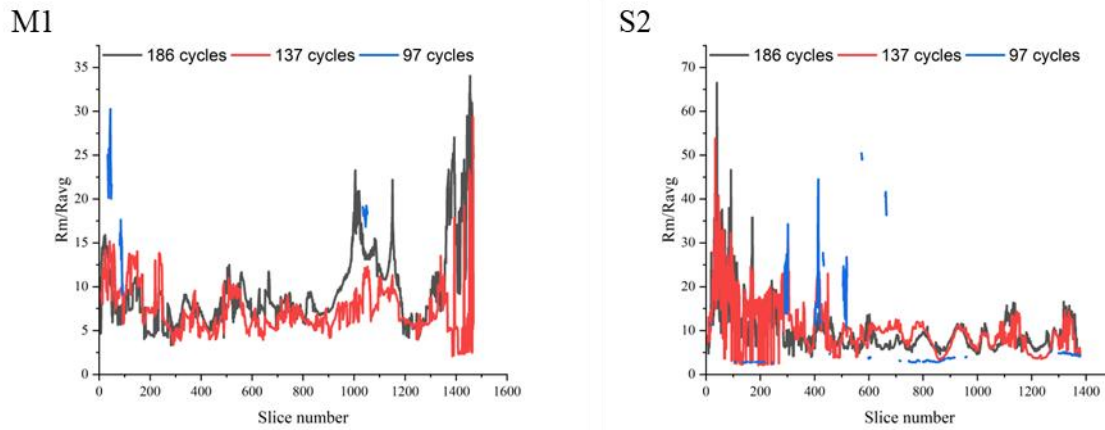


Figure 80. Ratios of maximum radial loss to average radial loss of the steel bar along the longitude direction

6.3.2.3 Corrosion rust distribution

The distribution of corrosion rust around the steel bar is crucial for assessing and predicting the service life of reinforced concrete structures. The accumulation of corrosion rust at the SCI or SMI and its propagation toward the cover significantly influence crack development within the concrete. Figure 74 presents the extracted corrosion rust, which was analysed to determine the overall distribution around the rebar. The treatment process of the corrosion rust has been detailed in Section 3.4.3.4. Using this method, the thickness of corrosion products was measured at 1° intervals from 0° to 360° , ensuring for comprehensive analysis. An example of measured corrosion rust thickness is shown in Figure 81.

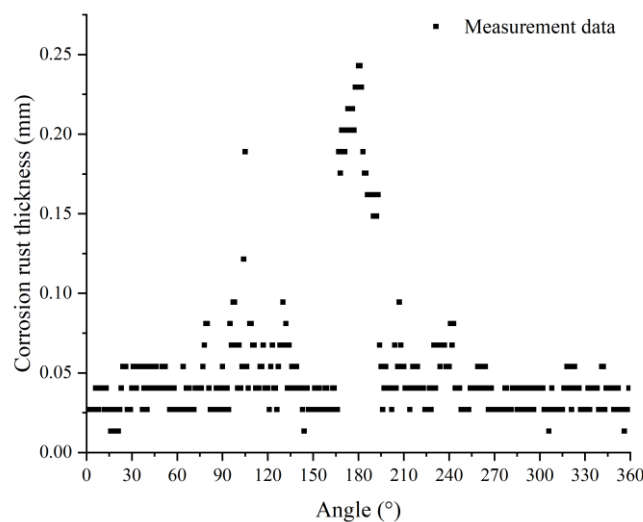


Figure 81. Corrosion rust thickness along the circumference of the steel bar

The measured thickness data of the corrosion rust were then validated using the non-uniform corrosion model developed by Xi and Yang [235]. This model characterises the non-uniform distribution of corrosion rust around the steel bar using a modified von Mises distribution with three parameters: the corrosion degree indicator λ , the non-uniform coefficient k , and the degree for the maximum corrosion rust thickness μ . The equations used in this model are provided below [235]:

$$T_{cl} = \lambda \frac{e^{k \cos(\theta - \mu)}}{2\pi I_0(k)} \quad \text{Eq. 43}$$

$$I_0(k) = \sum_{m=0}^{\infty} \frac{\left(\frac{k}{2}\right)^{2m}}{(m!)^2} \quad \text{Eq. 44}$$

where $I_0(k)$ is the modified Bessel function of order 0.

Regression analysis (R^2) between von Mises model and X-CT data for corrosion rust thickness was also performed. Figure 82 exhibits the R^2 coefficient for sample M1 and S2 at the completion of 137 and 186 cycles of accelerated corrosion. Notably, R^2 values are absent in certain regions of the sample, despite the presence of measurable corrosion rust thickness (as shown in Figure 77). This discrepancy arises from the low corrosion degree in these zones, where pitting corrosion has only just initiated, leading to insufficient data points for accurate regression analysis. As a result, negative R^2 values obtained in these zones indicate a poor correlation between von Mises model and X-CT data. To address this issue, these values were redefined as 0.

In sample M1, the R^2 values at 186 cycles are generally higher than those at 137 cycles, reaching up to 0.8. In contrast, the R^2 values in sample S2 at 186 cycles are lower than those at 137 cycles, falling below to 0.6. Figure 83 provides a detailed comparison of corrosion rust thickness and fitted curve with R^2 values for slice 851 from S2 at two different time points: after 137 cycles and after 186 cycles. The comparison highlights distinct differences in the distribution of corrosion rust around the steel bar. At 137 cycles, the corrosion rust shows a

concentrated distribution, whereas at 186 cycles, it becomes more widely distributed. This is attributed to the progressive corrosion of the steel bar, which leads to an increased spread of corrosion products over time.

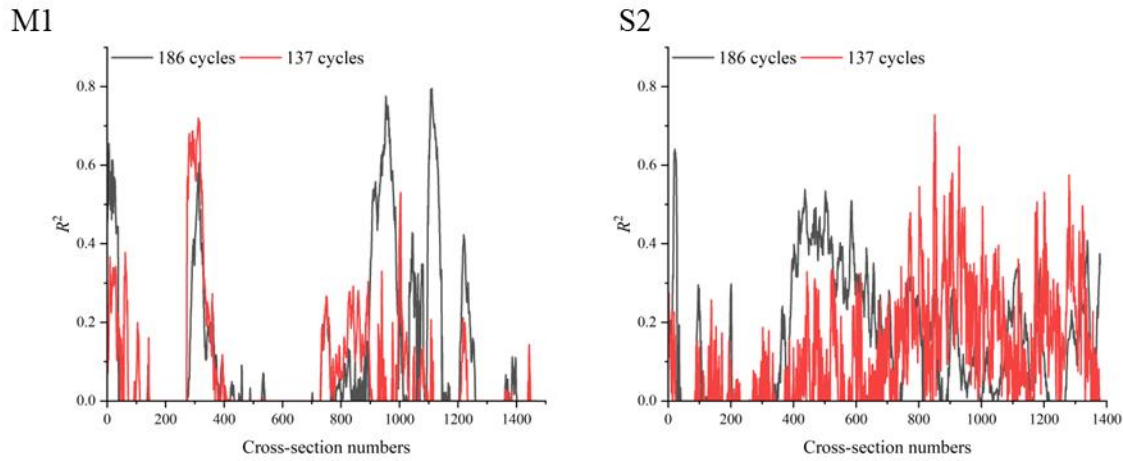


Figure 82. Coefficient of determination R^2 of fitting results for M1 and S2

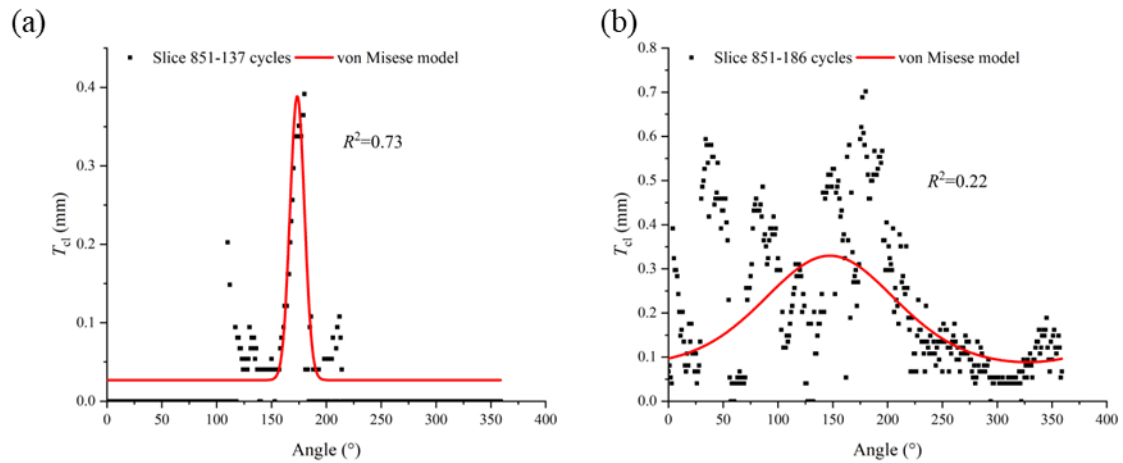


Figure 83. The comparison between slice 851 for S2 at 137 and 186 cycles

Another example from M1 after 187 cycles, showing slices with higher R^2 values, is depicted in Figure 84. These images reveal relatively uniform corrosion at various positions along the steel bar, with the exception of a concentrated area in the middle part of the curve, where corrosion is more pronounced. The highest corrosion rust thickness, concentrated in the middle, is greater than that observed at other angles. Compared to the distribution of corrosion product thickness around the steel bar in sample S2, the peak-like distribution of corrosion rust in

sample M1 provides a better alignment with the von Mises model, thereby resulting in higher R^2 values.

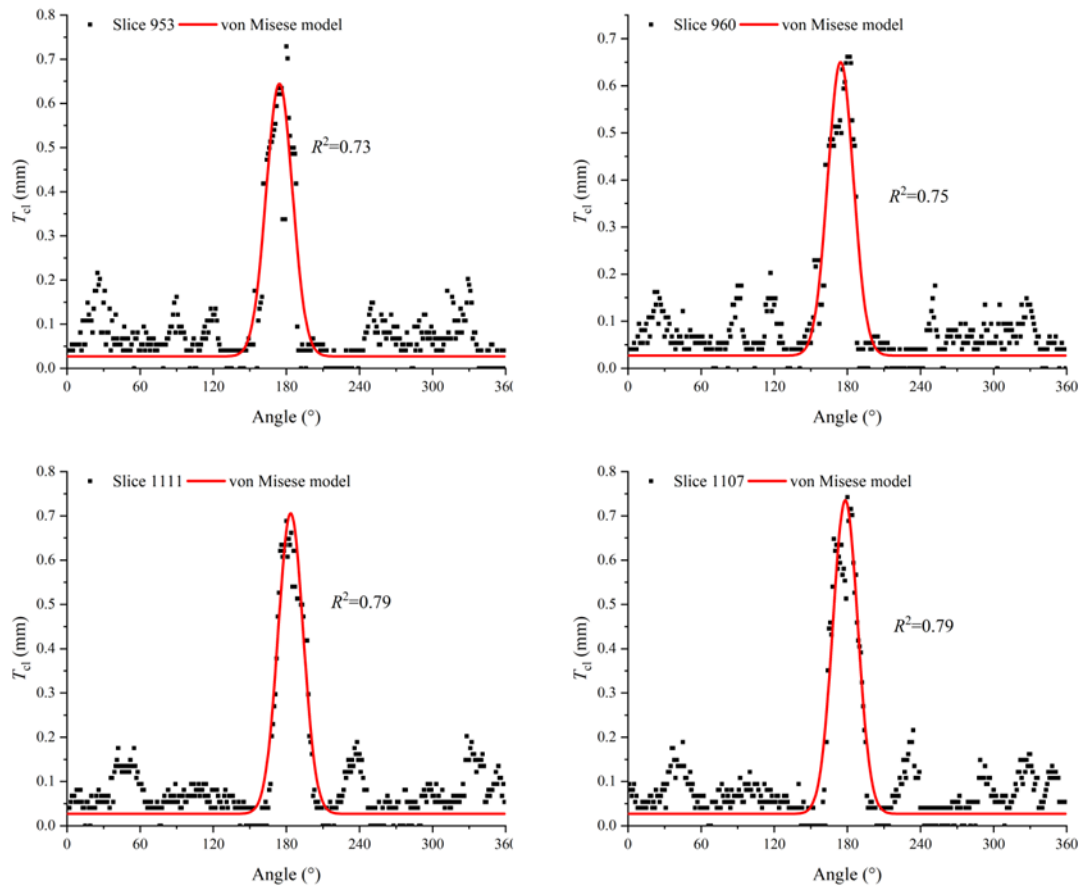


Figure 84. Regression analysis of von Mises model with X-CT data

Based on the results above, the irregular distribution of corrosion products in sample S2 significantly reduces the accuracy of the model fitting, particularly in regions with discontinuous corrosion patterns. The von Mises model describes a continuous probability distribution on a circle [162], making it suitable for representing corrosion patterns with a single peak-like shape, as observed in Figure 84. However, non-circular and discontinuous corrosion patterns, such as those observed in slice 851 from sample S2 at a later stage, pose challenges for the von Mises model, as these patterns deviate from the model's assumptions of continuity. Additionally, the pitting corrosion observed at the early stage of corrosion cannot be effectively interpreted using the von Mises model.

An advanced von Mises model with two peaks, referred to as the asymmetrical generalised von Mises (AGvM) model, was proposed by Bui and Tan [310] to address the limitations of von-Mises model. Building on the corrosion model developed by Xi et al. [162], the AGvM model is designed to simulate multi-peak, asymmetrical rust layer around the circumference of the steel bar. This advanced model has also been employed to fit corrosion rust distribution observed in measured X-CT data. A comparative example for these two models is present in Figure 85, using data from slice 1379 from samples S2 to illustrate their respective fitting capabilities. From the figure, it is evident that the von Mises model is symmetric, with a single peak centred, whereas the AGvM model displays asymmetry, better capturing the distribution with one primary peak and one sub-peak. Based on the distribution of data points and fitted models, the AGvM model provides a more accurate representation of data fitting. This is further supported by the higher R^2 value obtained from AGvM model.

Moreover, a comparison of R^2 values between the two models for sample M1 and S2 at 137 cycles and 186 cycles is shown in Figure 86. It can be observed that there is a significant increase in R^2 values for the AGvM model, particularly for S2 at 137 cycles. However, all R^2 values are below 0.9, particularly at 186 cycles. Although the AGvM model exhibits a better fitting efficiency, the R^2 values indicates its limitations in capturing the corrosion distribution with multi-peaks, which represent more complex corrosion patterns. Consequently, this model is not suitable for describing corrosion distributions during the initiation period, where highly localised pitting corrosion dominates, as observed from the 3D views of steel corrosion (Figure 73).

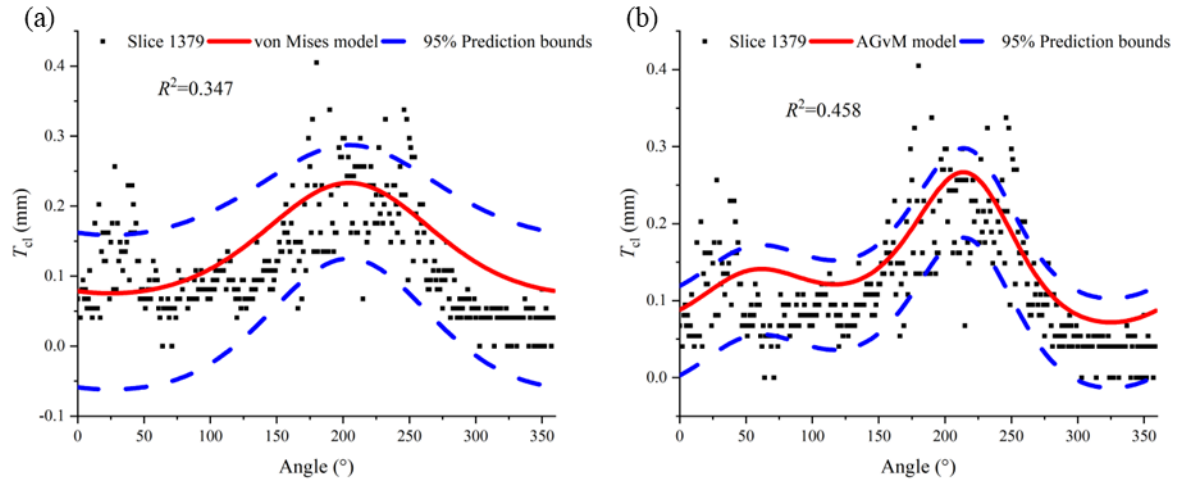


Figure 85. Comparison between the fitting of von Mises model and AGvM model

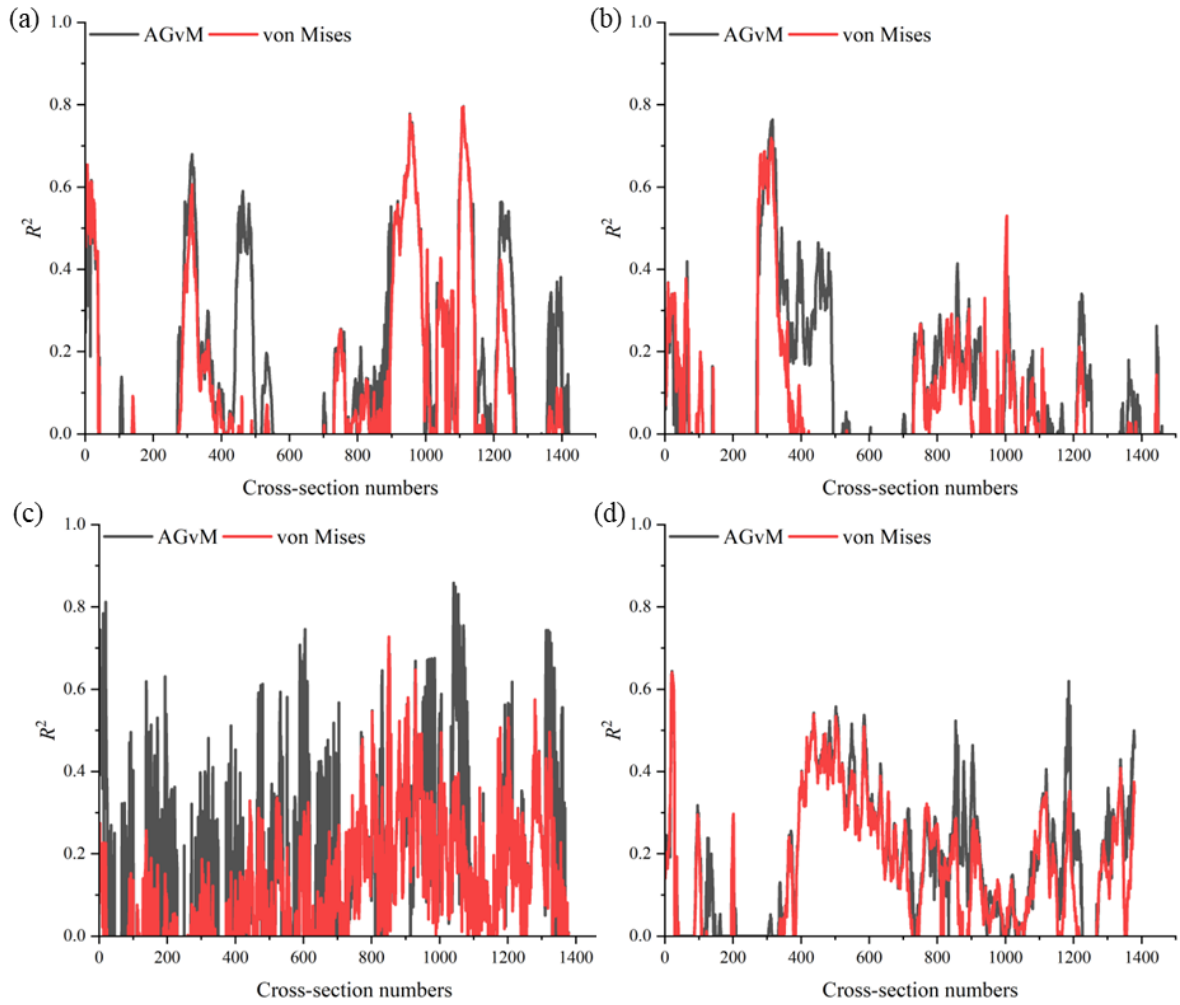


Figure 86. Comparison of R^2 for M1 (a), after 137 cycles (b) after 186 cycles, S2, (c) after 137 cycles and (d) after 186 cycles

6.4 Bond Strength

As described in Section 3.2.5, pull-out tests were conducted to investigate the relationship between bond stress and slip for the 50SA-50FA group of reinforced AAFS concrete and the reference group of reinforced OPC concrete. Within the 50SA-50FA group, two types of coarse aggregates, 10 mm gravel and 20 mm limestone, were used to examine how the influence of aggregate type on bond strength. The reinforced AAFS concrete with gravel is referred to as AAFS-G, while the group with limestone is named as AAFS-L. In contrast, the reinforced OPC concrete used only limestone as the coarse aggregate and is named as OPC-L.

Two test methods, load-control and displacement-control, were employed for the 50SA-50FA group. The load-control method was used to evaluate the maximum bond strength, while the displacement-control method focussed on capturing the evolution trend of the bond stress-slip curve. Although the load-control method is effective for measuring maximum bond strength, it faces challenges in capturing the post-peak evolution due to abrupt force drops. In contrast, the displacement-control method effectively captures the bond evolution in the post-peak region. The differences between these methods are illustrated in Figure 87. In the post-peak region, both curves exhibit limited plateau stages, reflecting the effect of residual bond stress at the SCI. However, these plateau stages are less pronounced in the load-control method compared to the displacement-control method.

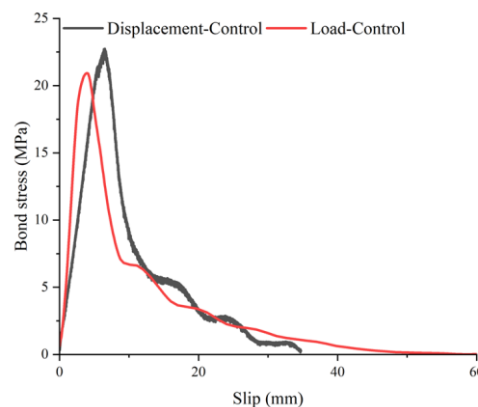


Figure 87. The comparison between the bond stress-slip curve for Load-control and Displacement-control methods

For the AAFS-G group, the pull-out test results, along with representative bond stress-slip curves, are shown in Figure 88. From Figure 88 (a), it can be observed that the maximum bond strength for the non-corroded sample is approximately 22 MPa. As the corrosion of the embedded steel rebar increases, the maximum bond strength initially rises but decreases at higher corrosion levels. When the corrosion level reaches 0.29%, a plateau (a stable horizontal region) appears in the curve after the peak bond stress. This plateau corresponds to the residual bond capacity, maintained by the combined effects of corrosion rust accumulation at the SCI filling the porous zone, residual mechanical interlocking, and other factors. This behaviour disappears as the corrosion level increases further. Additionally, for AAFS-G samples, the failure mode is identified as splitting failure, as shown in Figure 88 (a), with the fracture surface depicted in Figure 88 (b). The fracture surface indicates that the failure occurred through both the aggregate and concrete matrix. This behaviour is attributed to the low adhesion effect of gravel, due to its smooth surface, and the reduced mechanical interlocking caused by its the circular or elliptical shape. Consequently, gravel was replaced with limestone, and the bond position of the steel bar was adjusted from the middle part of the concrete (Figure 88 (b)) to the bottom part (as described in Section 3.2.5) to improve sample casting and performance.

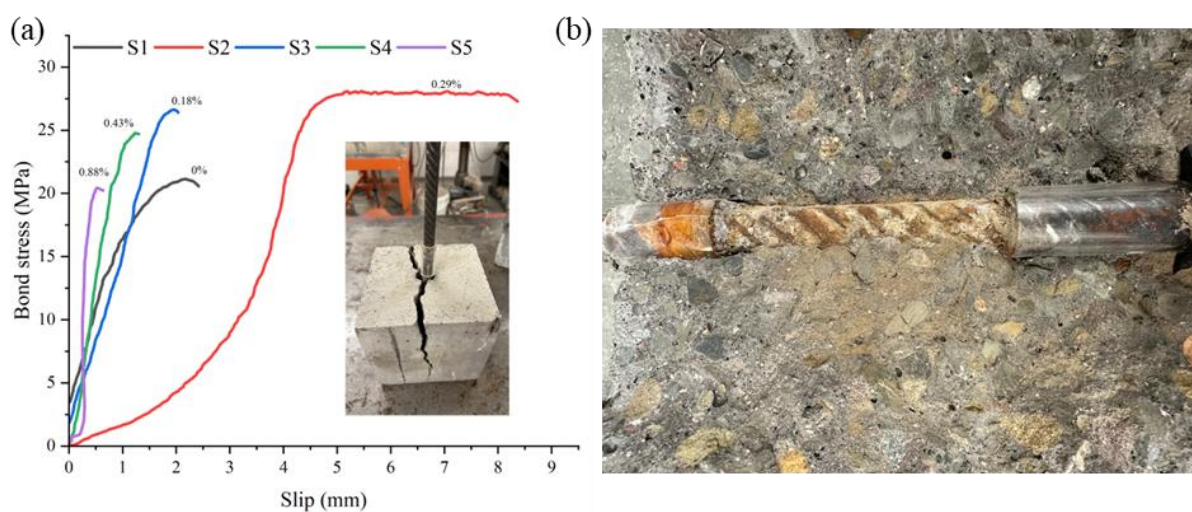


Figure 88. (a) The representative bond stress-slip curve for the AAFS-G samples, (b) the fracture surface of sample after split failure

For the AAFS-L and OPC-L groups, the pull-out test results for samples subjected to different corrosion durations and tested under the load-control method are shown in Figure 89. From Figure 89 (a), it can be observed that the non-corroded sample exhibits the highest bond strength, approximately 25 MPa. As the duration of accelerated corrosion increases, the peak bond strength shows a slight increase for the sample subjected to 4 days of corrosion compared to the sample subjected to 2 days. However, the overall trend indicates a gradual decrease in peak bond strength with extended corrosion durations. In addition, with longer corrosion durations, the accumulated corrosion rust progressively fills the porous zone at the SCI. This accumulation causes the samples to reach their maximum bond strength with less slip.

After reaching their maximum bond strength, the bond stress decreases rapidly to a certain level within a short slip distance. This behaviour is attributed to the residual friction and the mechanical interlocking between the steel rebar and concrete, which continue to resist the pull-out of the steel rebar. Additionally, corrosion rust contributes to the residual adhesion at the SCI, though this effect depends on the corrosion level of the steel rebar. This relationship can be observed in the difference between the curve for the non-corrosion sample and the sample subjected to 2 days of corrosion. In this case, slight corrosion increased the residual bond stress. However, as the corrosion level increases, the accumulation of corrosion rust at SCI generates microcracks due to local tensile stresses, reducing adhesion between the steel rebar and the concrete. Consequently, the residual bond strength for the sample subjected to 6 days of accelerated corrosion is lower than that of the sample subjected to 2 days of corrosion.

From Figure 89 (b), it can be observed that for the AAFS-L group, the maximum bond strength increases with the duration of accelerated corrosion, reaching approximately 26 MPa for the sample subjected to 8 days of accelerated corrosion. These curves exhibit similar behaviour to the reference OPC group, showing an increase in initial bond strength with less slip as the corrosion duration increases.

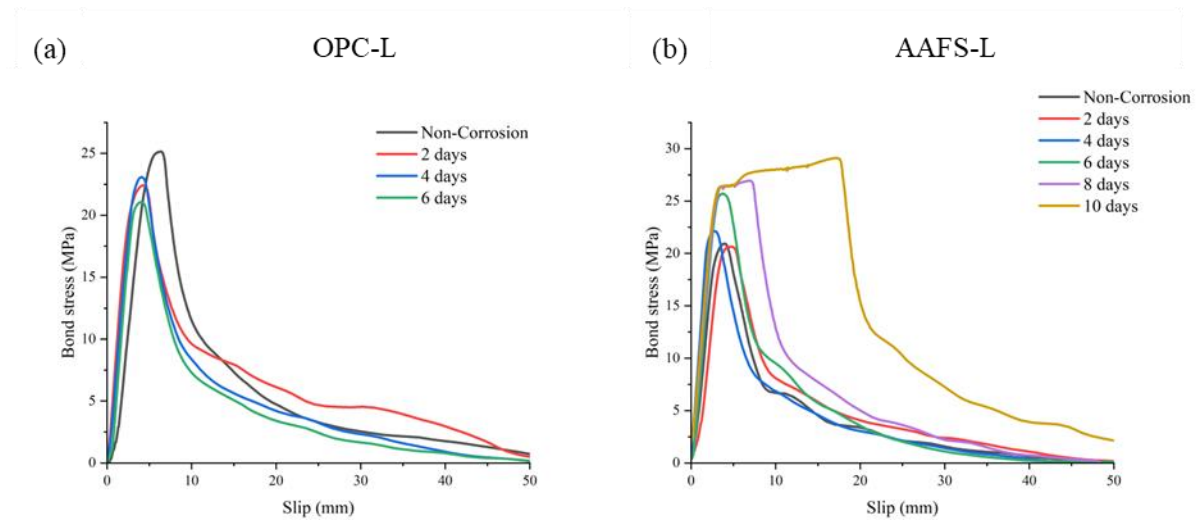


Figure 89. Pull-out test results for 50SA-50FA AAFS group and control OPC group

For samples subjected to 8 and 10 days of accelerated corrosion, a relatively horizontal plateau is observed after the peak, with the bond stress value gradually increasing. This increase is attributed to the plastic deformation of the steel rebar, as the local stress exceeds the critical value, and the applied load approaches the steel's yield strength. The increase in slip and bond stress during this stage is primarily due to plastic deformation, as illustrated in Figure 90.



Figure 90. Plastic deformation of the steel bar

To capture the evolution of the curve in the post-peak region, displacement-controlled pull-out tests were conducted on AAFS-L samples at a loading rate of 1 mm/min. Figure 91 presents the representative bond stress-slip curves for samples tested under the displacement-control method. The post-peak evolution of these curves, characterised by a distinct plateau stage followed by a gradual decrease in bond stress, differs significantly from those obtained under

load-controlled conditions, where the bond stress exhibits a sudden drop. Plastic deformation of the rebar was observed in all cases. In the post-peak regions, the curves for samples S7 and S8 exhibit a relatively small decline in bond stress and a prolonged plateau stage, highlighting the effect of residual bond capacity at the SCI. Although S9 has a higher corrosion degree than S10, the interface damage in S10 is more severe, as evidenced by the evolution curve. This results in reduced ductility and a more rapid loss of bond stress for S10. The splitting failure of S9, however, was attributed to stress concentration caused by rebar misalignment, as indicated in Figure 91 by the red rectangle.

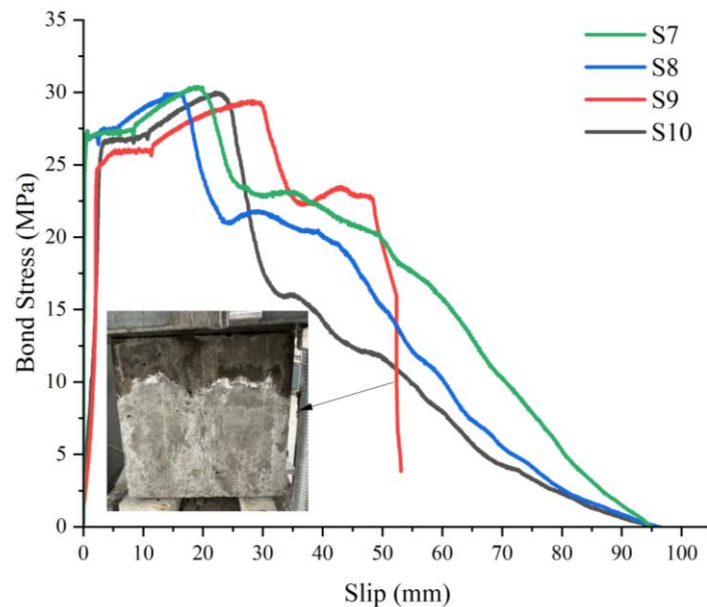


Figure 91. Bond stress-slip curve for AAFS sample under displacement control.

The corrosion level of the steel rebar in the bond zone was measured by splitting the specimen to extract the rebar after the tests were completed. Additionally, the condition of the bonded interface was examined, as shown in Figure 92. In the non-corrosion sample, rib marks are clearly visible on the bonded interface after the pull-out test, indicating strong bond performance between the steel bar and concrete. This observation also suggests that mechanical interlocking at the SCI plays a major role at low corrosion levels. As corrosion rust continues to accumulate at the SCI, the bonded interface deteriorates. This is evident in the interface of S7, where some rib marks are no longer visible compared to the non-corroded sample.

Although a small amount of corrosion rust at the SCI can enhance bond strength to some extent, excessive corrosion causes significant deterioration, as observed in S10. Consequently, the bond stress-slip curve for S10 in the post-peak region shows a rapid decline.



Figure 92. Surface after corrosion was split.

Based on the test results, a comparison of the average bond strength versus the corrosion degree for the AAFS-G, AAFS-L and OPC-L groups is presented in Figure 93. The average maximum bond strength of the AAFS-G samples is higher than that of the AAFS-L samples, which is attributed to the differences in rebar placement positions. In AAFS-G samples, when the non-bonded section (bottom section) of the rebar passes through the bonded zone during the pull-out process, the remaining rib marks in the bonded section create additional resistance, enhancing bond strength to some extent. In contrast, for the AAFS-L samples, the rebar is positioned at the bottom, leaving the upper part as non-bonded zone. As a result, no additional resistance from rib marks is observed in AAFS-L samples, leading to slightly lower average bond strength compared to AAFS-G samples.

For the overall evolution of average bond strength in AAFS-G samples, the maximum bond strength is reached at a corrosion degree of approximately 0.4%. Beyond this point, the average bond strength decreases rapidly as the corrosion degree increases. When the corrosion degree reaches around 0.9%, the average bond strength falls below that of the uncorroded samples. In

the AAFS-L samples, the maximum bond strength is achieved at a corrosion degree of approximately 0.6% and remains relatively high even as corrosion progresses. This behaviour is attributed to limestone providing a better ITZ compared to gravel, resulting in a more uniform distribution of corrosion products at the ITZ. This uniformity helps to mitigate stress concentrations caused by the accumulation of corrosion products. Moreover, although the OPC samples exhibit better bond properties than both AAFS samples at lower corrosion levels, their bond performance falls below that of AAFS samples at higher corrosion levels.

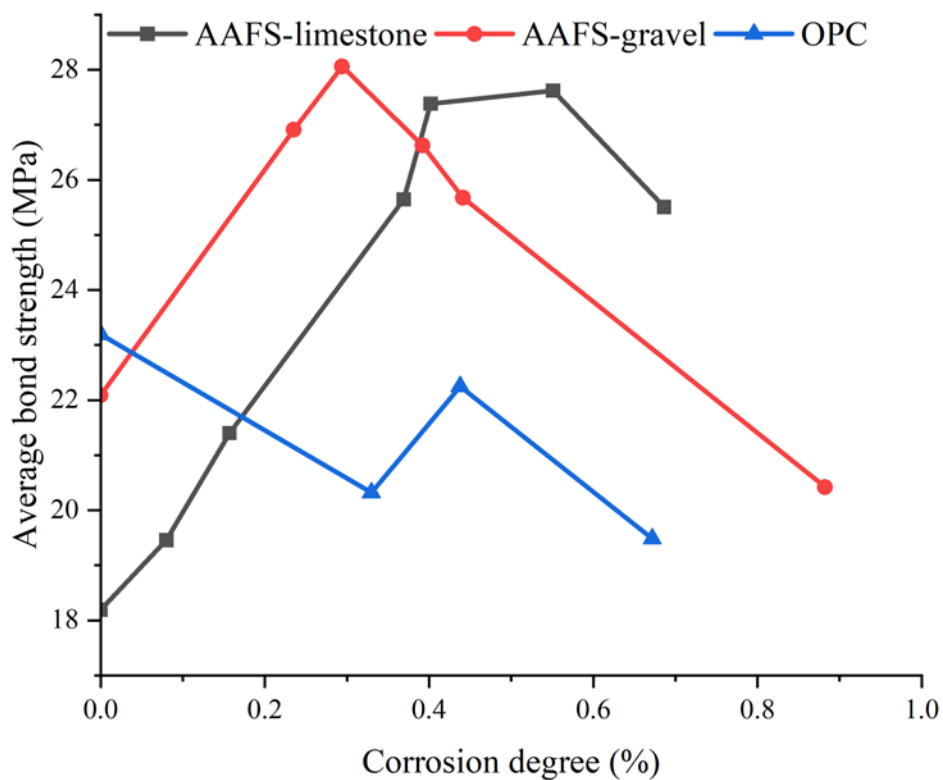


Figure 93. Bond strength relates to the corrosion degree

6.5 Discussion

As stated in Chapter 5, the hypothesis that sulphide products from SA cause low E_{corr} values and a weak passive film formed on the steel rebar surface [191,198,234] is not supported by the SEM-EDS measurements from this research. The SEM-EDS images reveal that the micro-gap thickness at the SMI for five types of reinforced AAFS mortars decreases as the SA content in the precursors increases, particularly in the nano-scale micro-gaps observed in 100SA samples. This behaviour is attributed to insufficient oxygen availability to form a stable passive

film, rather than sulphide-oxygen reactions weakening the passive film, as the sulphide content in the precursors is low (as shown in Table 6). Although the porous zone may contain some oxygen, its transport is restricted by the microstructural characteristics, specifically the presence of C-A-S-H gel [301,302]. Therefore, the more accurate explanation for the lower E_{corr} and C_{crit} values with the higher SA content lies in their microstructure characteristics, which limit oxygen availability.

The corrosion mechanisms in reinforced AAFS mortars, including microcell corrosion and macrocell corrosion, are evidenced by SEM-EDS and X-CT images. A critical micro-gap thickness range for corrosion mechanisms has been identified: microcell corrosion initiates when the thickness exceeds 10 μm , while macrocell corrosion occurs when the micro-gap thickness is below 2 μm . However, the corrosion behaviour in the intermediate range remains unclear. Observations from SEM-EDS images indirectly confirm the reduced oxygen availability at the SMI in small-thickness micro-gap, leading to the formation of unstable passive films.

The spatiotemporal evolution of corrosion in reinforced AAFS mortar samples with different steel rebar positions reveals variations in corrosion patterns and rates. Centrally positioned steel rebar exhibits relatively uniform corrosion distribution, whereas eccentrically positioned rebar shows irregular corrosion patterns due to non-uniform corrosion. Discontinuities around the rebar circumstance result in irregular corrosion distribution, making the von Mises model unsuitable for describing this behaviour unless the maximum corrosion part is significantly greater than other areas, as shown in the Figure 83. Although the AGvM model provides a better fit than the von Mises model, it is not applicable during early stages corrosion, where the distribution is discontinuous and exhibits multiple peaks.

Transverse cracks originating on the mortar surface and propagating toward the steel surface were identified through 3D reconstructed X-CT images (Figure 76), consistent with observations by Xi and Yang [235]. This crack pattern differs from corrosion-induced crack patterns that originate at the steel bar surface and propagate outward. Such patterns may be overlooked due to external factors, such as applied loads or impressed current methods [244,245,306]. This transverse crack pattern indicates a typical three-dimensional fracture process, as shown in Figure 76, rather than crack development along a single plane. Additionally, efflorescence caused by alkali leaching accelerates the fracture process in AAFS mortars by damaging the pore network.

Regarding the bond properties of reinforced AAFS concrete, limestone aggregate improves bond strength due to its larger size and shape compared to gravel. The position of the steel rebar influences bond strength during the early stages but has less impact after corrosion initiation, as stated in Section 6.4. Figure 93 shows that AAFS-L samples exhibit better corrosion resistance and retain higher bond strength than OPC-L samples. This performance is attributed to differences in microstructures; the C-A-S-H gel in AAFS has a finer microstructure than the C-S-H gel in OPC, enhancing the overall performance of AAFS-L samples.

6.6 Summary

In this chapter, the corrosion evolution and mechanisms of reinforced AAFS mortars were investigated through complementary use of SEM-EDS and X-CT techniques. The study further examined how steel bar corrosion affects the bond performance of AAFS concrete. Unlike general descriptions of corrosion in alkali-activated systems, the current findings provide quantitative microstructural insights that clarify how pore-scale features govern electrochemical behaviour and bond degradation.

- **Corrosion mechanisms:** SEM-EDS analysis confirm the presence of both microcell corrosion and macrocell corrosion mechanisms in reinforced AAFS mortar samples. A

critical micro-gap thickness range was identified: microcell corrosion initiates when the micro-gap at the SMI thickness exceeds 10 μm , while macrocell corrosion dominates when it falls below 2 μm . This threshold links the morphological characteristics at the SMI to specific corrosion types, offering a microstructural interpretation of corrosion initiation in AAFS. Furthermore, oxygen availability, limited by microstructural compactness, was confirmed to be the primary control parameter governing passive film stability and E_{corr} behaviour. This conclusion supports the findings presented in Chapter 5.

- **Corrosion evolution:** X-CT analysis revealed a spatiotemporal corrosion evolution in AAFS mortars. Centrally placed rebars exhibited more uniform corrosion, while eccentric positioning led to non-uniform, multi-peak degradation patterns. This geometric dependence limits the applicability of traditional models like von Mises unless corrosion localises significantly. Additionally, transverse cracks initiating at the mortar surface and propagating inward indicate a three-dimensional cracking mode, which is distinct from typical corrosion-induced cracking that initiates at the steel bar and propagates outward the surface. This type of cracking is likely to be misinterpreted in accelerated corrosion setups, especially in the absence of effective observation techniques, such as X-CT.
- **Bond degradation:** Pull-out test results demonstrated that limestone aggregate significantly improves bond strength, both before and after corrosion initiation. SEM evidence attributes this to the finer C-A-S-H gel matrix in AAFS compared to the C-S-H in OPC, which enhances the integrity of the SCI. Notably, the influence of bounded rebar position diminishes after corrosion initiation, implying that microstructural factors outweigh geometrical ones in long-term performance.

Overall, this study establishes that corrosion resistance and bond durability in AAFS systems are governed more by microstructure-driven oxygen transport dynamics than by the influence of sulphide content. These insights pave the way for performance-based durability models in AAFS concrete, with implications for both material design and structural assessment strategies.

7 Numerical Modelling Simulations

7.1 Introduction

As described in Section 3.5, numerical modelling simulations of the corrosion process in 50SA-50FA reinforced mortar were conducted, including the chloride transport within the mortar, corrosion initiation and propagation, as well as the distribution of corrosion rust. In this chapter, the simulation results are presented through the following aspects: the effect of isolated pores on chloride diffusion in the 50SA-50FA mortar based on the stated assumptions, the influence of steel bar position on corrosion initiation and propagation, the distribution of corrosion rust, and the fitting of the von Mises model. To distinguish the models, the one with the side-positioned steel bar is named S2-S, while the one with the centre-positioned steel bar is named M1-S.

An example of the COMSOL operation interface is shown in Figure 94. The parameters, including geometric configuration, diffusion of substances, potential distribution, electrochemical kinetics for corrosion evolution, and boundary conditions (such as surface chloride concentration), have already been introduced in Section 3.5.

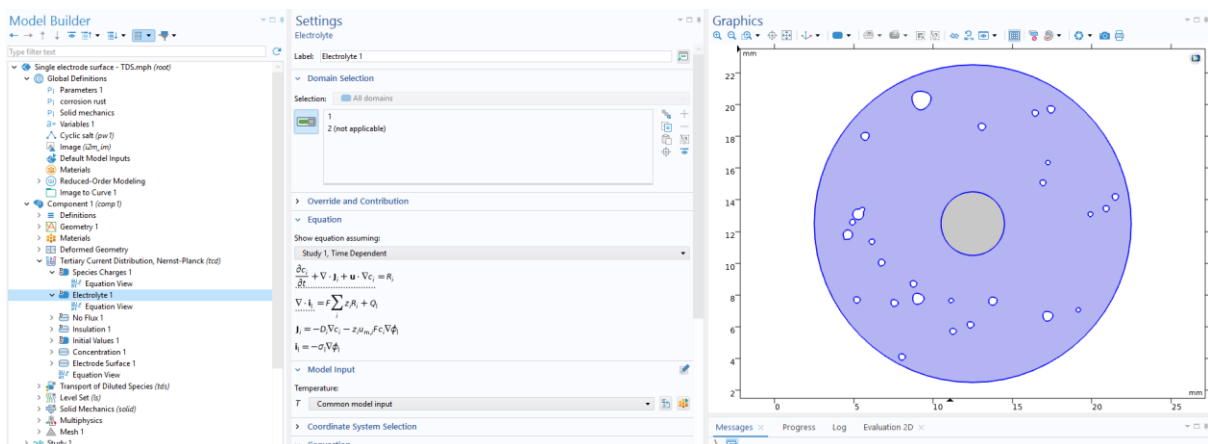


Figure 94. COMSOL operation interface

7.2 Chloride Diffusion and Oxygen Transportation

Figure 95 illustrates the simulated chloride ion concentration in the mortar at different time intervals. The concentration profile is visualised using a colour gradient, with a colour legend positioned on the right side of the graph. Additionally, contour lines represent zone of equal chloride ion concentration, highlighting the spatial pattern of chloride ion diffusion within the mortar. From the graph, it can be observed that the time required for chloride ions to initiate corrosion differs between the two models. Therefore, three representative time points were selected: the first day, the last day (corresponding to the initiation of steel bar corrosion), and the midpoint in time between these two days.

From Figure 95, it is observed that the chloride diffusion front reaches approximately one-third of the mortar model. The contour lines are not perfectly circular, showing disruptions around the isolated pores. This behaviour indicates that the isolated pores can delay the diffusion of chloride ions, though their smaller size reduces the efficiency of this effect, even with their non-uniform distribution in the mortar. In contrast, chloride diffusion in concrete samples is more significantly influenced by coarse aggregates, which act as more effective buffers and delay the diffusion process, as reported by Wang et al. [311].

On day 23 for the M1-S model and day 10 for the S2-S model, both simulations indicate that chloride ions have reached the steel surface. This can be observed through the colour gradient and legend bar for the M1-S model, and from the contour lines in the S2-S model. In the S2-S model, the presence of the steel bar significantly increases the diffusion path of chloride ions compared to linear diffusion observed in the M1-S model. While chloride ions accumulate more rapidly near the mortar boundary due to the shorter diffusion distance, transport toward the centre is delayed because the steel bar blocks direct transport, forcing ions to take a longer, curved route around the rebar. This occurs because the steel acts as a physical barrier, as shown in Figure 96. At these times points, although chloride ions have accumulated on the steel

surface to a certain extent, corrosion has not yet initiated, as the local chloride concentration remains below the C_{crit} value defined in Table 9. Consequently, corrosion does not initiate until chloride concentration exceeds this threshold.

At 45 days for the M1-S model and 22 days for the S2-S model, as chloride ions diffusion continues, their concentration gradually accumulates at the steel surface and exceeds the C_{crit} . The difference in corrosion initiation times between these two models is attributed to the placement of the steel bars, which results in different diffusion distances for chloride ions to reach the steel surface. In addition, the corrosion initiation in simulation will be discussed in the following section.

The oxygen transport behaviour in the mortar is illustrated in Figure 95. It can be observed that the oxygen concentration in the region surrounding the steel bar reaches the surface concentration defined in Table 9 after only one day. This is attributed to the high oxygen diffusion coefficient, which is approximately three orders of magnitude greater than that of chloride ions. Due to the lack of reliable data, the oxygen diffusion coefficient in AAFS mortar was approximated using the value reported for OPC mortar. This assumption is reasonably justified by the fact that oxygen can diffuse through both gaseous and liquid phases, resulting in a significantly higher effective diffusion rate compared to chloride ions. In addition, the 50SA-50FA mortar exhibits mechanical strength compared to OPC mortar, indicating a similar microstructural property, which justifies this assumption.

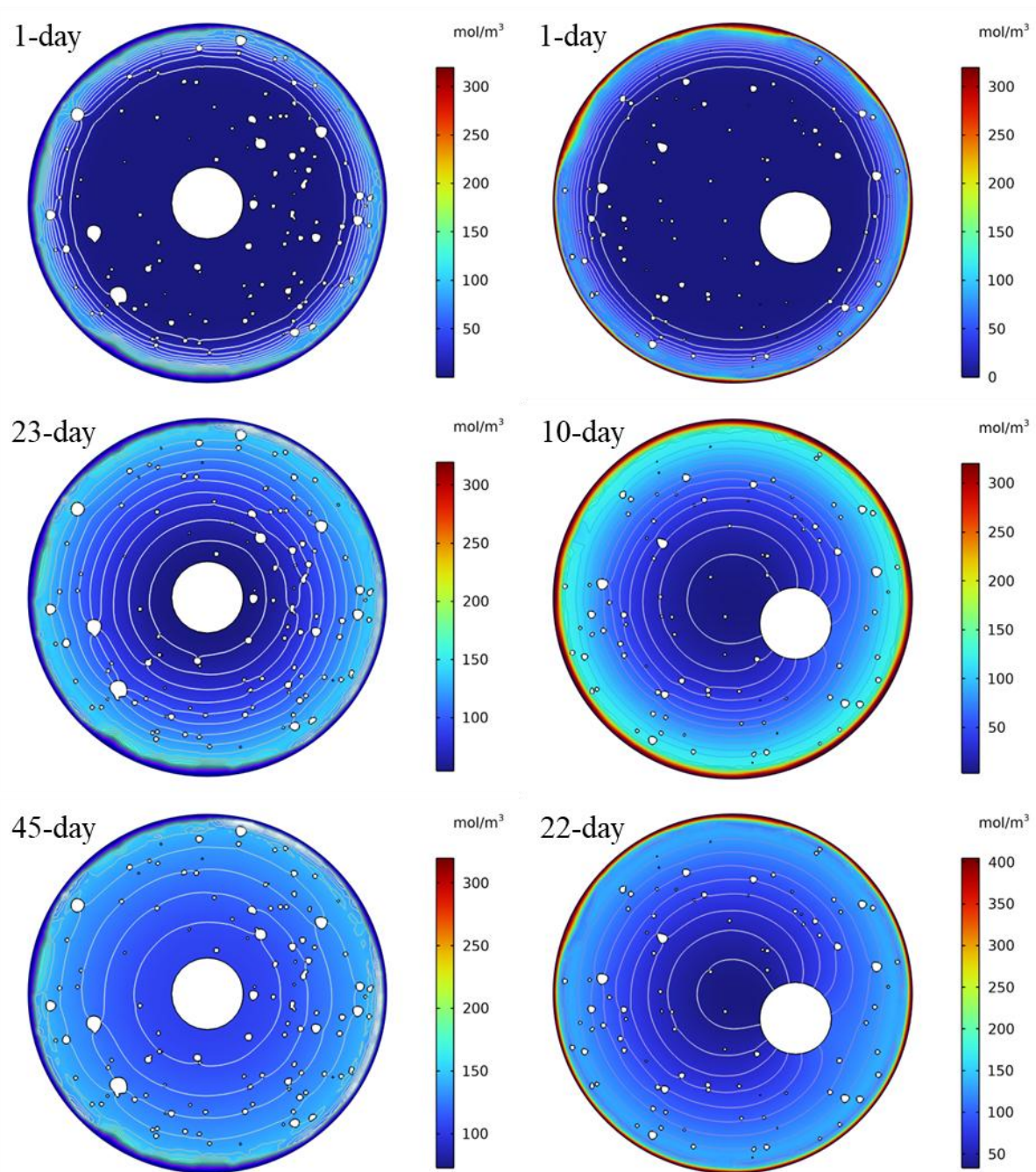


Figure 95. Concentration of chloride ions in mortars at different days of diffusion

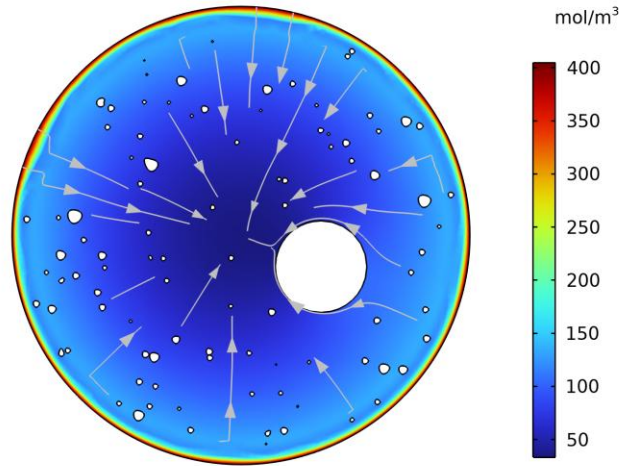


Figure 96. The diffusion pattern of chloride ions across the steel bar

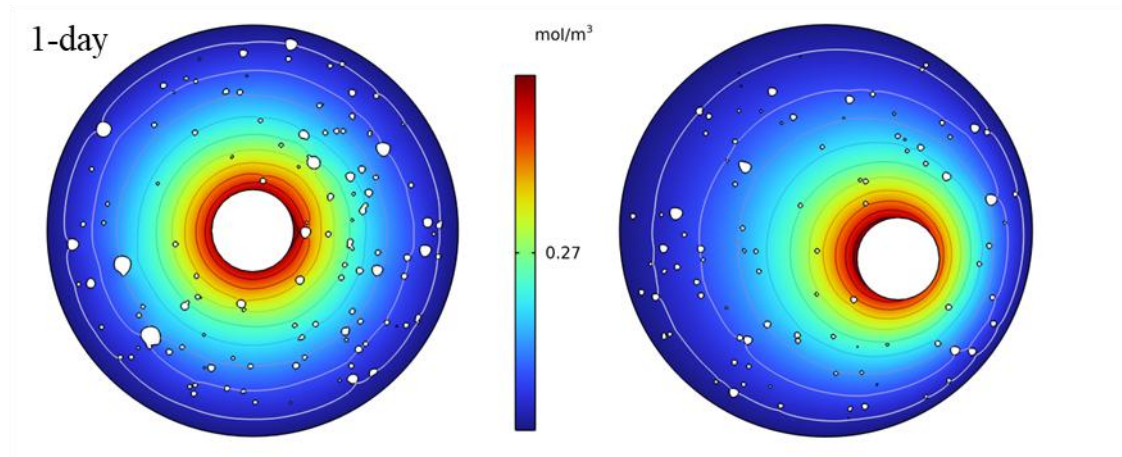


Figure 97. Oxygen concentration in the mortar for two models after 1-day

7.3 Corrosion Initiation and Propagation

Corrosion of the steel bar is initiated once the local chloride ion concentration exceeds the C_{crit} . Due to the non-uniform diffusion paths of chloride ions within the mortar, corrosion does not begin simultaneously along the entire steel surface; instead, different regions undergo corrosion initiation at different times. Figure 98 and Figure 99 depict the evolution of regions showing changes in electrolyte potential and electrode potential for the M1-S and S2-S models after corrosion initiation at various time intervals. The arrowed streamlines represent the electric current density vectors formed between the anode and cathode during the macrocell corrosion process.

In Figure 98 (a) and (b), corrosion in the M1-S model initiates in the top-left region, where the anode and cathode are closely adjacent. After 4 hours of corrosion, the active region gradually expands outward, while the passive region shifts, as shown in Figure 98 (c) and (d). By 8 hours, as shown in Figure 98 (e) and (f), the top region of the electrode fully transitions from the passive to the active, leaving only a small passive zone in the bottom-left corner. In contrast, the S2-S model, as shown in Figure 99, exhibits a more uniform transition between passive and active states, unlike the abrupt shifts seen in the M1-S model. This difference is attributed to the variation in chloride ion diffusion routes from the mortar surface to the steel surface between the two models. As detailed in the previous section, the diffusion route, combined with the buffering effect of isolated pores, results in the distinct corrosion initiation behaviours in the two models.

Both microcell and macrocell corrosion mechanisms are captured in the simulation. Using the M1-S model for illustration, Figure 100 presents the electric current densities in both selected active and passive region after 4 hours of corrosion initiation. As shown in Figure 100 (a) the active region is highlighted, with Figure 100 (b) displaying the corresponding anodic, cathodic, and total electric current densities. The anodic and cathodic current densities are nearly equal in magnitude, resulting in a total current density close to zero, characteristic of microcell corrosion, as illustrated in Figure 33. In contrast, the passive region (Figure 100 (c)), which remains inactivated state at this stage, as confirmed in Figure 98, exhibits a cathodic current density of approximately $-6.9\text{E-}10 \mu\text{A}/\text{cm}^2$ (Figure 100 (d)), nearly 10 orders of magnitude lower than that in the anode region.

These results suggest that although both microcell and macrocell corrosion mechanisms are present in AAFS system, the contribution of macrocell corrosion is considerably less

significant than that of microcell corrosion. A detailed discussion of this comparison is provided in the following section.

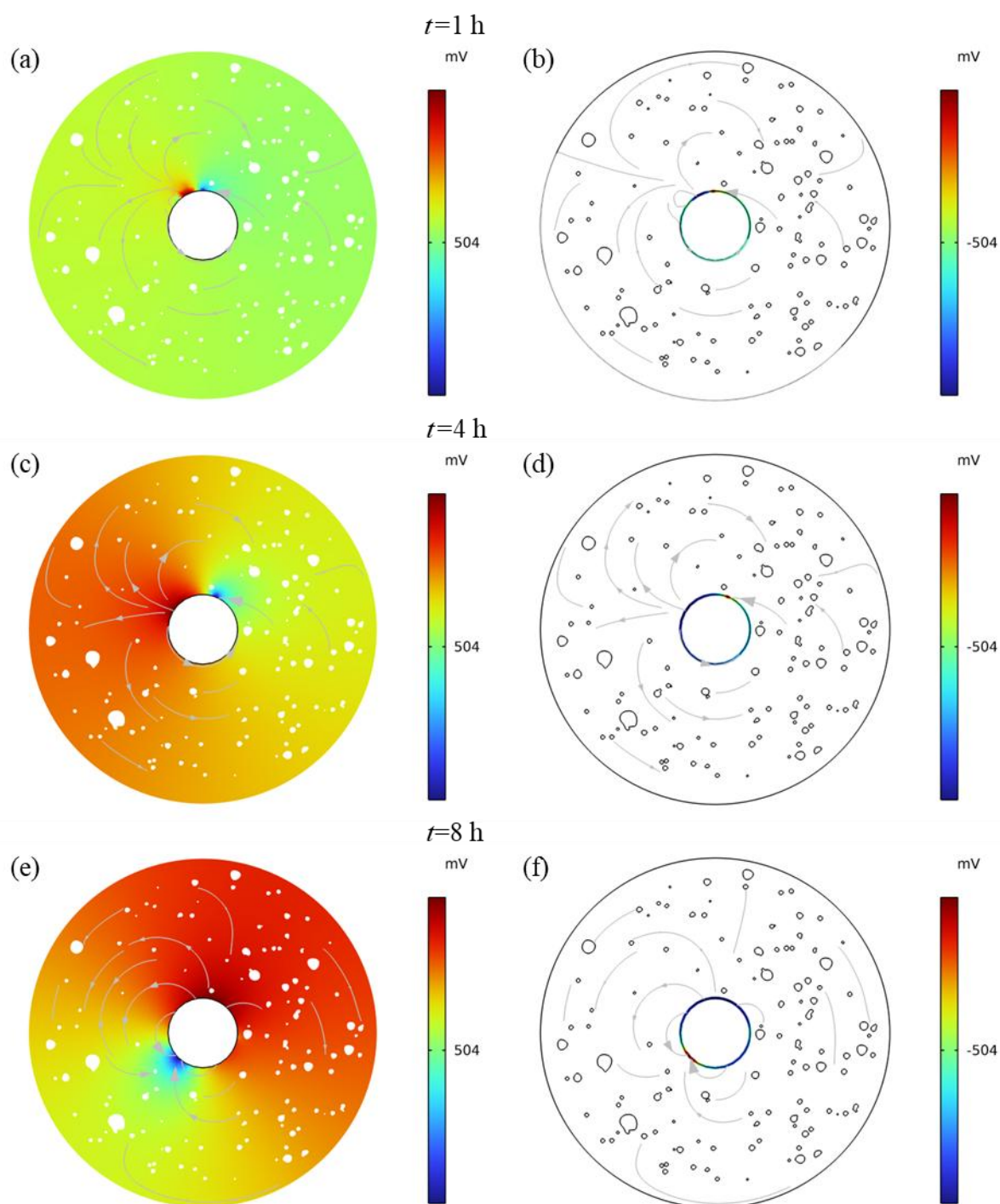


Figure 98. The evolution of the electrolyte potential (left) and electrode potential (right) for M1-S after corrosion initiation

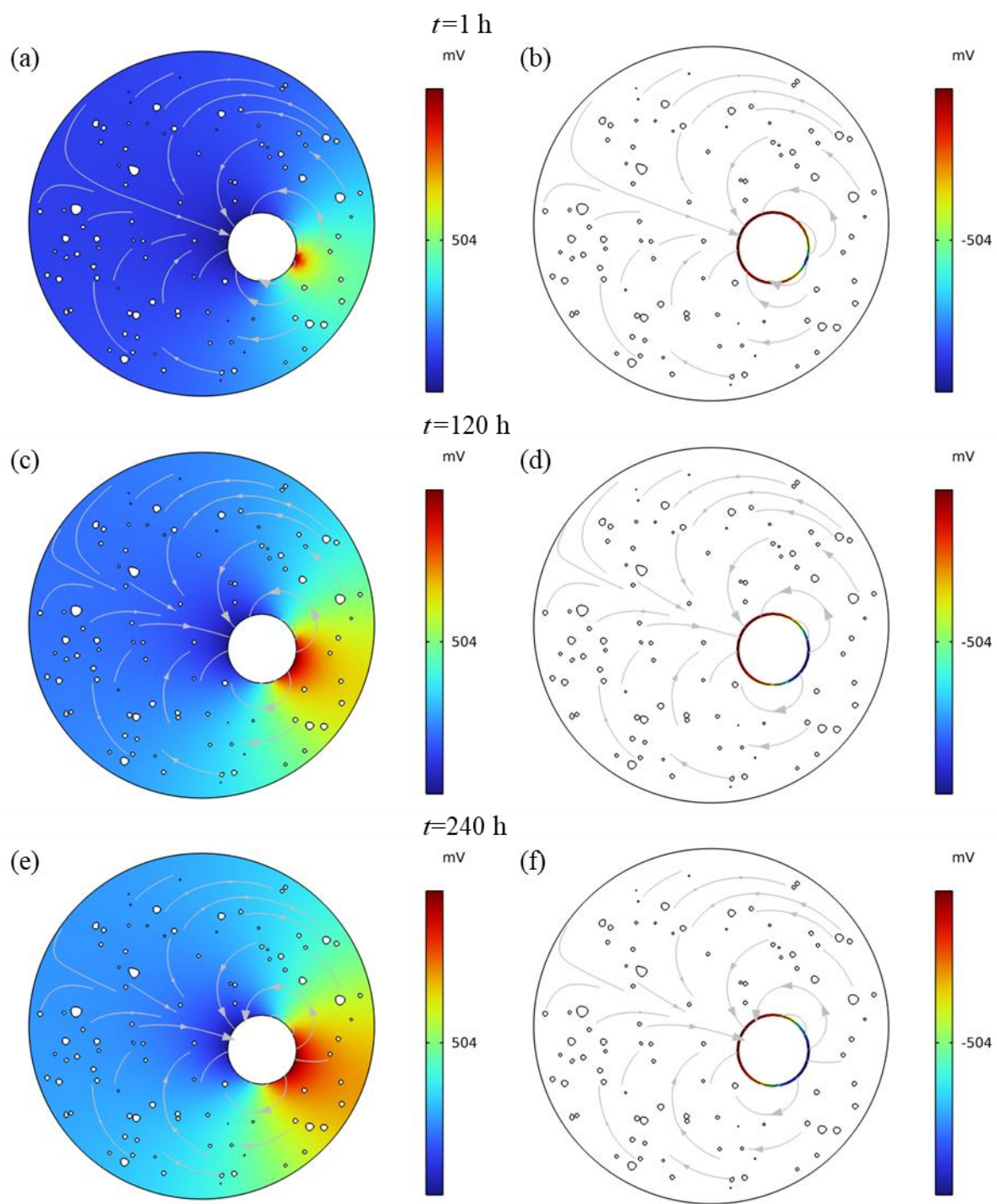


Figure 99. The evolution of the electrolyte potential (left) and electrode potential (right) for S2-S after corrosion initiation

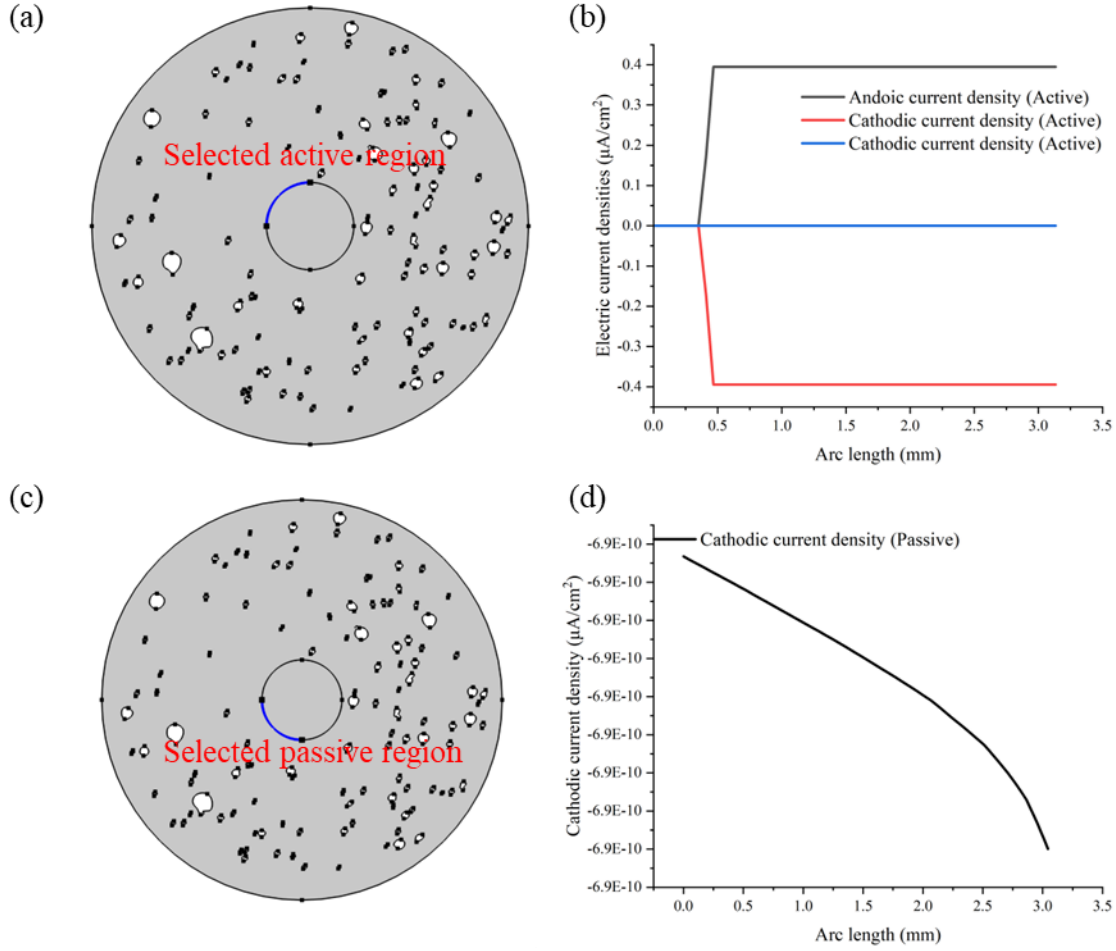


Figure 100. Electric current densities at electrode after corrosion initiation at 4 hours, (a) the active region and (b) the corresponding of anodic, cathodic and total electric current densities, (c) the passive region of the electrode and (d) the corresponding cathodic electric current densities at this region

7.4 Corrosion Rust Distribution

After corrosion initiation was identified in the simulation, an additional 240 hours of simulation time was conducted for both numerical models to investigate the corrosion evolution on the steel surface. Figure 98 and Figure 99 show that both models exhibit characteristics of microcell and macrocell corrosion. However, the transition from the passive to the active state of the steel occurs more rapidly in the M1-S model than in the S2-S model, leading to a distinct distribution corrosion rust on the steel surface.

To analysis the impact of this transition on corrosion distribution, polar plots depicting the radial loss of the steel bar along its full circumference at selected time points (25, 49, 73, 97,

196, and 240 hours) are presented in Figure 101. In Figure 101 (a), the radial losses profile of the centrally positioned steel shows an approximately circular pattern with more pronounced degradation in the top-left quadrant (between 90° and 150°). This observation aligns with the early corrosion initiation identified in this angular range in Figure 98. Due to the rapid depassivation process, microcell corrosion dominates in this model, resulting in a relatively uniform and concentric corrosion loss profile.

In contrast, for the S2-S model, a proportion of the steel bar remains in the passive state throughout the 240-hour post-corrosion initiation simulation, as shown in Figure 102. This is because the chloride concentration at certain regions of the steel surface does not reach the C_{crit} . Consequently, corrosion-induced radial losses are confined primarily to the bottom-right section of the steel bar. As shown in Figure 101 (b), the radial loss pattern appears radiation-like, with distinct peaks. As corrosion progresses, the sharpness of the peaks diminishes, and the profile becomes smoother. For example, the curves at 97 and 240 hours indicate a trend toward more uniform corrosion as the process continues.

Figure 103 presents the ratio of maximum to average radial loss along the steel circumference. With increasing corrosion time, this ratio stabilises in both models. In the M1-S model, the ratio initially exceeds 1 but rapidly declines to 1 and remains stable, indicating a transition to uniform corrosion. In contrast, the S2-S model shows an initial ratio of 15.4, which gradually decreases to approximately 5. This trend is consistent with previous findings [235,307-309] and reflects the differences between uniform and non-uniform corrosion behaviour. Although the M1-S model exhibits initial localised corrosion, the rapid progression and even distribution of depassivation ultimately result in a uniform corrosion classification.

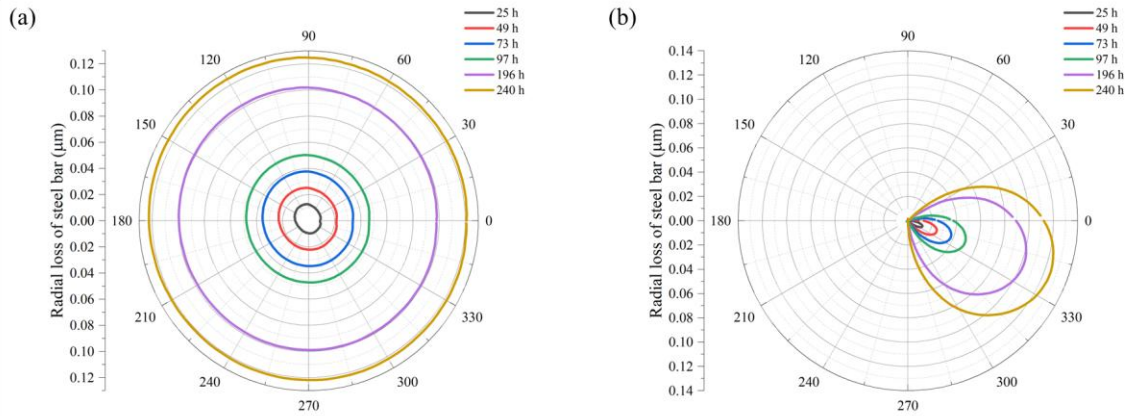


Figure 101. Radial loss of steel bar at different simulation hours after corrosion initiation

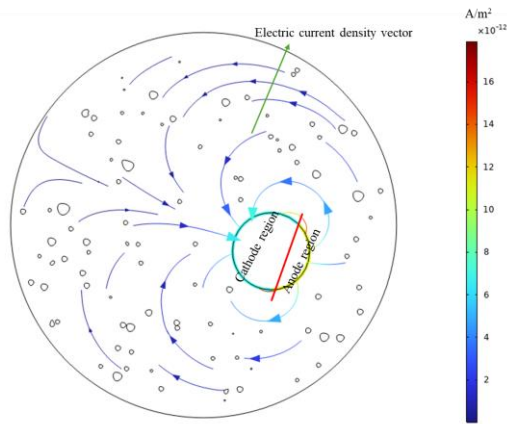


Figure 102. Corrosion condition for side-positioned steel bar at the 240 h after corrosion initiation

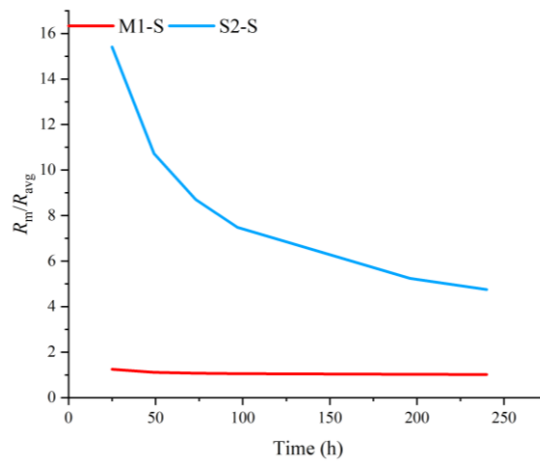


Figure 103. Ratios of maximum radial loss to average radial loss of the steel bar along the longitude direction

Figure 104 shows the corrosion distribution for both models. The thickness of the corrosion rust layer obtained from the simulations was extracted and fitted using the von Mises model

proposed by Xi and Yang [235], with the fitting results shown in Figure 105. This model is commonly used to describe angular distributions, particularly in circular or cylindrical systems, and is suitable for modelling directional variability, such as the non-uniform spread of corrosion around a steel bar. Figure 105 (a) and (b) show the fitting results for the S2-S model at 25 hours and 240 hours after corrosion initiation, while Figure 105 (c) and (d) depict the corresponding results for the M1-S model.

For the S2-S model, the initial spread of corrosion rust is limited to a narrow angular region but gradually expands over time. The corrosion rust thickness around the side-positioned steel bar demonstrates excellent agreement with the von Mises model throughout the simulation period. The R^2 exceeds 0.95 in both cases, indicating a high-quality fit.

In contrast, the M1-S model exhibits a more complex distribution pattern, characterised by two distinct peaks in corrosion rust thickness due to the non-uniformity initiation and progression of corrosion. Consequently, the von Mises model fails to adequately capture the spatial variability in corrosion development along the steel circumference. The R^2 values in this model range from 0.7 to 0.75, reflecting a relatively poor fit. Moreover, the R^2 value at 240 hours is lower than at 25 hours, suggesting that the corrosion distribution becomes increasingly non-uniform over time.

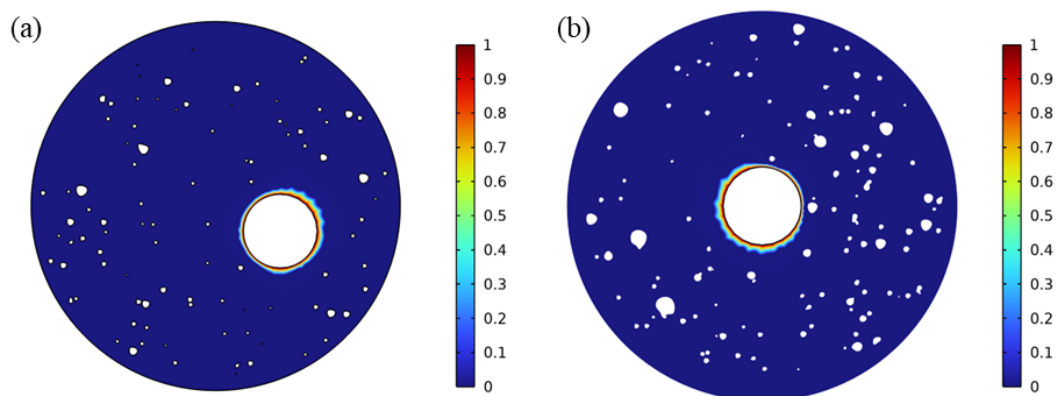


Figure 104. The corrosion distribution around the steel circumference at the 240 hours of accelerated corrosion

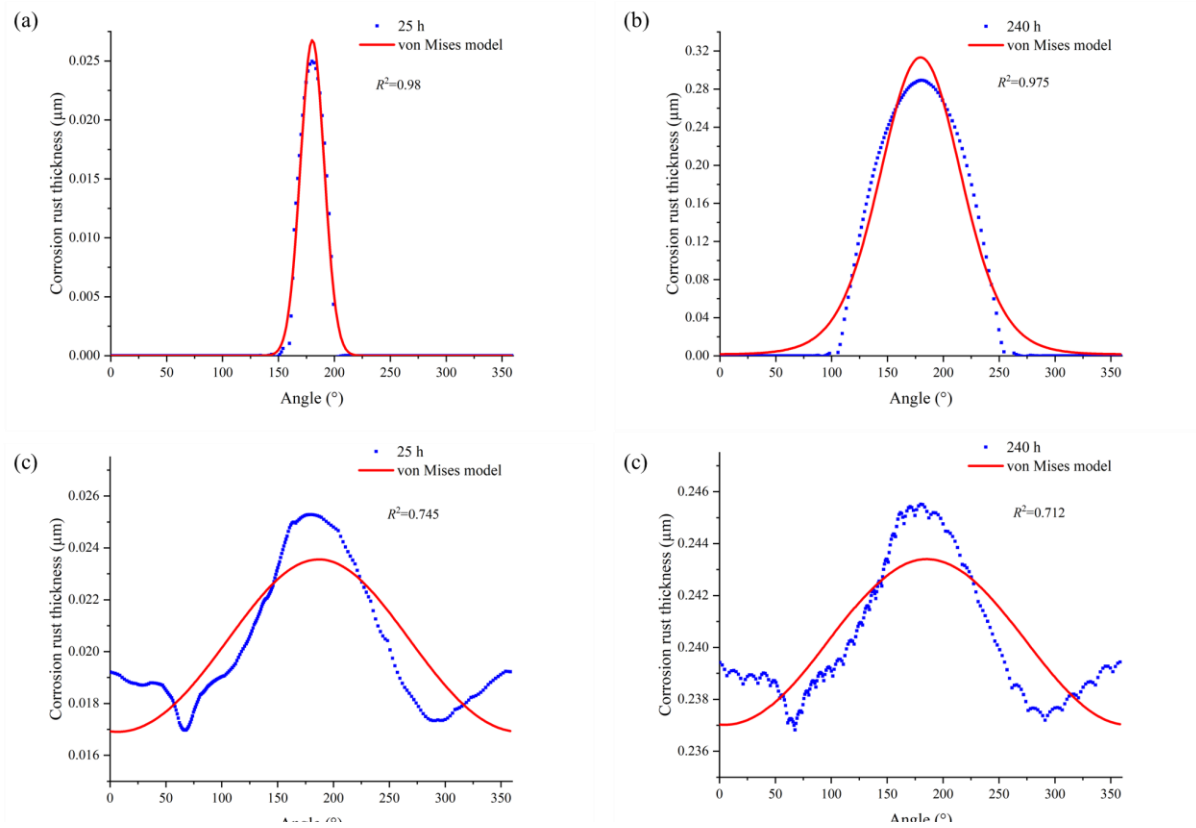


Figure 105. Corrosion rust thickness with von Mises model fitting of simulation results

7.5 Discussion

In this section, the simulation results are compared with the X-CT measurement data and discussed. The analysis begins with the timing of corrosion initiation. Based on the X-CT data, corrosion of the steel bar was observed at 97 cycles for both samples, M1 and S2. In the numerical simulation, corrosion initiation occurred earlier for S2-S (88 cycles (22 days)) and later for M1-S (180 cycles (45 days)). The relatively good agreement between S2 sample and the S2-S simulation model suggests that chloride diffusion coefficient and C_{crit} values used in the simulation align well with the accelerated corrosion conditions in the environmental chamber. Notably, slight corrosion was evident on steel bar in the S2 sample, as observed from the X-CT results, indicating that corrosion had likely initiated earlier. In contrast, the simulated corrosion initiation for M1-S model was significantly delayed compared to the experiment results. This discrepancy could be attributed to the C_{crit} value used in the simulation, which was

set as the average of the measured values (Table 17), possibly underestimating localised susceptibility.

As shown in Figure 95, chloride ions are observed to reach the steel bar surface in the simulation after 10 days of accelerated corrosion. When combined with the micro-gap thickness findings discussed in Section 6.2, it can be inferred that the passive film on the steel bar surface is not uniformly distributed under real conditions, leading to circumference variation in the C_{crit} . Additionally, efflorescence caused by alkali leaching and surface cracks observed in the mortar (Figure 50) likely accelerate corrosion initiation by increasing surface permeability and providing easier routes for chloride ingress, as discussed in Section 2.2.3.2. Therefore, the earlier onset of corrosion in the real M1 sample, compared to the delayed initiation in the M1-S simulation model, can be attributed to the combined effects of these factors.

Moreover, the microcracks observed on the surfaces of the M1 and S2 samples did not pre-exist but developed during the accelerated corrosion process. This distinction is important because most simulations studies on chloride diffusion in cracked concrete consider pre-existing cracks, rather than those formed dynamically during corrosion [312,313]. Due to the lack of mechanistic understanding, the effects of these corrosion-induced cracks were not included in the simulation.

As noted in Figure 100, the electric current density associated with macrocell corrosion is significantly lower than that associated with microcell corrosion, owing to the high electrical resistance of AAFS mortars. Consequently, although macrocell corrosion is present, its contribution to overall corrosion progression is minimal. Based on SEM-EDS analysis (Figure 67), macrocell corrosion may still play a role by establishing a potential field that facilitates

ion transport, such as Fe^{2+} , within the matrix. This effect may lead to the formation of corrosion rust even in passive regions not undergoing active corrosion, as shown in Figure 104.

The thickness of corrosion obtained from simulations was fitted using the von Mises model, as illustrated in Figure 105. This model, originally developed for circular distributions, is well-suited to representing angular variation around cylindrical steel surfaces. In the simulations, the von Mises model showed good agreement with the predicted corrosion rust profiles. However, the real sample exhibited less consistency with the von Mises model, as shown in Figure 106. This discrepancy arises because the real specimens are inherently 3D structure, allowing spatial effects to influence corrosion propagation, whereas the simulations were conducted in a 2D structure framework. Additionally, spatial variation in C_{crit} values within the real sample also contributes to the differences in corrosion behaviour.

Despite these differences, comparison of the R^2 values from Figure 105 (simulation) and Figure 84 (X-CT measurements) indicates a general agreement between simulated and experimental results. The simulated suggests that the von Mises model can describe corrosion rust distribution effectively when there is a single dominant peak or when the primary peak significantly exceeds secondary peaks. However, its applicability becomes limited in the presence of multiple peaks of comparable magnitude. This conclusion is further supported by the simulation results.

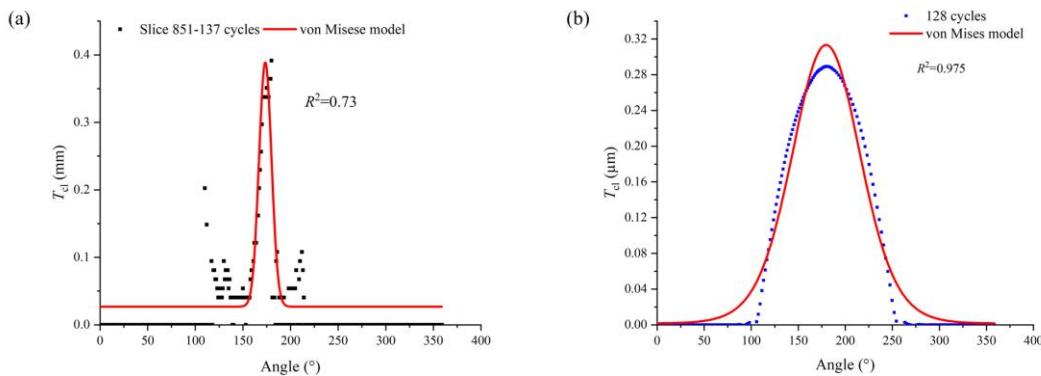


Figure 106. Comparison of von Mises model in real X-CT measurement and simulated results

7.6 Summary

In these two numerical simulations, the effects of isolated pore structure and the steel bar positioning on chloride diffusion were investigated. The simulations incorporated both macrocell and microcell corrosion mechanisms and analysed corrosion rust distribution using the von Mises model. The results were cross-validated against X-CT and SEM-EDS measurements, reinforcing the reliability of the simulation framework. Based on these findings, the following conclusions were drawn:

- **Effect of isolated pores and cover thickness:** The sizes and distribution of isolated pores in the mortar act as buffers that delay chloride transport by increasing tortuosity. However, their influence is significantly minor when compared to the impact of coarse aggregates in concrete. In mortar samples, cover thickness remains the dominant factor affecting corrosion initiation by controlling the diffusion path length. This highlights the importance of geometric parameters over local heterogeneities in pore structure.
- **Effect of microcell and macrocell corrosion:** Simulation results indicate that while macrocell corrosion exists, it contributes little to overall current generation due to the high electrical resistance of AAFS mortar. Its primary role is indirect: it helps establish a potential gradient that promotes Fe^{2+} ion migration within the matrix. In contrast, microcell corrosion dominates the degradation process and governs the observed material loss distribution.
- **Validation of simulation parameters:** The good agreement between simulation-predicted corrosion initiation times and X-CT observations, particularly in the S2-S model, demonstrates the suitability of the chosen chloride diffusion coefficients and C_{crit} values. This supports the reliability of these parameters for modelling corrosion in AAFS systems under accelerated conditions.

- **Performance of the von Mises model:** The von Mises distribution effectively captures the evolution of corrosion rust when a single dominant peak is present. However, its accuracy diminishes in cases with multiple corrosion fronts or sub-peaks of comparable magnitude. This limitation is especially evident in the M1-S model, where non-uniform corrosion progression due to complex diffusion patterns leads to poor fitting at later stages. Thus, while useful for identifying overall rust symmetry, the model lacks sensitivity for spatially complex corrosion development.

Overall, these simulations offer mechanistic insights into the interplay between pore structure, steel positioning, and electrochemical behaviour in AAFS mortars, providing a computational tool to predict corrosion evolution and evaluate model assumptions. The findings also suggest that simplified assumptions (e.g., uniform C_{crit}) may need refinement to fully capture corrosion variability under real-world conditions.

8 Conclusions and Future Work

8.1 Conclusions

This research investigated the corrosion behaviour of reinforced AAFS concretes, beginning with an evaluation of the mechanical properties across five mix proportions, ranging from high- to low-calcium systems. The measured mechanical strengths reveal the influence of microstructural development on mechanical properties, as calcium content varied. Electrochemical samples were then tested under cyclic wetting-drying accelerated conditions to monitor corrosion in reinforced AAFS mortars. Key parameters such as the Tafel constant B and E_{corr} were measured and compared with values typical for OPC-based systems. Furthermore, morphological and spatiotemporal analyses of SMI, combined with pull-out tests and numerical simulations, provided a comprehensive understanding of corrosion initiation and progression. The main findings are summarised below:

Mechanical properties:

- Compressive strength increases with SA content, especially at early ages. Mortar samples exhibit reduced strength at 28 days compared to 14 days, while concrete samples show continued strength gain, attributed to the "wall effect" from aggregates that enhance reactivity at the ITZ.
- Higher SA content improves fracture toughness but also increases brittleness, reducing ductility in AAFS concrete beams.

Electrochemical properties:

- Saturation significantly affect E_{corr} measurements; Saturated samples generally exhibit misleadingly low E_{corr} values, potentially leading to incorrect corrosion assessments.

- Tafel constant B values in reinforced AAFS mortars, ranging from 20 to 22 mV in the passive state and 50 to 55 mV in the corrosion state, differ significantly from the empirical values commonly used for reinforced OPC.
- A corrosion determination method tailored for reinforced AAFS mortars is proposed, with guidance on environmental conditions for valid measurement.

Steel-mortar/concrete interface:

- Passive film thickness decreases with increasing SA content, as supported by reduced chloride threshold C_{crit} values and SEM-EDS observations.
- Both microcell and macrocell corrosion were identified, but simulations and imaging confirm microcell corrosion as the dominant mechanism in AAFS.
- X-CT measurements revealed spatiotemporal corrosion evolution, including transverse cracks propagating from the mortar surface to the steel bar and longitudinal cracking around the rebar.
- Pull-out test results indicated that the reinforced AAFS concrete samples with limestone aggregates exhibit superior bond properties compared to reinforced OPC concrete samples, particularly after corrosion initiation.

Numerical simulations:

- Simulations confirmed the dominant influence of microcell corrosion on reinforcement degradation, with macrocell corrosion playing a minor role in ionic redistribution.
- Experimentally obtained data, such as the chloride threshold, are validated through the numerical simulations, confirming their accuracy under the simulated conditions.
- The von Mises distribution accurately represents corrosion rust evolution when a single dominant peak is present. However, its predictive ability diminishes in cases of multiple corrosion fronts.

8.2 Future work

Future work will focus on the following directions:

- Optimisation of mix proportions: The current mix proportions, designed to achieve maximum sample strength, will be optimised. The concentration of the alkaline activator will be adjusted to minimise alkali leaching and reduce efflorescence.
- Extension to fibre-reinforced AAFS concrete: Mechanical and fracture tests will be extended from plain AAFS concrete to fibre-reinforced AAFS concrete. This will explore the effect of fibres on mechanical strength and fracture properties, as fibres are known to enhance the ductility of concrete.
- Comprehensive bond performance study: Pull-out tests will be conducted to additional mix proportions to comprehensively investigate bond performance across different gel phases.
- Spatiotemporal evolution via X-CT (continuation): The spatiotemporal evolution of X-CT samples will continue to be studied to further trace material phase changes as corrosion progresses. The data obtained will contribute to the development and refinement of numerical simulation models.
- Advancement of numerical simulations: Numerical simulations will be expanded from 2D to 3D to better represent actual sample conditions. This will involve determining parameters such as the porosity through literature review or experiments. Additionally, the effects of efflorescence, such as surface spalling and volume reduction, which accelerate chloride ions diffusion and oxygen transport, will be incorporated. The 3D corrosion model will be gradually refined and improved.

References

- [1] Scrivener, K.L. et al. (2018) 'Eco-efficient cements: Potential economically viable solutions for a low-CO₂ cement-based materials industry', *Cement and Concrete Research*, 114 pp. 2-26. doi:<http://dx.doi.org/10.1016/j.cemconres.2018.03.015>.
- [2] Chen, C. et al. (2022) 'A striking growth of CO₂ emissions from the global cement industry driven by new facilities in emerging countries', *Environmental Research Letters*, 17 (4), pp. 044007. doi:<http://dx.doi.org/10.1088/1748-9326/ac48b5>.
- [3] Habert, G. et al. (2010) 'Cement production technology improvement compared to factor 4 objectives', *Cement and Concrete Research*, 40 (5), pp. 820-826. doi:<http://dx.doi.org/10.1016/j.cemconres.2009.09.031>.
- [4] Ali, M.B., Saidur, R. and Hossain, M.S. (2011) 'A review on emission analysis in cement industries', *Renewable and Sustainable Energy Reviews*, 15 (5), pp. 2252-2261. doi:<http://dx.doi.org/10.1016/j.rser.2011.02.014>.
- [5] Allen, M.R. et al. (2022) 'Net Zero: Science, Origins, and Implications', *Annual Review of Environment and Resources*, 47 (1), pp. 849-887. doi:<http://dx.doi.org/10.1146/annurev-environ-112320-105050>.
- [6] Provis, J.L. (2013) 'Geopolymers and other alkali activated materials: why, how, and what?', *Materials and Structures*, 47 (1-2), pp. 11-25. doi:<http://dx.doi.org/10.1617/s11527-013-0211-5>.
- [7] Awoyera, P. and Adesina, A. (2019) 'A critical review on application of alkali activated slag as a sustainable composite binder', *Case Studies in Construction Materials*, 11 pp. e00268. doi:<http://dx.doi.org/10.1016/j.cscm.2019.e00268>.
- [8] Provis, J.L. et al. (2012) 'X-ray microtomography shows pore structure and tortuosity in alkali-activated binders', *Cement and Concrete Research*, 42 (6), pp. 855-864. doi:<http://dx.doi.org/10.1016/j.cemconres.2012.03.004>.
- [9] García-Lodeiro, I., Fernández-Jiménez, A. and Palomo, A. (2013) 'Variation in hybrid cements over time. Alkaline activation of fly ash–portland cement blends', *Cement and Concrete Research*, 52 pp. 112-122. doi:<http://dx.doi.org/10.1016/j.cemconres.2013.03.022>.
- [10] Duxson, P. et al. (2005) 'Understanding the relationship between geopolymer composition, microstructure and mechanical properties', *Colloids and Surfaces A: Physicochemical and Engineering Aspects*, 269 (1-3), pp. 47-58. doi:<http://dx.doi.org/10.1016/j.colsurfa.2005.06.060>.
- [11] Guo, X.L., Shi, H.S. and Dick, W.A. (2010) 'Compressive strength and microstructural characteristics of class C fly ash geopolymer', *Cement and Concrete Composites*, 32 (2), pp. 142-147. doi:<http://dx.doi.org/10.1016/j.cemconcomp.2009.11.003>.
- [12] Mo, K.H., Alengaram, U.J. and Jumaat, M.Z. (2016) 'Structural performance of reinforced geopolymer concrete members: A review', *Construction and Building Materials*, 120 pp. 251-264. doi:<http://dx.doi.org/10.1016/j.conbuildmat.2016.05.088>.
- [13] Provis, J.L. and Bernal, S.A. (2014) 'Geopolymers and Related Alkali-Activated Materials', *Annual Review of Materials Research*, 44 (1), pp. 299-327. doi:<http://dx.doi.org/10.1146/annurev-matsci-070813-113515>.
- [14] Angst, U. et al. (2009) 'Critical chloride content in reinforced concrete - A review', *Cement and Concrete Research*, 39 (12), pp. 1122-1138. doi:<http://dx.doi.org/10.1016/j.cemconres.2009.08.006>.
- [15] Manera, M., Vennesland, O. and Bertolini, L. (2008) 'Chloride threshold for rebar corrosion in concrete with addition of silica fume', *Corrosion Science*, 50 (2), pp. 554-560. doi:<http://dx.doi.org/10.1016/j.corsci.2007.07.007>.

- [16] Yu, Y.G. et al. (2020) 'Modelling steel corrosion under concrete non-uniformity and structural defects', *Cement and Concrete Research*, 135 pp. 106109. doi:<http://dx.doi.org/10.1016/j.cemconres.2020.106109>.
- [17] Chen, E. and Leung, C.K.Y. (2015) 'Finite element modeling of concrete cover cracking due to non-uniform steel corrosion', *Engineering Fracture Mechanics*, 134 pp. 61-78. doi:<http://dx.doi.org/10.1016/j.engfracmech.2014.12.011>.
- [18] Xi, X. et al. (2018) 'Meso-scale mixed-mode fracture modelling of reinforced concrete structures subjected to non-uniform corrosion', *Engineering Fracture Mechanics*, 199 pp. 114-130. doi:<http://dx.doi.org/10.1016/j.engfracmech.2018.05.036>.
- [19] Zhao, Y.X. et al. (2011) 'Comparison of uniform and non-uniform corrosion induced damage in reinforced concrete based on a Gaussian description of the corrosion layer', *Corrosion Science*, 53 (9), pp. 2803-2814. doi:<http://dx.doi.org/10.1016/j.corsci.2011.05.017>.
- [20] Dekoster, M. et al. (2003) 'Modelling of the flexural behaviour of RC beams subjected to localised and uniform corrosion', *Engineering Structures*, 25 (10), pp. 1333-1341. doi:[http://dx.doi.org/10.1016/S0141-0296\(03\)00108-1](http://dx.doi.org/10.1016/S0141-0296(03)00108-1).
- [21] Monticelli, C. et al. (2016) 'Corrosion behavior of steel in alkali-activated fly ash mortars in the light of their microstructural, mechanical and chemical characterization', *Cement and Concrete Research*, 80 pp. 60-68. doi:<http://dx.doi.org/10.1016/j.cemconres.2015.11.001>.
- [22] Ma, Q.M. et al. (2016) 'Chloride transport and the resulting corrosion of steel bars in alkali activated slag concretes', *Materials and Structures*, 49 (9), pp. 3663-3677. doi:<http://dx.doi.org/10.1617/s11527-015-0747-7>.
- [23] Runci, A. and Serdar, M. (2022) 'Effect of curing time on the chloride diffusion of alkali-activated slag', *Case Studies in Construction Materials*, 16 pp. e00927. doi:<http://dx.doi.org/10.1016/j.cscm.2022.e00927>.
- [24] Royal Academy of Engineering (2021) 'Decarbonising construction: building a new net zero industry'. doi: <https://raeng.org.uk/news/construction-sector-must-move-further-and-faster-to-curb-carbon-emissions-say-engineers>.
- [25] UK Government (2021) 'Net Zero Strategy: Build Back Greener'. doi: <https://www.gov.uk/government/publications/net-zero-strategy>.
- [26] Stewart, M.G. and Bastidas-Arteaga, E. (2019) 'Corrosion of concrete and steel structures in a changing climate'. *Climate Adaptation Engineering*. Elsevier, pp. 99-125.
- [27] Andrade, C. et al. (2004) 'Test methods for on-site corrosion rate measurement of steel reinforcement in concrete by means of the polarization resistance method', *Materials and Structures*, 37 (273), pp. 623-643. doi:<http://dx.doi.org/10.1007/Bf02483292>.
- [28] Elsener, B. et al. (2003) 'Half-cell potential measurements - Potential mapping on reinforced concrete structures', *Materials and Structures*, 36 (261), pp. 461-471. doi:<http://dx.doi.org/10.1007/Bf02481526>.
- [29] Criado, M. et al. (2018) 'Influence of slag composition on the stability of steel in alkali-activated cementitious materials', *Journal of Materials Science*, 53 (7), pp. 5016-5035. doi:<http://dx.doi.org/10.1007/s10853-017-1919-3>.
- [30] Tennakoon, C. et al. (2017) 'Chloride ingress and steel corrosion in geopolymer concrete based on long term tests', *Materials & Design*, 116 pp. 287-299. doi:<http://dx.doi.org/10.1016/j.matdes.2016.12.030>.
- [31] Lv, W., Sun, Z.Q. and Su, Z.J. (2020) 'Study of seawater mixed one-part alkali activated GGBFS-fly ash', *Cement and Concrete Composites*, 106 pp. 103484. doi:<http://dx.doi.org/10.1016/j.cemconcomp.2019.103484>.
- [32] Gunasekara, C. et al. (2019) 'Chloride induced corrosion in different fly ash based geopolymer concretes', *Construction and Building Materials*, 200 pp. 502-513. doi:<http://dx.doi.org/10.1016/j.conbuildmat.2018.12.168>.

- [33] Yodsudjai, W. and Pattarakittam, T. (2017) 'Factors influencing half-cell potential measurement and its relationship with corrosion level', *Measurement*, 104 pp. 159-168. doi:<http://dx.doi.org/10.1016/j.measurement.2017.03.027>.
- [34] van Deventer, J.S.J. et al. (2010) 'Chemical Research and Climate Change as Drivers in the Commercial Adoption of Alkali Activated Materials', *Waste and Biomass Valorization*, 1 (1), pp. 145-155. doi:<http://dx.doi.org/10.1007/s12649-010-9015-9>.
- [35] Provis, J.L. (2018) 'Alkali-activated materials', *Cement and Concrete Research*, 114 pp. 40-48. doi:<http://dx.doi.org/10.1016/j.cemconres.2017.02.009>.
- [36] Provis, J.L. and Van Deventer, J.S. (2013) *Alkali activated materials: state-of-the-art report*, RILEM TC 224-AAM. Springer Dordrecht.
- [37] Ding, Y., Dai, J.G. and Shi, C.J. (2016) 'Mechanical properties of alkali-activated concrete: A state-of-the-art review', *Construction and Building Materials*, 127 pp. 68-79. doi:<http://dx.doi.org/10.1016/j.conbuildmat.2016.09.121>.
- [38] Ma, C.K., Awang, A.Z. and Omar, W. (2018) 'Structural and material performance of geopolymer concrete: A review', *Construction and Building Materials*, 186 pp. 90-102. doi:<http://dx.doi.org/10.1016/j.conbuildmat.2018.07.111>.
- [39] Ismail, I. et al. (2014) 'Modification of phase evolution in alkali-activated blast furnace slag by the incorporation of fly ash', *Cement and Concrete Composites*, 45 pp. 125-135. doi:<http://dx.doi.org/10.1016/j.cemconcomp.2013.09.006>.
- [40] Duxson, P. et al. (2007) 'The role of inorganic polymer technology in the development of 'green concrete'', *Cement and Concrete Research*, 37 (12), pp. 1590-1597. doi:<http://dx.doi.org/10.1016/j.cemconres.2007.08.018>.
- [41] Li, N. et al. (2017) 'Composition design and performance of alkali-activated cements', *Materials and Structures*, 50 (3), pp. doi:<http://dx.doi.org/10.1617/s11527-017-1048-0>.
- [42] Gao, X., Yu, Q. and Brouwers, H. (2015) 'Characterization of alkali activated slag-fly ash blends containing nano-silica', *Construction and Building Materials*, 98 pp. 397-406. doi:<http://dx.doi.org/10.1016/j.conbuildmat.2015.08.086>.
- [43] Zhang, F., Xi, X. and Yang, S.T. (2021) 'Research Progress in Corrosion Mechanism of Reinforced Alkali-Activated Concrete Structures', *Corrosion and Materials Degradation*, 2 (4), pp. 641-656. doi:<http://dx.doi.org/10.3390/cmd2040034>.
- [44] Duxson, P., Lukey, G.C. and van Deventer, J.S. (2006) 'Evolution of gel structure during thermal processing of Na-geopolymer gels', *Langmuir*, 22 (21), pp. 8750-8757. doi:<http://dx.doi.org/10.1021/la0604026>.
- [45] Duxson, P. et al. (2007) 'The effect of alkali and Si/Al ratio on the development of mechanical properties of metakaolin-based geopolymers', *Colloids and Surfaces A: Physicochemical and Engineering Aspects*, 292 (1), pp. 8-20. doi:<http://dx.doi.org/10.1016/j.colsurfa.2006.05.044>.
- [46] Criado, M., Aperador, W. and Sobrados, I. (2016) 'Microstructural and Mechanical Properties of Alkali Activated Colombian Raw Materials', *Materials*, 9 (3), pp. 158. doi:<http://dx.doi.org/10.3390/ma9030158>.
- [47] Nath, S. and Kumar, S. (2017) 'Reaction kinetics, microstructure and strength behavior of alkali activated silico-manganese (SiMn) slag-Fly ash blends', *Construction and Building Materials*, 147 pp. 371-379. doi:<http://dx.doi.org/10.1016/j.conbuildmat.2017.04.174>.
- [48] Ye, H.L. and Radlinska, A. (2016) 'Fly ash-slag interaction during alkaline activation: Influence of activators on phase assemblage and microstructure formation', *Construction and Building Materials*, 122 pp. 594-606. doi:<http://dx.doi.org/10.1016/j.conbuildmat.2016.06.099>.
- [49] Reddy, K.C. and Subramaniam, K.V.L. (2021) 'Investigation on the roles of solution-based alkali and silica in activated low-calcium fly ash and slag blends', *Cement and Concrete Composites*, 123 pp. 104175. doi:<http://dx.doi.org/10.1016/j.cemconcomp.2021.104175>.

- [50] Rafeet, A. et al. (2019) 'Effects of slag substitution on physical and mechanical properties of fly ash-based alkali activated binders (AABs)', *Cement and Concrete Research*, 122 pp. 118-135. doi:<http://dx.doi.org/10.1016/j.cemconres.2019.05.003>.
- [51] Lau, C.K. et al. (2019) 'Investigation of geopolymers containing fly ash and ground-granulated blast-furnace slag blended by amorphous ratios', *Construction and Building Materials*, 222 pp. 731-737. doi:<http://dx.doi.org/10.1016/j.conbuildmat.2019.06.198>.
- [52] Zhao, X.H. et al. (2019) 'Investigation into the effect of calcium on the existence form of geopolymerized gel product of fly ash based geopolymers', *Cement and Concrete Composites*, 103 pp. 279-292. doi:<http://dx.doi.org/10.1016/j.cemconcomp.2018.11.019>.
- [53] Marjanović, N. et al. (2015) 'Physical-mechanical and microstructural properties of alkali-activated fly ash-blast furnace slag blends', *Ceramics International*, 41 (1), pp. 1421-1435. doi:<http://dx.doi.org/10.1016/j.ceramint.2014.09.075>.
- [54] Xing, J. et al. (2019) 'Microstructural and Mechanical Properties of Alkali Activated Materials from Two Types of Blast Furnace Slags', *Materials*, 12 (13), pp. 2089. doi:<http://dx.doi.org/10.3390/ma12132089>.
- [55] Deir, E., Gebregziabher, B.S. and Peethamparan, S. (2014) 'Influence of starting material on the early age hydration kinetics, microstructure and composition of binding gel in alkali activated binder systems', *Cement and Concrete Composites*, 48 pp. 108-117. doi:<http://dx.doi.org/10.1016/j.cemconcomp.2013.11.010>.
- [56] Srinivasamurthy, L. et al. (2021) 'Phase changes under efflorescence in alkali activated materials with mixed activators', *Construction and Building Materials*, 283 pp. 122678. doi:<http://dx.doi.org/10.1016/j.conbuildmat.2021.122678>.
- [57] Ruengsillapanun, K. et al. (2021) 'Mechanical properties, shrinkage, and heat evolution of alkali activated fly ash concrete', *Construction and Building Materials*, 299 pp. 123954. doi:<http://dx.doi.org/10.1016/j.conbuildmat.2021.123954>.
- [58] Bernal, S.A. et al. (2013) 'Gel nanostructure in alkali-activated binders based on slag and fly ash, and effects of accelerated carbonation', *Cement and Concrete Research*, 53 pp. 127-144. doi:<http://dx.doi.org/DOI 10.1016/j.cemconres.2013.06.007>.
- [59] Gao, X., Yu, Q.L. and Brouwers, H.J.H. (2015) 'Reaction kinetics, gel character and strength of ambient temperature cured alkali activated slag-fly ash blends', *Construction and Building Materials*, 80 pp. 105-115. doi:<http://dx.doi.org/10.1016/j.conbuildmat.2015.01.065>.
- [60] Kumar, S., Kumar, R. and Mehrotra, S.P. (2010) 'Influence of granulated blast furnace slag on the reaction, structure and properties of fly ash based geopolymer', *Journal of Materials Science*, 45 (3), pp. 607-615. doi:<http://dx.doi.org/10.1007/s10853-009-3934-5>.
- [61] Nath, P. and Sarker, P.K. (2014) 'Effect of GGBFS on setting, workability and early strength properties of fly ash geopolymer concrete cured in ambient condition', *Construction and Building Materials*, 66 pp. 163-171. doi:<http://dx.doi.org/10.1016/j.conbuildmat.2014.05.080>.
- [62] Fang, G.H. et al. (2018) 'Workability and mechanical properties of alkali-activated fly ash-slag concrete cured at ambient temperature', *Construction and Building Materials*, 172 pp. 476-487. doi:<http://dx.doi.org/10.1016/j.conbuildmat.2018.04.008>.
- [63] Mallikarjuna Rao, G. and Gunneswara Rao, T.D. (2015) 'Final Setting Time and Compressive Strength of Fly Ash and GGBS-Based Geopolymer Paste and Mortar', *Arabian Journal for Science and Engineering*, 40 (11), pp. 3067-3074. doi:<http://dx.doi.org/10.1007/s13369-015-1757-z>.
- [64] Kong, Y.K. and Kurumisawa, K. (2023) 'Fresh properties and characteristic testing methods for alkali-activated materials: A review', *Journal of Building Engineering*, 75 pp. 106830. doi:<http://dx.doi.org/10.1016/j.job.2023.106830>.

- [65] Athira, V.S. et al. (2021) 'Influence of different curing methods on mechanical and durability properties of alkali activated binders', *Construction and Building Materials*, 299 pp. 123963. doi:<http://dx.doi.org/10.1016/j.conbuildmat.2021.123963>.
- [66] Ahmad, M.R., Chen, B. and Shah, S.F.A. (2020) 'Influence of different admixtures on the mechanical and durability properties of one-part alkali-activated mortars', *Construction and Building Materials*, 265 pp. 120320. doi:<http://dx.doi.org/10.1016/j.conbuildmat.2020.120320>.
- [67] Wardhono, A., Law, D.W. and Strano, A. (2015) 'The strength of alkali-activated slag/fly ash mortar blends at ambient temperature', *Civil Engineering Innovation for a Sustainable*, 125 pp. 650-656. doi:<http://dx.doi.org/10.1016/j.proeng.2015.11.095>.
- [68] Fang, G.H., Bahrami, H. and Zhang, M.Z. (2018) 'Mechanisms of autogenous shrinkage of alkali-activated fly ash-slag pastes cured at ambient temperature within 24 h', *Construction and Building Materials*, 171 pp. 377-387. doi:<http://dx.doi.org/10.1016/j.conbuildmat.2018.03.155>.
- [69] Somna, K. et al. (2011) 'NaOH-activated ground fly ash geopolymer cured at ambient temperature', *Fuel*, 90 (6), pp. 2118-2124. doi:<http://dx.doi.org/10.1016/j.fuel.2011.01.018>.
- [70] Nodehi, M. et al. (2022) 'The effect of curing regimes on physico-mechanical, microstructural and durability properties of alkali-activated materials: A review', *Construction and Building Materials*, 321 pp. 126335. doi:<http://dx.doi.org/10.1016/j.conbuildmat.2022.126335>.
- [71] Wang, A.G. et al. (2020) 'The Durability of Alkali-Activated Materials in Comparison with Ordinary Portland Cements and Concretes: A Review', *Engineering*, 6 (6), pp. 695-706. doi:<http://dx.doi.org/10.1016/j.eng.2019.08.019>.
- [72] Mohamed, R. et al. (2022) 'Heat evolution of alkali-activated materials: A review on influence factors', *Construction and Building Materials*, 314 pp. 125651. doi:<http://dx.doi.org/10.1016/j.conbuildmat.2021.125651>.
- [73] Sindhunata et al. (2006) 'Effect of curing temperature and silicate concentration on fly-ash-based geopolymerization', *Industrial & Engineering Chemistry Research*, 45 (10), pp. 3559-3568. doi:<http://dx.doi.org/10.1021/ie051251p>.
- [74] Wang, J.J. et al. (2020) 'Study on the optimum initial curing condition for fly ash and GGBS based geopolymer recycled aggregate concrete', *Construction and Building Materials*, 247 pp. 118540. doi:<http://dx.doi.org/10.1016/j.conbuildmat.2020.118540>.
- [75] Collins, F. and Sanjayan, J.G. (2001) 'Microcracking and strength development of alkali activated slag concrete', *Cement and Concrete Composites*, 23 (4-5), pp. 345-352. doi:[http://dx.doi.org/10.1016/S0958-9465\(01\)00003-8](http://dx.doi.org/10.1016/S0958-9465(01)00003-8).
- [76] Bakharev, T. (2005) 'Geopolymeric materials prepared using Class F fly ash and elevated temperature curing', *Cement and Concrete Research*, 35 (6), pp. 1224-1232. doi:<http://dx.doi.org/10.1016/j.cemconres.2004.06.031>.
- [77] Shi, J.Y. et al. (2020) 'Effect of curing regime on long-term mechanical strength and transport properties of steam-cured concrete', *Construction and Building Materials*, 255 pp. 119407. doi:<http://dx.doi.org/10.1016/j.conbuildmat.2020.119407>.
- [78] Kovalchuk, G., Fernández-Jiménez, A. and Palomo, A. (2007) 'Alkali-activated fly ash: Effect of thermal curing conditions on mechanical and microstructural development – Part II', *Fuel*, 86 (3), pp. 315-322. doi:<http://dx.doi.org/10.1016/j.fuel.2006.07.010>.
- [79] Wu, R. et al. (2024) 'Effect of curing conditions on the alkali-activated blends: Microstructure, performance and economic assessment', *Journal of Cleaner Production*, 445 pp. 141344. doi:<http://dx.doi.org/10.1016/j.jclepro.2024.141344>.
- [80] Xue, L. et al. (2022) 'Drying shrinkage behavior of hybrid alkali activated cement (HAAC) mortars', *Construction and Building Materials*, 316 pp. 126068. doi:<http://dx.doi.org/10.1016/j.conbuildmat.2022.129721>.

- [81] Aydın, S. and Baradan, B. (2012) 'Mechanical and microstructural properties of heat cured alkali-activated slag mortars', *Materials & Design*, 35 pp. 374-383. doi:<http://dx.doi.org/10.1016/j.matdes.2011.10.005>.
- [82] Maghsoodloordad, H., Khalili, H. and Allahverdi, A. (2018) 'Alkali-Activated Phosphorous Slag Performance under Different Curing Conditions: Compressive Strength, Hydration Products, and Microstructure', *Journal of Materials in Civil Engineering*, 30 (1), pp. 04017253. doi:[http://dx.doi.org/10.1061/\(Asce\)Mt.1943-5533.0002101](http://dx.doi.org/10.1061/(Asce)Mt.1943-5533.0002101).
- [83] Yong, C.L., Mo, K.H. and Koting, S. (2022) 'Phosphorus slag in supplementary cementitious and alkali activated materials: A review on activation methods', *Construction and Building Materials*, 352 pp. 129028. doi:<http://dx.doi.org/10.1016/j.conbuildmat.2022.129028>.
- [84] Cai, Y. et al. (2019) 'Effect of Early Age-Curing Methods on Drying Shrinkage of Alkali-Activated Slag Concrete', *Materials*, 12 (10), pp. 1633. doi:<http://dx.doi.org/10.3390/ma12101633>.
- [85] Suescum-Morales, D. et al. (2022) 'Effect of reactive magnesium oxide in alkali-activated fly ash mortars exposed to accelerated CO₂ curing', *Construction and Building Materials*, 342 pp. 127999. doi:<http://dx.doi.org/10.1016/j.conbuildmat.2022.127999>.
- [86] Liang, C.F. et al. (2020) 'Utilization of CO₂ curing to enhance the properties of recycled aggregate and prepared concrete: A review', *Cement and Concrete Composites*, 105 pp. 103446. doi:<http://dx.doi.org/10.1016/j.cemconcomp.2019.103446>.
- [87] Babaei, M., Khan, M.S.H. and Castel, A. (2018) 'Passivity of embedded reinforcement in carbonated low-calcium fly ash-based geopolymer concrete', *Cement and Concrete Composites*, 85 pp. 32-43. doi:<http://dx.doi.org/10.1016/j.cemconcomp.2017.10.001>.
- [88] Bernal, S.A. and Provis, J.L. (2014) 'Durability of Alkali- Activated Materials: Progress and Perspectives', *Journal of the American Ceramic Society*, 97 (4), pp. 997-1008. doi:<http://dx.doi.org/10.1111/jace.12831>.
- [89] Jun, Y. et al. (2019) 'Effects of CO₂ Curing on Alkali-Activated Slag Paste Cured in Different Curing Conditions', *Materials*, 12 (21), pp. 3513. doi:<http://dx.doi.org/10.3390/ma12213513>.
- [90] Mei, K.Y. et al. (2021) 'Effectiveness and microstructure change of alkali-activated materials during accelerated carbonation curing', *Construction and Building Materials*, 274 pp. 122063. doi:<http://dx.doi.org/10.1016/j.conbuildmat.2020.122063>.
- [91] Shi, J.J., Wu, M. and Ming, J. (2021) 'Long-term corrosion resistance of reinforcing steel in alkali-activated slag mortar after exposure to marine environments', *Corrosion Science*, 179 pp. 109175. doi:<http://dx.doi.org/10.1016/j.corsci.2020.109175>.
- [92] Alharbi, Y.R. et al. (2021) 'Engineering properties of alkali activated materials reactive powder concrete', *Construction and Building Materials*, 271 pp. 121550. doi:<http://dx.doi.org/10.1016/j.conbuildmat.2020.121550>.
- [93] Somaratna, J., Ravikumar, D. and Neithalath, N. (2010) 'Response of alkali activated fly ash mortars to microwave curing', *Cement and Concrete Research*, 40 (12), pp. 1688-1696. doi:<http://dx.doi.org/10.1016/j.cemconres.2010.08.010>.
- [94] Bai, Y., Shi, S. and McCague, C. (2017) 'Potential of Microwave Curing for Precast Concrete Manufacture', *Institute of Concrete Technology Yearbook*, 2017 pp. 61-66.
- [95] Shi, S. et al. (2014) 'Comparative study of alkali-activated fly ash manufactured under pulsed microwave curing and thermal oven curing'. 4th International Conference on the Durability of Concrete Structures. Purdue University, West Lafayette, Indiana, USA, Emerging Binder Materials.
- [96] El-Feky, M.S. et al. (2020) 'Effect of microwave curing as compared with conventional regimes on the performance of alkali activated slag pastes', *Construction and Building Materials*, 233 pp. 117268. doi:<http://dx.doi.org/10.1016/j.conbuildmat.2019.117268>.

- [97] Bernal, S.A. et al. (2012) 'Accelerated carbonation testing of alkali-activated binders significantly underestimates service life: The role of pore solution chemistry', *Cement and Concrete Research*, 42 (10), pp. 1317-1326. doi:<http://dx.doi.org/10.1016/j.cemconres.2012.07.002>.
- [98] Görhan, G. and Kürklü, G. (2014) 'The influence of the NaOH solution on the properties of the fly ash-based geopolymer mortar cured at different temperatures', *Composites Part B: Engineering*, 58 pp. 371-377. doi:<http://dx.doi.org/10.1016/j.compositesb.2013.10.082>.
- [99] Yahya, Z. et al. (2015) 'Effect of Solids-To-Liquids, Na₂SiO₃-To-NaOH and Curing Temperature on the Palm Oil Boiler Ash (Si + Ca) Geopolymerisation System', *Materials*, 8 (5), pp. 2227-2242. doi:<http://dx.doi.org/10.3390/ma8052227>.
- [100] Phoo-ngernkham, T. et al. (2015) 'Effects of sodium hydroxide and sodium silicate solutions on compressive and shear bond strengths of FA-GBFS geopolymer', *Construction and Building Materials*, 91 pp. 1-8. doi:<http://dx.doi.org/10.1016/j.conbuildmat.2015.05.001>.
- [101] Hadi, M.N.S., Al-Azzawi, M. and Yu, T. (2018) 'Effects of fly ash characteristics and alkaline activator components on compressive strength of fly ash-based geopolymer mortar', *Construction and Building Materials*, 175 pp. 41-54. doi:<http://dx.doi.org/10.1016/j.conbuildmat.2018.04.092>.
- [102] Zhang, X. et al. (2024) 'Research on hydration characteristics of OSR-GGBFS-FA alkali-activated materials', *Engineering*, 411 pp. 134321. doi:<http://dx.doi.org/10.1016/j.conbuildmat.2023.134321>.
- [103] Ruiz-Santaquiteria, C. et al. (2012) 'Alkaline solution/binder ratio as a determining factor in the alkaline activation of aluminosilicates', *Cement and Concrete Research*, 42 (9), pp. 1242-1251. doi:<http://dx.doi.org/10.1016/j.cemconres.2012.05.019>.
- [104] Chi, M. (2017) 'Effects of the alkaline solution/binder ratio and curing condition on the mechanical properties of alkali-activated fly ash mortars', *Science and Engineering of Composite Materials*, 24 (5), pp. 773-782. doi:<http://dx.doi.org/10.1515/secm-2015-0305>.
- [105] Bakharev, T., Sanjayan, J.G. and Cheng, Y.B. (1999) 'Alkali activation of Australian slag cements', *Cement and Concrete Research*, 29 (1), pp. 113-120. doi:[http://dx.doi.org/10.1016/S0008-8846\(98\)00170-7](http://dx.doi.org/10.1016/S0008-8846(98)00170-7).
- [106] Krizan, D. and Zivanovic, B. (2002) 'Effects of dosage and modulus of water glass on early hydration of alkali-slag cements', *Cement and Concrete Research*, 32 (8), pp. 1181-1188. doi:[http://dx.doi.org/10.1016/S0008-8846\(01\)00717-7](http://dx.doi.org/10.1016/S0008-8846(01)00717-7).
- [107] Al-Otaibi, S. (2008) 'Durability of concrete incorporating GGBS activated by water-glass', *Construction and Building Materials*, 22 (10), pp. 2059-2067. doi:<http://dx.doi.org/10.1016/j.conbuildmat.2007.07.023>.
- [108] Chi, M. (2012) 'Effects of dosage of alkali-activated solution and curing conditions on the properties and durability of alkali-activated slag concrete', *Construction and Building Materials*, 35 pp. 240-245. doi:<http://dx.doi.org/10.1016/j.conbuildmat.2012.04.005>.
- [109] Chi, M. (2015) 'Effects of modulus ratio and dosage of alkali-activated solution on the properties and micro-structural characteristics of alkali-activated fly ash mortars', *Construction and Building Materials*, 99 pp. 128-136. doi:<http://dx.doi.org/10.1016/j.conbuildmat.2015.09.029>.
- [110] Wang, W.C., Wang, H.Y. and Lo, M.H. (2015) 'The fresh and engineering properties of alkali activated slag as a function of fly ash replacement and alkali concentration', *Construction and Building Materials*, 84 pp. 224-229. doi:<http://dx.doi.org/10.1016/j.conbuildmat.2014.09.059>.
- [111] Babaei, M. and Castel, A. (2016) 'Chloride-induced corrosion of reinforcement in low-calcium fly ash-based geopolymer concrete', *Cement and Concrete Research*, 88 pp. 96-107. doi:<http://dx.doi.org/10.1016/j.cemconres.2016.05.012>.

- [112] Yusuf, M.O. et al. (2014) 'Influence of curing methods and concentration of NaOH on strength of the synthesized alkaline activated ground slag-ultrafine palm oil fuel ash mortar/concrete', *Construction and Building Materials*, 66 pp. 541-548. doi:<http://dx.doi.org/10.1016/j.conbuildmat.2014.05.037>.
- [113] Chindaprasirt, P., Chareerat, T. and Sirivivatnanon, V. (2007) 'Workability and strength of coarse high calcium fly ash geopolymer', *Cement and Concrete Composites*, 29 (3), pp. 224-229. doi:<http://dx.doi.org/10.1016/j.cemconcomp.2006.11.002>.
- [114] Ibrahim, M. et al. (2019) 'Influence of composition and concentration of alkaline activator on the properties of natural-pozzolan based green concrete', *Construction and Building Materials*, 201 pp. 186-195. doi:<http://dx.doi.org/10.1016/j.conbuildmat.2018.12.117>.
- [115] Shariati, M. et al. (2021) 'Alkali-activated slag (AAS) paste: Correlation between durability and microstructural characteristics', *Construction and Building Materials*, 267 pp. 120886. doi:<http://dx.doi.org/10.1016/j.conbuildmat.2020.120886>.
- [116] Nath, P. and Sarker, P.K. (2017) 'Fracture properties of GGBFS-blended fly ash geopolymer concrete cured in ambient temperature', *Materials and Structures*, 50 (1), pp. doi:<http://dx.doi.org/10.1617/s11527-016-0893-6>.
- [117] Rooholamini, H., Bayat, A. and Kazemian, F. (2020) 'Mechanical and fracture properties of alkali activated concrete containing different pozzolanic materials', *Road Materials and Pavement Design*, 23 (4), pp. 802-821. doi:<http://dx.doi.org/10.1080/14680629.2020.1845783>.
- [118] Zhang, S.Z. et al. (2021) 'Fracture properties and microstructure formation of hardened alkali-activated slag/fly ash pastes', *Cement and Concrete Research*, 144 pp. 106447. doi:<http://dx.doi.org/10.1016/j.cemconres.2021.106447>.
- [119] Ding, Y., Dai, J.G. and Shi, C.J. (2018) 'Fracture properties of alkali-activated slag and ordinary Portland cement concrete and mortar', *Construction and Building Materials*, 165 pp. 310-320. doi:<http://dx.doi.org/10.1016/j.conbuildmat.2017.12.202>.
- [120] Pan, Z., Sanjayan, J.G. and Rangan, B.V. (2011) 'Fracture properties of geopolymer paste and concrete', *Magazine of Concrete Research*, 63 (10), pp. 763-771. doi:<http://dx.doi.org/10.1680/mac.2011.63.10.763>.
- [121] Sarker, P.K., Haque, R. and Ramgolam, K.V. (2013) 'Fracture behaviour of heat cured fly ash based geopolymer concrete', *Materials & Design*, 44 pp. 580-586. doi:<http://dx.doi.org/10.1016/j.matdes.2012.08.005>.
- [122] Zhang, B., Zhu, H. and Lu, F. (2021) 'Fracture properties of slag-based alkali-activated seawater coral aggregate concrete', *Theoretical and Applied Fracture Mechanics*, 115 pp. 103071. doi:<http://dx.doi.org/10.1016/j.tafmec.2021.103071>.
- [123] Xu, S.L. and Reinhardt, H.W. (1999) 'Determination of double-K criterion for crack propagation in quasi-brittle fracture, Part I: Experimental investigation of crack propagation', *International Journal of Fracture*, 98 (2), pp. 111-149. doi:<http://dx.doi.org/10.1023/A:1018668929989>.
- [124] CEB-FIP (1990) CEB-FIP model code 1990: Design code. Thomas Telford Publishing.
- [125] Ding, Y., Shi, C.J. and Li, N. (2018) 'Fracture properties of slag/fly ash-based geopolymer concrete cured in ambient temperature', *Construction and Building Materials*, 190 pp. 787-795. doi:<http://dx.doi.org/10.1016/j.conbuildmat.2018.09.138>.
- [126] Bažant, Z.P. and Becq-Giraudon, E. (2002) 'Statistical prediction of fracture parameters of concrete and implications for choice of testing standard', *Cement and Concrete Research*, 32 (4), pp. 529-556. doi:[http://dx.doi.org/10.1016/S0008-8846\(01\)00723-2](http://dx.doi.org/10.1016/S0008-8846(01)00723-2).
- [127] Zhao, Y. et al. (2021) 'Influence of steel slag on the properties of alkali-activated fly ash and blast-furnace slag based fiber reinforced composites', *Cement and Concrete Composites*, 116 pp. 103875. doi:<http://dx.doi.org/10.1016/j.cemconcomp.2020.103875>.

- [128] Sun, X.J. et al. (2019) 'Fracture performance and numerical simulation of basalt fiber concrete using three-point bending test on notched beam', *Construction and Building Materials*, 225 pp. 788-800. doi:<http://dx.doi.org/10.1016/j.conbuildmat.2019.07.244>.
- [129] Amran, M. et al. (2022) 'Fiber-reinforced alkali-activated concrete: A review', *Journal of Building Engineering*, 45 pp. 103638. doi:<http://dx.doi.org/10.1016/j.jobbe.2021.103638>.
- [130] Kumarappa, D.B., Peethamparan, S. and Ngami, M. (2018) 'Autogenous shrinkage of alkali activated slag mortars: Basic mechanisms and mitigation methods', *Cement and Concrete Research*, 109 pp. 1-9. doi:<http://dx.doi.org/10.1016/j.cemconres.2018.04.004>.
- [131] Nguyen, Q.D. et al. (2022) 'Autogenous and total shrinkage of limestone calcined clay cement (LC3) concretes', *Construction and Building Materials*, 314 pp. 125720. doi:<http://dx.doi.org/10.1016/j.conbuildmat.2021.125720>.
- [132] Deb, P.S., Nath, P. and Sarker, P.K. (2015) 'Drying shrinkage of slag blended fly ash geopolymer concrete cured at room temperature', *Civil Engineering Innovation for a Sustainable*, 125 pp. 594-600. doi:<http://dx.doi.org/10.1016/j.proeng.2015.11.066>.
- [133] Thomas, R.J., Lezama, D. and Peethamparan, S. (2017) 'On drying shrinkage in alkali-activated concrete: Improving dimensional stability by aging or heat-curing', *Cement and Concrete Research*, 91 pp. 13-23. doi:<http://dx.doi.org/10.1016/j.cemconres.2016.10.003>.
- [134] Fernández-Jiménez, A.M., Palomo, A. and López-Hombrados, C. (2006) 'Engineering properties of alkali-activated fly ash concrete', *ACI Materials Journal*, 103 (2), pp. 106-112. doi:<http://dx.doi.org/10.14359/15261>.
- [135] Hardjito, D. et al. (2004) 'On the development of fly ash-based geopolymer concrete', *ACI Materials Journal*, 101 (6), pp. 467-472. doi:<http://dx.doi.org/10.14359/13485>.
- [136] Ma, Y. and Ye, G. (2015) 'The shrinkage of alkali activated fly ash', *Cement and Concrete Research*, 68 pp. 75-82. doi:<http://dx.doi.org/10.1016/j.cemconres.2014.10.024>.
- [137] Huang, D.W. et al. (2021) 'A review and comparison study on drying shrinkage prediction between alkali-activated fly ash/slag and ordinary Portland cement', *Construction and Building Materials*, 305 pp. 124760. doi:<http://dx.doi.org/10.1016/j.conbuildmat.2021.124760>.
- [138] Li, Z. et al. (2023) 'Autogenous shrinkage of alkali-activated slag: A critical review', *Cement and Concrete Research*, 172 pp. 107244. doi:<http://dx.doi.org/10.1016/j.cemconres.2023.107244>.
- [139] El-Hassan, H., Shehab, E. and Al-Sallamin, A. (2021) 'Effect of curing regime on the performance and microstructure characteristics of alkali-activated slag-fly ash blended concrete', *Journal of Sustainable Cement-Based Materials*, 10 (5), pp. 289-317. doi:<http://dx.doi.org/10.1080/21650373.2021.1883145>.
- [140] Thomas, R.J. et al. (2018) 'Comparison of chloride permeability methods for Alkali-Activated concrete', *Construction and Building Materials*, 165 pp. 104-111. doi:<http://dx.doi.org/10.1016/j.conbuildmat.2018.01.016>.
- [141] Osio-Norgaard, J., Gevaudan, J.P. and Srubar, W.V. (2018) 'A review of chloride transport in alkali-activated cement paste, mortar, and concrete', *Construction and Building Materials*, 186 pp. 191-206. doi:<http://dx.doi.org/10.1016/j.conbuildmat.2018.07.119>.
- [142] Neto, A.A.M., Cincotto, M.A. and Repette, W. (2008) 'Drying and autogenous shrinkage of pastes and mortars with activated slag cement', *Cement and Concrete Research*, 38 (4), pp. 565-574. doi:<http://dx.doi.org/10.1016/j.cemconres.2007.11.002>.
- [143] Li, Z.M. et al. (2021) 'A comparative study on the mechanical properties, autogenous shrinkage and cracking proneness of alkali-activated concrete and ordinary Portland cement concrete', *Construction and Building Materials*, 292 pp. 123418. doi:<http://dx.doi.org/10.1016/j.conbuildmat.2021.123418>.
- [144] Humad, A.M. et al. (2019) 'The Effect of Blast Furnace Slag/Fly Ash Ratio on Setting, Strength, and Shrinkage of Alkali-Activated Pastes and Concretes', *Frontiers in Materials*, 6 pp. doi:<http://dx.doi.org/10.3389/fmats.2019.00009>.

- [145] Li, Z.M. et al. (2020) 'Mechanisms of autogenous shrinkage of alkali-activated slag and fly ash pastes', *Cement and Concrete Research*, 135 pp. 106107. doi:<http://dx.doi.org/10.1016/j.cemconres.2020.106107>.
- [146] Fang, G., Bahrami, H. and Zhang, M. (2018) 'Mechanisms of autogenous shrinkage of alkali-activated fly ash-slag pastes cured at ambient temperature within 24 h', *Construction and Building Materials*, 171 pp. 377-387. doi:<http://dx.doi.org/10.1016/j.conbuildmat.2018.03.155>.
- [147] Lee, N.K., Jang, J.G. and Lee, H.K. (2014) 'Shrinkage characteristics of alkali-activated fly ash/slag paste and mortar at early ages', *Cement and Concrete Composites*, 53 pp. 239-248. doi:<http://dx.doi.org/10.1016/j.cemconcomp.2014.07.007>.
- [148] Huang, D. et al. (2022) 'Effect of activator properties on drying shrinkage of alkali-activated fly ash and slag', *Journal of Building Engineering*, 62 pp. 105341. doi:<http://dx.doi.org/10.1016/j.jobbe.2022.105341>.
- [149] Srinivasamurthy, L. et al. (2022) 'Mechanical property and microstructure development in alkali activated fly ash slag blends due to efflorescence', *Construction and Building Materials*, 332 pp. 127273. doi:<http://dx.doi.org/10.1016/j.conbuildmat.2022.127273>.
- [150] Longhi, M.A. et al. (2019) 'Efflorescence of Alkali-Activated Cements (Geopolymers) and the Impacts on Material Structures: A Critical Analysis', *Frontiers in Materials*, 6 pp. 89. doi:<http://dx.doi.org/10.3389/fmats.2019.00089>.
- [151] Jia, R., Wang, Q. and Luo, T. (2022) 'Understanding the workability of alkali-activated phosphorus slag pastes: Effects of alkali dose and silicate modulus on early-age hydration reactions', *Cement and Concrete Composites*, 133 pp. 104649. doi:<http://dx.doi.org/10.1016/j.cemconcomp.2022.104649>.
- [152] Zhang, Z.H. et al. (2018) 'Efflorescence and subflorescence induced microstructural and mechanical evolution in fly ash-based geopolymers', *Cement and Concrete Composites*, 92 pp. 165-177. doi:<http://dx.doi.org/10.1016/j.cemconcomp.2018.06.010>.
- [153] Zhang, Z.H. et al. (2014) 'Fly ash-based geopolymers: The relationship between composition, pore structure and efflorescence', *Cement and Concrete Research*, 64 pp. 30-41. doi:<http://dx.doi.org/10.1016/j.cemconres.2014.06.004>.
- [154] Fernando, S. et al. (2023) 'Assessment of long term durability properties of blended fly ash-Rice husk ash alkali activated concrete', *Construction and Building Materials*, 369 pp. 130449. doi:<http://dx.doi.org/10.1016/j.conbuildmat.2023.130449>.
- [155] Yao, X., Yang, T. and Zhang, Z. (2016) 'Compressive strength development and shrinkage of alkali-activated fly ash-slag blends associated with efflorescence', *Materials and Structures*, 49 pp. 2907-2918. doi:<http://dx.doi.org/10.1617/s11527-015-0694>.
- [156] Wang, J.B. et al. (2018) 'Effect of zeolite on waste based alkali-activated inorganic binder efflorescence', *Construction and Building Materials*, 158 pp. 683-690. doi:<http://dx.doi.org/10.1016/j.conbuildmat.2017.10.065>.
- [157] Wang, J.B. et al. (2018) 'Effect of nano-silica on the efflorescence of waste based alkali-activated inorganic binder', *Construction and Building Materials*, 167 pp. 381-390. doi:<http://dx.doi.org/10.1016/j.conbuildmat.2018.02.006>.
- [158] Tang, D.S. et al. (2021) 'Mitigation of efflorescence of alkali-activated slag mortars by incorporating calcium hydroxide', *Construction and Building Materials*, 298 pp. 123873. doi:<http://dx.doi.org/10.1016/j.conbuildmat.2021.123873>.
- [159] Kang, S.P. and Kwon, S.J. (2017) 'Effects of red mud and Alkali-Activated Slag Cement on efflorescence in cement mortar', *Construction and Building Materials*, 133 pp. 459-467. doi:<http://dx.doi.org/10.1016/j.conbuildmat.2016.12.123>.
- [160] Wang, Y.G. et al. (2020) 'Effects of Si/Al ratio on the efflorescence and properties of fly ash based geopolymer', *Journal of Cleaner Production*, 244 pp. 118852. doi:<http://dx.doi.org/10.1016/j.jclepro.2019.118852>.

- [161] Xue, X. et al. (2018) 'Inhibiting efflorescence formation on fly ash-based geopolymer via silane surface modification', *Cement and Concrete Composites*, 94 pp. 43-52. doi:<http://dx.doi.org/10.1016/j.cemconcomp.2018.08.013>.
- [162] Xi, X., Yang, S.T. and Li, C.Q. (2018) 'A non-uniform corrosion model and meso-scale fracture modelling of concrete', *Cement and Concrete Research*, 108 pp. 87-102. doi:<http://dx.doi.org/10.1016/j.cemconres.2018.03.009>.
- [163] Tahri, W. et al. (2021) 'Review on corrosion of steel reinforcement in alkali-activated concretes in chloride-containing environments', *Construction and Building Materials*, 293 pp. 123484. doi:<http://dx.doi.org/10.1016/j.conbuildmat.2021.123484>.
- [164] Kupwade-Patil, K. and Allouche, E.N. (2013) 'Examination of Chloride-Induced Corrosion in Reinforced Geopolymer Concretes', *Journal of Materials in Civil Engineering*, 25 (10), pp. 1465-1476. doi:[http://dx.doi.org/10.1061/\(ASCE\)MT.1943-5533.0000672](http://dx.doi.org/10.1061/(ASCE)MT.1943-5533.0000672).
- [165] Pasupathy, K. et al. (2017) 'Durability of low-calcium fly ash based geopolymer concrete culvert in a saline environment', *Cement and Concrete Research*, 100 pp. 297-310. doi:<http://dx.doi.org/10.1016/j.cemconres.2017.07.010>.
- [166] Pasupathy, K., Cheema, D.S. and Sanjayan, J. (2021) 'Durability performance of fly ash-based geopolymer concrete buried in saline environment for 10 years', *Construction and Building Materials*, 281 pp. 122596. doi:<http://dx.doi.org/10.1016/j.conbuildmat.2021.122596>.
- [167] Ma, Y., Hu, J. and Ye, G. (2013) 'The pore structure and permeability of alkali activated fly ash', *Fuel*, 104 pp. 771-780. doi:<http://dx.doi.org/10.1016/j.fuel.2012.05.034>.
- [168] Chindaprasirt, P. and Chalee, W. (2014) 'Effect of sodium hydroxide concentration on chloride penetration and steel corrosion of fly ash-based geopolymer concrete under marine site', *Construction and Building Materials*, 63 pp. 303-310. doi:<http://dx.doi.org/10.1016/j.conbuildmat.2014.04.010>.
- [169] Noushini, A. et al. (2020) 'Chloride diffusion resistance and chloride binding capacity of fly ash-based geopolymer concrete', *Cement and Concrete Composites*, 105 pp. 103290. doi:<http://dx.doi.org/10.1016/j.cemconcomp.2019.04.006>.
- [170] Roy, D.M., Jiang, W.M. and Silsbee, M.R. (2000) 'Chloride diffusion in ordinary, blended, and alkali-activated cement pastes and its relation to other properties', *Cement and Concrete Research*, 30 (12), pp. 1879-1884. doi:[http://dx.doi.org/10.1016/S0008-8846\(00\)00406-3](http://dx.doi.org/10.1016/S0008-8846(00)00406-3).
- [171] Ismail, I. et al. (2013) 'Influence of fly ash on the water and chloride permeability of alkali-activated slag mortars and concretes', *Construction and Building Materials*, 48 pp. 1187-1201. doi:<http://dx.doi.org/10.1016/j.conbuildmat.2013.07.106>.
- [172] Babaee, M. and Castel, A. (2018) 'Chloride diffusivity, chloride threshold, and corrosion initiation in reinforced alkali-activated mortars: Role of calcium, alkali, and silicate content', *Cement and Concrete Research*, 111 pp. 56-71. doi:<http://dx.doi.org/10.1016/j.cemconres.2018.06.009>.
- [173] Luo, R. et al. (2003) 'Study of chloride binding and diffusion in GGBS concrete', *Cement and Concrete Research*, 33 (1), pp. 1-7. doi:[http://dx.doi.org/10.1016/S0008-8846\(02\)00712-3](http://dx.doi.org/10.1016/S0008-8846(02)00712-3).
- [174] Khan, M.S.H., Kayali, O. and Troitzsch, U. (2016) 'Chloride binding capacity of hydrotalcite and the competition with carbonates in ground granulated blast furnace slag concrete', *Materials and Structures*, 49 (11), pp. 4609-4619. doi:<http://dx.doi.org/10.1617/s11527-016-0810-z>.
- [175] Hong, S.Y. and Glasser, F.P. (2002) 'Alkali sorption by C-S-H and C-A-S-H gels - Part II. Role of alumina', *Cement and Concrete Research*, 32 (7), pp. 1101-1111. doi:[http://dx.doi.org/10.1016/S0008-8846\(02\)00753-6](http://dx.doi.org/10.1016/S0008-8846(02)00753-6).
- [176] Ke, X.Y., Bernal, S.A. and Provis, J.L. (2017) 'Uptake of chloride and carbonate by Mg-Al and Ca-Al layered double hydroxides in simulated pore solutions of alkali-activated slag

- cement', Cement and Concrete Research, 100 pp. 1-13.
doi:<http://dx.doi.org/10.1016/j.cemconres.2017.05.015>.
- [177] Khan, M.S.H. et al. (2016) 'Utilisation of steel furnace slag coarse aggregate in a low calcium fly ash geopolymer concrete', Cement and Concrete Research, 89 pp. 220-229.
doi:<http://dx.doi.org/10.1016/j.cemconres.2016.09.001>.
- [178] Zhang, J.X. et al. (2020) 'Chloride diffusion in alkali-activated fly ash/slag concretes: Role of slag content, water/binder ratio, alkali content and sand-aggregate ratio', Construction and Building Materials, 261 pp. 119940.
doi:<http://dx.doi.org/10.1016/j.conbuildmat.2020.119940>.
- [179] Mohammed, T.U. and Hamada, H. (2006) 'Corrosion of steel bars in concrete with various steel surface conditions', ACI Materials Journal, 103 (4), pp. 233-242.
doi:<http://dx.doi.org/10.14359/16606>.
- [180] Castellote, M., Andrade, C. and Alonso, C. (2002) 'Accelerated simultaneous determination of the chloride depassivation threshold and of the non-stationary diffusion coefficient values', Corrosion Science, 44 (11), pp. 2409-2424.
doi:[http://dx.doi.org/10.1016/S0010-938x\(02\)00060-4](http://dx.doi.org/10.1016/S0010-938x(02)00060-4).
- [181] Hansson, C.M. and Sørensen, B. (1990) 'The threshold concentration of chloride in concrete for the initiation of reinforcement corrosion'. Corrosion Rates of Steel in Concrete. ASTM International, pp. 14.
- [182] Alonso, C. et al. (2000) 'Chloride threshold values to depassivate reinforcing bars embedded in a standardized OPC mortar', Cement and Concrete Research, 30 (7), pp. 1047-1055. doi:[http://dx.doi.org/10.1016/S0008-8846\(00\)00265-9](http://dx.doi.org/10.1016/S0008-8846(00)00265-9).
- [183] Hausmann, D.A. (1967) 'Steel corrosion in concrete--How does it occur?', Materials Protection, 6 (11), pp. 19-23.
- [184] Gouda, V.K. (2013) 'Corrosion and Corrosion Inhibition of Reinforcing Steel: I. Immersed in Alkaline Solutions', British Corrosion Journal, 5 (5), pp. 198-203.
doi:<http://dx.doi.org/10.1179/000705970798324450>.
- [185] Hussain, S.E. et al. (1995) 'Factors Affecting Threshold Chloride for Reinforcement Corrosion in Concrete', Cement and Concrete Research, 25 (7), pp. 1543-1555.
doi:[http://dx.doi.org/10.1016/0008-8846\(95\)00148-6](http://dx.doi.org/10.1016/0008-8846(95)00148-6).
- [186] Thomas, M. (1996) 'Chloride thresholds in marine concrete', Cement and Concrete Research, 26 (4), pp. 513-519. doi:[http://dx.doi.org/10.1016/0008-8846\(96\)00035-X](http://dx.doi.org/10.1016/0008-8846(96)00035-X).
- [187] Alonso, C., Castellote, M. and Andrade, C. (2002) 'Chloride threshold dependence of pitting potential of reinforcements', Electrochimica Acta, 47 (21), pp. 3469-3481.
doi:[http://dx.doi.org/10.1016/S0013-4686\(02\)00283-9](http://dx.doi.org/10.1016/S0013-4686(02)00283-9).
- [188] Morris, W. et al. (2002) 'Corrosion of reinforcing steel evaluated by means of concrete resistivity measurements', Corrosion Science, 44 (1), pp. 81-99.
doi:[http://dx.doi.org/10.1016/S0010-938x\(01\)00033-6](http://dx.doi.org/10.1016/S0010-938x(01)00033-6).
- [189] Shi, X.M. et al. (2011) 'Strength and corrosion properties of Portland cement mortar and concrete with mineral admixtures', Construction and Building Materials, 25 (8), pp. 3245-3256.
doi:<http://dx.doi.org/10.1016/j.conbuildmat.2011.03.011>.
- [190] RILEM (1994) 'Draft recommendation for repair strategies for concrete structures damaged by reinforcement corrosion', Materials and Structures, 27 (171), pp. 415-436.
doi:<http://dx.doi.org/10.1007/BF02473446>.
- [191] Scott, A. and Alexander, M.G. (2016) 'Effect of supplementary cementitious materials (binder type) on the pore solution chemistry and the corrosion of steel in alkaline environments', Cement and Concrete Research, 89 pp. 45-55.
doi:<http://dx.doi.org/10.1016/j.cemconres.2016.08.007>.

- [192] Mangat, P.S., Ojedokun, O.O. and Lambert, P. (2021) 'Chloride-initiated corrosion in alkali activated reinforced concrete', *Cement and Concrete Composites*, 115 pp. 103823. doi:<http://dx.doi.org/10.1016/j.cemconcomp.2020.103823>.
- [193] Mundra, S. et al. (2017) 'Chloride-induced corrosion of steel rebars in simulated pore solutions of alkali-activated concretes', *Cement and Concrete Research*, 100 pp. 385-397. doi:<http://dx.doi.org/10.1016/j.cemconres.2017.08.006>.
- [194] Perez, N. (2004) *Electrochemistry and corrosion science*. Springer, Boston, MA.
- [195] ASTM International (2022) ASTM C876-22b, Standard Test Method for Corrosion Potentials of Uncoated Reinforcing Steel in Concrete. West Conshohocken, PA, ASTM International. doi:<http://dx.doi.org/10.1520/C0876-22B>.
- [196] Pour-Ghaz, M., Isgor, O.B. and Ghods, P. (2009) 'Quantitative Interpretation of Half-Cell Potential Measurements in Concrete Structures', *Journal of Materials in Civil Engineering*, 21 (9), pp. 467-475. doi:[http://dx.doi.org/10.1061/\(Asce\)0899-1561\(2009\)21:9\(467\)](http://dx.doi.org/10.1061/(Asce)0899-1561(2009)21:9(467)).
- [197] Hussain, R.R., Ishida, T. and Wasim, M. (2012) 'Oxygen Transport and Corrosion of Steel in Concrete under Varying Concrete Cover, w/c, and Moisture.', *ACI Materials Journal*, 109 (1), pp. 3-10. doi:<http://dx.doi.org/10.14359/51683565>.
- [198] Criado, M. and Provis, J.L. (2018) 'Alkali Activated Slag Mortars Provide High Resistance to Chloride-Induced Corrosion of Steel', *Frontiers in Materials*, 5 pp. doi:<http://dx.doi.org/10.3389/fmats.2018.00034>.
- [199] Mundra, S. et al. (2023) 'Application of electrochemical methods for studying steel corrosion in alkali-activated materials', *Materials and Corrosion*, 74 (7), pp. 988-1008. doi:<http://dx.doi.org/10.1002/maco.202313743>.
- [200] Stern, M. and Geaby, A.L. (1957) 'Electrochemical Polarization', *Journal of The Electrochemical Society*, 104 (1), pp. 56. doi:<http://dx.doi.org/10.1149/1.2428496>.
- [201] Andrade, C. and Gonzalez, J.A. (1978) 'Quantitative Measurements of Corrosion Rate of Reinforcing Steels Embedded in Concrete Using Polarization Resistance Measurements', *Materials and Corrosion*, 29 (8), pp. 515-519. doi:<http://dx.doi.org/10.1002/maco.19780290804>.
- [202] Elsener, B. (2005) 'Corrosion rate of steel in concrete - Measurements beyond the Tafel law', *Corrosion Science*, 47 (12), pp. 3019-3033. doi:<http://dx.doi.org/10.1016/j.corsci.2005.06.021>.
- [203] Flitt, H.J. and Schweinsberg, D.P. (2005) 'Evaluation of corrosion rate from polarisation curves not exhibiting a Tafel region', *Corrosion Science*, 47 (12), pp. 3034-3052. doi:<http://dx.doi.org/10.1016/j.corsci.2005.06.014>.
- [204] Runci, A., Provis, J.L. and Serdar, M. (2023) 'Revealing corrosion parameters of steel in alkali-activated materials', *Corrosion Science*, 210 pp. 110849. doi:<http://dx.doi.org/10.1016/j.corsci.2022.110849>.
- [205] Robayo-Salazar, R.A., Aguirre-Guerrero, A.M. and de Gutiérrez, R.M. (2020) 'Carbonation-induced corrosion of alkali-activated binary concrete based on natural volcanic pozzolan', *Construction and Building Materials*, 232 pp. 117189. doi:<http://dx.doi.org/10.1016/j.conbuildmat.2019.117189>.
- [206] Momayez, A. et al. (2005) 'Comparison of methods for evaluating bond strength between concrete substrate and repair materials', *Cement and Concrete Research*, 35 (4), pp. 748-757. doi:<http://dx.doi.org/10.1016/j.cemconres.2004.05.027>.
- [207] Albitar, M. et al. (2017) 'Bond Slip Models for Uncorroded and Corroded Steel Reinforcement in Class-F Fly Ash Geopolymer Concrete', *Journal of Materials in Civil Engineering*, 29 (1), pp. 04016186. doi:[http://dx.doi.org/10.1061/\(Asce\)Mt.1943-5533.0001713](http://dx.doi.org/10.1061/(Asce)Mt.1943-5533.0001713).

- [208] Adak, D. and Mandal, S. (2019) 'Strength and Durability Performance of Fly Ash–Based Process-Modified Geopolymer Concrete', *Journal of Materials in Civil Engineering*, 31 (9), pp. 04019174. doi:[http://dx.doi.org/10.1061/\(asce\)mt.1943-5533.0002793](http://dx.doi.org/10.1061/(asce)mt.1943-5533.0002793).
- [209] Al-Azzawi, M., Yu, T. and Hadi, M.N.S. (2018) 'Factors Affecting the Bond Strength Between the Fly Ash-based Geopolymer Concrete and Steel Reinforcement', *Structures*, 14 pp. 262-272. doi:<http://dx.doi.org/10.1016/j.istruc.2018.03.010>.
- [210] Zhang, H.Y. et al. (2018) 'Effect of temperature on bond characteristics of geopolymer concrete', *Construction and Building Materials*, 163 pp. 277-285. doi:<http://dx.doi.org/10.1016/j.conbuildmat.2017.12.043>.
- [211] Ramagiri, K.K. et al. (2021) 'High-temperature performance of ambient-cured alkali-activated binder concrete', *Innovative Infrastructure Solutions*, 6 (2), pp. doi:<http://dx.doi.org/10.1007/s41062-020-00448-y>.
- [212] Liu, Y. et al. (2023) 'Bond performance of steel rebar in alkali-activated slag-based concrete after exposure to elevated temperature', *Construction and Building Materials*, 394 pp. 132281. doi:<http://dx.doi.org/10.1016/j.conbuildmat.2023.132281>.
- [213] Castel, A. and Foster, S.J. (2015) 'Bond strength between blended slag and Class F fly ash geopolymer concrete with steel reinforcement', *Cement and Concrete Research*, 72 pp. 48-53. doi:<http://dx.doi.org/10.1016/j.cemconres.2015.02.016>.
- [214] Cui, Y. et al. (2023) 'Effect of Corrosion on the Bond Behavior of Steel-Reinforced, Alkali-Activated Slag Concrete', *Materials*, 16 (6), pp. 2262. doi:<http://dx.doi.org/10.3390/ma16062262>.
- [215] Yan, F., Lin, Z.B. and Yang, M.J. (2016) 'Bond mechanism and bond strength of GFRP bars to concrete: A review', *Composites Part B-Engineering*, 98 pp. 56-69. doi:<http://dx.doi.org/10.1016/j.compositesb.2016.04.068>.
- [216] Angst, U.M. et al. (2017) 'The steel–concrete interface', *Materials and Structures*, 50 (2), pp. doi:<http://dx.doi.org/10.1617/s11527-017-1010-1>.
- [217] Wong, H.S. et al. (2022) 'Methods for characterising the steel–concrete interface to enhance understanding of reinforcement corrosion: a critical review by RILEM TC 262-SCI', *Materials and Structures*, 55 (4), pp. 124. doi:<http://dx.doi.org/10.1617/s11527-022-01961-5>.
- [218] Chen, F.J. et al. (2018) 'Quantification of steel-concrete interface in reinforced concrete using Backscattered Electron imaging technique', *Construction and Building Materials*, 179 pp. 420-429. doi:<http://dx.doi.org/10.1016/j.conbuildmat.2018.05.246>.
- [219] Chen, F.J. et al. (2019) 'Effect of design parameters on microstructure of steel-concrete interface in reinforced concrete', *Cement and Concrete Research*, 119 pp. 1-10. doi:<http://dx.doi.org/10.1016/j.cemconres.2019.01.005>.
- [220] Castel, A. et al. (2006) 'Effect of reinforcing bar orientation and location on bond with self-consolidating concrete', *ACI Structural Journal*, 103 (4), pp. 559-567. doi:<http://dx.doi.org/10.14359/16432>.
- [221] Zhang, R., Castel, A. and François, R. (2011) 'Influence of steel–concrete interface defects owing to the top-bar effect on the chloride-induced corrosion of reinforcement', *Magazine of Concrete Research*, 63 (10), pp. 773-781. doi:<http://dx.doi.org/10.1680/macr.2011.63.10.773>.
- [222] Zhang, R.J., Castel, A. and François, R. (2011) 'Influence of steel-concrete interface defects owing to the top-bar effect on the chloride-induced corrosion of reinforcement', *Magazine of Concrete Research*, 63 (10), pp. 773-781. doi:<http://dx.doi.org/10.1680/macr.2011.63.10.773>.
- [223] Chen, L.J. and Su, R.K.L. (2021) 'Influence of rebar geometry on the steel-concrete interface of reinforced concrete', *Construction and Building Materials*, 304 pp. 124668. doi:<http://dx.doi.org/10.1016/j.conbuildmat.2021.124668>.

- [224] Zhang, Z., Studer, P. and Angst, U. (2022) 'A multi-technique study of corrosion products at the steel-concrete interface under two exposure conditions', *Journal of Microscopy*, 286 (2), pp. 191-197. doi:<http://dx.doi.org/10.1111/jmi.13100>.
- [225] Doi, K. et al. (2020) 'Role of mill scale on corrosion behavior of steel rebars in mortar', *Corrosion Science*, 177 pp. 108995. doi:<http://dx.doi.org/10.1016/j.corsci.2020.108995>.
- [226] Česen, A., Kosec, T. and Legat, A. (2013) 'Characterization of steel corrosion in mortar by various electrochemical and physical techniques', *Corrosion Science*, 75 pp. 47-57. doi:<http://dx.doi.org/10.1016/j.corsci.2013.05.015>.
- [227] Pacheco, J. and Çopuroglu, O. (2016) 'Quantitative Energy-Dispersive X-Ray Microanalysis of Chlorine in Cement Paste', *Journal of Materials in Civil Engineering*, 28 (1), pp. 04015065. doi:[http://dx.doi.org/10.1061/\(ASCE\)MT.1943-5533.0001336](http://dx.doi.org/10.1061/(ASCE)MT.1943-5533.0001336).
- [228] Shi, J.J., Ming, J. and Wu, M. (2020) 'Passivation and corrosion behavior of 2304 duplex stainless steel in alkali-activated slag materials', *Cement and Concrete Composites*, 108 pp. 103532. doi:<http://dx.doi.org/10.1016/j.cemconcomp.2020.103532>.
- [229] Aperador, W., de Gutiérrez, R.M. and Bastidas, D.M. (2009) 'Steel corrosion behaviour in carbonated alkali-activated slag concrete', *Corrosion Science*, 51 (9), pp. 2027-2033. doi:<http://dx.doi.org/10.1016/j.corsci.2009.05.033>.
- [230] Bernal, S.A. et al. (2015) 'Accelerated carbonation testing of alkali-activated slag/metakaolin blended concretes: effect of exposure conditions', *Materials and Structures*, 48 (3), pp. 653-669. doi:<http://dx.doi.org/10.1617/s11527-014-0289-4>.
- [231] Galan, I., Andrade, C. and Castellote, M. (2013) 'Natural and accelerated CO₂ binding kinetics in cement paste at different relative humidities', *Cement and Concrete Research*, 49 pp. 21-28. doi:<http://dx.doi.org/10.1016/j.cemconres.2013.03.009>.
- [232] Xu, H. et al. (2008) 'Characterization of aged slag concretes', *ACI Materials Journal*, 105 (2), pp. 131-139. doi:<http://dx.doi.org/10.14359/19753>.
- [233] Chen, R. et al. (2020) 'Characterization of the passive film formed on the reinforcement surface in alkali activated fly ash: Surface analysis and electrochemical evaluation', *Corrosion Science*, 165 pp. 108393. doi:<http://dx.doi.org/10.1016/j.corsci.2019.108393>.
- [234] Wang, Y.Y. et al. (2021) 'Surface characteristics and electrochemical behaviors of passive reinforcing steel in alkali-activated slag', *Corrosion Science*, 190 pp. 109657. doi:<http://dx.doi.org/10.1016/j.corsci.2021.109657>.
- [235] Xi, X. and Yang, S.T. (2019) 'Investigating the spatial development of corrosion of corner-located steel bar in concrete by X-ray computed tomography', *Construction and Building Materials*, 221 pp. 177-189. doi:<http://dx.doi.org/10.1016/j.conbuildmat.2019.06.023>.
- [236] Skarzynski, L., Kibort, K. and Malachowska, A. (2021) '3D X-ray Micro-CT Analysis of Rebar Corrosion in Reinforced Concrete Subjected to a Chloride-Induced Environment', *Molecules*, 27 (1), pp. 192. doi:<http://dx.doi.org/10.3390/molecules27010192>.
- [237] Li, C.Q., Yang, S.T. and Saafi, M. (2014) 'Numerical Simulation of Behavior of Reinforced Concrete Structures considering Corrosion Effects on Bonding', *Journal of Structural Engineering*, 140 (12), pp. doi:[http://dx.doi.org/10.1061/\(ASCE\)ST.1943-541X.0001021](http://dx.doi.org/10.1061/(ASCE)ST.1943-541X.0001021).
- [238] Li, C.Q. and Yang, S.T. (2011) 'Prediction of Concrete Crack Width under Combined Reinforcement Corrosion and Applied Load', *Journal of Engineering Mechanics*, 137 (11), pp. 722-731. doi:[http://dx.doi.org/10.1061/\(ASCE\)EM.1943-7889.0000289](http://dx.doi.org/10.1061/(ASCE)EM.1943-7889.0000289).
- [239] Beck, M., Goebbels, J. and Burkert, A. (2007) 'Application of X-ray tomography for the verification of corrosion processes in chloride contaminated mortar', *Materials and Corrosion*, 58 (3), pp. 207-210. doi:<http://dx.doi.org/10.1002/maco.200604049>.
- [240] Šavija, B. et al. (2015) 'Corrosion induced cover cracking studied by X-ray computed tomography, nanoindentation, and energy dispersive X-ray spectrometry (EDS)', *Materials and Structures*, 48 pp. 2043-2062.

- [241] Dong, B.Q. et al. (2017) 'Monitoring reinforcement corrosion and corrosion-induced cracking by X-ray microcomputed tomography method', *Cement and Concrete Research*, 100 pp. 311-321. doi:<http://dx.doi.org/10.1016/j.cemconres.2017.07.009>.
- [242] Dong, B.Q. et al. (2018) '3D visualized tracing of rebar corrosion-inhibiting features in concrete with a novel chemical self-healing system', *Construction and Building Materials*, 168 pp. 11-20. doi:<http://dx.doi.org/10.1016/j.conbuildmat.2018.02.094>.
- [243] Itty, P.A. et al. (2014) '3D monitoring of corrosion on carbon steel and ferritic stainless steel embedded in cement paste', *Corrosion Science*, 83 pp. 409-418. doi:<http://dx.doi.org/10.1016/j.corsci.2014.03.010>.
- [244] Shi, J.J., Ming, J. and Sun, W. (2018) 'Accelerated Corrosion Behavior of Steel in Concrete Subjected to Sustained Flexural Loading Using Electrochemical Methods and X-Ray Computed Tomography', *Journal of Materials in Civil Engineering*, 30 (7), pp. 04018131. doi:[http://dx.doi.org/10.1061/\(Asce\)Mt.1943-5533.0002337](http://dx.doi.org/10.1061/(Asce)Mt.1943-5533.0002337).
- [245] Wang, P.H. et al. (2020) 'Three-dimensional characteristics of steel corrosion and corrosion-induced cracks in magnesium oxychloride cement concrete monitored by X-ray computed tomography', *Construction and Building Materials*, 246 pp. 118504. doi:<http://dx.doi.org/10.1016/j.conbuildmat.2020.118504>.
- [246] Wang, X.X. et al. (2021) 'Research on internal monitoring of reinforced concrete under accelerated corrosion, using XCT and DIC technology', *Construction and Building Materials*, 266 pp. 121018. doi:<http://dx.doi.org/10.1016/j.conbuildmat.2020.121018>.
- [247] Kashani, M.M., Crewe, A.J. and Alexander, N.A. (2013) 'Use of a 3D optical measurement technique for stochastic corrosion pattern analysis of reinforcing bars subjected to accelerated corrosion', *Corrosion Science*, 73 pp. 208-221. doi:<http://dx.doi.org/10.1016/j.corsci.2013.03.037>.
- [248] Guha, R. and Ouellet-Plamondon, C.M. (2024) 'Analysis of porous alkali activated materials using bauxite residue as principal precursor', *Journal of Building Engineering*, 96 pp. 110502. doi:<http://dx.doi.org/10.1016/j.jobee.2024.110502>.
- [249] Brakat, A. and Zhang, Y.M. (2019) 'Shrinkage mitigation of alkali-activated slag with natural cellulose fibres', *Advances in Cement Research*, 31 (2), pp. 47-57. doi:<http://dx.doi.org/10.1680/jadcr.17.00147>.
- [250] Ling, Y. et al. (2024) 'Bond performance of reinforcing bars in fly ash-based engineered geopolymer composites under uniform and nonuniform corrosion conditions', *Cement and Concrete Composites*, 152 pp. 105680. doi:<http://dx.doi.org/10.1016/j.cemconcomp.2024.105680>.
- [251] Fu, C.Q. et al. (2018) 'Non-uniform corrosion of steel in mortar induced by impressed current method: An experimental and numerical investigation', *Construction and Building Materials*, 183 pp. 429-438. doi:<http://dx.doi.org/10.1016/j.conbuildmat.2018.06.183>.
- [252] Chen, D. and Mahadevan, S. (2008) 'Chloride-induced reinforcement corrosion and concrete cracking simulation', *Cement and Concrete Composites*, 30 (3), pp. 227-238. doi:<http://dx.doi.org/10.1016/j.cemconcomp.2006.10.007>.
- [253] Liu, Q.-f. et al. (2023) 'A numerical study on chloride transport in alkali-activated fly ash/slag concretes', *Cement and Concrete Research*, 166 pp. 107094. doi:<http://dx.doi.org/10.1016/j.cemconres.2023.107094>.
- [254] Chen, X. et al. (2020) 'A multi-phase mesoscopic simulation model for the diffusion of chloride in concrete under freeze-thaw cycles', *Construction Building Materials*, 265 pp. 120223. doi:<http://dx.doi.org/10.1016/j.conbuildmat.2020.120223>.
- [255] Van der Zanden, A., Taher, A. and Arends, T. (2015) 'Modelling of water and chloride transport in concrete during yearly wetting/drying cycles', *Construction Building Materials*, 81 pp. 120-129. doi:<http://dx.doi.org/10.1016/j.conbuildmat.2015.02.012>.

- [256] Bentz, D.P. et al. (2013) 'Modeling of the influence of transverse cracking on chloride penetration into concrete', *Cement and Concrete Composites*, 38 pp. 65-74. doi:<http://dx.doi.org/10.1016/j.cemconcomp.2013.03.003>.
- [257] Cao, C. (2014) '3D simulation of localized steel corrosion in chloride contaminated reinforced concrete', *Construction and Building Materials*, 72 pp. 434-443. doi:<http://dx.doi.org/10.1016/j.conbuildmat.2014.09.030>.
- [258] Jones, S. et al. (2015) 'Simulation studies of methods to delay corrosion and increase service life for cracked concrete exposed to chlorides', *Cement and Concrete Composites*, 58 pp. 59-69. doi:<http://dx.doi.org/10.1016/j.cemconcomp.2014.12.014>.
- [259] Samson, G. et al. (2020) 'An alternative method to measure corrosion rate of reinforced concrete structures', *Cement and Concrete Composites*, 112 pp. 103672. doi:<http://dx.doi.org/10.1016/j.cemconcomp.2020.103672>.
- [260] Michel, A. et al. (2016) 'Propagation of steel corrosion in concrete: Experimental and numerical investigations', *Cement and Concrete Composites*, 70 pp. 171-182. doi:<http://dx.doi.org/10.1016/j.cemconcomp.2016.04.007>.
- [261] Yang, P. et al. (2020) 'Simulation of chloride diffusion in fly ash and limestone-calcined clay cement (LC3) concretes and the influence of damage on service-life', *Cement and Concrete Research*, 130 pp. 106010. doi:<http://dx.doi.org/10.1016/j.cemconres.2020.106010>.
- [262] Zhang, P. et al. (2020) 'Fabrication and engineering properties of concretes based on geopolymers/alkali-activated binders - A review', *Journal of Cleaner Production*, 258 pp. 120896. doi:<http://dx.doi.org/10.1016/j.jclepro.2020.120896>.
- [263] British Standards Institution (2021) BS EN 12390-1: Testing hardened concrete. Sand other requirements for specimens and moulds. London, BSI. doi:<http://dx.doi.org/10.3403/30397529>.
- [264] British Standards Institution (2016) BS EN 196-1: Methods of testing cement. Determination of strength. London, BSI. doi:<http://dx.doi.org/10.3403/30291447>.
- [265] RILEM (1994) RILEM Technical Recommendations for the testing and use of construction materials. London: CRC Press.
- [266] British Standards Institution (2005) BSEN 14651: 2005+ A1: 2007. Test method for metallic fibre concrete—Measuring the flexural tensile strength (limit of proportionality (LOP), residual). London, UK, BSI. doi:<http://dx.doi.org/10.3403/30092475U>.
- [267] Yuan, Y.S., Ji, Y.S. and Shah, S.P. (2007) 'Comparison of two accelerated corrosion techniques for concrete structures', *ACI Structural Journal*, 104 (3), pp. 344-347. doi:<http://dx.doi.org/10.14359/18624>.
- [268] Zhu, J. et al. (2021) 'Electrochemical and microstructural evaluation of acidification damage induced by impressed current cathodic protection after incorporating a hydroxy activated-Mg/Al-double oxide in the external anode mortar', *Construction and Building Materials*, 309 pp. 125116. doi:<http://dx.doi.org/10.1016/j.conbuildmat.2021.125116>.
- [269] Zhang, Y. and Lu, Z. (2013) 'Bond property test of reinforced concrete with all soaking and impressed current method corrosion', *Transactions of Tianjin University*, 19 (5), pp. 366-371. doi:<http://dx.doi.org/10.1007/s12209-013-1984-x>.
- [270] British Standards Institution (2019) BS EN 12390-3: Testing hardened concrete. Compressive strength of test specimens. London, BSI. doi:<http://dx.doi.org/10.3403/30360097>.
- [271] British Standards Institution (2009) BS EN 12390-6: Testing hardened concrete. Tensile splitting strength of test specimens. London, BSI. doi:<http://dx.doi.org/10.3403/30454320>.
- [272] Hillerborg, A. (1983) 'Concrete fracture energy tests performed by 9 laboratories according to a draft RILEM recommendation'.
- [273] Peterson, P.J.C. and research, C. (1980) 'Fracture energy of concrete: Method of determination', *Cement and Concrete Research*, 10 (1), pp. 79-89. doi:[http://dx.doi.org/10.1016/0008-8846\(80\)90054-X](http://dx.doi.org/10.1016/0008-8846(80)90054-X).

- [274] Visintin, P., Oehlers, D.J. and Haskett, M. (2013) 'Partial-interaction time dependent behaviour of reinforced concrete beams', *Engineering Structures*, 49 pp. 408-420. doi:<http://dx.doi.org/10.1016/j.engstruct.2012.11.025>.
- [275] Zhang, T. et al. (2014) 'Presliding Shear Failure in Prestressed RC Beams. I: Partial-Interaction Mechanism', *Journal of Structural Engineering*, 140 (10), pp. 04014069. doi:[http://dx.doi.org/10.1061/\(ASCE\)St.1943-541x.0000988](http://dx.doi.org/10.1061/(ASCE)St.1943-541x.0000988).
- [276] Scribner, L.L. (1990) The measurement and correction of electrolyte resistance in electrochemical tests. ASTM International.
- [277] Martínez, I. and Andrade, C. (2011) 'Polarization resistance measurements of bars embedded in concrete with different chloride concentrations: EIS and DC comparison', *Materials and Corrosion*, 62 (10), pp. 932-942. doi:<http://dx.doi.org/10.1002/maco.200905596>.
- [278] ASTM International (2020) ASTM C1218/C1218M-20, Standard Test Method for Water-Soluble Chloride in Mortar and Concrete. West Conshohocken, PA, ASTM International. doi:http://dx.doi.org/10.1520/C1218_C1218M-20.
- [279] ASTM International (2020) ASTM C1152/C1152M-20, Standard Test Method for Acid-Soluble Chloride in Mortar and Concrete. West Conshohocken, PA, ASTM International. doi:http://dx.doi.org/10.1520/C1152_C1152M-20.
- [280] Zhang, Z.D. et al. (2020) 'A laboratory investigation of cutting damage to the steel-concrete interface', *Cement and Concrete Research*, 138 pp. 106229. doi:<http://dx.doi.org/10.1016/j.cemconres.2020.106229>.
- [281] Cao, C. and Cheung, M.M.S. (2014) 'Non-uniform rust expansion for chloride-induced pitting corrosion in RC structures', *Construction and Building Materials*, 51 pp. 75-81. doi:<http://dx.doi.org/10.1016/j.conbuildmat.2013.10.042>.
- [282] Zhang, G.Y. et al. (2020) 'A self-balanced electrochemical model for corrosion of reinforcing steel bar in considering the micro-environments in concrete', *Construction and Building Materials*, 254 pp. 119116. doi:<http://dx.doi.org/10.1016/j.conbuildmat.2020.119116>.
- [283] Rettich, T.R., Battino, R. and Wilhelm, E.J.T.J.o.C.T. (2000) 'Solubility of gases in liquids. 22. High-precision determination of Henry's law constants of oxygen in liquid water from T= 274 K to T= 328 K', *The Journal of Chemical Thermodynamics*, 32 (9), pp. 1145-1156. doi:<http://dx.doi.org/10.1006/jcht.1999.0581>.
- [284] Hussain, R.R. (2011) 'Effect of moisture variation on oxygen consumption rate of corroding steel in chloride contaminated concrete', *Cement and Concrete Composites*, 33 (1), pp. 154-161. doi:<http://dx.doi.org/10.1016/j.cemconcomp.2010.09.014>.
- [285] Kobayashi, K. and Shuttoh, K. (1991) 'Oxygen Diffusivity of Various Cementitious Materials', *Cement and Concrete Research*, 21 (2-3), pp. 273-284. doi:[http://dx.doi.org/10.1016/0008-8846\(91\)90009-7](http://dx.doi.org/10.1016/0008-8846(91)90009-7).
- [286] Wei, X.B. et al. (2021) 'Influence of low-temperature curing on the mechanical strength, hydration process, and microstructure of alkali-activated fly ash and ground granulated blast furnace slag mortar', *Construction and Building Materials*, 269 pp. 121811. doi:<http://dx.doi.org/10.1016/j.conbuildmat.2020.121811>.
- [287] Suda, K., Misra, S. and Motohashi, K. (1993) 'Corrosion Products of Reinforcing Bars Embedded in Concrete', *Corrosion Science*, 35 (5-8), pp. 1543-1549. doi:[http://dx.doi.org/10.1016/0010-938x\(93\)90382-Q](http://dx.doi.org/10.1016/0010-938x(93)90382-Q).
- [288] Chen, W. et al. (2023) 'Impact of heat curing regime on the compressive strength and drying shrinkage of alkali-activated slag mortar', *Developments in the Built Environment*, 14 pp. 100123. doi:<http://dx.doi.org/10.1016/j.dibe.2023.100123>.
- [289] Fang, G.H. and Zhang, M.Z. (2020) 'The evolution of interfacial transition zone in alkali-activated fly ash-slag concrete', *Cement and Concrete Research*, 129 pp. 105963. doi:<http://dx.doi.org/10.1016/j.cemconres.2019.105963>.

- [290] San Nicolas, R. and Provis, J.L. (2015) 'The Interfacial Transition Zone in Alkali-Activated Slag Mortars', *Frontiers in Materials*, 2 pp. doi:<http://dx.doi.org/10.3389/fmats.2015.00070>.
- [291] Rashad, A.M. (2022) 'Effect of limestone powder on the properties of alkali-activated materials—A critical overview', *Construction and Building Materials*, 356 pp. 129188. doi:<http://dx.doi.org/10.1016/j.conbuildmat.2022.129188>.
- [292] Li, H. et al. (2023) 'Flexural behaviors of concrete beams under monotonic and cyclic loadings', *Construction and Building Materials*, 362 pp. 129721. doi:<http://dx.doi.org/10.1016/j.conbuildmat.2022.129721>.
- [293] Liu, Z.Y., Zhang, Y.S. and Jiang, Q. (2014) 'Continuous tracking of the relationship between resistivity and pore structure of cement pastes', *Construction and Building Materials*, 53 pp. 26-31. doi:<http://dx.doi.org/10.1016/j.conbuildmat.2013.11.067>.
- [294] Azarsa, P. and Gupta, R. (2017) 'Electrical Resistivity of Concrete for Durability Evaluation: A Review', *Advances in Materials Science and Engineering*, 2017 (1), pp. 8453095. doi:<http://dx.doi.org/10.1155/2017/8453095>.
- [295] Miranda, J.M. et al. (2005) 'Corrosion resistance in activated fly ash mortars', *Cement and Concrete Research*, 35 (6), pp. 1210-1217. doi:<http://dx.doi.org/10.1016/j.cemconres.2004.07.030>.
- [296] Zhang, Z.M. et al. (2021) 'Corrosion behavior of the reinforcement in chloride-contaminated alkali-activated fly ash pore solution', *Composites Part B-Engineering*, 224 pp. 109215. doi:<http://dx.doi.org/10.1016/j.compositesb.2021.109215>.
- [297] Yip, C.K. and Van Deventer, J.S.J. (2003) 'Microanalysis of calcium silicate hydrate gel formed within a geopolymeric binder', *Journal of Materials Science*, 38 (18), pp. 3851-3860. doi:<http://dx.doi.org/10.1023/A:1025904905176>.
- [298] Yip, C.K. et al. (2008) 'Effect of calcium silicate sources on geopolymerisation', *Cement and Concrete Research*, 38 (4), pp. 554-564. doi:<http://dx.doi.org/10.1016/j.cemconres.2007.11.001>.
- [299] Liu, T. et al. (2020) 'Effect of MgO, Mg-Al-NO₃ LDH and calcined LDH-CO₃ on chloride resistance of alkali activated fly ash and slag blends', *Construction and Building Materials*, 250 pp. 118865. doi:<http://dx.doi.org/10.1016/j.conbuildmat.2020.118865>.
- [300] Ma, G. et al. (2022) 'Enhanced inhibition performance of NO₂-intercalated MgAl-LDH modified with nano-SiO₂ on steel corrosion in simulated concrete pore solution', *Corrosion Science*, 204 pp. 110387. doi:<http://dx.doi.org/10.1016/j.corsci.2022.110387>.
- [301] Balcikanli, M. and Ozbay, E. (2016) 'Optimum design of alkali activated slag concretes for the low oxygen/chloride ion permeability and thermal conductivity', *Composites Part B-Engineering*, 91 pp. 243-256. doi:<http://dx.doi.org/10.1016/j.compositesb.2016.01.047>.
- [302] Bondar, D. et al. (2012) 'Oxygen and Chloride Permeability of Alkali-Activated Natural Pozzolan Concrete', *ACI Materials Journal*, 109 (1), pp. 53-62. doi:<http://dx.doi.org/10.14359/51683570>.
- [303] Dellinghausen, L.M. et al. (2012) 'Total shrinkage, oxygen permeability, and chloride ion penetration in concrete made with white Portland cement and blast-furnace slag', *Construction and Building Materials*, 37 pp. 652-659. doi:<http://dx.doi.org/10.1016/j.conbuildmat.2012.07.076>.
- [304] Shi, J.J., Ming, J. and Sun, W. (2018) 'Electrochemical behaviour of a novel alloy steel in alkali-activated slag mortars', *Cement and Concrete Composites*, 92 pp. 110-124. doi:<http://dx.doi.org/10.1016/j.cemconcomp.2018.06.004>.
- [305] Forbes, C. et al. (2011) *Statistical distributions*. John Wiley & Sons.
- [306] Bernachy-Barbe, F. et al. (2020) 'Using X-ray microtomography to study the initiation of chloride-induced reinforcement corrosion in cracked concrete', *Construction and Building Materials*, 259 pp. 119574. doi:<http://dx.doi.org/10.1016/j.conbuildmat.2020.119574>.

- [307] Gonzalez, J. et al. (1995) 'Comparison of rates of general corrosion and maximum pitting penetration on concrete embedded steel reinforcement', *Cement and Concrete Research*, 25 (2), pp. 257-264. doi:[http://dx.doi.org/10.1016/0008-8846\(95\)00006-2](http://dx.doi.org/10.1016/0008-8846(95)00006-2).
- [308] Jang, B.S. and Oh, B.H. (2010) 'Effects of non-uniform corrosion on the cracking and service life of reinforced concrete structures', *Cement and Concrete Research*, 40 (9), pp. 1441-1450. doi:<http://dx.doi.org/10.1016/j.cemconres.2010.03.018>.
- [309] Šavija, B. et al. (2013) 'Cracking of the concrete cover due to reinforcement corrosion: A two-dimensional lattice model study', *Construction and Building Materials*, 44 pp. 626-638. doi:<http://dx.doi.org/10.1016/j.conbuildmat.2013.03.063>.
- [310] Bui, H.T. and Tan, K.H. (2023) 'Multi-peak nonuniform model of rust distribution and corrosion-induced concrete cracking in reinforced concrete slabs', *Cement Concrete Composites*, 140 pp. 105087. doi:<http://dx.doi.org/10.1016/j.cemconcomp.2023.105087>.
- [311] Wang, G. et al. (2021) 'Diffusion of chloride ion in coral aggregate seawater concrete under marine environment', *Construction and Building Materials*, 284 pp. 122821. doi:<http://dx.doi.org/10.1016/j.conbuildmat.2021.122821>.
- [312] Ji, Y.S. et al. (2016) 'Laboratory studies on influence of transverse cracking on chloride induced corrosion rate in concrete', *Cement and Concrete Composites*, 69 pp. 28-37. doi:<http://dx.doi.org/10.1016/j.cemconcomp.2015.12.006>.
- [313] Subramaniam, K.V. and Bi, M.D. (2010) 'Investigation of steel corrosion in cracked concrete: Evaluation of macrocell and microcell rates using Tafel polarization response', *Corrosion Science*, 52 (8), pp. 2725-2735. doi:<http://dx.doi.org/10.1016/j.corsci.2010.04.030>.